Universidade de Lisboa
Faculdade de Ciências
Departamento de Engenharia Geográfica, Geofísica e Energia

Continental Surface Water and Energy Budgets in the XX and XXI Centuries

Sandra Maria de Carvalho Gomes

Doutoramento em Ciências Geofísicas e da Geoinformação
(Meteorologia)
2014

Universidade de Lisboa
Faculdade de Ciências
Departamento de Engenharia Geográfica, Geofísica e Energia

Continental Surface Water and Energy Budgets in the XX and XXI Centuries

Sandra Maria de Carvalho Gomes

Tese orientada pelo Prof. Doutor Pedro Miranda e pelo Doutor Pedro Viterbo, especialmente elaborada para a obtenção do grau de doutor em Ciências Geofísicas e da Geoinformação especialidade de Meteorologia

2014

Contents

Acknowledgements

At the end of my thesis, it is a pleasant task to express my thanks to all those who contributed in many ways to the success of this study and made it an unforgettable experience for me. This thesis has been kept on track and been seen through to completion with the support and encouragement of numerous people including my friends, family, colleagues and various institutions.

My first acknowledgement goes to Doctor Pedro Viterbo, my PhD supervisor. His guidance and support during the long period of this work were important to overcome the several difficulties that arose. His belief in the successful completion of this thesis and the logistic support were essential. Thanks to my co-supervisor Professor Doctor Pedro Miranda and Dr Graham Weedon from the Centre for Ecology & Hydrology (CEH).

To "Fundação para a Ciência e a Tecnologia" (FCT) I am grateful for the financial support through a PhD scholarship (SFRH/BD/76852/2011). I am also indebted to the financial support from Integrated Project Water and Global Change (WATCH, 2007-2011), funded under the EU FP6 and to the logistic support of "Faculdade de Ciências da Universidade de Lisboa" (FCUL), "Instituto Dom Luiz" (IDL) and "Instituto Português do Mar e da Atmosfera" (IPMA). I would like to express a special thanks to all colleagues from IPMA and IDL.

Dear Mum, Dad and my siblings it is hard to express my thanks to you in words. Your understanding, the faith, advise, intellectual spirit and indescribable support to me throughout my whole life are invaluable. Last but not least, I would like to pay high regards to my husband José, who listened and discussed ideas about this thesis with me on many occasions, and my son Jorge for their sincere encouragement and inspiration throughout my research work and lifting me uphill this phase of life. I owe everything to them. To my son by his lovely smile. Their guidance and support during the long period of this work were important to overcome the several difficulties that arose. Their belief in the successful completion of this thesis and the logistic support were essential.

Besides this, several people have knowingly and unknowingly helped me in the successful completion of this project.

Thanks again to everyone who made this thesis possible.

Resumo

Diversos estudos emergiram nas últimas décadas tendo em vista a caracterização e estimativa do ciclo hidrológico terrestre bem como do ciclo energético. O Programa GEWEX ("Global Energy and Water Cycle Experiment"), iniciado nos anos 90 do século XX, tem sido a entidade que enquadra estas atividades a nível global e continental; o projeto FP5 WATCH ("WATer and global CHange"), no qual esta tese está inserida, contribuiu para o conhecimento, caracterização e previsão de variações no ciclo hidrológico e energético à superfície nos séculos XX e XXI, bem como alterações nos processos hidrológicos e dos recursos hídricos a escalas regionais.

Uma das formas de caracterizar as trocas de água à superfície é o recurso a observações *in-situ* capazes de reproduzir séries hidrológicas. As observações *in-situ*, limitadas a pontos de medidas de caudais de cursos de água, podem ser complementadas por modelos de superfície forçados por séries meteorológicas. Os primeiros registos de observações de variáveis meteorológicas começaram a surgir, à escala continental, há cerca de 120 anos. Atualmente existem sínteses de observações mensais, para todo o globo desde o início do século XX, por exemplo o conjunto de dados da CRU ("Climatic Research Unit") e do GPCC ("Global Precipitation Climatology Centre"), disponibilizando séries mensais de precipitação, entre outras variáveis, no caso do CRU. Para compensar a irregularidade na distribuição espacial de observações surgiram as reanálises obtidas por assimilação multivariada de dados provenientes de diversas fontes (medições *in-situ*, radiosondas e deteção remota) combinadas com estimativas *a priori* de modelos de previsão. Exemplos incluem as reanálises da NASA ("National Aeronautics and Space Administration"), do NCEP ("National Centers for Environmental Prediction"), do ECMWF ("European Centre for Medium-Range Weather Forecasts") e do JMA ("Japan Meteorological Agency"). Muitos dos dados utilizados atualmente para forçar modelos de superfície foram construídos a partir de reanálises disponíveis essencialmente para a segunda metade do século XX até à atualidade. Os erros sistemáticos inerentes às reanálises são minimizados quando corrigidos com as observações disponíveis. Bases de dados globais a 1 grau de resolução incluem: NCC, construída para 1948-2000 a partir da reanálise do NCEP/NCAR; e PGF ("Princeton Global Forcing"), corrigida pelas observações do CRU. O projeto WATCH produziu a WFD ("WATCH Forcing Data") recriada a partir da reanálise ERA-40 e das observações do CRU e GPCC. A WFD tem uma resolução espacial de 0.5 graus, gerada em 67420 pontos de terra (excluindo a Antártica) e disponibiliza cinco variáveis com 6h de resolução temporal e os fluxos a 3h. A primeira metade do século XX, onde é bastante mais difícil recriar reanálises de boa qualidade devido à insuficiência dos sistemas de observação, pode ser reproduzida através de métodos estatísticos e de desagregação diária aplicados a estimativas mensais. Os "weather generators" estocásticos produzem séries temporais de dados meteorológicos sintéticos para um determinado local de acordo com as características estatísticas das variáveis. Paralelamente surgiram os modelos lineares generalizados (GLM – "Generalized Linear Model"), que permitem a estimativa de uma variável através de uma combinação linear de covariáveis. A aproximação GLM pode ser aplicada a um "weather generator" paramétrico, para várias variáveis no mesmo local simultaneamente. De modo a poder aplicar os resultados obtidos pelo GLM foi necessário desenvolver métodos de desagregação diária que permitem a utilização desses dados para forçar modelos de superfície.

O clima futuro, essencial para a representação do ciclo da água no século XXI, pode ser estimado recorrendo a modelos de circulação atmosférica. O projeto WATCH disponibiliza forçamento atmosférico diário à escala global, 0.5º apenas pontos de terra, para o clima atual [1960-2000] e cenários B1 e A2 [2001-2100] do quarto relatório do IPCC, fornecendo as condições necessárias para guiar modelos hidrológicos e modelos de superfície. Nesta tese, o forçamento resulta da projeção de três modelos atmosfera-oceano acoplados (ECHAM5/MPIOM, CNRM-CM3 e LMDZ-4) seguindo os cenários de emissão B1 (otimista) e A2 (pessimista) do IPCC. Devido aos erros sistemáticos inerentes aos resultados dos modelos climáticos, foi aplicada uma correção estatística ao output de forma a eliminar o viés, podendo assim ser posteriormente utilizado como forçamento de modelos hidrológicos

globais e calcular as variações no ciclo hidrológico e fluxos de energia em vários cenários do clima futuro.

Dependendo do objetivo, os modelos hidrológicos são divididos em duas categorias: modelos de superfície (LSM – "Land Surface Models") e modelos de balanço de água (WBM – "Water Balance Models"), também denominados modelos hidrológicos globais (GHM – "Global terrestrial Hydrological Models"). Nos modelos GHMs o ciclo da água é tratado de forma conceptual, enquanto os LSMs resolvem tanto o balanço água como o de energia. Para além disso os dois tipos de modelos podem diferir na resolução espacial e temporal, detalhes nos processos, número de parâmetros e de dados necessários. Apesar destas diferenças tanto os GHMs como os LSMs são usados para estimar variáveis de estado hidrológicas e fluxos de água e energia. De modo a analisar as incertezas associadas ao ciclo da água, diferentes comunidades (hidrologia, meteorológica e de clima) juntaram-se de modo a comparar resultados e criar um ensemble de dados a partir de diferentes modelos. A intercomparação de modelos (PILPS, ALMIP, GSWP2, WaterMIP) permite a avaliação da incerteza associada a diversos fatores, entre eles as parametrizações próprias de cada modelo.

Esta tese está dividida em duas partes: desenvolvimento de dados de forçamento para modelos hidrológicos; respetiva validação e estimativa do ciclo hidrológico e energético nos séculos XX e XXI. O forçamento é utilizado pelos modelos de superfície, o que permitiu a criação de um ensemble de modelos hidrológicos (GHMs e LSMs)) contribuindo para a caracterização da hidrologia em ambos os séculos e da estimativa da incerteza associada. A base de dados de forçamento meteorológico, desenvolvida no âmbito do projeto WATCH, é uma base de dados longa e globalmente consistente de variáveis meteorológicas utilizada para conduzir modelos hidrológicos. A coerência da base de dados foi testada em simulações hidrológicas com alguns dos modelos hidrológicos participantes no projeto de intercomparação de modelos do WATCH (WaterMIP), para o qual esta tese contribuiu com simulações HTESSEL, um LSM. De modo a caracterizar o balanço de energia, foram feitos vários testes de sensibilidade ao forçamento e às parametrizações físicas do modelo.

Paralelamente foi utilizado o forçamento atmosférico proveniente de modelos climáticos para os séculos XX e XXI (clima atual e cenários B1 e A2) estimado por modelos climáticos que fornecem as condições necessárias para guiar modelos hidrológicos em cenários futuros. A componente terrestre do ciclo hidrológico foi avaliada e analisada focando no período [2071-2100] e comparada com o clima presente [1971-2000]. Nesta tese foram apenas apresentados os resultados das simulações com o modelo de superfície HTESSEL conduzido com o forçamento proveniente do modelo de circulação global ECHAM para o clima presente e os cenários futuros B1 e A2. Aspetos hidrológicos associados a eventos extremos de seca e precipitação intensa nos séculos XX e XXI, foram igualmente analisados.

Os resultados obtidos permitem a caracterização dos ciclos hidrológico e energético à superfície em ambos os séculos. O ciclo hidrológico, apresentado apenas para o período 1985 a 1999, foi comparado com cinco modelos hidrológicos integrantes no projeto WaterMIP. A precipitação sobre os continentes estimada é de 880 mm/ano, dos quais 510 mm são libertados para a atmosfera devido ao processo de evapotranspiração e 368 mm de escoamento superficial e subterrâneo. O balanço de energia à superfície foi igualmente calculado e avaliado. A radiação disponível à superfície tem um saldo de aproximadamente 70 Wm^{-2}, dos quais 24 Wm^{-2} são libertados para a atmosfera sobre a forma de fluxo de calor sensível e 46 Wm^{-2} como fluxo de calor latente.

Apesar dos bons resultados à escala continental, os métodos de desagregação diária nas zonas polares podem ser melhorados, o que irá beneficiar os resultados no inverno nessas zonas. Além disso será benéfico a utilização de mais modelos para o ensemble de modelos no século XX e para o estudo da hidrologia no futuro. No último ano de execução desta tese foi desenvolvida uma base de dados similar à WFD, a WFDEI. Esta tem como ponto de partida a reanálise ERA-Interim disponível em tempo real e os resultados são disponibilizados pelo projeto WATCH.

Palavras-chave: Balanço de água e energia à superfície, superfície continental, modelos de superfície, forçamento atmosférico, alterações climáticas

Abstract

The global water cycle is an integral part of the Earth system, playing a central role in our climate and controlling the global energy cycle as well as carbon, nutrient, and sediment cycles.

The development of hydrological models and respective driving forcing allows a better knowledge of the land surface. There are a diversity of hydrological models and approaches, ranging from conceptually based lumped models to distributed physically based hydrology models. This range was developed in response to many different requirements in terms of scale, purpose, and availability data. Model intercomparison efforts have helped to reveal the strengths and weaknesses of the individual models. This exercise provides useful feedback to modellers and improved our understanding of the water cycle. Aspects like seasonal and interannual behaviour were analysed improving our knowledge about the land surface modelling. The methods and datasets developed in this thesis allow us to make estimates of past and future global water availability. The forcing data were used as input to hydrological and land surface models to produce comprehensive global water cycle data sets, which were also validated. The global water cycle data sets also provided invaluable historical data for areas of the world where little data or no observed climate and hydrological data exist.

The first step was the production of the WATCH Forcing Data, merging a 3-hourly reanalysis and monthly observations. The forcing data were then used as input to hydrological and land surface models, producing an ensemble of global water and energy cycle datasets. The use of this data assessed the hydrology of continental surface, focus on Europe.

The main purpose of this thesis was to provide a more consistent analysis of components of the terrestrial surface water and energy budgets for the twentieth and twentieth-first centuries. The forcing data is available to everyone.

Keywords: Surface hydrological and energy cycles, land surface, land surface models, atmospheric forcing, climate change

List of acronyms and abbreviations

20C3M	20th Century Climate in Coupled Models
AGCM	Atmosphere General Circulation Model
AIC	Akaike information criterion
ALMIP	AMMA – Land surface Model Intercomparison Project
AMMA	African Monsoon Multidisciplinary Analysis
AR4	IPCC Fourth Assessment Report
AR5	IPCC Fifth Assessment Report
BIC	Bayesian Information Criterion
CNRM-CM3	Centre National de Recherches Météorologiques Coupled Model Version 3
CR	Catch Ratio
CRU	Climate Research Unit
CTESSEL	Carbon Tiled ECMWF Scheme for Surface Exchanges over Land
DDM	Daily Disaggregator Method
DJF	December, January and February
ECHAM5/MPIOM	ECMWF and Hamburg (Coupled climate model consisting of atmospheric general circulation model and MPI-OM ocean-sea ice component developed at the Max Planck Institute for Meteorology - MPIM).
ECMWF	European Centre for Medium-Range Weather Forecasts
EI	El Niño index
ENSO	El Nino-Southern Oscillation
ERA-40	ECMWF 40-years reanalysis
ERAI	ECMWF Interim reanalysis
ESPI	ENSO precipitation index
FLUXNET	Global Network of Flux Towers
GCIP	GEWEX Continental Scale International Project
GCM	General Circulation Model
GEWEX	Global Energy and Water Cycle Experiment
GHM	Global terrestrial Hydrological Models
GLM	Generalized Linear Models
GPCC	Global Precipitation Climatology Centre
GPCP	Global Precipitation Climatology Project
GSWP	Global Soil Wetness Project
GWSP	Global Water System Project
HTESSEL	Hydrology Tiled ECMWF Scheme for Surface Exchanges over Land
IFS	Integrated Forecast System
IPCC	Intergovernmental Panel on Climate Change
ISLSCP	International Satellite Land Surface Climatology Project
ITCZ	Inter-tropical Convergence Zone
JJA	June, July and August
LI	La Niña index
LMDZ-4	Climate model developed at Laboratoire de Météorologie Dynamique
LPJmL	Lund-Potsdam-Jena managed Land Dynamic Global Vegetation and Water Balance Model
LSM	Land Surface Model
MacPDM	Macro-scale - Probability-Distributed Moisture model.
MAM	March, April and May
MPI-HM	Max Planck Institute – Hydrology Model
NASA	National Aeronautics and Space Administration

NCAR	National Center for Atmospheric Research
NCEP	National Centers for Environmental Prediction
NSM	Normalized Soil Moisture
NWP	Numerical weather prediction
OGCM	Oceanic General Circulation Models
PDSI	Palmer Drought Severity Index
PGF	Princeton Global Forcing
PILPS	Project for the Intercomparison of Land-Surface Parameterization Schemes
SON	September, October and November
SPI	Standard Precipitation Index
SRES	Special Report on Emission Scenarios
TESSEL	Tiled ECMWF Scheme for Surface Exchanges over Land
TWS	Terrestrial Water Storage
VIC	Variable Infiltration Capacity model
WATCH	WATer and global CHange
WaterGAP	Water - Global Assessment and Prognosis
WaterMIP	Water Model Intercomparison Project
WFD	WATCH Forcing Data
WFDEI	WATCH Forcing Data methodology applied to ERA-Interim data

Chapter 1 - Introduction

1.1 Motivation and brief state of the art

Peixoto and Oort (1992) defined the global hydrosphere as various reservoirs connected by the transfers of water in the various phases, playing a central role in the Earth climate system. The hydrological cycle has two major branches. The terrestrial branch consists of the inflow, outflow, and storage of water in its various forms on and in the continents and oceans, while the atmospheric branch consists of the atmospheric transports of water, mainly in the vapour phase. The two branches of the hydrological cycle communicate at the atmosphere-earth surface interface.

The Earth climate fluctuates and changes both regionally and globally. These changes are reflected in the variability and change of Earth's water budget and the complex and dynamic energy balance. The first description of the energy budget for the Earth was proposed by Dines (1917). Over the last two decades, improvements in estimating the global annual mean energy budget have resulted from satellite observations (Kiehl and Trenberth, 1997; Fasullo and Trenberth, 2008a, 2008b; Trenberth and Fasullo, 2008; Trenberth et al., 2009; Trenberth et al., 2011). Recently, an assessment of the global energy and hydrological cycles from eight current atmospheric reanalyses and their depiction of changes over time were made by Trenberth et al. (2011). Early studies of the water cycle include Chahine (1992), and Oki (1999); Peixoto and Oort (1992) provided an estimated global water cycle partly based on their computations for atmospheric vapour transport. Oki (1999) compiled a water cycle based on estimates of atmospheric transports from ECMWF and precipitation data. However, there are still very few studies on a global scale, providing a synthesis of the mean and variability of the global water cycle, and corresponding error estimates (Oki and Kanae 2006; Trenberth et al. 2007; Trenberth et al. 2011; Trenberth and Asrar 2014). Due to the scarcity of data on a global scale of its various components, e.g., precipitation, surface evapotranspiration, terrestrial runoff, our knowledge of the global cycle is limited. Sheffield et al. (2010) study was a first step in quantifying the long-term variation in global land evapotranspiration from remote sensing data. Nevertheless satellite data do not adequately close the water budget at regional scale (Gao et al., 2010; Sheffield et al., 2010; Vinukollu et al., 2011; Sahoo et al., 2011).

The terrestrial hydrological cycle is an important component of the global climate and biospheric system, influencing the climate in a variety of ways. The water is recycled in a continuous process known as the water cycle. Exchanges of moisture and energy between the atmosphere and the Earth's surface affect the dynamics and thermodynamics of the climate system. In the forms of vapour, cloud liquid and ice water, rain, snow and hail, as well as during phase transitions, water plays opposing roles in heating and cooling the environment. The energy from the Sun triggers the global movement of water, the water cycle. The Sun's differential heating, varying with latitude and time of the year, drives a continuous exchange of water among the reservoirs. On the other hand, the exchange pathways are controlled by surface properties and atmospheric and ocean circulation.

Water and energy cycles are expressed with similar equations (Seneviratne et al., 2010). They are both governed by conservation laws for water mass and energy. Cycles have similar components: storage and transport terms. The storage terms represent the great reservoirs of water and energy, and the transport terms represent the flux of water and energy from place to place. In addition, water phase transitions contribute to the energy cycle, and its internal, kinetic, and potential components. For these reasons, water and energy cycles are closely interlinked and cannot be treated independently. The water cycle is linked to the energy cycle via the evaporative cooling at the surface and latent heating release in the atmosphere, as atmospheric systems play a primary role in moving heat upward. Water vapour in the atmosphere absorbs the incoming solar radiation and partially traps the long wave radiation from the Earth's surface. Exchanges of moisture and heat between the atmosphere and the surface fundamentally affect the dynamics and the thermodynamics of the climate system.

The water cycle is a closed system: the volume of water in the hydrosphere today is the same amount of water that has always been present in the Earth system. Water evaporated from the oceans, lakes, river, or soil is driven by solar energy. In addition, water moves from plants to the atmosphere due to transpiration. It forms water vapour and clouds, which eventually comes back to Earth as rain, snow, dew or hail, or other forms of precipitation. Precipitation runs at surface as runoff or as ground water, and eventually, back into the surface reservoirs. Rain or melt water may be intercepted by vegetation cover or retained by land surface depressions, may infiltrate into the soil, or may run over the land surface into streams. Infiltrated water may be stored in the soil as soil moisture or may percolate to deeper layers to be stored as groundwater. During cold periods a portion of infiltrated water may freeze in the soil. Part of water intercepted by vegetation, accumulated in land surface depressions, and stored in the soil, may return back to the atmosphere as a result of evaporation. Plants take up a significant portion of the soil moisture from the root zone and evaporate most of this water through their leaves. In addition to the redistribution of water, the hydrological cycle is also responsible for the absorption and redistribution of solar energy from one location to another. Latent heat release occurs when condensed (liquid or soil) water transforms to vapour and plays a fundamental role in the Earth's radiation balance. Evaporation absorbs energy from the surface and releases it into the atmosphere where water vapour condenses into clouds. Redistribution of moisture and precipitation is controlled by surface such as orography and coastlines, influencing the hydrological cycle. Soil moisture evaporation, canopy evaporation and plant transpiration affect the distribution of precipitation and air temperature. On bare land surfaces, soil moisture controls soil heat flux and land albedo; drier soils have higher emissivity and are more reflective. Soil moisture availability determines the type and amount of vegetation. Processes described above are an integral part of atmospheric numerical models.

Computation of the seasonal cycle of water and energy fluxes between the atmosphere and land may be carried out in three ways (Kinter and Shukla, 1990). First, the existing operational analyses of atmospheric data can be used. Second, a set of reanalysed data must be created from the historical record to broaden the database and to develop an internally consistent, homogeneous, and multivariate time series of climate observations. Third, a long integration of the most realistic, high resolution global climate model available should be made for comparison with the first two datasets in order to validate the model and identify and eliminate sources of systematic error.

There have been several projects for the study of hydrology and energy globally. The Global Energy and Water Cycle Experiment (GEWEX), an international programme, was implemented to observe and characterize the full hydrological cycle and energy fluxes in the atmosphere, at the land surface and in the upper ocean. This programme provided the essential remote sensing and *in situ* measurements and undertook modelling and field studies of the hydrological cycle. The programme provided the necessary knowledge to predict variations of the global hydrological regimes as well as changes in regional hydrological processes and water resources. A central component of GEWEX was GCIP (GEWEX Continental Scale International Project), whose major goals were: 1) determination of the temporal and spatial variation of water and energy budgets by observations on a continental scale, 2) development and testing of large-scale models of the interactions between land surface hydrology and the atmosphere suitable for coupling with general circulation models (GCM) and numerical weather prediction (NWP) models, and 3) development and testing of models and procedures for assessing the impact of possible climate variations on water resources systems.

Recently a new international project, the WATCH project (WATer and global CHange, Harding et al. 2011, and papers in the same special volume of J. Hydrometeorology; see also http://www.eu-watch.org/), joined water resources and climate communities to analyse, quantify and predict the components of the current and future global water cycles and related water resources states. New meteorological forcing data were developed by the WATCH project in order to investigate the nature of global water cycle on land and used to run land surface and hydrological models. These data are derived from reanalysis and bias corrected with global observations. Reanalysis represent a merger between

satellite observations and models and provide globally continuous data. The WATCH forcing data (WFD) were analysed from a global water and energy cycles perspective to characterize the hydrology and surface energy at a regional scale to global in current climate (20th century) and future climate (21st century) with the aid of large-scale models (50 km resolution). These models represent the balance of energy and water at the land surface, requiring long series of consistent meteorological forcing with preferably a semi-diurnal temporal resolution. The estimates of various components that enter into the hydrological cycle have considerable uncertainty whether they come from *in situ* data, satellite data, hybrid merged products, or reanalysis products (Trenberth et al., 2011).

A variety of models of the terrestrial hydrological cycle (hydrological and land surface models) were compared by WaterMIP (Water Model Intercomparison Project), producing a multi-model ensemble estimates of the state of the world's water resources for the 20th and 21st centuries (Haddeland et al., 2011). The main goals were 1) to understand the differences between hydrological and land surface models to improve these models; 2) to estimate and understand the impacts of global change of the global hydrological cycle and water resources. The uncertainty of the output of hydrological models is characterized as well as the uncertainty in forcing data used to conduct the model. The effect of the uncertainty associated with the forcing is assessed by running the disturbed versions with the same land surface model. An ensemble of hydrological and land surface models with the same forcing will be used to determine the uncertainty due to inaccuracies in the models. The combination of both methods allows the production of a realistic assessment of total uncertainty in hydrological and energy cycle over land.

A main reason for the model uncertainties is the lack of adequate data at the large scales considered here. These deficiencies apply both to the data that are required to drive the models as well as to data needed to evaluate simulation results. Given that precipitation is the most important climate input variable to force hydrological models, unrealistic precipitation data has been identified as one of the main factors causing deficient simulation results (Nijssen et al. 2001). Among the other components of the continental water balance that potentially could serve for model validation, evapotranspiration is not measured directly at large scales and may at best be estimated with considerable uncertainties from satellite data and on surface meteorological data.

1.2 Overview of water and energy budget

1.2.1 Global hydrological cycle

The water cycle and climate are intimately related. All land processes depend on water, which has a crucial role in Earth's climate and environment. Hydrological processes are key controls on human-driven changes in global cycling of carbon, nitrogen, and other elements. Water, evaporated from ocean and land surface, is driven by solar heating, transported by winds and condensed to form clouds. Precipitation over land may be stored as snow or soil moisture, while excess precipitation runs off into the oceans completing the global water cycle. There have been several studies about the water cycle. Hirabayashi et al. (2005) derived 100-year daily estimation of terrestrial land surface water fluxes. These fluxes were estimated for the 20th century driving a LSM under the long-term atmospheric forcing that was stochastically estimated from monthly mean time series. Trenberth et al. (2007) provided a new estimate of the global hydrological cycle for long term annual means that includes estimates of the main reservoirs of water as well the flows of water among them (Figure 1.1).

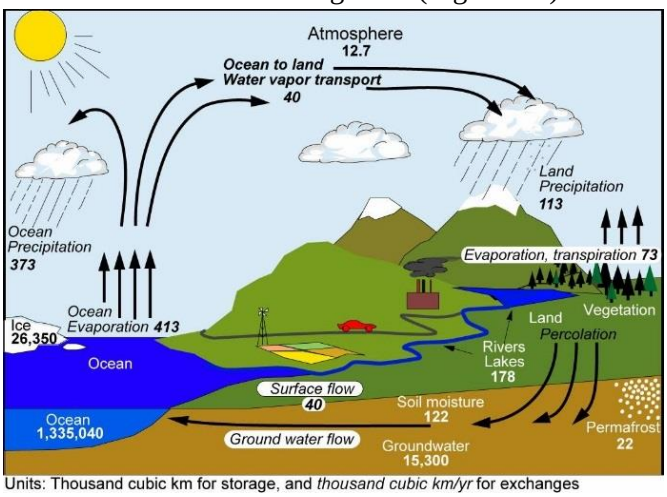

Figure 1.1: The hydrological cycle. Estimates of the main water reservoirs, given in plain font in 10^3 km^3, and the flow of moisture through the system, given in slant font (10^3 km^3 yr^{-1}), equivalent to Eg (10^{18} g) yr^{-1}. (From Trenberth et al., 2007)

In general terms, the continental water balance accounts for four major components, i.e., precipitation on land surface is balanced by evapotranspiration, discharge and changes in terrestrial water storage (Adam et al., 2006 and Seneviratne et al., 2010). This section presents the terrestrial, atmospheric, and combined water-balance equations. Peixoto and Oort (1992, chapter 12), Yeh et al. (1998), and Oki (1999) give good reviews on this topic. The variation of the terrestrial water storage (TWS) is governed by the following equation (Balsamo et. al, 2009):

$$\frac{dTWS}{dt} = P + E + (Q_S + Q_{sb}) = P + E + R \qquad (1.1)$$

where P, E, R are the precipitation, evapotranspiration and runoff respectively (Qs: surface runoff and Qsb: subsurface runoff); dTWS is the net change in storage during a given time increment dt (Figure 1.2). TWS accounts for both snow-pack and soil moisture variations. Equation (1.1) can be combined with the atmospheric water balance to eliminate the P and E terms which in atmospheric reanalysis are only indirectly constrained by observations and strongly rely on model estimates.

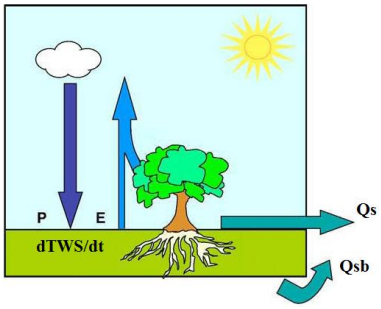

Figure 1.2: Schematic of the land water balance for a given surface soil layer. dTWS/dt refers to the change in water content within the layer (soil moisture, surface water, snow; depending on the depth of the layer, this may include ground water changes) (figure 4left, Seneviratne et al., 2010).

Terrestrial water storage refers to the total amount of water stored at the surface or subsurface (Seneviratne et al., 2004; Troch et al., 2007). TWS is a fundamental component of the global water cycle, including groundwater, soil moisture, snow water equivalent and water in river, lakes, ponds, reservoirs and wetlands, important for water resources, climate, agriculture and ecosystems. It controls the partitioning of precipitation into evapotranspiration and runoff, and the partitioning of net radiation into the sensible and latent heat fluxes. On the other hand, terrestrial water storage change is a basic quantity in closing the terrestrial water balance (Ngo-Duc et al., 2005b; Hirabayashi et al. 2005; Güntner et al., 2007; Yeh and Famiglietti, 2008).

Due to insufficient *in situ*-data of hydrological stores (snow, soil moisture, groundwater) and fluxes (precipitation, evapotranspiration) the direct determination of TWS is difficult. However, alternative methods using new data sets show great potential to improve of intra-annual and inter-annual TWS changes. TWS affects stream flows at various timescales and defines the land response to atmospheric forcing. Increases in TWS will reduce the risk of prolonged drought but too much TWS increase can increase the potential for flooding.

The basin-scale water balance (BSWB) method (Seneviratne et al., 2004; Troch et al., 2007) is based on the coupled atmospheric and terrestrial water balance applied to large river basins. The method relates TWS changes to measured streamflow and atmospheric moisture convergence and to changes in atmospheric moisture content (total atmospheric water vapour contained in a vertical column) derived from reanalysis data sets. TWS can also be estimated based on hydrological modelling (Troch et al., 2007). A hydrological model or an ensemble of such models can be used to solve the water and energy balance equations at a user-specified spatial resolution.

Results obtained are used to provide a new estimate of the global hydrological cycle for long-term annual means that includes estimates of global evapotranspiration as well global runoff over land.

1.2.2 Surface energy budgets

The surface energy budget is determined by the surface net radiative flux at different wavelengths (Kiehl and Trenberth, 1997). At the top of the atmosphere the net energy input, net shortwave radiative flux, is determined by the incident shortwave radiation flux from the sun minus the reflected energy. A fraction of that energy arrives to the surface, after absorption and reflection in the atmosphere; the net surface solar radiation is the incident radiation minus the reflected radiation, determined by the surface albedo. Net surface longwave radiative flux results from the difference between the upwelling and downwelling longwave energy at the surface. The remaining fluxes required to close the surface energy budget represent turbulent exchanges of sensible heat and latent heat between the surface and the atmosphere. From conservation of water mass, the global surface evaporative flux is equal to the global mean rate of precipitation.

The mean annual cycle into the climate system and its storage, and transport in the atmosphere, ocean and land surface have been estimated by several authors (Fasullo and Trenberth, 2008a; Trenberth et al., 2009; Fasullo, 2010; Trenberth et al., 2011; Wild et al., 2013). The net radiative flux was summarized for the globe (Trenberth et al. 2009), for global land and ocean (Fasullo and Trenberth 2008a), for the zonal mean (Fasullo and Trenberth 2008b) and for the ocean (Trenberth and Fasullo 2008). The Earth energy budget was estimated by Trenberth et al. (2009) and modified by Trenberth et al. (2011), revealing that the biggest uncertainty and bias comes from the downward longwave radiation, mainly from clouds. In that analysis the land and ocean domains were examined separately. The conservation of energy and the assumption that, on a time scale of years, the change in heat storage within the atmosphere is very small, is used in Figure 1.3.

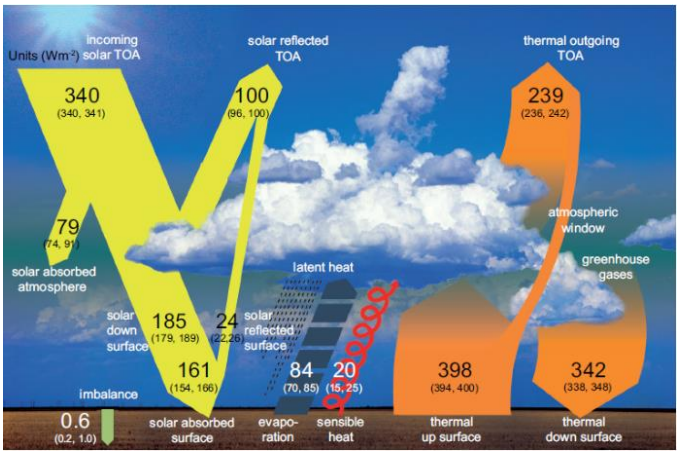

Figure 1.3: Global mean energy budget under present-day climate conditions. Numbers state magnitudes of the individual energy fluxes in W m^{-2}, adjusted within their uncertainty ranges to close the energy budgets. Number in parentheses attached to the energy fluxes cover the range of values in line with observational constraints. (Wild et al., 2013; Hartmann et al., 2013)

The movement of energy in the climate system is associated with a variety of mechanisms involved in its absorption, transport, storage, and emission (Trenberth et al., 2009). Energy enters the system as solar radiation, approximately 70 % of which is absorbed by the atmosphere or surface. A large latitudinal gradient in absorption exists due to the sun-earth geometry, the presence of clouds and other factors such as surface albedo and aerosols. These temperature gradients contribute to a more uniform emission of outgoing longwave radiation than would otherwise occur. The energy is stored, transported and released by the atmosphere, oceans and land surface.

The net flux of radiation at the Earth's surface results from a balance between the solar and terrestrial radiation fluxes (Peixoto and Oort, 1992). There are essentially four types of energy fluxes at the Earth's surface, in which energy is exchanged between the surface and the atmosphere: radiative flux, or net radiation (solar and longwave radiation), sensible heat flux, and latent heat flux (Figure 1.4). The latent heat flux, caused by evapotranspiration, plays an important role in the surface energy budget, as well as in the surface water balance. Processes at the land surface govern the input of heat and moisture to the atmosphere by the absorption of solar radiation and the partitioning of net radiation into sensible and latent heat (Seneviratne et al., 2010).

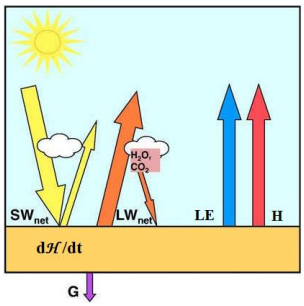

Figure 1.4: Schematic of the land energy balance for a given surface soil layer. $d\mathcal{H}/dt$ refers to the rate of change of energy within the same layer. SWnet refers to the net shortwave radiation (SWin−SWout) and LWnet refers to the net longwave radiation (LWin−LWout). Note that H_2O and CO_2 refer to atmospheric water vapour and atmospheric CO_2 and their role as greenhouse gases. For simplicity other greenhouse gases are not indicated on the figure. (Figure 4 Seneviratne et al., 2010).

The net radiation flux Rn, the (direct) sensible heat flux LE, the (indirect) latent heat flux H, and the heat flux into the subsurface layers $F_G^{\downarrow}$, under steady state conditions, follow the balance equation:

$$R_n - LE - H - G - F_M = 0 \quad (1.2)$$

where F_M is the energy involved in melting snow and ice or in freezing water (Seneviratne et al., 2010). The sensible heat, H, results from the difference in the temperature of the surface and the overlying air. The latent heat flux, LE, results mainly from the evaporation and sublimation at the surface. Evaporation takes place from water surfaces, such as lakes, rivers, and oceans, and from moist soil and vegetation. This transfer of heat is indirect and is associated with the phase transitions of water substance, first between liquid and vapour and liquid or solid phases. The flux of energy into the subsurface medium G is due to heat conduction. The last term F_M is the energy used for melting snow and ice at the rate M_S and for freezing water at the rate F_S:

$$F_M = L_m(M_S - F_S) \quad (1.3)$$

The nature of Earth's surface is important to the energy budget through its albedo, infrared emissivity, thermal conductivity, and evapotranspiration characteristics. For annual-mean conditions over land, the flux of sensible heat $F_G^{\downarrow}$, into the ground can be neglected, leading to:

$$R_n - LE - H - L_m(M_S - F_S) = 0 \quad (1.4)$$

The land energy balance can be expressed as:

$$\frac{d\mathcal{H}}{dt} = R_n - LE - H - G = SWnet + LWnet - LE - H - G \quad (1.5)$$

where $d\mathcal{H}/dt$ is the rate of change of energy within the considered surface soil layer (including vegetation), in Wm^{-2}, assumed to include all water storage components considered in equation (1.1) (temperature change, phase changes associated with soil freezing/melting or snow melt), Rn is the net radiation (solar and long wave radiation flux), LE is the latent heat flux, H the sensible heat flux and G the ground heat flux to deeper layers. For an infinitesimally small layer, $d\mathcal{H}/dt$ tends to zero and G is the ground heat flux at the surface (Seneviratne et al., 2010). From equation (1.5), the surface energy balance can be written as:

$$R_n = SWnet + LWnet = LE + H + G \quad (1.6)$$

where Rn is the net radiation, LE is the latent heat flux (L is the latent heat of vaporization and E is the evapotranspiration), H is the sensible heat flux and G is the soil heat flux. Units are in Wm^{-2}. The land surface radiation budget, characterized by the net radiation, represents the balance between incoming radiation from the atmosphere and outgoing longwave and reflected shortwave radiation from the Earth surfaces.

1.3 Research objectives and thesis organization

The main tasks of this thesis are the reconstruction of global hydrology over the past decades and project the climate-hydrology into mid and end of 21st century. The hydrological and energy cycles can be reconstructed over a period of several years, using a combination of observational data and high resolution modelling. This study evaluates the WATCH Forcing Data, based on ERA-40 reanalysis and corrected by CRU TS2.1 and GPCCv4, from a global water and energy cycles perspective.

This thesis is organized as follows. Chapter 2 describes the land surface model and the creation of WFD in the presence of reanalysis (i.e., for the period 1958-2001), while Chapter 3 describes data creation prior to the existence of reanalysis (1901-1957). FLUXNET data are used in Chapter 2 for evaluation of the model based data. The following chapter, Chapter 4, contains a simulation of the present climate and corresponding results of global water and energy cycles over land; results are also compared with FLUXNET data. Chapter 5 contains simulations of future climate, and compares results with current climate estimates. Conclusions follow in Chapter 6. There are 3 technical appendices, with Appendix II describing an alternative daily forcing data using statistical tools, and can serve as an alternative methodology to the method presented in Chapter 3.

Chapter 2 - The land surface model and forcing data in the presence of reanalysis

This chapter is closely based on Weedon et al. (2011).

2.1 Introduction

Understanding the variability of the terrestrial hydrologic cycle is central to determine the potential for extreme events and susceptibility in the future. In the absence of long-term, large-scale observation of the components of the hydrologic cycle, modelling can provide consistent fields of land surface fluxes and states.

The availability of large-scale, long-term datasets of the land surface water and energy budgets is essential for understanding the global environmental system and its interaction with human activity. Therefore there has been a growing demand for datasets with high spatial (e.g., 0.5º lat/lon) and temporal (monthly, daily or even subdaily) resolution that are also continuous over the space-time domain of interest. However, there are not many observations on global components of the land surface water and energy budgets.

The use of remote sensing has provided great potential for the large scale measurement of some variables but is restricted to indirect quantities and to low-vegetated regions and the top few centimetres (as albedo, radiative surface temperature, and soil moisture). Observed surface energy fluxes and evaporation are difficult to measure and are non-existent over large scales. Surface energy fluxes, evaporation, and soil moisture *in situ* measurement networks are sparse and inadequate for large scale hydrological studies. Model soil moisture from atmospheric reanalysis data has been used directly or indirectly (in the latter, air surface atmospheric variables, precipitation and radiative fluxes are used to force an offline land surface model) (Maurer et al. 2001; Kanamitsu et al. 2003; Dirmeyer et al. 2004; Fan et al. 2011). These studies show that the quality of soil moisture datasets from the global analyses is not very good, when compared to the limited observations.

Despite substantial improvements to weather forecast models and to observation systems, the necessary atmospheric information over large areas of the globe is not available at the temporal and spatial scales required by the majority of land surface parameterization schemes. Over these regions, reanalysis products may offer the only source of the necessary climate information. Reanalysis data is complete in space and time, but reflect the model errors, particularly on flux estimates (e.g., precipitation, surface radiative fluxes) and state variables (e.g., surface air temperature and humidity) in regions that have little observational data input (Kalnay et al., 1996). The main reason may be the widespread bias in precipitation, surface air temperature, and surface radiation. The quality of calculated variables crucially depends on the quality of input forcing data and of the land surface (LSM) or general hydrological models (GHM) used. Bias in reanalysis products has been the subject of much research (Betts et al., 1996, 1998a, 1998b, 1998c; Maurer et al., 2001; Roads and Betts, 2000; Berg et al., 2003). The use of reanalysis forcing to drive offline land surface models can result in unrealistic estimates of energy, mass, and momentum exchanges between the land and atmosphere (Lenters et al., 2000; Maurer et al., 2001). The adjustment process of reanalyses by global observationally based data sets allows the creation of a reliable meteorological data set to force LSMs and GHMs. There are several meteorological datasets to drive hydrological simulations derived by combining reanalysis with observations (Ngo-Duc et al., 2005a; Sheffield et al. 2006; Hirabayash et al., 2008; Li et al., 2010; Weedon et al. 2011; Chaney et al., 2014). Some of these forcing data are based on NCEP/NCAR reanalysis. Ngo-Duc et al. (2005a) provided a 6-hourly data set, NCC (NCEP/NCAR data corrected by CRU), from 1948 to 2000 at a spatial resolution of 1ºx1º. It is based on NCEP reanalysis and a number of independent *in situ* observations. The global meteorological forcing data set for land surface modelling developed by Sheffield et al. (2006), PGF (Princeton Global Forcing), blends NCEP reanalysis with observations and disaggregates in time and space. This is a global 1º, 3-hourly resolution for 1948-2008 dataset). The near-surface meteorological data for GSWP (Global Soil Wetness Project) are based on atmospheric

reanalyses (NCEP-DOE Reanalysis 2 for the baseline simulations) at 3-hour intervals (Dirmeyer et al., 2006). The reanalysis data was hybridized with observational data, and corrected for differences in elevation between the reanalysis model topography and the ISLSCP Initiative II mean topography.

Recently Weedon et al. (2010, 2011) created a consistent meteorological forcing data for hydrological studies used to force LSMs and GHMs, the WATCH Forcing Data (WFD). Creation of WFD precipitation (rainfall and snowfall) is described in this chapter. Construction of WFD data involves two steps: interpolation of the ECMWF Re-Analysis to a grid of 0.5ºx0.5º and correction of reanalysis with the observationally based data. Variables in meteorological data are divided in two types: state variables (near-surface air temperature, specific humidity, wind speed and surface pressure) and flux fields (radiation and precipitation). The WFD was derived from the surface variables of the 40 years European Centre for Medium-Range Weather Forecasts (ECMWF) Re-Analysis (ERA-40) (Uppala et al. 2005) for the period 1958 to 2001, but from reshuffled ERA-40 data for the period 1901 to 1957 (Table 3.1). The WFD consist of subdaily, gridded, half-degree resolution, meteorological forcing data. Variables included are (i) wind speed at 10 m, (ii) air temperature at 2 m, (iii) surface pressure, (iv) specific humidity at 2 m, (v) downward longwave radiation flux, (vi) downward shortwave radiation flux, (vii) rainfall rate, and (viii) snowfall rate. Meteorological data was produced at both daily and subdaily time steps: flux fields are provided 3-hourly, while state variables are 6-hourly. These global data are stored at 67 420 points over land (excluding Antarctica). Data is available as WFD-land-longitude-latitude-z files either in NetCDF or DAT formats.

ERA-40 data was interpolated to ½º resolution on the CRU land mask, adjusted for elevation changes where needed, and bias corrected using monthly observations. The main procedures described by Ngo-Duc et al. (2005) and Sheffield et al. (2006) were adopted to generate the WFD. Temperature, surface pressure, specific humidity, and downward longwave radiation were adjusted sequentially in that order because they are interdependent via the elevation adjustment. Diurnal air temperature was bias corrected with CRU data (New et al., 1999, 2000; Mitchell and Jones, 2005). Shortwave downward radiation (SWdown) was corrected using CRU cloud cover fractions, having found the grid point-specific correlations between monthly average SWdown and ERA-40 cloud fraction. SWdown was also adjusted in clear sky and cloudy sky for the effects of tropospheric and stratospheric aerosol loading. ERA-40 precipitation output consists of both rainfall and snowfall (Betts and Beljaars, 2003), and the convective and large-scale precipitation are added to produce the total precipitation. The most serious problem diagnosed in the ERA-40 analyses is excessive tropical oceanic precipitation in later years, particularly in stream 1 after 1991 (Troccoli and Kallberg, 2004). To avoid these problems precipitation was adjusted using both a wet days correction from CRU and precipitation totals from the GPCCv4 full data product (Rudolf and Schneider 2005; Schneider et al. 2008; Fuchs 2009), and corrected for undercatch (snowfall and rainfall separately) based on Adam and Lettenmaier (2003). Observation based datasets are used to spatially downscale the reanalysis, which is available at high temporal resolution, and at the same time remove biases in the reanalysis.

In the next section WFD precipitation (rainfall and snowfall rate) is described; for more detailed information of state and radiation variables see Weedon et al. (2010, 2011).

2.2 Correction for rainfall and snowfall rate

WFD precipitation is produced by carrying out a set of empirical corrections to precipitation of reanalysis and observations. The reanalysis systematic errors are removed via a multiplicative scaling factor that is based on the ratio of observed monthly rainfall to reanalysis estimates. The generation of precipitation data involved six steps: 1) bilinear interpolation, 2) combining rainfall and snowfall totals while retaining the rainfall/snowfall ratio for each location and time step, 3) adjusting the number of "wet" (i.e., rain or snow) days per month to match the CRU TS2.1 observations, 4) adjusting the monthly precipitation totals to match GPCCv4 precipitation (or CRU precipitation), 5) reassigning the precipitation into rain and snow using the original ratio, and 6) adjusting the monthly totals using gridded average precipitation gauge correction (separately for rainfall and snowfall).

CRU and GPCC observation based data, were used for correcting systematic errors, in particular reduction of the number of wet days covering global land areas at monthly resolution. CRU data is a set of mean monthly surface climate data over global land areas, excluding Antarctica, for nearly all of the twentieth century. The data set is gridded at 0.5 degree latitude/longitude resolution and includes seven variables: precipitation, mean temperature, diurnal temperature range, wet day's frequency, vapour pressure, cloud cover, and ground-frost frequency (New et al., 2000; Mitchell and Jones, 2005). All variables have mean monthly values for the period 1901-2001 (TS2.1 version). The Global Precipitation Climatology Project (GPCP), presented in this chapter, has produced and released monthly mean estimates of precipitation on a 0.5º lat × 0.5º lon grid for the period 1901-2001 (GPCCv4). GPCC precipitation is a combination of gauge observations with satellite estimates and includes estimates of uncertainty for each location and month.

2.2.1 Wet days correction

Betts et al. (2003a, 2003b), Hagemann et al. (2005) and Uppala et al. (2005) found disparities between ERA-40 monthly precipitation total and both CRU and GPCC totals. Due to the presence of too many wet days (number of days per month with rainfall/snowfall) in the tropics (Betts and Beljaars, 2003; Hagemann et al., 2005; Uppala et al., 2005), a wet days correction has been adopted. Figure 2.1 compares the zonal average of ERA-40 precipitation (dashed blue line) before bilinear interpolation and wet days correction with observational zonal average from CRU (TS 2.1 and TS 3.1) and GPCC (v4 and v6) from 1958 to 2001. ERA-40 precipitation is overestimated in the tropics over land compared to GPCC and CRU data. In the mid-latitudes ERA-40 patterns (not shown) are similar to observations. The need for a wet day correction is evident in the mid-latitudes.

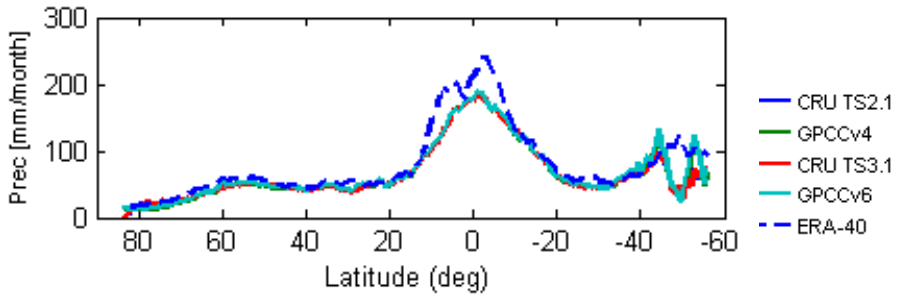

Figure 2.1: Zonal average of precipitation for the ERA-40 period (1958 to 2001), only land points.

The method adopted for wet days correction is the main difference in the derivation of previous precipitation forcing datasets. Ngo-Duc et al. (2005), for example, did not correct wet days, whereas Sheffield et al. (2006) used a statistical correction (Sheffield et al. 2004) that was designed to cope with spurious standing wavelike patterns in the high northern-latitude wet days characteristics of the NCAR–NCEP data. However, the Sheffield et al. (2004) correction meant that spatial continuity of individual precipitation events was sometimes compromised (see Fig. 7 of Sheffield et al., 2004), and it also required the adjustment of several associated variables when wet days were ''created'' to match the CRU data. Additionally, Sheffield et al. (2006) introduced the correction of number of CRU wet days as well as correction of precipitation gauge-undercatch via the gridded average catch ratios of Adam and Lettemaier (2003).

During the wet days correction only the smallest daily totals are reset, therefore the spatial continuity and coherence of significant (non-drizzle) frontal precipitation across grid boxes are not compromised. It means that large-scale (multigrid box) hydrological modelling remains meaningful at the daily scale. For locations where there were too few wet days per month relative to the CRU observations, no changes were made, thus avoiding the need to artificially modify downward shortwave, specific humidity, and 2-m temperature on dry days to make them consistent with conversion to wet days (Sheffield et al. 2006). For simplicity and ease of coding, in places and at times when precipitation has been removed, no attempt has been made to modify the other meteorological variables.

2.2.2 Monthly bias correction

Figure 2.2 and Figure 2.6 show time series of global and land average precipitation for: the CRU (TS 2.1 and TS 3.1); GPCC (v4 and v5) datasets (only WFD land-mask) and ERA-40 or WFD precipitation (CRU and GPCC version) before and after corrections. The ERA40 dataset is biased by 42 mm/month over global land areas excluding Antarctica. Errors in the ERA reanalysis precipitation at monthly scales translate into errors in land surface fields like evapotranspiration, soil moisture, and snow cover (Sheffield et al., 2004). Ngo-Duc et al. (2005a) investigated the effect of precipitation bias on runoff generation. These biases contributed for larger errors in resultant large basin river discharge than biases in air temperature and radiation.

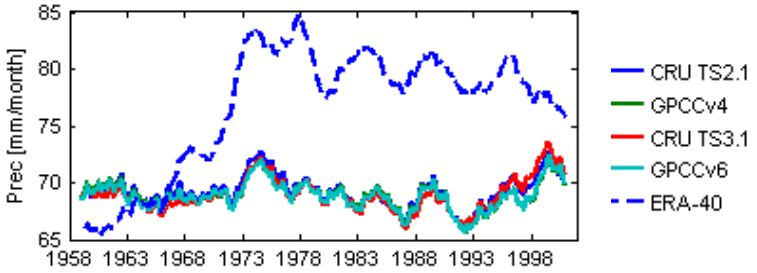

Figure 2.2: Running average (annual) of precipitation over continental area excluding Antarctica for CRU, GPCC and ERA-40 datasets. ERA-40 is discretized here at 1°x1° grid.

Information on the precipitation averaged over land, for each of the three decades is shown in Table 2.1. From the 70s onwards, a succession of satellite-borne instruments and the increasing numbers of observations from aircraft, ocean-buoys and other surface platforms, provided assimilable data; however there was a declining number of radiosonde ascents (Uppala et al., 2005). In order to cover the entire ERA-40 period, the first and last column in the table represent 13 and 11 years, respectively. ERA-40 results (based on 3h, and 1°x1° data) are compared with global observations (CRU and GPCC monthly data). There is an increase in ERA40 average precipitation from 60s to 70s decades. There are no satellite data available for assimilation until 1961. In the observational datasets for the various periods the average precipitation is about 69 mm/month.

Table 2.1: Global precipitation over land for the years 1958-70, 1971-80, 1981-90 and 1991-2001, in mm per month, from the reanalysis performed at ECMWF (ERA-40) and from other data sources: CRU (TS 2.1 and TS 3.1) and GPCC (v4 and v6). Antarctica is excluded.

Period	Decade 60s 1958-70	Decade 70s 1971-80	Decade 80s 1981-90	Decade 90s 1991-01
ERA-40 (land, 1°x1°)	69	81	80	79
CRU TS2.1	69	70	69	69
CRU TS3.1	69	70	68	70
GPCCv4	69	70	69	69
GPCCv6	69	70	68	69

A bias correction procedure was implemented to minimize the discrepancies between the monthly observations and reanalysis. The monthly bias correction was applied to the reanalysis data (after bilinear interpolation and wet-days correction) so that the mean monthly values match those from GPCCv4 and CRU monthly precipitation, respectively. To remove the bias in the reanalysis the 3-hourly, after wet-days correction, values are scaled so that their monthly totals match those the GPCC dataset (Ngo-Duc et al., 2005a, Sheffield et al., 2006 and Weedon et al., 2010, 2011):

$$P^{*}_{ERA,3h} = \frac{P_{obs,mon}}{P_{ERA,mon}} \times P_{ERA,3h} \qquad (2.1)$$

where the asterisk indicates a corrected value and the subscripts indicate the data source (observations and reanalysis) and the temporal resolution (3 hourly or monthly). Observations have been obtained from the Global Precipitation Climatology Centre half-degree version 4 full product (GPCC v4). This consists of monthly gridded precipitation totals from rain-gauge observations For some places, especially islands, represented by one or very few boxes in the CRU grid that are not covered by GPCC v4, we have employed the CRU TS2.1 precipitations totals. A similar bias correction was applied using CRU TS2.1 precipitation totals.

In a small number of grid boxes and some months, precipitation rates are close to zero. The monthly bias correction then had the effect of increasing these rates such as to imply there was spurious background drizzle between more normal precipitation events. In semiarid areas this is inconsistent with local climatic conditions but, fortunately from the point of view of hydrological modelling, this spurious low-level background precipitation is not significant. When there were too few wet days in interpolated ERA-40, for the (very few) locations, the adjustment of monthly precipitation totals sometimes implied high precipitation rates. These "outliers" rates were limited to a rate corresponding to the 99.999 % lognormal probability precipitation rate for the relevant calendar month and grid box (Weedon et al., 2010, 2011).

2.2.3 Maximum precipitation: outliers

The statistical characterization of precipitation is useful in understanding the large-scale space and time variability of the process and is helpful in assessing the accuracy of the precipitation retrievals by imposing constraints that must be satisfied by the spatial and temporal averages of the reanalysis or observations. One topic of interest is the probability density function (PDF) of precipitation rates. This PDF is indispensable and particularly so when it comes to the estimation of the maximum of precipitation that occurred at single location. The PDF of precipitation rate over large areas is fairly stable over time and space (Meneghi and Jones, 1993), for this reason, the parameters of the particular distribution can be used for representing very different climatological conditions (Wilks, 1995). The lognormal distribution, as well as the gamma distribution, is commonly used to represent precipitation rates. The lognormal distribution assumes that the logarithms of the data are normally distributed.

Cho et al. (2004) analysed the spatial characteristics of nonzero rain rates to develop a PDF model of precipitation using satellite rainfall data. The lognormal distribution overestimates the sample mean, whereas the gamma distribution underestimates it. These differences are caused by the inflated tail in the lognormal distribution and the small shape parameter in the gamma distribution. The gamma fits outperformed the lognormal fits in rainy regions, while the lognormal fits were better than the gamma fits in dry regions (Cho et al., 2004). To avoid extreme values, also known as outliers, in our data we fitted a lognormal distribution at the probability of 99.999 %.

Considering the ECMWF's reanalysis (ERA-40 and, recently, ERA-interim), the properties of precipitation were investigated, characterizing the PDF of precipitation rates. At each WFD land point (½ degree) the lognormal distribution was fitted and the maximum of precipitation rate was calculated based on the parameters of the distribution. No-rain data (i.e., P = 0) are included to avoid overestimating mean rain rates.

Three standard techniques for fitting a theoretical PDF to data are the method of moments, the maximum likelihood method, and the minimum $\chi 2$ method. The methods of moments use the sample mean and variance as the mean and variance of the fitted distribution. Although inefficient (Wilks, 1995) we used this method due to deadline limitations.

Maximum of precipitation is concentrated over tropical zone in the intertropical convergence zone and monsoon areas. The highest precipitation occurs over South America and Eastern America (over than 50 mm per hour). Figure 2.3 shows differences between the seasonal average of maximum precipitation of ERA-I and ERA-40. Positive differences (yellow to red in pictures) indicate that maximum of precipitation is higher on ERA-I than ERA-40. The highest positive differences occur on South America during the second semester of the year (SON and DJF). The maximum values in Central Africa, near Congo, are underestimated by ERA-40, except in JJA. Precipitation near the Congo Basin is characterized by very high intensities in a short period of time.

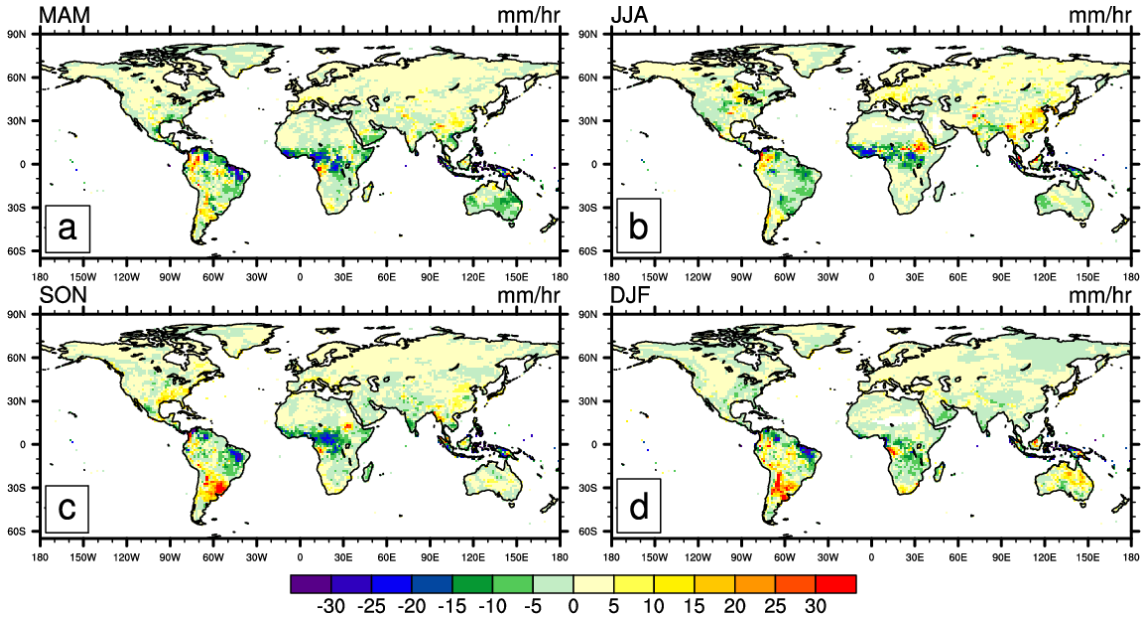

Figure 2.3: Differences between max ERA-I and ERA-40 maximum of precipitation. For each location and month, the 99.999% percentile was computed (see text); each seasonal panel represents averaged values of respective monthly 99.999% percentiles.

2.2.4 Correction for gauge undercatch

Adam and Lettenmaier (2003) developed gridded mean monthly catch ratios (CRs) for adjustment of wind-induced undercatch and wetting losses for global gridded precipitation products. The precipitation gauge correction used separate average calendar monthly catch ratios for rainfall and snowfall rates at each half-degree grid box. No attempt was made to adjust precipitation rates to allow for effects of orography (Adam et al., 2006).

The seasonally averaged spatial distribution of 0.5º global correction ratios of rainfall (RainCR) and snowfall (SnowCR) are shown in Figure 2.4 and Figure 2.5, respectively. These correction ratios were applied to the 3-hourly ERA-40 after wet days and bias corrections. In general, the CRs increase from north to south with lower values in high-altitude regions and in high wind speeds (Adam and Lettenmaier, 2003). Seasonal CRs are smaller than 1, about 0.8, causing a slightly increase of rainfall, except in the Canadian Rockies during the cold season (see Figure 2.4a). Positive values of catch rations that only happens in the Canadian Rockies during DJF, can reach 1.2, reduce more than 83 % the original rainfall.

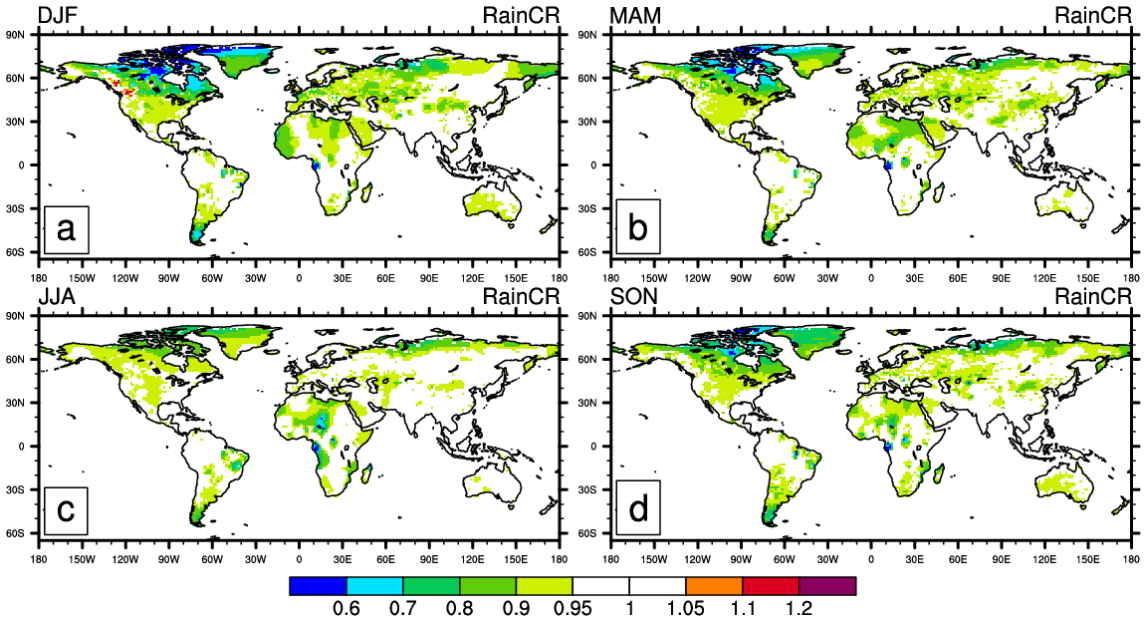

Figure 2.4: Seasonally averaged gauge catch ratios for rain, RainCR, from Adam and Lettenmaier (2003). Values larger (smaller) than 1 decrease (increase) ERA-40 rainfall. Corrected Rainf = Rainf/RainCR

These bias adjustment methodology applied to snowfall rate results in a slight increase in snowfall (see Figure 2.5). Blue and green values indicate an increase of snowfall, as rainfall. Over the Canadian Rockies during the warm season, CRs correction will reduce winter snowfall (correction ratios are about 1.1). In South Hemisphere and some location in North Hemisphere (e.g. Iberian Peninsula) there are no snowfall correction.

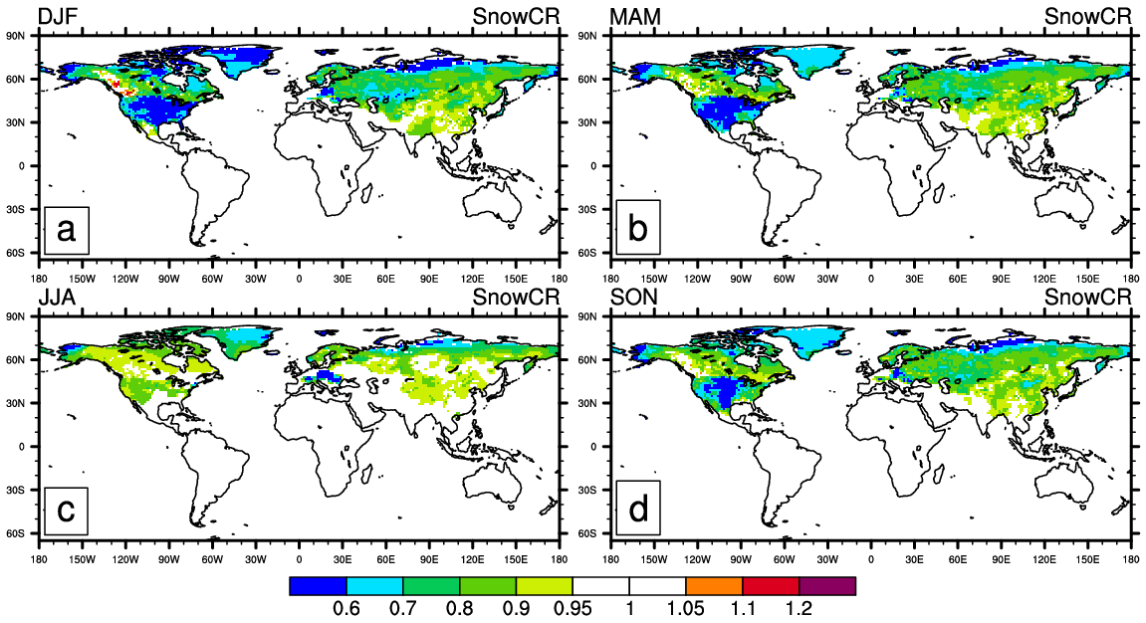

Figure 2.5: Seasonally averaged gauge catch ratios for snow, SnowCR, from Adam and Lettenmaier (2003). Values larger (smaller) than 1 decrease (increase) ERA-40 snowfall. Corrected Snowf = Snowf/SnowCR.

The running average of precipitation over continental area for WFD and observed precipitation are presented in Figure 2.6. The global average reflects the inter-annual variability of the observations, but the average amount is slightly higher than the observed result of subsequent corrections to bias elimination.

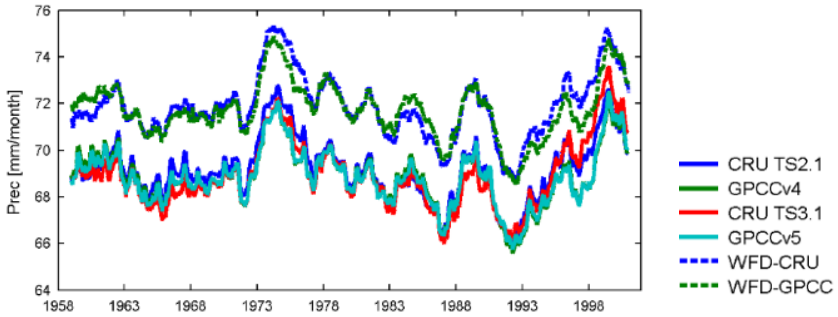

Figure 2.6: As Figure 2.2 but ERA-40 was replaced by WFD (CRU and GPCC version) datasets.

2.3 Land Surface Model – HTESSEL and CTESSEL

The land surface model TESSEL (Tiled ECMWF Scheme for Surface Exchanges over Land) was the land surface scheme used by ERA-40. It is a one-dimensional model with four levels of prediction for the soil temperature and water content, and free drainage zero heat flux lower boundary condition. The land surface scheme includes up to six coexisting land surface tiles (bare ground, low and high vegetation, intercepted water and shaded and exposed snow). Soil freezing is parameterized according to Viterbo et al. (1999), while soil water and energy transfers are described in Viterbo and Beljaars (1995), with significant model upgrades, developed for ERA40, are described in van den Hurk et al. (2000). Revisions concerning the snow and the soil hydrology, labelled as HTESSEL, are detailed by Dutra et al. (2010) and Balsamo et al. (2011a, 2011b), respectively. The carbon enabled version, CTESSEL (Boussetta et al., 2013), is described in 2.3.4.

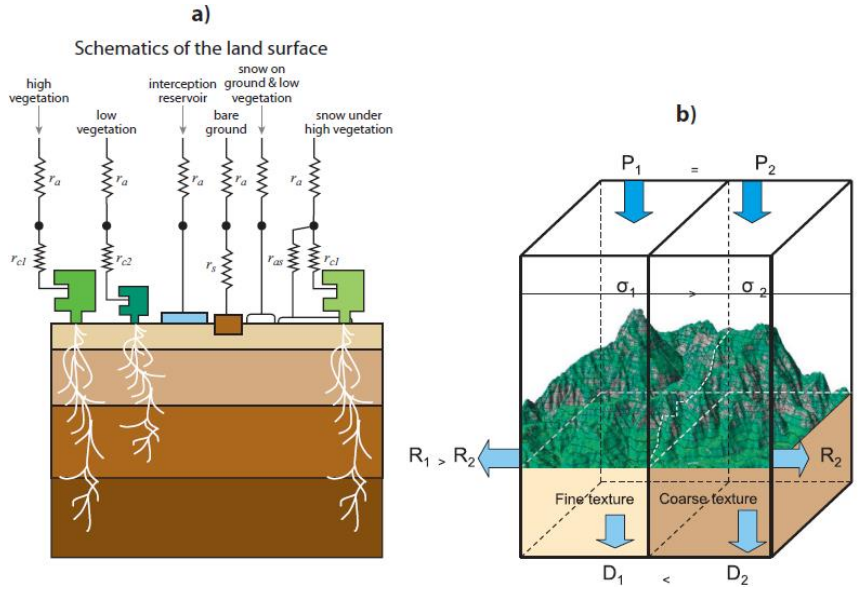

Figure 2.7: Schematic representation of the structure of (a) TESSEL land-surface scheme and (b) spatial structure added in H-TESSEL. For a given precipitation, P_1=P_2 the scheme distributes the water as surface runoff, R, and drainage, D, with functional dependencies on orography, σ, and soil texture, respectively. (Balsamo et al., 2009).

2.3.1 TESSEL hydrology

The TESSEL scheme is shown schematically in Figure 2.7a. The scheme includes up to six land surface tiles (bare ground, low and high vegetation, intercepted water and shaded and exposed snow) and two over water (open and frozen water), with separate surface energy and water balances. It considers a four-layer soil. The depths are chosen in an approximate geometric relation: 7 cm for the top layer, 21 cm, 72 cm and 189 cm. These four layers are enough for representing correctly all time-scales from one day to one year. The soil can be covered by a single layer snow. In each grid box, two vegetation types are present: a high and a low vegetation type.

2.3.1.1 Soil heat budget

The soil heat transfer is assumed to obey the Fourier law of diffusion:

$$(\rho C)_s \frac{\partial T}{\partial t} = \frac{\partial}{\partial z}\left(\lambda_T \frac{\partial T}{\partial z}\right) + L_f \rho_w \frac{\partial \theta_I}{\partial t} \qquad (2.2)$$

where $(\rho C)_s$ is the volumetric soil heat capacity [J $m^{-3}K^{-1}$], T is the soil temperature [K], z is the vertical coordinate in m, λ_T is the thermal conductivity [W $m^{-1}K^{-1}$], L_f is the latent heat of fusion [Jkg^{-1}], ρ_w is the water density [kgm^{-3}], and θ_I is the ice water contents [m^3m^{-3}]. The heat fluxes are predominantly in the vertical direction. The second term of r.h.s of the equation represents the thermal effects of phase changes, of relevance in cold environments; they are described in detail in Viterbo et al. (1999).

Boundary conditions for the energy equation (2.2) are a net heat flux at the surface (sum of the radiative, latent and sensible heat fluxes) and a zero flux at the bottom.

2.3.1.2 Energy balance

The energy balance equation is solved for each tile, with the partial absorption of the net shortwave radiation, $1 - f_{Rs,i}$ in the skin layer. The remaining energy is directly passed to the soil or snow:

$$(1 - \alpha_i)\left(1 - f_{Rs,i}\right)R_s + \varepsilon\left(R_T - \sigma T_{sk,i}^4\right) + H_i + L_{v,s}E_i = \Lambda_{sk,i}\left(T_{sk,i} - T_1\right) \quad (2.3)$$

where i is the tile index. R_s and R_T [W m^{-2}] are downward shortwave and longwave radiation, respectively, σ [W m^{-2} K^{-4}]is the Stefan-Bolzman constant, T_1 the temperature of the upper soil or snow layer, H_i the sensible heat flux, and $L_{v,s}E_i$ the latent heat flux from the skin layer. Latent heat of vaporization, L_s [J kg^{-1}] is used for all evaporation terms not including snow evaporation, while L_s [J kg^{-1}], the sublimation energy, is used for evaporation of snow. The components of the energy balance are parameterized as follows:

$$R_n = (1 - \alpha)K^{\downarrow} + L^{\downarrow} - \epsilon \cdot \sigma \cdot T_s^4 \quad (2.4)$$

$$H = \rho \cdot C_H \cdot U\left(C_p \cdot T_a + gz - C_p \cdot T_s\right) \quad (2.5)$$

$$\lambda E = \lambda \cdot \rho \cdot C_H \cdot U(\alpha_a \cdot q_\alpha + \alpha_s \cdot q_{sat} \cdot T_s) \quad (2.6)$$

$$G_s = \Lambda_s(T_s - T_{sl})^4 \quad (2.7)$$

where $K^{\downarrow}$ is the incoming solar radiation and $(1 - \alpha)K^{\downarrow}$ is the reflected solar radiation (α is the surface albedo), $L^{\downarrow}$ is the incoming longwave radiation (which comes from the atmosphere and depends on the vertical temperature profile, the clouds and the vertical distribution of absorbers), ϵ is the emissivity of the Earth's surface, σ is the Stefan-Boltzmann constant, T_s the surface temperature, ρ the air density, C_H the aerodynamic turbulent transfer (expressing the efficiency of the transport of heat or moisture away from or towards the surface by turbulent missing, U is the horizontal wind speed, C_p the heat capacity of air, $C_p \cdot T_a + gz$ the dry static energy of the atmosphere, λ the latent heat of evapotranspiration (Lv or Ls), α_a and α_s the atmospheric and surface moisture conductances, q_a is the atmospheric specific humidity and q_{sat} is the saturated specific humidity, Λ_s is the soil heat and conductance T_{sl} is the temperature of the top soil layer.

2.3.2 Soil water budget

The vertical movement of water in the unsaturated zone of the soil matrix obeys the following equation:

$$\rho_w \frac{\partial \theta}{\partial t} = -\frac{\partial F}{\partial z} + \rho_w S_\theta \quad (2.8)$$

where ρ_w is the water density [kg m^{-3}], F is the water flux in the soil [positive downward, kg m^{-2}s^{-1}], and S_θ is a volumetric source term [m^{3}m^{-3}] corresponding to root extraction. Using Darcy's law, F can be specified as:

$$F = -\rho_w\left(\lambda\frac{\partial \theta}{\partial t} - \gamma\right) \quad (2.9)$$

where λ [m^{2}s^{-1}] and γ [m s^{-1}] are the hydraulic diffusivity and hydraulic conductivity, respectively. Replacing (2.9) in (2.8) and defining parametric relations for λ and γ as functions of soil water, a partial differential equation for θ is obtained:

$$\frac{\partial \theta}{\partial t} = \frac{\partial}{\partial z}\left(\lambda\frac{\partial \theta}{\partial z} - \gamma\right) + S_\theta \quad (2.10)$$

The top boundary condition is given by precipitation plus snowmelt minus bare ground evaporation minus surface runoff. The bottom boundary condition assumes free drainage.

The precipitation is accumulated in an interception layer until it is saturated. The remaining precipitation (throughfall) is partitioned between surface runoff and infiltration. Subsurface water fluxes are determined by Darcy's law, used in a soil water equation solved with a four-layer discretization shared with the heat budget equation. The top boundary condition is infiltration plus surface evaporation, free drainage is assumed at the bottom, and each layer has an additional sink of water in the form of root extraction over vegetated areas.

2.3.3 H-TESSEL and snow revisions

The H-TESSEL (Hydrology-TESSEL) scheme (Balsamo et al. 2009, 2011a, 2011b), includes the following revisions to the soil hydrology: (a) a spatially varying soil type replacing the single loamy soil; (b) the van Genuchten (VG) formulation of soil hydraulic properties replacing the Clapp and Hornberger (CH) scheme; and (c) the surface runoff generation changing according to a variable infiltration capacity based on soil type and local topography. In Figure 2.7b, the H-TESSEL changes are illustrated: in two adjacent model grid points with the same land surface conditions and receiving an equal amount of precipitation, the surface runoff will be different and proportional to the terrain complexity, while the soil water drainage will depend on the soil texture class. The van Genuchten (1980) formulation provides a closed-form analytical expression for the conductivity, given as a function of the pressure head h, as:

$$\gamma = \gamma_{sat} \frac{\left[(1+\alpha h^n)^{(1-1/n)} - \alpha h^{n-1}\right]^2}{(1+\alpha h^n)^{(1-1/n)(l+2)}} \tag{2.11}$$

where α, n, and l are soil texture-dependent parameters. Pressure head h is linked to the soil moisture by the expression:

$$\theta(h) = \theta_r + \frac{\theta_{sat} - \theta_r}{(1+\alpha h^n)^{(1-1/n)}} \tag{2.12}$$

HTESSEL uses the dominant soil texture class for each grid point. The permanent wilting point and the soil field capacity are obtained by a specified matric potential of $\psi(\theta_{pwp}) = -15$ bar and $\psi(\theta_{cap}) = -0.10$ bar, respectively. A new snow scheme (Dutra et al. 2010) includes separate storages of snow liquid and frozen water, revised formulations of areal fraction of snow, snow density and snow albedo.

2.3.4 The C-TESSEL

A carbon module (Boussetta et al., 2013) has been added to the ECMWF land surface model version, to create CTESSEL, in- order to simulate the photosynthesis processes fixing carbon dioxide into the biomass (the so-called gross primary production, GPP) and the release of carbon dioxide via land biogenic processes (ecosystem respiration, RECO). Photosynthesis and carbon emission parameterizations originated from the Ags-scheme developments (Calvet et al. 1998, Calvet 2000, Calvet and Soussana 2001, Calvet et al. 2004, Gibelin et al. 2006, Albergel et al. 2010). CTESSEL allows for coupling of the surface water and energy budgets with the carbon budget. In addition, CTESSEL allows for the coupling of the surface and atmospheric branches of the carbon cycle.

2.3.5 Model Versions

For the sake of clarity, Table 2.2 summarizes the relevant code switches for each of the three model versions used in this thesis.

Table 2.2: List of main activated parameterized of TESSEL, HTESSEL and CTESSEL and respective model cycle.

Parameterized physics (T: True; F: False)		**TESSEL Cy35R3**	**HTESSEL Cy35R3**	**CTESSEL Cy37R3**
New hydrology (Balsamo et al., 2009)				
LEVGEN	Van Genuchten hydrology	F	T	T
LESSRO	Sub-grid surface runoff	F	T	T
LEFLAKE	FLAKE model	F	F	F
LEOCML	Ocean	F	F	F
New snow parameterization (Dutra et al., 2010)				
LESNWD	Snow liquid water diagnostic	T	T	T
LESNRF	Interception of rainfall by the snowpack	T	T	T
LESNRSN	Revised snow density (Dutra et al., 2010)	T	T	T
LESNWP	Snow liquid water prognostic	F	F	F
LESNFA	Forest snow albedo	T	T	T
LESNCF	Snow cover fraction	T	T	T
LESNAS	Exposed snow albedo	T	T	T
New Carbon scheme (Boussetta et al., 2013)				
LECTESSEL	CTESSEL	-	-	T
LESN09	New snow parameterization	-	-	T
LELAIV	LAI seasonal	-	-	T

2.4 Evaluation of the land surface model HTESSEL against FLUXnet data

The main purpose of the meteorological dataset created, is to drive hydrology or land surface models. To test the consistency of the database two global land surface simulations were performed from 1980 to 2001: GPCC and CRU version. The land surface model HTESSEL (Balsamo et al. 2009, 2011a, 2011b) was driven by tri-hourly WFD atmospheric forcing: air temperature, wind speed, short wave radiation, longwave radiation, surface pressure, specific humidity and precipitation (snowfall and rainfall separately). Both simulations (GPCC and CRU precipitation, respectively) contain data from 1980 to 2001 and 67420 land points, from all continents except Antarctica. To verify the consistency of simulation, daily output (net radiation, latent and sensible heat flux) were compared with daily observed data from FLUXnet sites. These sites are located within the northern hemisphere and temperate climates (Table 2.3).

2.4.1 FLUXNET sites

The flux network (FLUXNET; Baldocchi et al., 2001) performs long series (5-10 years) of ground based observations of surface energy fluxes at a network of locations across the world in different terrestrial ecosystem dataset currently available. The micrometeorological technique samples a footprint of a few hundred meters upwind; however, unlike remotely sensed or catchment water balance estimates of evaporation, FLUXNET observations are provided continuously over long periods and at subdaily time scale.

Surface energy flux measurements from a sample of 8 flux network sites selected to represent a range of climate conditions were used to assess the performance of the HTESSEL land surface model. The FLUXNET database contains information about the site location and site characteristics as well as data availability. Data are available for each site and year gap-filled flux products and meteorological data for half-hourly, daily, weekly, monthly, and annual time intervals are available. Flux tower sites use eddy covariance methods to measure the exchanges of carbon dioxide, water vapour, and energy between terrestrial ecosystems and the atmosphere. The observed data used in this analysis were derived from the Marconi Conference Gap-Filled Flux and Meteorology Dataset (Falge et al., 2005). The FLUXNET database contains also error estimates of latent heat and sensible heat flux. The uncertainty in the surface energy budget ranged from 10 % to 30 %, while uncertainty in measuring available energy was approximately 10 % (Twine et al., 2000).

For this analysis 8 FLUXNET (Table 2.3) sites were selected; only daily and monthly latent heat, LE, sensible heat, H, soil heat and net radiation are used to compare with model equivalent variables.

Table 2.3: Flux measurement site abbreviations, site names, and locations.

Site Name		Data Range	Latitude		Longitude		Type Climate	Land Cover	Elevation (m)	
			Obs	WFD	Obs	WFD			Obs	WFD
NB	MB-Northern Old Black Spruce, Canada	1994-1998	55.88	55.75	-98.48	-98.25	Dfc - Snow fully humid cool summer	Evergreen Needleleaf Vegetation	259	249
WL	Park Falls/WLEF, Wisconsin, USA	1997-1999	45.95	45.75	-90.27	-90.25	Dfb - Snow fully humid warm summer	Deciduous Broadleaf Vegetation	473	478
BL	Blodgett Forest, USA	1997-2000	38.90	38.75	-120.63	-120.75	Csb - Warm temperate with dry, warm summer	Evergreen Needleleaf Vegetation	1280	742
SKo	SKy Oaks- Old Stand, USA	1997-2000	33.37	33.25	-116.62	-116.75	Csa - Warm temperate with dry, hot summer	Annual Broadleaf Vegetation	1414	969
SKy	SKy Oaks- Young Stand, USA	1997-2000	33.38	33.25	-116.62	-116.75	Csa - Warm temperate with dry, hot summer	Annual Broadleaf Vegetation	1435	969
LW	Little Washita Watershed, USA	1996-1998	34.96	34.75	-97.98	-97.75	Cfa - Warm temperate fully humid with hot summer	Annual Grass Vegetation	365	351
WB	Walker Branch Watershed, USA	1995-1998	35.96	35.75	-84.29	-84.25	Cfa - Warm temperate fully humid with hot summer	Deciduous Broadleaf Vegetation	365	293
HE	Hesse Forest, France	1996-1999	48.67	48.75	7.07	7.25	Cfb - Warm temperate fully humid with warm summer	Deciduous Broadleaf Vegetation	293	329

Selected sites correspond to the longest records fitting the 1985-1999 simulation period. Eight FLUXNET sites that satisfied that requirement were then further selected to sample a range of climate zones (temperate, Mediterranean, and boreal). All FLUXNET sites chosen are located in the Northern Hemisphere: USA, Canada and Europe (see Figure 2.8).

4 of the sites in USA are at similar latitude (33º N to 36º N) sampling an east-west precipitation gradient from the dry climate in SKy Oaks (SKy and SKo sites), toward wetter regions in the east (Little Washita LW, Walker Branch Watershed, WB). The selected sites also include a Mediterranean climate (Blodgett Forest, BL), two sites with a cold winter (WL and NB), and one with a continental climate with warm summer (Hesse Forest, France, HE).

The difference in surface altitude between the measuring station and the model grid contributes to an almost constant bias in surface downward longwave radiation (Wild et al., 1995). The correction factor, about 3 Wm^{-2}/100 m, is used to correct the difference in height between model and observations (Table 2.4).

Table 2.4: Height differences between model and real topography and respective longwave radiation correction. The height correction factor is about 3 Wm^{-2}/100 m.

Site Name	Altitude			LWnet Correction (Wm^{-2})
	Site (m)	Model (m)	Δ h (m)	
NB	259	249	10	0.30
WL	473	478	-5	-0.15
BL	1280	742	538	16.14
SKo	1414	969	445	13.35
SKy	1435	969	466	13.98
LW	365	351	14	0.42
WB	365	293	72	2.16
HE	293	329	-36	-1.08

WFD and perturbed simulations were assessed using 6 years of simulated fluxes (1994-1999) chosen for maximum overlap with FLUXNET observations. Daily averaged values of observed latent heat flux, sensible heat flux and net radiation from fluxnet sites were used as validation data. The ability of the model to reproduce the observations was evaluated based on: 1) the coefficient of determination (r^2) obtained by the linear regression of simulated versus observed values; 2) mean absolute error (MAE); 3) root mean square error (RMSE); and 4) mean bias error (MBE).

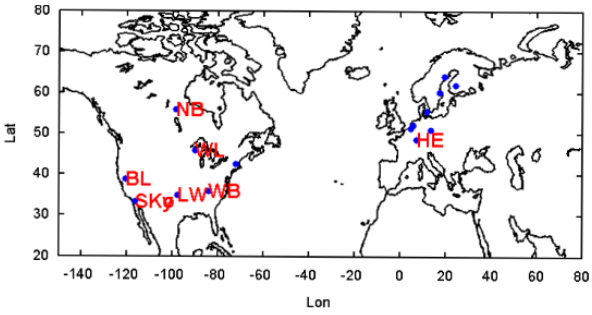

Figure 2.8: Location of the FLUXNET sites used in this study labelled as follows: BL= Blodgett Forest, USA; NB=Northern Old Black Spruce, Canada; LW = Little Washita Watershed, USA; WL = Park Falls/WLEF, Wisconsi, USA; SKo = SKy Oaks-Old Stand, USA; SKy = SKy Oaks-Young Standv, USA; WB = Walker Branch Watershed, USA; and HE = Hesse Forest, France. (See Table 2.3).

2.4.2 Site and observations

Measurements taken at the eight flux-towers (NB, WL, BL, SKo, SKy, LW, WB and HE) from the FLUXnet database (Falge et al., 2005) (Figure 2.8) are compared with the nearest grid point from the global simulation performed with HTESSEL in order to evaluate the model's ability to predict atmospheric fluxes. Unfortunately, some sites only had available data for the growing season, and many others had gaps. Results are presented for common years presented in both series.

Simulated mean monthly fluxes are generally in good agreement with observations (Figure 2.9), with the exception of BL flux tower. At this site, comparison between simulated and measured fluxes indicates some discrepancies between observations and modelled data, with mean sensible heat flux, H, showing a model positive bias, compensated by a corresponding negative bias of the latent heat flux. Model net radiation seems to compare favourably with observations. For the period and locations chosen, changes in precipitation do not appear to have a significant impact (GPCC and CRU version).

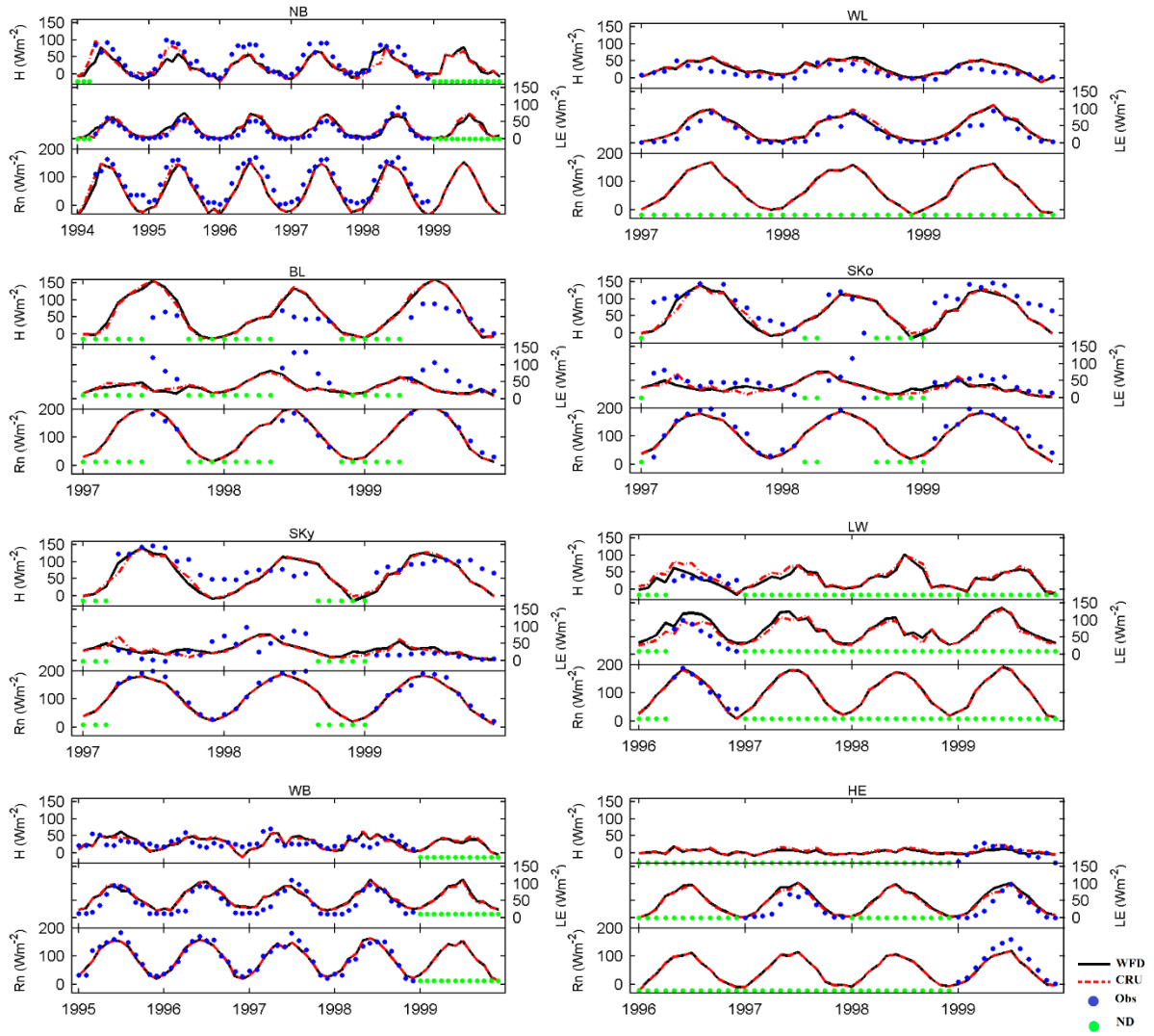

Figure 2.9: Monthly time-series of Rn, LE and H. Units are in Wm^{-2}. The blue dots represent the observations, the black line GPCC simulation and the red dashed line the CRU simulation. Green dots are no data (ND). Note different scales.

Differences between simulated values and observations are presented in boxplot of Figure 2.10 for energy cycle components (Rnet, LE and H). Most significant differences occur at BL. Note that none of the sites have observations covering the whole period for all variables which limits the scope of verification of model results. The boxplot of differences between simulated values and observations show a systematic underestimation of net radiation at all sites except WB and LW sites. This behaviour is common to both simulations, GPCC or CRU. There are no significant differences between WFD and CRU simulations, with differences in precipitation source (upper and lower rows, Figure 3.10). BL site presents, in addition to the largest differences, the widest range of about 30 and 50 W/m^2 for latent and sensible heat flux, respectively. Such differences may be due to the altitude difference between the site and the WFD data, of about 500 m.

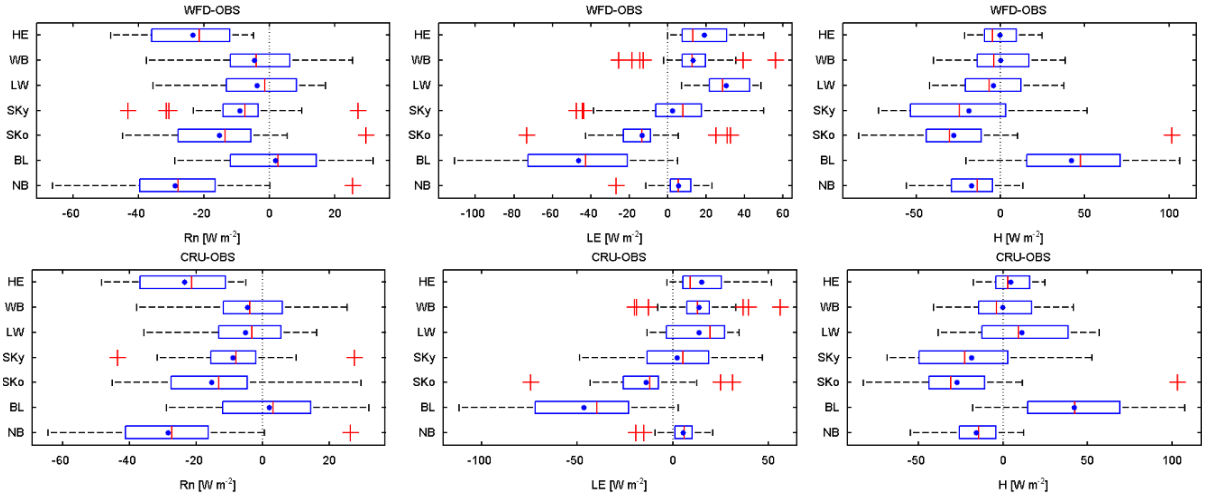

Figure 2.10: Boxplot of monthly differences between simulated and observations for Rn, LE and H. Results for 7 FLUXnet sites: HE, WB, LW, SKy, SKo, BL and NB. Results based on monthly values. Note different scales.

Analysis of the correlation and RMSE evaluate the performance of the model. In general, WFD simulation errors are slightly smaller than the corresponding CRU simulation except for the sensible and latent heat flux in LW site; there is a difference of about 10 Wm^{-2} (only 8 months of observations). Nevertheless, in this station the latent heat flux data, LE, is 92 % correlated with simulations.

Figure 2.11 presents the Nash-Sutcliffe efficiencies (see Appendix I) of modelled latent and sensible heat flux and net radiation to the observed data. BL latent heat flux model data do not agree with observations (see Figure 2.9), explaining the poor efficiency. H efficiency of most sites is close to zero (NS=0), the model predictions are as accurate as the mean of the observed data. Rn efficiency are higher than 0.7 indicating that the model predictions are more accurate than the mean of observed data. The largest differences between simulations (GPCC and CRU) occur on LW site (only 8 months are available in this site). CRU simulation has a better performance for the latent heat flux, but worse for the sensible heat flux. In this case, both simulations have an efficiency less than zero (NS < 0) indicating that the observed mean is a better predictor than the model, the residual variance is larger than the data variance. Note that mismatch of model results vs. observations cannot be attributed solely to the quality of WFD data. If each of the sites contained continuous observation forcing data (T, q, wind speed, surface pressure, precipitation, SW and LW incident flux) the model could have been tested for each site. Comparing model results and observations of surface energy fluxes and net radiation would have given a clear message of deficiencies in the surface model used. Since the observation forcing data is very incomplete, it was unfeasible to perform that simulation. Errors in results presented in Table 2.5 reflect model deficiencies as well as limitations in the forcing data.

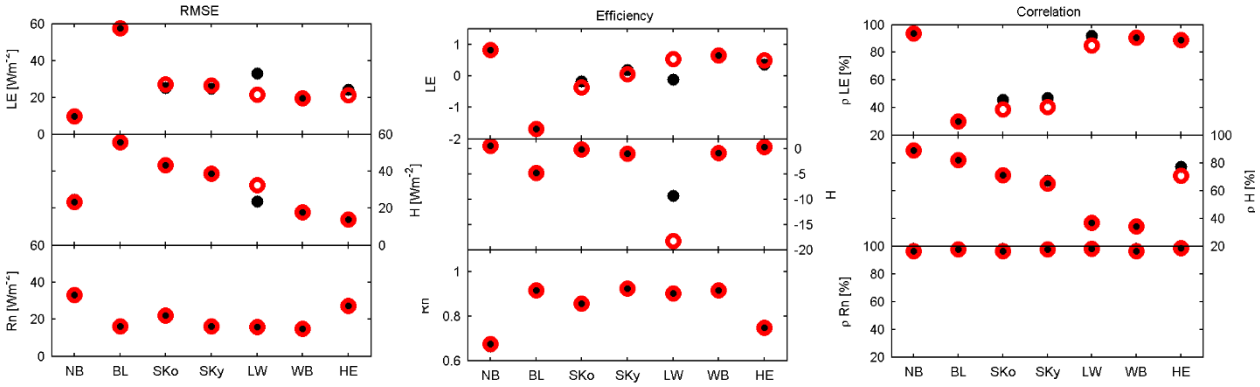

Figure 2.11: RMSE in Wm^{-2} (left panel), correlation (middle panel) and efficiency, NS, (right panel) between model (WFD, black dots, and CRU, red circles) simulations and observations in seven FLUXnet sites (NB, BL, SKo, SKy, LW, WB and HE). Results from monthly values. Note different scales.

Table 2.5 presents the scores of the five statistical performances measures (RMSE, MBE, MAE, correlation coefficient, r, and coefficient of determination, r^2) for Rnet, LE and H. Statistical criteria were computed with a daily time step for the entire available record observed.

Table 2.5: Performance statistics for the WFD simulation vs. fluxnet observations. The results are estimated using only days common to both datasets from 1994 to 1999. Units are in Wm^{-2}. Calculated p-value exceeding 5 %, represented in grey, are not statistically significant.

WFD	NB	BL	SKo	SKy	LW	WB	HE
Rn							
RMSE	34	16	22	16	16	15	27
MBE	29	-2	15	9	4	5	23
MAE	30	13	18	12	13	12	23
r	0.96	0.98	0.96	0.97	0.98	0.96	0.99
r^2	0.66	0.92	0.86	0.93	0.90	0.92	0.75
LE							
RMSE	25	55	44	39	24	18	14
MBE	-6	47	14	-3	-30	-13	-19
MAE	9	47	21	20	30	16	19
r	0.92	0.29	0.46	0.47	0.92	0.90	0.90
r^2	0.78	0	0	0.18	0	0.63	0.36
H							
RMSE	25	55	44	39	24	18	14
MBE	17	-42	28	19	4	0.02	0.52
MAE	19	47	36	34	20	16	12
r	0.89	0.83	0.71	0.67	0.36	0.35	0.77
r^2	0.53	0	0	0	0	0	0.38

2.5 Conclusions

This chapter described the Watch Forcing Data created at half degree resolution for the purpose of driving LSMs and GHMs through the twentieth century. The period 1958-2001 provides a good representation of the real meteorological events, synoptic activity, seasonal cycles, and climate trends. The wet-day correction can destroy the spatial coherence of significant precipitation events associated with frontal systems that occur across several half-degree grid squares. The mixture of rainfall and snowfall was preserved as in the original ERA-40 reanalysis rather using a simplistic rain/snow threshold based on 2-m temperature.

WFD forcing data was successfully created. WFD were used to drive a land surface model, HTESSEL, and compared to flux energy observed locally. In general, seasonality of energy components during the study period was modelled successfully using HTESSEL forced by WFD data. It was tested on WaterMIP simulations (see results in Chapter 4). Updates to near real/time can be done using essentially the same procedures as outlined above, but with ERA-interim data corrected by the latest global observations as CRU TS3.1 and GPCCv5 (Weedon et al., 2014). The new dataset was named as WFDEI (WATCH Forcing Data ERA interim).

Chapter 3 - Forcing data prior to reanalyses

3.1 Introduction

The reanalyses products used in the previous chapter are only available for the second half of de 20th century due to the scarcity of global observations in the period prior to 1958. For the first half of the XX century, we rely on datasets of surface climate, such as GPCC and CRU, developed at the global scale to monitor current climate, climate change detection and GCM evaluation (New et al. 2000; Rudolf and Schneider, 2005). Global observations, although covering the whole century, are available at a coarser time scale and only for some fields (air temperature, precipitation, humidity...), insufficient to conduct hydrological studies.

These products, at monthly resolution, can be associated to reanalysis from the second half of 20th century, to reconstruct forcing data prior to 1958. The method developed ensures monthly observed precipitation amounts, while the daily evolution in each month does not match reality (Weedon et al., 2011).

Statistical tools to generate an alternative time series of air temperature and precipitation are presented in Appendix II.

3.2 Extension to early 20th century (1901-1957)

The WFD data was generated in two tranches with slightly different methodology: 1901-1957 (the current chapter) and 1958-2001 (the previous chapter). In order to complete the entire 20th century, the ERA-40 reanalysis, only available between 1958 and 2001, and global monthly observations, available since 1901, were used to fill this gap. The period 1901-1957 was constructed reordering the ERA-40 (see Table 3.1) and using the methodology described by Weedon et al. (2011).

Separate years of ERA-40 data were extracted in their entirety to provide basic data. The extraction order used was random, based on ran1 algorithm of Press et al. (1992). 44 ERA-40 years were extracted in random order and assigned without replacement to the years 1901-57. The 13 remaining years were assigned again in random order without replacement until all 57 years had been allocated. Leap years were assigned to leap years and only non-leap year were assigned to non-leap years in the selection process. The statistical characteristics (e.g., overall frequency of daily to seasonal extremes), as a global average, of the assigned data for 1901-57 are the same as for 1958-2001. This method does not ensure particular weather events at any particular site. WFD precipitation was corrected by CRU and GPCC data (wet-day and bias correction) available at monthly scale since 1901. This approach has the advantage of ensuring spatial coherency of frontal rainfall and snowfall events across grid boxes, which is very important for hydrological modelling of large river basins but which is difficult to ensure in data created using a weather generator. The same temporal variability (diurnal, sub-monthly variations), the same autocorrelation characteristics (serial dependence from subdiurnal to yearly scales), and the same covariance relationships between variables as during ERA-40 interval were guaranteed. No year-end ramps were applied to the rainfall, snowfall, or downward shortwave data because these variables change greatly from day to day largely in response to cloud cover, and imposing a ramp in the daily values for those variables is therefore unrealistic. Information on the remaining variables is described in Weedon et al. (2011).

Earlier twentieth-century (1901-1957), constructed based on the period 1958-2001, have similar subdaily to seasonal statistical characteristics (averages, extremes, covariance between meteorological variables, and subdaily to seasonal autocorrelation). Such subdaily to seasonal hydrological statistics are characterized, but they do not represent particular historical events.

Table 3.1: The order of the ERA-40 basis years as used in the WFD 1901–57 (Weedon et al., 2011).

year	WFD year	year	WFD year	year	WFD year
1901	1974	1920	1984	1939	1969
1902	1958	1921	1987	1940	1980
1903	1986	1922	1961	1941	1970
1904	1976	1923	1977	1942	1995
1905	1988	1924	1966	1943	1982
1906	1983	1925	1973	1944	1971
1907	1979	1926	1968	1945	1975
1908	1974	1927	1959	1946	1962
1909	1998	1928	2001	1947	1964
1910	1962	1929	1979	1948	1982
1911	1992	1930	1994	1949	1978
1912	1985	1931	1989	1950	1992
1913	1967	1932	1991	1951	1981
1914	1972	1933	1991	1952	1986
1915	1980	1934	2000	1953	1996
1916	1965	1935	1999	1954	1987
1917	1966	1936	1998	1955	1997
1918	1993	1937	1963	1956	1977
1919	1990	1938	1960	1957	1993

3.3 Daily disaggregation method

A common problem in hydrologic studies is the limited availability of data at appropriately fine temporal and/or spatial resolution. Most hydrological models require a daily step or smaller while observed climatology and Global Circulation models (GCMs) outputs are generally available on a monthly to daily time steps and, exceptionally 3-hourly or hourly. In hydrological simulation studies, a model may require as input a synthetic series of a process at a coarse scale while another model may require a series of the same process at a finer scale (Haddeland et al., 2011).

The hydrological models participating in WaterMIP cover a wide range of characteristics, ranging from physically based models run at sub-hourly time steps (Land Surface Models) to more conceptual models run at daily time steps (Hydrological Models). The daily and sub-daily meteorological data are vital inputs for hydrological modelling. The lack of meteorological data at a finer time scale often limits the full use of these models. Hydrological model predictions are sensitive to the parameterizations of physical processes, input parameters, as well as model forcing. In addition, model results are sensitive to the method of spatial and temporal disaggregation of precipitation. Improving methods for spatial or temporal resolution of forcing data downscaling pays off in the quality of hydrological model's output. Consistent downscaling algorithms have been developed to generate sub-daily data from monthly observations. A weather generator, applied to monthly data, for use in climate impact is described on Appendix II. This type of generator produces consistent time series of meteorological variables (precipitation, air temperature, humidity, etc.) at daily resolution, using two stochastic models in series, first for precipitation which is then used for a second model generating the other variables. Safeeq and Fares (2011) evaluated the full use of one stochastic weather generator, ClimGen, and the various approaches to disaggregating daily weather data into hourly data in tropical conditions. Disaggregation techniques are especially useful for extending a subdaily record to a period of time when only daily data are available. Previous studies have focused on generating daily met data at specific sites (Running et al. 1987, Waichler and Wigmosta, 2003) or over large areas (Thornton et al. 1997; Thornton and Running 1999). Debele et al. (2007) examined the applicability of various approaches of disaggregating daily weather data into hourly data.

3.3.1 Methodology

Land surface models (e.g. HTESSEL, ORCHIDEE, Jules …) need 3-hourly forcing steps to obtain reasonable estimates of the diurnal cycle. Such sub-daily data can be reconstructed using a model able to disaggregate daily data. The daily disaggregator method (DDM) was developed to produce 3-hourly data from daily datasets. This model was applied to reconstruct the actual climatology and future scenarios. 3-hourly values of air temperature, precipitation, wind speed, shortwave and longwave radiation, surface pressure and specific humidity are obtained from daily values (see Table 3.2).

Table 3.2: Daily disaggregation methods from daily to sub-daily.

Variable		Input	Method	Ref.
Tair	Air temperature	Tmax, Tmin, Tmean	Sinusoidal function	Debele et al. (2007)
Wind	Wind Speed	Daily mean wind speed	Stochastic model (Weibull distribution)	Debele et al. (2007)
SWdown	Shortwave radiation	Daily SWdown	Solar geometry model	Allen et al. (1998)
Rainf & Snowf	Precipitation	Statistical parameters; Daily rainfall and snowfall rate	Random multiplicative cascade processes	Güntner et al. (2001)
Qair	Specific humidity	Daily Qair, Tair and PSurf	Linear interpolation (relative humidity followed by transformation to Qair and supersaturation	Weedon et al. (2011)
LWdown	Longwave radiation	Daily LWdown	Linear interpolation	-
PSurf	Surface pressure	Daily PSurf	Linear interpolation	-

3.3.1.1 Air Temperature

Debele et al. (2007) fitted a cosine function to estimate hourly temperature distributions from daily, maximum and minimum temperature:

$$T_t = (T_{max} - T_{min})/2 \cdot \cos(\pi\,(t - 15)/12) + T_{av} \tag{3.1}$$

where T_t is temperature (ºC) at time t (h) starting from midnight (in the range 1-24); Tmax, Tmin and $T_{av}$are the maximum, minimum and average daily temperatures, respectively, (ºC).

3.3.1.2 Wind Speed

Wind speed can be modelled following random distributions. A modified exponential equation was fitted by generating random numbers from a uniform distribution. We distributed the wind speed using the method recommended by Debele et al. (2007):

$$W_t = W_{day}[-\log(\mathrm{rnd}[0,1))]^{0.3} \tag{3.2}$$

where W_t is the wind speed for day (m/s), W_{day} is the average wind speed for daily (m/s) and rnd[0,1) is a random number between 0.0 and 1.0.

3.3.1.3 Surface Shortwave Radiation

The solar radiation received at the top of Earth's atmosphere on a horizontal surface is called the top of the atmosphere (solar) radiation. The radiation, R, is estimated for each day of the year and for different latitudes using the solar constant, the solar declination and the time of the year by:

$$R = \int_{\omega_1}^{\omega_2} d_r S \cos\Psi \frac{dt}{d\omega} d\omega \tag{3.3}$$

where S is the solar constant, Ψ the zenital angle, $d_r$the inverse of Earth-Sun distance and ω is the hour angle ($\omega = 0$ at solar noon, and before and after solar noon the $\cos(\pm\omega)$ the same value for morning (negative hour angle) or afternoon (positive hour angle).

$$\begin{aligned} d_r &= 1 + 0.033\cos(2\pi/365) & \cos\Psi &= \sin\phi\sin\delta + \cos\phi\cos\delta \\ \delta &= 0.409\sin(2\pi/365\,J - 1.39) & \omega &= (t - 12)\,2\pi/365 + \mathrm{longitude} \end{aligned} \tag{3.4}$$

J is the julian day, δ the solar declination and ϕ the latitude.

For hourly or shorter periods the solar time angle at the beginning and end of the period should be considered when calculating R_t:

$$R_t = \tau R \tag{3.5}$$

τ is the daily mean atmospheric transmittance, calculated as a ratio between the daily values of surface solar radiation, R_t and top of the atmosphere shortwave radiation.

3.3.1.4 Precipitation rate: Rainfall and Snowfall

Precipitation distribution is characterized by extreme variability in space and time. The variability of certain rainfall characteristics with the scale is given by a simple scale-independent relation (Olsson, 1995; de Lima and Grasman, 1999; Güntner et al., 2001). Transformation of precipitation from one scale to another generally involves a fundamental assumption that the properties associated with the precipitation process at these scales are related to each other. If the properties of the process are assumed to be independent of the scale of observation, then the process is said to exhibit "scaling-invariance".

The model is based on the principles of random multiplicative cascade processes. Random cascade process, to model the statistical distribution of the rainfall, repeatedly divides the available space (of any dimension, time or space) into smaller regions, in each step, redistributing some associated quantity according to rules specified by the cascade generator. Its parameters are dependent on (1) the volume and (2) the position in the precipitation sequence of the time interval with precipitation to be disaggregated.

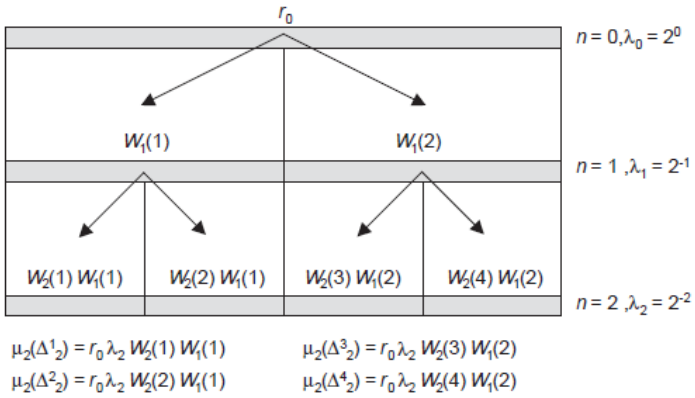

Figure 3.1: Framework of canonical RMC with branching number b=2 and cascade generator W for scales n=0, 1 and 2. R0 denotes rainfall at scale 0. (Molnar and Burlando, 2005)

The canonical random multiplicative model, random multiplicative cascade model (RMC model) distributes precipitation on successive sub division with b as the branching number. As such, the i^{th} interval after n levels of subdivisions is denoted as Δ_n^i. The dimensionless scale is defined as $\lambda_n = b^{-n}$. The distribution of mass then occurs via a multiplicative process through all levels, b of the cascade, such that the mass I, in such division Δ_n^i is:

$$I_{j,k} = r_0 \prod_{i=1}^{k} W_{f(j,i),i} \tag{3.6}$$

where r_0 is the initial precipitation depth (in our case, daily precipitation) at n=0, and $W_{f(j,i),i}$ (denoted as just W for "weights") is a range of weights that essentially forms the cascade generator. W is treated as an independent and identically distributed (iid) random variable, with the important condition that E(W)=1 so that mass is conserved, on average though all levels of the cascade although weights at each time step are not constrained to add up to unity.

The model applied is a multiplicative random cascade of branching number 2 with conservation of the mean and 3 levels (n=3). The methodology involves two steps: (1) identification of scaling behaviour in the precipitation process; and (2) generation of synthetic data possessing similar scaling properties to the observed process. Proprieties of W can be estimated from the moment scaling function behaviour across all scales of interest. To investigate to which degree the scaling properties of the disaggregated data obtained by the final model agree with the observed data, analyses of statistical moments were performed. The analysis was done by averaging the values over different non-overlapping time intervals of length λ. To obtain the q-th order moment M(λ,q), all averaged values are raised to the power q, and

then summed. If the data exhibit scaling, M(λ,q) is related to λ by M(λ,q)≈λτ(q), where τ(q) is a characteristic function of the scaling behaviour. For synthetic data generation, at each level of the cascade model, the total precipitation at the coarser resolution is multiplied by two random numbers to obtain the intensities at the finer resolution. The distribution of the random numbers W assumed is log-Poisson (Gaume et al., 2007).

3.3.1.5 Specific Humidity

Sub-daily specific humidity is calculated from daily specific humidity, e_d, and corrected with temperature and surface pressure.

Table 3.3: Equations for calculating e where T is in ºC and e are in hPa (Willet et al., 2007).

Equation	e	Enhancement factor (f_w or f_i)	Range of T	Max. error
wet-bulb	$6.1121 f_w \exp\left(\frac{18.729 - \left(\frac{T}{227.3}\right)T}{T + 227.3}\right)$	$f_w = 1 + 7.2 \times 10^{-4} + \left(3.20 \times 10^{-6} + (5.9 \times 10^{-10} T^2)\right) P$	-40 to 50 ºC	0.23 % at -40 ºC
ice-bulb	$6.1115 f_i \exp\left(\frac{23.036 - \left(\frac{T}{333.7}\right)T}{T + 279.82}\right)$	$f_i = 1 + 2.2 \times 10^{-4} + \left(3.38 \times 10^{-6} + (6.4 \times 10^{-10} T^2)\right) P$	-80 to 0 ºC	0.06 % at -80 ºC

Following Weedon et al. (2011), daily saturated water vapour pressure, $e_{sat,d}$, is calculated using an equation on Table 3.3. Daily relative humidity, RH_d, is calculated and then interpolated to 3-hourly, RH_{3h}.

$$RH_d = e_d / e_{sat,d} \quad (3.7)$$

The specific humidity, e_{3h}, is finally calculated as:

$$e_{3h} = e_{sat,3h} \times RH_{3h} \quad (3.8)$$

where $e_{sat,3h}$ is calculated using air temperature and surface pressure disaggregated.

3.3.1.6 Longwave Surface Radiation and Surface Pressure

Longwave surface radiation and surface pressure are simply downscaled in time from daily mean to 3-hourly resolution using linear interpolation. No attempt is made to adjust these variables to make them consistent with the disaggregated 3-hourly precipitation, as the relationships between precipitation and other meteorological variables are often weak.

3.4 Global offline simulations

Due to the lack of global sub-daily data, there is no way to verify the disaggregation procedure independently. However, the daily disaggregator method, DDM, can be evaluated through simulations based on modified forcing data.

Global offline simulations forced by WFD dataset have been performed for 20th century. Tri-hourly data (DDM dataset) was created from WFD, available in WATCH ftp site. The suitability of 3-hourly data disaggregation methods was tested by forcing the land surface model HTESSEL. The LSM HTESSEL represents vertical transfers of water and energy using four vertical layers to represent soil temperature and moisture. The land surface scheme HTESSEL has been driven offline with tri-hourly prescribed WFD and DDM atmospheric forcing (1980–1999). This experimental setup is computationally affordable and allows simulations over an extended period of time concentrating on merits and errors of the land surface exposed to a fixed atmospheric forcing. A spin up period of 5 years is considered, as indicated by the WaterMIP protocol, to allow all the considered schemes to reach equilibrium.

Table 3.4: Simulation design of sensitivity test. WFD is the 3-hourly data of WATCH and DDM is the 3-hourly data disaggregated from WFD daily data. The nomenclature indicates the key variable and witch forcing data (WFD or DDM) is used in the simulation.

Simulation	**Forcing data (1980-1999)**	
	WFD	**DDM**
WFD (GPCC)	Prec GPCC (unbiased)	No variable
WFD (CRU)	Prec CRU (unbiased)	No variable
WFD (TPQ)	Others variables	Rainf, PSurf, Wind, LWdown e SWdown
WFD (Prec)	Others variables	Tair, PSurf, Qair, Wind, LWdown e SWdown
DDM (Prec)	Others variables	Rainf e Snowf
DDM (TPQ)	Others variables	Tair, PSurf e Qair
DDM (Wind)	Others variables	Wind
DDM (SW)	Others variables	SWdown
DDM (LW)	Others variables	LWdown
DDM	No variable	All variables (Rainf and Snowf GPCC unbiased)

A detailed quantitative assessment of impacts of disaggregated input data was done by comparison of outputs from reference simulations (conducted using original WFD 3-hourly data, GPCC and CRU versions) with disaggregated simulations (with disaggregated input data, DDM data). Forcing for DDM simulations was created by daily aggregating WFD data, followed by the application of DDM methods to obtain 3-hourly data. Difference between outputs of WFD and DDM simulations represent the impact of the disaggregation. Subselecting variables for applying this method allows the identification of the impact of the corresponding disaggregation algorithms. Each line in Table 3.4 represents one simulation, labelled in the first column and forced by the combination of WFD and DDM data in the 2nd and 3rd columns, respectively. For instance, WFD (TPQ) simulation is driven by temperature, surface pressure and specific humidity from WFD and the remaining data are the other DDM variables; WFD (Prec) is forced with DDM variables and WFD precipitation.

3.5 Performance of DDM method

In this analysis we focus on daily evapotranspiration estimated by the HTESSEL model. WFD (TPQ) and WFD (Prec) are simulations conducted using a combination of WFD and DDM variables. Temperature, pressure and specific humidity in the former; and rainfall and snowfall rate in the latter. The Nash-Sutcliffe efficiency (NS) measures the performance of the forecast, it ranges from $-\infty$ to 1.0 for cases with better performances.

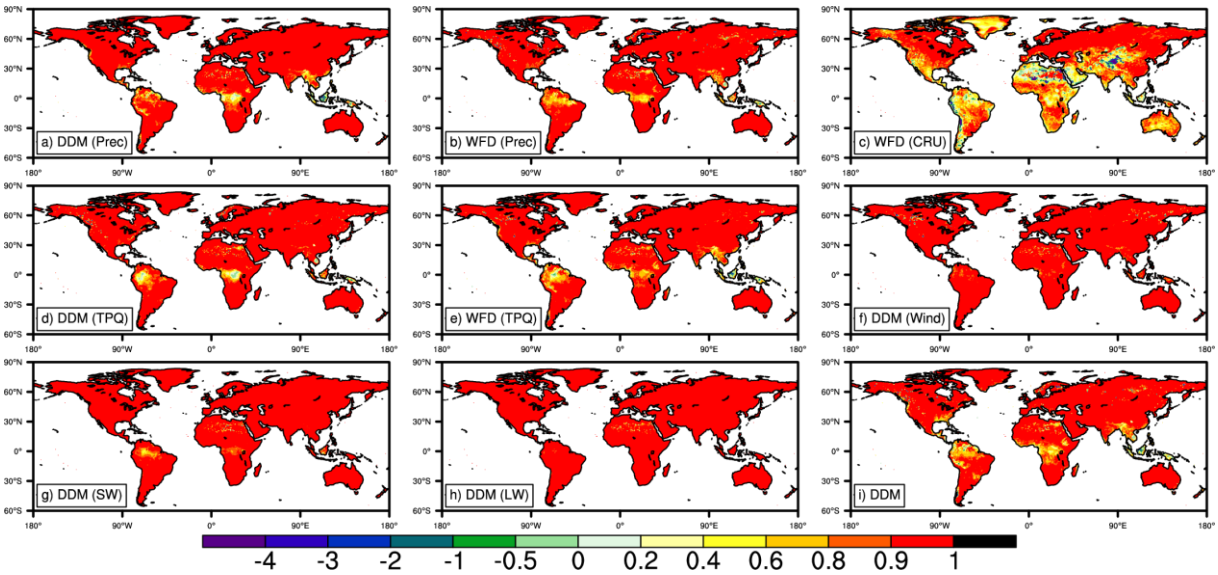

Figure 3.2: Nash–Sutcliffe efficiency coefficients (NS) maps of evapotranspiration rate. The panels show efficiency coefficients between GPCC and each simulation. The closer the values to +1, the better the model performances are.

Simulations DDM (Prec) and DDM (TPQ), panels a and d of Figure 3.2, isolate the effect of disaggregation of precipitation and temperature, pressure and relative humidity, respectively. These simulations show, on average, good results; boreal regions show poor fit in winter with a limited period of daylight. The performance of the model is good for the simulations DDM (Prec), DDM (TPQ) and CRU with high levels of efficiency (Figure 3.2, panels a, d and c). The algorithms of disaggregation of precipitation have virtually no global impact on evapotranspiration (Figure 3.2, panel a). Differences between CRU and GPCC simulations are larger than DDM and GPCC, suggesting that the impact of disaggregation on the results is smaller than the uncertainty on observed precipitation datasets.

3.5.1 Temperature disaggregation

Daily average temperature values were disaggregated into 3-hourly values using a sinusoidal model, equation (3.1). Simulations WFD (TPQ) and DDM (TPQ) were conducted in order to study the impact of the disaggregation of temperature. The first simulation evaluates the impact of non-disaggregated temperature, while the latter isolates the effect of that disaggregation.

The impact of temperature and specific humidity (Figure 3.3 and Figure 3.4, panel a) seems important in winter and merits further analysis; such impact is confined to boreal regions. Note that this impact dominates the efficiency of the DDM simulations. In the remaining months, the model has good performance, with values higher than efficiency coefficient of -1.

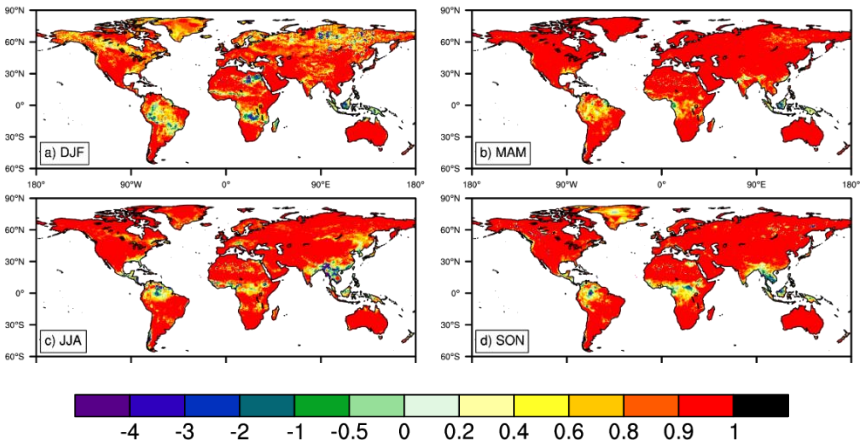

Figure 3.3: Seasonally Nash–Sutcliffe efficiency coefficients for WFD (TPQ).

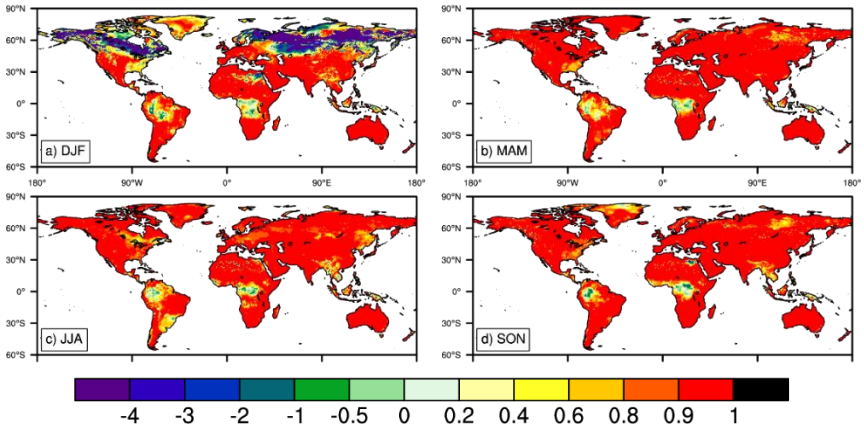

Figure 3.4: As Figure 3.3 but for DDM (TPQ) simulation.

3.5.2 Precipitation disaggregation

Daily precipitation was disaggregated using a multiplicative cascade model, equation (3.6). The mean daily precipitation is distributed throughout the day taking a weight determined randomly but with conditioning of the model parameters at each time step. By definition, the average daily precipitation is conserved. Several simulations were made to evaluate the impact of precipitation: source (WFD-Prec or WFD-CRU) and method (DDM-Prec). Figure 3.5 shows the seasonal efficiency of WFD (Prec) simulation, with precipitation from WFD dataset. To confirm the efficiency of precipitation method WFD-Prec is compared with WFD-CRU and DDM-Prec (Figure 3.7). Lower values of efficiency in winter (panel a, Figure 3.5) reflect the effect of temperature disaggregation. This simulation does not present the disaggregated precipitation. In northern latitudes, with the absence of sunlight during the winter, the daily cycle of air temperature was not solved correctly by the DDM method. A sinusoidal daily cycle is imposed even when the sub-daily variation is small. During summers, with almost continuous daylight, this effect is not relevant. The performance of WFD-Prec simulation, without precipitation disaggregated, is similar to DDM results.

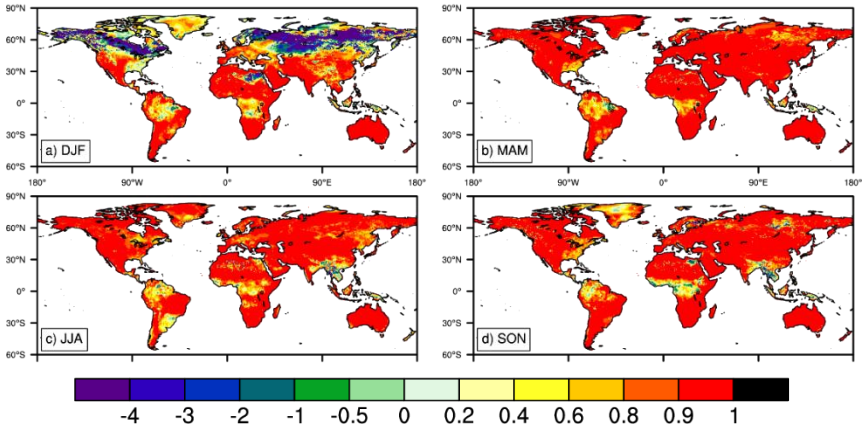

Figure 3.5: As Figure 3.3 but for WFD (Prec) simulation.

There are no significant impacts on evapotranspiration with disaggregated precipitation. The algorithms of disaggregation of precipitation have virtually no global impact on evapotranspiration (DDM-Prec, Figure 3.7). The WFD (CRU) efficiency is lower, suggesting that the disaggregation impact is smaller than uncertainty in precipitation (see Figure 3.6).

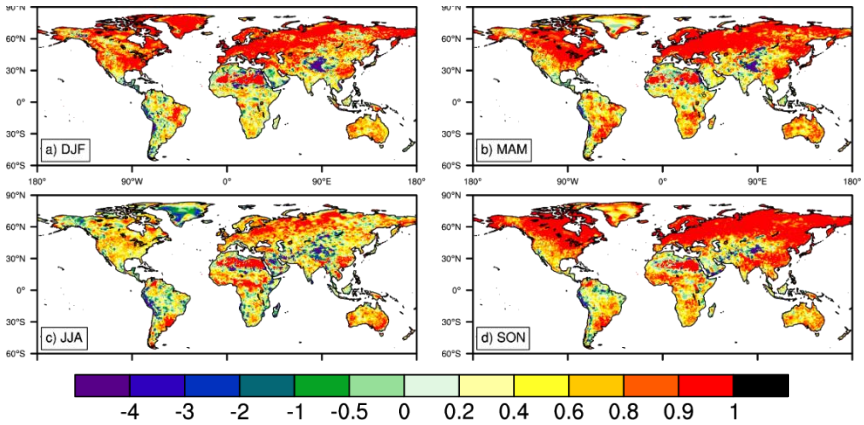

Figure 3.6: As Figure 3.3 but for WFD-CRU.

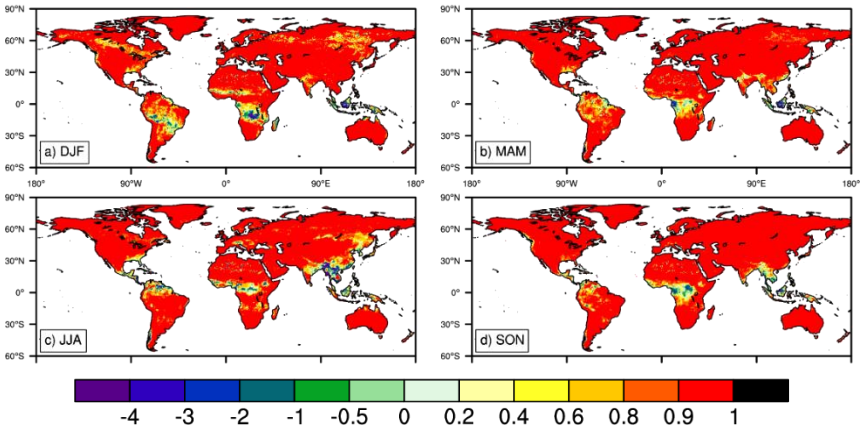

Figure 3.7: As Figure 3.3 but for DDM-Prec simulation.

3.5.3 Total disaggregation

The total impact of the daily disaggregator was tested by comparing the reference simulation with DDM simulation, forcing original and disaggregated, respectively. Figure 3.8 represents the seasonal variation of efficiency of DDM evapotranspiration.

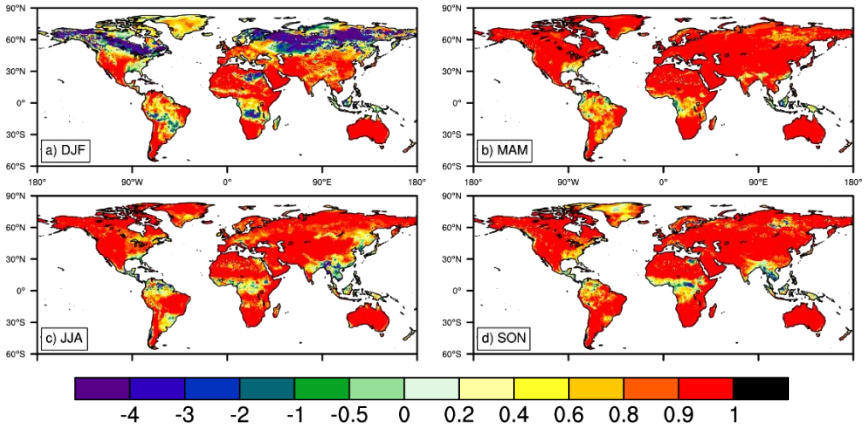

Figure 3.8: As Figure 3.3 but for DDM simulation.

The results presented suggest a good performance except in areas of lower evaporation (e.g. high latitudes). In areas with a very pronounced regime of convective rainfall the quality of model results is also lower. In summary, model evaluation reveals good performance except for regions of lower evaporation and for convective regions.

The model performs well for DDM (Prec) CRU, and WFD (TPQ) simulations (see Figure 3.2, panels a, c and e), with high values of efficiency. The impact of temperature and specific humidity (Figure 3.4) seems important and merits further analysis; such impact is confined to boreal regions. Note that this impact dominates the efficiency of the DDM simulations.

3.6 Balance of water and energy over land

A validation of WFD vs. observations is presented in Weedon et al. (2011). In this section we have chosen a different route. Five points in different climate/biomasses were chosen to exemplify the dataset proprieties.

Overall, the main driver of the forcing data used is the precipitation (CRU or GPCC). Choices of alternative combinations of DDM or WFD are overwhelmed by changes in precipitation. With the exception of boreal regions, uncertainties in the forcing are larger than DDM induced errors. In addition, the differences in DDM and WFD (GPCC) simulations are of the same order of magnitude as the difference between WFD (CRU) and WFD (GPCC). To understand all limitations of DDM methods, the annual cycle of the global water cycle was analysed: precipitation, evapotranspiration and runoff. Figure 3.9 summarizes the features of seasonal cycle for the globe over land areas (except Greenland and Antarctica). Vertical bars represent monthly mean precipitation (snowfall and rainfall rate): WFD (GPCC), as blue, DDM, as green, and WFD (CRU), as red. Solid lines represent evapotranspiration (Evap) and dashed lines are the total runoff of each sensitivity experience WFD (GPCC), DDM and WFD (CRU).

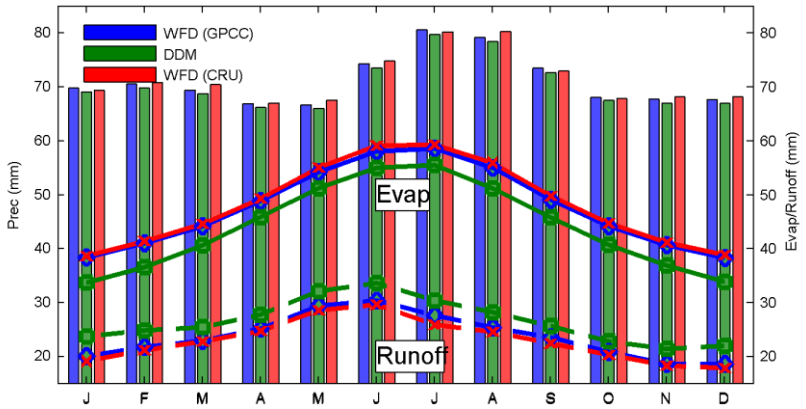

Figure 3.9: Annual cycle of precipitation, evapotranspiration and runoff rates over land13 areas (except Greenland and Antarctica). Blue, green and red bars are WFD, DDM and WFD (GPCC) precipitation, respectively. Uni0ts are in mm/month.

To evaluate the method of disaggregation, Figure 3.10 presents the annual cycle of evapotranspiration and total runoff of the various sensitivity tests performed. Air temperature is one of the forcing variables with the greatest impact in the annual cycle of runoff and evapotranspiration (red lines), in contrast to wind and radiation (SW or LW) that do not show significant differences from the reference simulation (WFD), black lines in the picture. Precipitation is also an important variable of input. Reduction in DDM precipitated water (green bars in Figure 3.9) will reduce the amount of water lost by evaporation and increase the total runoff. Changes due to the origin of precipitation (GPCC or CRU) have little impact on the annual cycle.

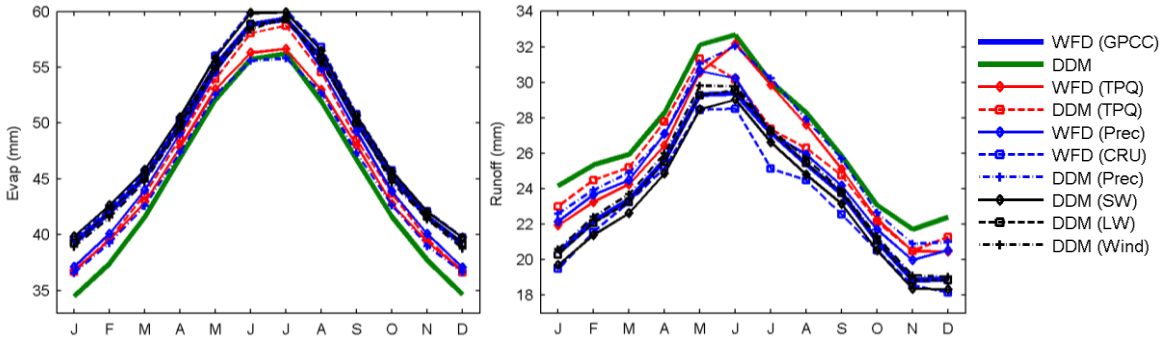

Figure 3.10: Global annual cycle (excluding Greenland) of evapotranspiration and total runoff. Blue and green lines represent evapotranspiration or runoff of WFD and DDM simulations, respectively. Intermediate colours represent simulations combining WFD and DDM data (see legend on the picture).

Simulations of the water cycle allow the DDM method to be evaluated in contrasting climate types. Such test complements the global analysis that was done in the last section.

3.6.1 Global water and energy cycle impact

In the previous section the global water and energy cycle were analysed for simulations WFD, WFD (CRU) and DDM. The annual water and energy cycle distribution depend on climate type. To analyse the impact in both cycles five grid points were selected to represent five different climate types: continental subarctic (Alaska); moderate Mediterranean (near Lisbon); dry semiarid (desert of Sahara); tropical wet and dry (Sahel region) and tropical wet (Central Africa, near Congo) (see Figure 3.11).

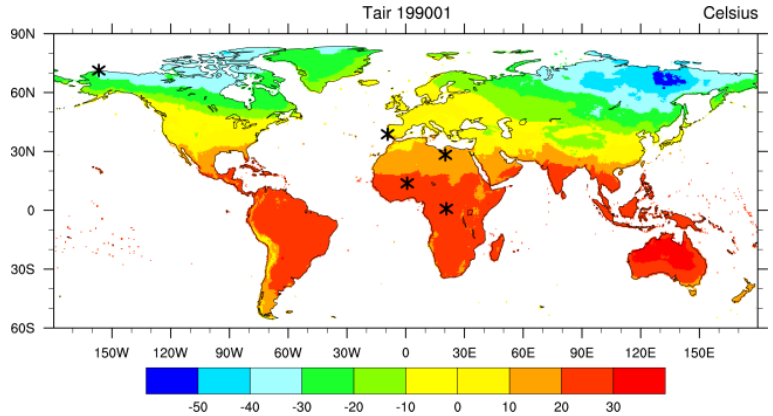

Figure 3.11: WFD air temperature in January 1990. The selected points were chosen to analyse the results.

Figure 3.12 shows scatterplots of original (WFD) and disaggregated (DDM) tri-hourly: Tair, Qair and SWdown, as blue, red and green, respectively, near Lisbon. Specific humidity, Qair, has the lowest coefficient of determination, r^2, 0.78. Both downwards shortwave radiation flux and air temperature at the surface, SWdown and Tair respectively, 3-hourly data have a good agreement at Lisbon, r^2 = 0.98 and 0.95. The higher values of Qair are lightly overestimated by DDM method.

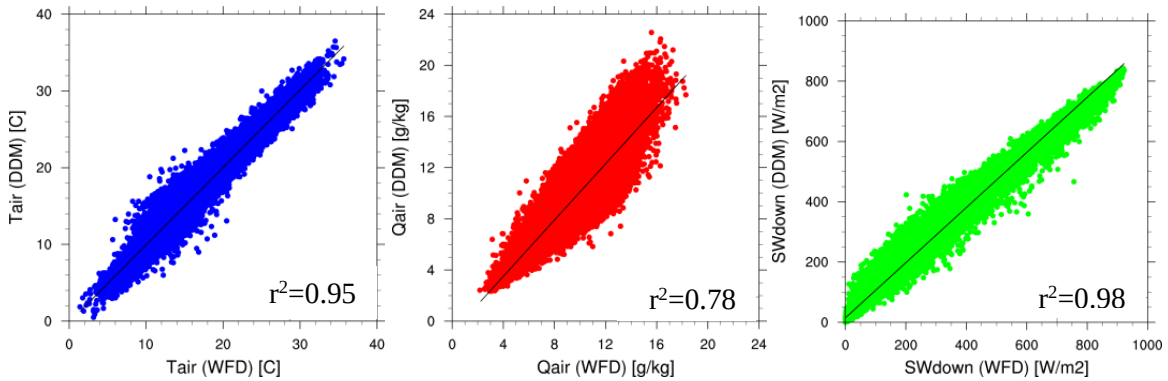

Figure 3.12: Original (WFD) and disaggregated (DDM) 3-hourly dataset: (a) air temperature (ºC), (b) specific humidity (g/kg) and (c) downwards shortwave radiation flux (W/ m^2), for Lisbon (lat=38.75 ºN lon=9.25 ºW). Data from 1985 to 1999.

a) Continental Subarctic (boreal) climate

Continental climate is characterized by the most extreme seasonal temperature variations on the planet. Precipitation, typically with moderate intensity, occurs mostly in summer (see Figure 3.13). It varies between 10 mm in January and 30 mm in August. The annual total evapotranspiration over high-latitudes is low, reflecting the prevailing low air and soil temperatures. The snow that falls during winter months is retained in surface storage until spring thaw releases it for infiltration and runoff. There are no significant differences between DDM and WFD annual cycles (Figure 3.13). There are no clear differences in the energy cycle (Figure 3.13b); bias is lesser than 3 Wm^{-2}.

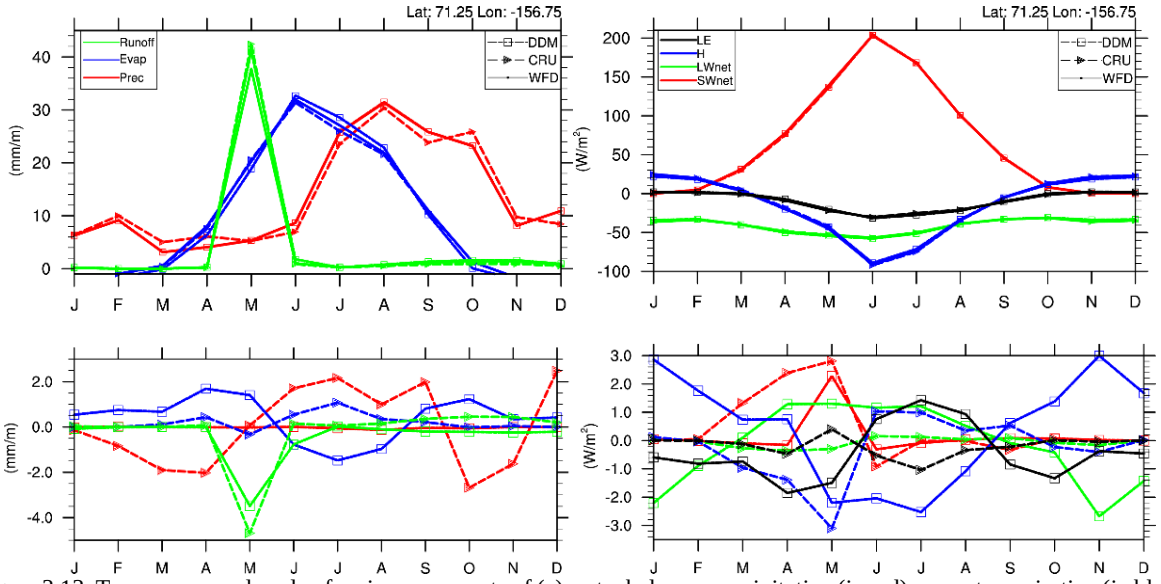

Figure 3.13: Top row: annual cycle of main components of (a) water balance: precipitation (in red), evapotranspiration (in blue) and runoff (in green); (b) energy balance at the surface: solar radiation – SWnet (in red), longwave radiation – LWnet (in green), sensible heat flux – H (in blue) and latent heat flux – LE (in black). Squares, triangles and dots represent DDM, CRU and WFD simulation, respectively. Bottom row: WFD minus DDM (squares) and CRU (triangles) simulations of water and energy cycles, respectively.

b) Mediterranean climate

Mediterranean climate is characterized by warm to hot dry summers, and mild to cool, wet winters. Figure 3.14 shows the monthly variation of the water cycle (precipitation, evaporation and runoff) and energy balance for a Mediterranean climate. The annual average of WFD and DDM simulations is similar. The WFD (CRU) simulation, forced with precipitation corrected with CRU observations, reveals significant differences: more precipitation and therefore more runoff than others.

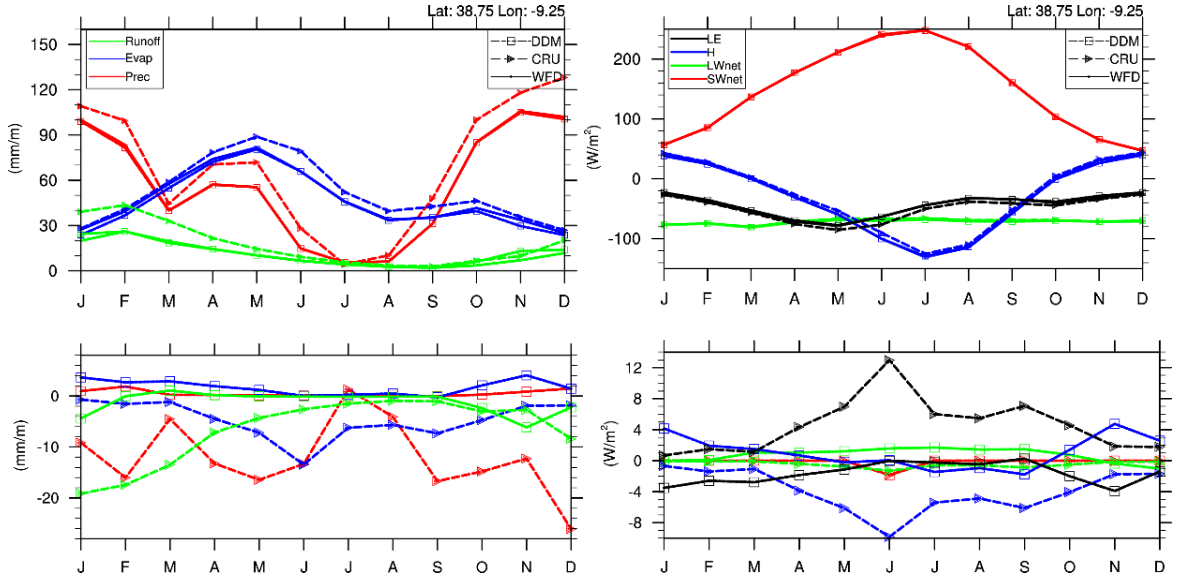

Figure 3.14: As Figure 3.13 but for Mediterranean climate.

c) Semiarid climate

Dry climates are characterized by little rain and a huge daily temperature range. Rainfall rate is less than 6 mm/month. Consequently, there is little or no runoff. Evapotranspiration is greater than precipitation, except in the rainy season (September to April) (see Figure 3.15). Differences between WFD and other simulations do not exceed 4 mm per month. The annual cycle of energy components is similar for all simulations.

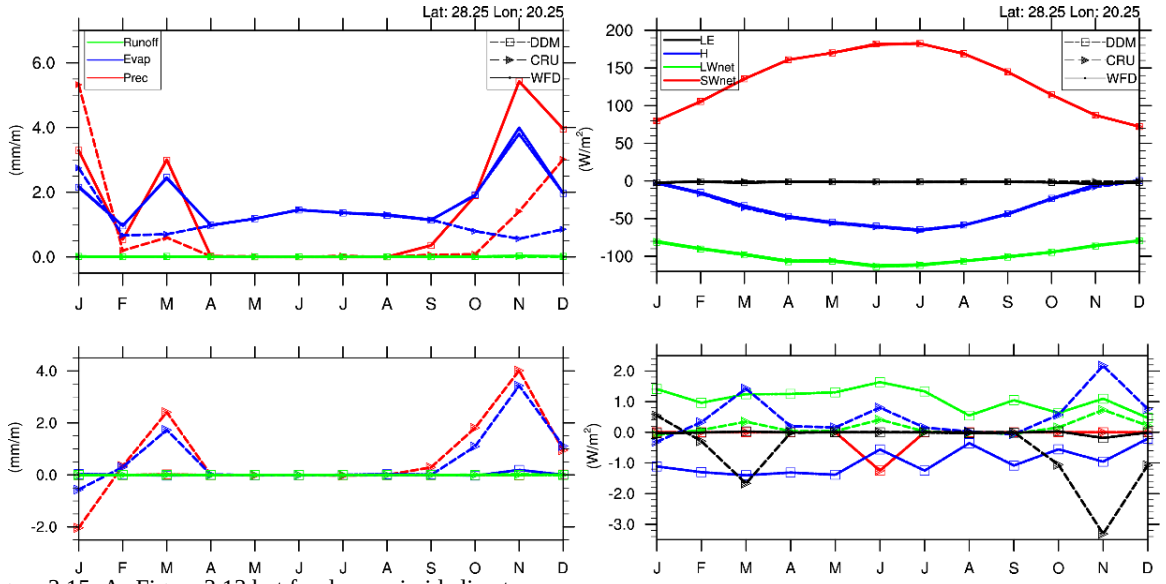

Figure 3.15: As Figure 3.13 but for dry semiarid climate.

d) Tropical climate

Tropical climates (wet and dry-wet) are controlled by solar radiation. Tropical temperature remains relatively constant throughout the year and seasonal variations are dominated by precipitation. Tropical wet-dry climate has a pronounced dry season, with seven months below 30 mm of precipitation (Figure 3.16).

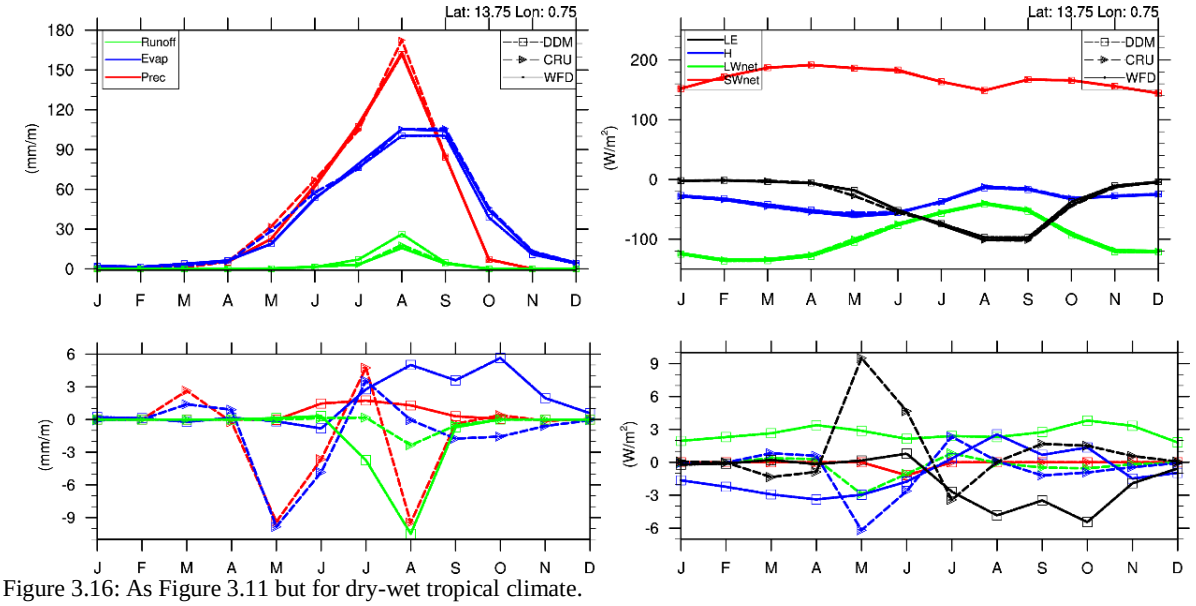

Figure 3.16: As Figure 3.11 but for dry-wet tropical climate.

Diurnal variations in temperature exceed seasonal variations because of the effect of sun angle on climate. In tropical climate, seasonal variations are dominated by changes in precipitation, which are in turn largely influenced by the position of the tropical rain belt or Intertropical Convergence Zone (ITCZ) cell. Monthly precipitation, on Figure 3.17, always exceeds 80 mm. CRU and GPCC precipitations are significantly different. The highest differences on precipitation occur in March and October, 40 mm and 60 mm, respectively (CRU is higher than GPCC). This difference has impact on runoff. In DDM simulation the surface loses more energy, by latent heat flux, than WFD simulation, about 10 mm more, between June and August.

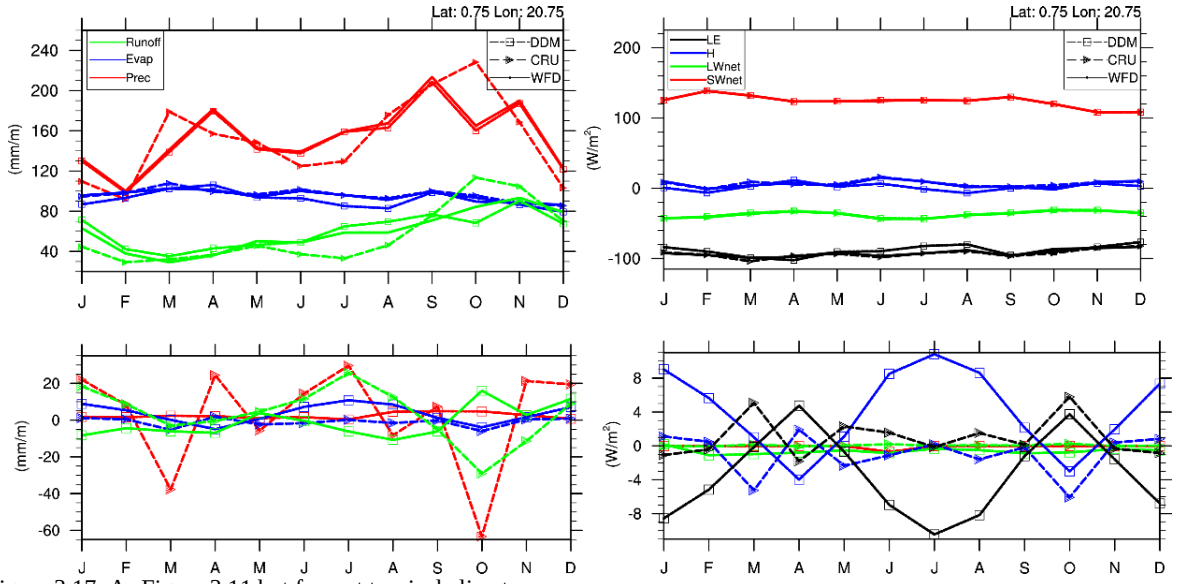

Figure 3.17: As Figure 3.11 but for wet tropical climate.

3.7 Conclusions

This study tested the disaggregated data as the input field for hydrological simulations. The results based on HTESSEL simulations with WFD and DDM forcing data showed that the DDM forcing could be globally used. Based on the coefficient of efficiency applied to monthly evapotranspiration, the developed forcing data (DDM data) performs well in most cases, with the notable exception of high latitudes. The model performance was found to be sensitive to Tair/Qair disaggregation in boreal latitudes. The most significant differences in evapotranspiration were related to differences in Tair/Qair method used during cold season. However the differences in observed precipitation datasets (GPCC or CRU version) have a larger impact than the difference between DDM and WFD, especially for Mediterranean and wet tropical climate.

These results suggest that the disaggregating model developed is ready to be applied to reconstruct current climatology and future scenarios (see Chapter 4 and Chapter 5, respectively), with special attention to boreal winter.

Chapter 4 - Current state of climate

4.1 Modelling of land surface processes

The study of land surface processes is vital to understanding the role of terrestrial land surface in the Earth's climate. A problem often reported in global studies is the lack of global observational data that can be assessed with mathematical models. These models, Global Circulation Models (GCMs), also known as Global Climate Models, are able to describe the physical processes in the atmosphere, ocean and land surface. They consist of Atmospheric and Oceanic General Circulation Models (AGCMs and OGCMs) along with sea-ice and land surface models (SIMs and LSMs). The numerical modelling focus on hydrological processes at the surface can be used to estimate the water and energy cycles and their components. This category of models describes hydrological and energy processes at a global scale, and is used to assess the effect of global change on the world's water resources at the surface. The number of models that simulate the terrestrial water cycle on large (continental and global) scales is continuously increasing. While climate models have been working at the global scales, with grid cells typically of 1 degree (~100 km x 100 km), hydrological models, catchment-based, work with scales smaller than 50 m x 50 m. Scale choice depends on cost-effectiveness, given that even the fastest super-computers cannot run global climate models at these small scales.

Depending on purpose, the hydrological models are divided in two main categories: land surface models (LSMs) and hydrological water balance models (WBMs), also called global terrestrial hydrological models (GHMs) (see a comprehensive overview by Haddeland et al., 2011). Both types can be used at global scales. Simulation of the global water balance components and energy budget are performed by different types of models (Widen-Nilsson et al., 2007) such as hydrological water balance models, globally operating dynamic vegetation models like LPJ (Gerten et al., 2004) and land surface schemes (or models) originally designed to be used on global circulation models. In GHMs, the land surface hydrology processes are treated in a rather conceptual way but the surface energy balance, critical to evaporation, is not treated. In contrast, LSMs used for climate modelling studies solve both water and energy balances. LSMs represent the land surface in climate models and numerical weather prediction simulations. They are apt to describe the vertical exchanges of heat, water, and sometimes carbon (Dirmeyer et al., 2006). The energy and water fluxes represented at the interface between atmosphere and land surface are based on fully coupled heat and mass balance equations. Most of them are confined to a limited depth soil and usually exclude model components for groundwater and water transport and storage in surface water bodies (Güntner, 2008). The most recent LSMs have advanced to include more detailed ecological and biogeochemical processes (Boussetta et al., 2013). See Pitman (2003) for an overview on the different generations of LSMs. In contrast, GHMs focus on water resources and lateral transfer of water; they do not necessary solve directly the surface energy balance. Nevertheless, GHMs represent the terrestrial hydrological cycle in a more complete way, including all its components in order to close the water balance for the area of interest (Widen-Nilsson et al., 2007). GHMs have a less detailed process representation compared to the LSMs, and use simple conceptual hydrological models to generate runoff, and they often contain parameters calibrated on river flow (e.g. WaterGAP). MacPDM uses regional model parameters tuned to a range of hydrological storage and human intervention, such as groundwater, irrigation, and water reservoirs and dams.

The hydrological and land surface models can differ in terms of spatial and temporal resolution, details in process representation, number of parameters or data demand. Common to all models at large scales is that they suffer from considerable uncertainties in terms of model structure and process description, parameter values and atmospheric forcing data used as model input. Consequently, simulation results for hydrological state variables and water fluxes on the continents vary considerably between the models (Dirmeyer et al., 2006), reflecting the multiple uncertainties in our understanding of the current water cycle.

Model intercomparison is one way to assess the uncertainty associated with land surface parameterizations. A common experiment is performed by different centres, offering the possibility to

compare results not just with observations, but with other models as well. Model intercomparison enables researchers to explore the range of model behaviours, to isolate the various strengths and weaknesses of different models in a controlled setting, and to interpret, through idealized experiments, the inter-model differences. These studies allow the comparison of LSM and GHM results in a consistent way in different communities (hydrology, climatology and meteorology). Model errors tend to be large, as shown by intercomparison model projects as PILPS, ALMIP, GSWP2 or more recently, WaterMIP (Table 4.1).

Table 4.1: List of intercomparison projects and main objectives.

Intercomparison Project	Main objectives	Models	References
PILPS Project for the Intercomparison of Land-Surface Parameterization Schemes	Improve the parameterization of the land-surface schemes, especially the parameterizations of hydrological, energy, and momentum exchanges	LSMs	Henderson-Sellers et al. (1995) Wood et al. (1998)
GSWP Global Soil Wetness Project	Produce state-of-the-art global data sets of land surface fluxes, state variables, and related hydrologic quantities. Develop and test large-scale validation, calibration, and assimilation techniques over land. Provide a large-scale validation and quality check data sets. Compare Land Surface Schemes (LSSs), and conduct sensitivity studies of specific parameterizations and forcing, to aid future model and data set development.	LSMs	Dirmeyer et al. (1999, 2006) Dirmeyer (2011)
ALMIP African Monsoon Multidisciplinary Analysis – AMMA – Land surface Model Intercomparison Project	Obtain a better understanding of the intra-seasonal and interannual variability of the west-African monsoon.	LSMs	Boone et al. (2004, 2009)
WaterMIP Water Model Intercomparison Project	Compare results of LSMs and GHMs; Estimate water availability and stress, as well as uncertainties thereof; will also be compared for both current and future conditions; Improve our understanding of current and future water availability and water stress at the global scale, with an emphasis on the available water resources of major river systems at the subannual time scale.	LSMs & GHMs	Haddeland et al. (2011)

Recently the Water Model Intercomparison Project (WaterMIP), the EU Water and Global Change (WATCH) FP6 project and the GWSP (Global Water System Project) joined activities (Haddeland et al., 2011). This model intercomparison project compares a variety of models (LSMs and GHMs) of terrestrial hydrological cycles, and produces multi-model ensemble estimates of the state of the world's water resources for the 20th and 21st centuries. The main objective is to estimate current and potential future global water resources based on common forcing data (i.e. the WATCH Forcing Data, see Chapter 2) and a standardized simulation protocol. The project helps to understand the differences between models and between broad groups of models, in order to improve models by exchanging ideas and parameterisations, particularly between traditionally separate communities (climate and hydrological), guided by analysis of WaterMIP simulations. These improvements in the representation of hydrological processes used in climate models will ensure that feedback processes will be better represented in climate change simulations. It will contribute to improved estimation and understanding of the impacts of global change on the global hydrological cycle and water resources, including its uncertainties. Note that large-scale hydrological models are, in contrast to catchment-scale models, usually not calibrated. Instead the model parameters are derived from mapped land properties, such as soil texture or vegetation density.

Ensemble methods are here used to explore the uncertainty in climate model simulations that arise from internal variability, boundary conditions, parameter values settings for a given model structure, and structural uncertainty due to different model formulations. A multi-model ensemble is created from model simulations from WaterMIP project to study the structural uncertainty and internal variability. The first step is to evaluate the different hydrological and land surface models, with different schemes, forced by the same atmospheric conditions. This type of intercomparison does not take into account the atmospheric feedback which might reduce or increase the differences between schemes.

In order to evaluate the global water cycle over land, this chapter addresses an ensemble of land and hydrological models driven by a common dataset. The main purpose of this is to estimate the water cycle

(precipitation, evapotranspiration and total runoff) from hydrological and land surface models. Next, this study uses simulations to compare drought indices over Europe.

4.1.1 Offline global simulations

In the present section, 30-year forced simulations were performed at a global scale for 1971–2000 period to simulate the global water cycle (see Table 4.2). All models used the WFD meteorological data described by Weedon et al. (2010, 2011), but they do not use the same variables or model time step (Table 4.2 and Table 4.3). The models were run from 1958 to 2000 at a global scale, with a 0.5ºx0.5º horizontal resolution by the WFD meteorological forcing. Only the last 30-years were analysed. The spatial resolution of the forcing data and the model simulations is 0.5º in latitude and longitude, covering the land area defined by the Climate Research Unit of the University of East Anglia (CRU) global land mask (except Antarctica) (Weedon et al., 2010, 2011). Their default soil and vegetation information are used to drive the models. While LSMs run using a sub-daily time step (3-hourly, preferably), hydrological models, in water balance mode alone, run with daily time steps (Haddeland et al., 2011). HTESSEL land surface model was driven using 3-hourly input.

Table 4.2: A list of WaterMIP model simulations used in this analysis (based on table 1 Haddeland et al., 2011). GHM: Global Hydrological Model; LSM: Land Surface Model.

	Model name		**Modelling group**	**Meteorological forcing variables** [1]
GHM	LPJmL	Lund-Potsdam-Jena managed Land Dynamic Global Vegetation and Water	PIK/WUR	P, T, LWnet, SW
	MacPDM	Macro-scale - Probability-Distributed Moisture model.	University of Reading	P, T, W, Q, LWnet, SW
	MPI-HM	SL scheme/ HD model	MPI – M	P, T
	WaterGAP	Water - Global Assessment and Prognosis	CESR – Kassel	P, T, LWnet, SW
LSM	VIC	Variable Infiltration Capacity model	VIC community	P, Tmax, Tmin, W, Q, LW, SW, SP
	HTESSEL	Hydrology - Tiled ECMWF Scheme of Surface Exchanges over Land	CGUL/IDL	T, Q, R, S, LW, SW, W, PS

[1]T: air temperature; Tmax: maximum daily temperature; Tmin: minimum daily temperature; Q: specific humidity; R: rainfall rate; S: Snowfall rate; P: Precipitation; LW: Longwave radiation flux (downward); SW: Shortwave radiation flux (downward); LWnet: longwave radiation flux (net); W: wind speed; SP: surface pressure.

The main characteristics of hydrological and land surface models are specified in Table 4.3. MPI-HM is the only model using the Thornthwaite evapotranspiration method, where potential evapotranspiration is calculated based on air temperature only.

Haddeland et al. (2011) verified that during the Indian monsoon the effect on evapotranspiration of reduced incoming solar radiation and high humidity is clearly visible in the result of all models other than MPI-HM. The MPI-HM estimated evapotranspiration (ET) can be substantially higher than that estimated by other models when shortwave radiation or humidity limits evaporation in models using, for example, the Penman-Monteith or Priestley-Taylor equation.

Table 4.3: Summary of characteristics of models used in this study (adapted from Haddeland et al., 2011).

Model name	**Model time step**	**Energy balance**	**ET schemes**	**Runoff schemes**	**Snow schemes**
LPJmL	Daily	No	Priestley-Taylor	Saturation excess	Degree-day
MacPDM	Daily	No	Penman- Monteith	Saturation excess/ beta function	Degree-day
MPI-HM	Daily	No	Thornthwaite	Saturation excess/beta function	Degree-day
WaterGAP	Daily	No	Priestley-Taylor	Beta function	Degree-day
VIC	Daily/3h	Snow season	Penman-Monteith	Saturation excess/ beta function	Energy balance
HTESSEL	1 h	Yes	Penman-Monteith	Infiltration excess/ Darcy	Energy balance

4.1.2 Multimodel analysis: hydrological cycle

A set of global hydrological simulations (data from WaterMIP project, 1971-2000) were tested and globally compared to obtain a global hydrological cycle over land. Hydrological consistency was verified on the monthly time-scale. The main goal of this analysis is obtaining a better understanding of the intra-seasonal and inter-annual variability of the global hydrological cycle, and to assess the ability of several large-scale hydrological and land surface models to capture important aspects of water cycle climatology. The model climate is characterized by the mean annual cycle, which is one of the most fundamental signals of large-scale hydrology. Characteristics of the mean annual cycle allow for insights into the water balance and the seasonality of water components.

For each water cycle component, precipitation P, evapotranspiration E, and total runoff (surface and subsurface) R, over land, a comparison among a multi-model ensemble simulation was done. In addition, results are presented for the mean annual cycle of the atmospheric hydrological cycle based on waterMIP simulations (Figure 4.7). These include monthly estimates of P, E, and R, zonal means over land (see Figure 4.12), hemispheric land means, and global land means. The global land area is calculated assuming that the Earth is a sphere with radius 6371 km; the total land area according to the according to the CRU land mask is 1.46×108 k m^2 (or 1.44×108 k m^2 when Greenland is excluded). A few models reduce precipitation when simulated snow water equivalent (SWE) exceeds a given level, which influences precipitation numbers in some northern areas (Haddeland et al., 2011). Because of this and because very few models include a glacier scheme, the values presented here do not include Greenland. However, Greenland is included in all model simulations. Finally, soil moisture anomalies and precipitation time series from waterMIP simulations are used in order to evaluate extreme events like floods and droughts over Europe.

4.1.2.1 Long term averages

The 1971-2000 model climate for each simulation is presented in this section. The contribution of each component, i.e. precipitation, evapotranspiration and surface and subsurface runoff, of each waterMIP model is presented in Figure 4.1. Forced with the same precipitation field, models show different partitions into evapotranspiration and runoff (surface and subsurface runoff). Surface runoff ratio (Qs/P), simulated by LSMs (VIC and HTESSEL) is smaller than GHMs: about 16% (142 mm/yr) and 10 % (88 mm/yr Figure 4.1. In MPI and HTESSEL models, total runoff ratio (R/P) is 34 %. 30-year average annual precipitation is 880 ± 64 mm/yr of which 58% and 42% leave as evaporation and runoff, respectively (Figure 4.2). Interannual and intraseasonal variability is also presented. Total precipitation average, is about 880 ± 64 mm/yr, globally balanced by evapotranspiration (510 ± 95 mm/yr, 58% evaporative fraction), surface runoff (203 ± 31 mm/yr, 24% of precipitation) and subsurface runoff (165 ± 23 mm/yr, 18% of precipitation), shown in Figure 4.2.

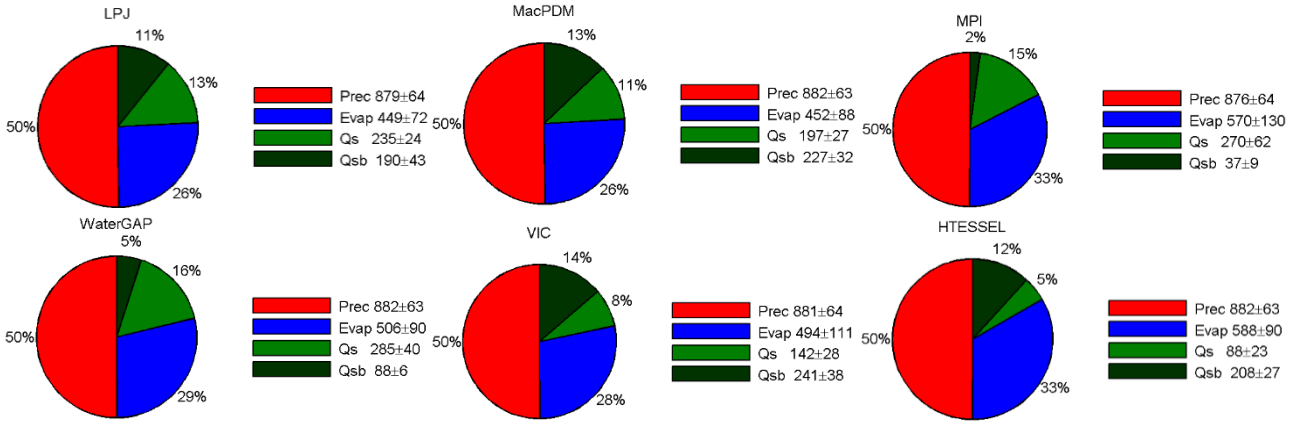

Figure 4.1: Long-term average terrestrial water balance (1971–2000) for each model, sigma are the interannual and intraseasonal variability. The 30-year averages of global water partition into water budget components: Prec, precipitation; Evap, evapotranspiration; Qsb: subsurface runoff; Qs, surface runoff. Evapotranspiration is consistently the largest outgoing component. Units in mm/year.

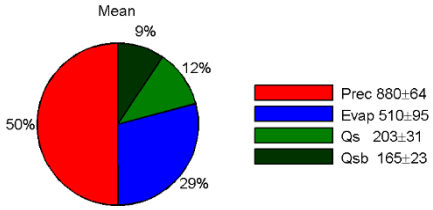

Figure 4.2: As Figure 4.1, but for ensemble of models thereof.

Each water balance component fluctuates from year to year (Figure 4.3). Precipitation is highly variable between years, varying between 832 and 919 mm/yr (MPI and HTESSEL, respectively). The precipitation variability between models is not significant, given that precipitation is a prescribed variable. Evaporation rates are the most constant between years, with a maximum range of 26 mm/yr, from 497 mm/yr to 523 mm/yr, (Table 4.4) and a standard deviation of 95 mm/yr (Table 4.4 and Figure 4.3b). Evaporation estimated by MPI has the highest range and standard deviation, 45 mm/yr and 130 mm/yr, respectively. Dirmeyer et al. (2006) showed global-mean terms of surface energy and water balance among GSWP2 models. Evapotranspiration varied between 272.0 and 441.5 with 48.1 mm/yr of standard deviation (table 3, Dirmeyer et al., 2006).

Dai and Trenberth (2002) estimated continental runoff about 37 000 km^3yr^{-1}, similar to the Fekete et al. (2000), about 38 000 km^3yr^{-1}. Haddeland et al. (2011) found 42 000 to 66 000 km^3yr^{-1}, calculated from 1985-1999. In this study the estimated continental runoff varies between 43 000 to 62 000 $km3yr^{-1}$, estimated by HTESSEL and LPJml, respectively. The land mask used by Fekete et al. (2000) covers only 92 % (1.33× 108 km^2) of the area reported here (Greenland excluded), which may explain the differences presented in Haddeland study and in this analysis.

Table 4.4: Global-mean and range of land average terms of water balance among models (precipitation, evapotranspiration and total runoff) and water imbalance. Units of water balance terms are kg $m^{-2}yr^{-1}$ (i.e., mm per year). Error: 1 standard deviation. Values estimated from global monthly means between 1971 and 2000 (Greenland and Antarctica excluded). Min and max values refer to monthly values.

Model	Precipitation (P) [mm/yr]			Evapotranspiration (E) [mm/yr]			Total runoff (R) (Qs+Qsb) [mm/yr]			Water imbalance P-(E+R) [mm/yr]		
	Min	Max	Mean ± Std	Min	Max	Mean ± Std	Min	Max	Mean ± Std	Min	Max	Mean ± Std
LPJmL	835	916	879 ± 64	440	461	449 ± 72	388	453	425 ± 62	-244	172	4 ± 103
MacPDM	838	919	882 ± 63	429	465	453 ± 88	381	458	424 ± 58	-251	384	5 ± 117
MPI-HM	832	913	876 ± 64	549	594	570 ± 130	276	330	307 ± 69	-311	244	-0.4 ± 147
WaterGAP	838	919	882 ± 63	493	521	506 ± 90	336	402	373 ± 45	-210	158	2 ± 103
VIC	838	918	881 ± 64	481	510	495 ± 111	346	408	383 ± 65	-290	206	4 ± 137
HTESSEL	838	919	882 ± 63	573	608	588 ± 90	260	328	296 ± 47	-237	319	-3 ± 105
Ensemble	837	917	880 ± 64	497	523	510 ± 95	331	395	368 ± 53	-230	181	2 ± 115

In the period 1985-1999 the global terrestrial mean precipitation was 872 mm/yr (or 126 000 km^3yr^{-1}), according to the WATCH forcing data (Haddeland et al., 2011). While the ensemble precipitation estimated in the period 1971-2001 was 880 mm/yr (about 127 000 km^3yr^{-1}), excluding Antarctica and Greenland.

Interannual variability of water budget components for each model simulation is shown in Figure 4.3. LPJ model simulates the lowest evapotranspiration (about 449 mm/yr, from 440 to 461 mm/yr) while HTESSEL has the highest value (~588 mm/yr, that ranges between 573 and 608 mm/yr) (see values in Table 4.4). WaterGAP evapotranspiration is the average model, closer to multi-model result, with 506 mm/yr in contrast with 510 mm/yr of the ensemble evapotranspiration (Table 4.4).

High/low total runoff is indirectly related with high/low precipitation events. LPJ, as well MacPDM, have the most intense runoff annual average (about 425 and 424 mm/yr, in contrast with HTESSEL with the lowest mean of runoff, 296 ± 47 mm/yr. These values are balanced by evapotranspiration values: the highest values for HTESSEL against the lowest values to LPJ and MacPDM (Table 4.3).

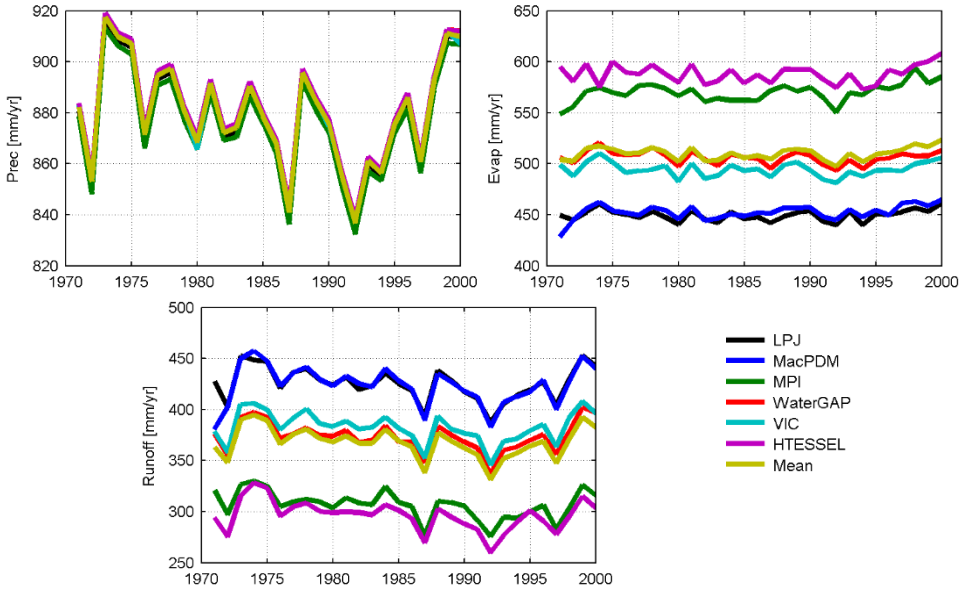

Figure 4.3: Interannual variability of water budget components: (left) precipitation, (middle) evapotranspiration and (right) total runoff. Thirty years of annual water apportionment of the water budget for global land (Antarctica and Greenland excluded). Runoff rate varies the most from year to year relative to their long-term averages.

The average and the standard deviation error, which measures the dispersion from the average, of P, E and R are present on Table 4.4. MPI-HM has the relatively largest standard deviation of P, E and R: 64, 130 and 69 mm/yr, respectively. Average water imbalance ($P - (E + R)$) floats around zero, from -0.4 ±147 mm/yr (MPI-HM) to 5±117 mm/yr (MacPDM). Model ensemble is 2 mm/yr with an intraseasonal variability of 115 mm/yr. The multi-model ensemble and its interannual range is expressed in Table 4.5. Precipitation ensemble average is 880 mm/yr, with individual year values ranging from 857 to 903 mm/yr.

Table 4.5: Long-term multimodel mean annual values and the interannual range of multimodel mean precipitation, runoff and evapotranspiration.

	Multimodel mean annual values (mm/yr)	**Interannual range of multimodel mean (mm/yr)**	
Precipitation	878	857	903
Evapotranspiration	510	485	535
Runoff	368	350	386

Precipitation is a forcing variable common to all models (daily in GHM and subdaily in LSM), which is partitioned into evaporation and runoff according to the parameterizations of each model. The linear relationship between evapotranspiration and runoff is revealed in Figure 4.4. The location in the line indicates the evapotranspiration and runoff partition. The alignment of points along the diagonal reflects the average precipitation, similar between models (about 880 mm/yr). HTESSEL and MPI have the higher evapotranspiration and lower runoff; the opposite occurs for MacPDM and LPJ models. Despite substantial differences in the model mean evaporation or runoff, the interannual variability is very similar. Variability seems to be driven by year to year variations in precipitation and details on model physical processes have little or no impact on interannual variability.

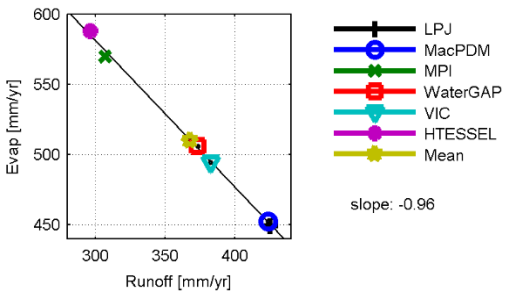

Figure 4.4: Global terrestrial mean model predicted runoff vs. evapotranspiration values (mm/yr, excluding Antarctica and Greenland).

4.1.2.2 Climate index influence

The El Niño-Southern Oscillation (ENSO) is one interannual phenomenon that deserves particular attention in climate studies. The warm phase (El Niño) is characterized in the tropical Pacific Ocean basin by anomalously warm waters in the east, weak trades, and anomalously low pressure and heavy rains in the east and high pressure and dry conditions in the west. Anomalies of the opposite sign tend to accompany the cold phase (La Niña). Several different indices quantify the evolution of the warm and cold phases of ENSO. We used here a normalized ENSO precipitation index (ESPI) developed by NASA (Curtis and Adler, 2000). Curtis and Adler (2000) constructed indices based on the zonal gradient of precipitation in the equatorial Pacific to monitor ENSO: EI (El Niño index), LI (La Niña index) and ESPI (ENSO precipitation index). Data were obtained from GPCP precipitation product. EI, LI, and ESPI are not only tools for monitoring ENSO, but can be used to analyse and compare historic and future events. ESPI index from 1979 to 2000 is shown in Figure 4.5 (vertical bars).

To focus the analysis on longer than seasonal variability, long-term monthly means were removed from the monthly time series of water cycle terms. The interannual variability of global anomalies of water balance components and the ESPI time series are presented in Figure 4.5. Positive ESPI values (e.g. 1982-83, 1986-87, 1991-92 and, 1994-95 and 1997-98 El Niño events), are related with negative anomalies of global precipitation as well as evapotranspiration and total runoff (red bars on Figure 4.5). This relationship can be expressed with a scatter plot between ESPI indices and precipitation anomalies (Figure 4.6).

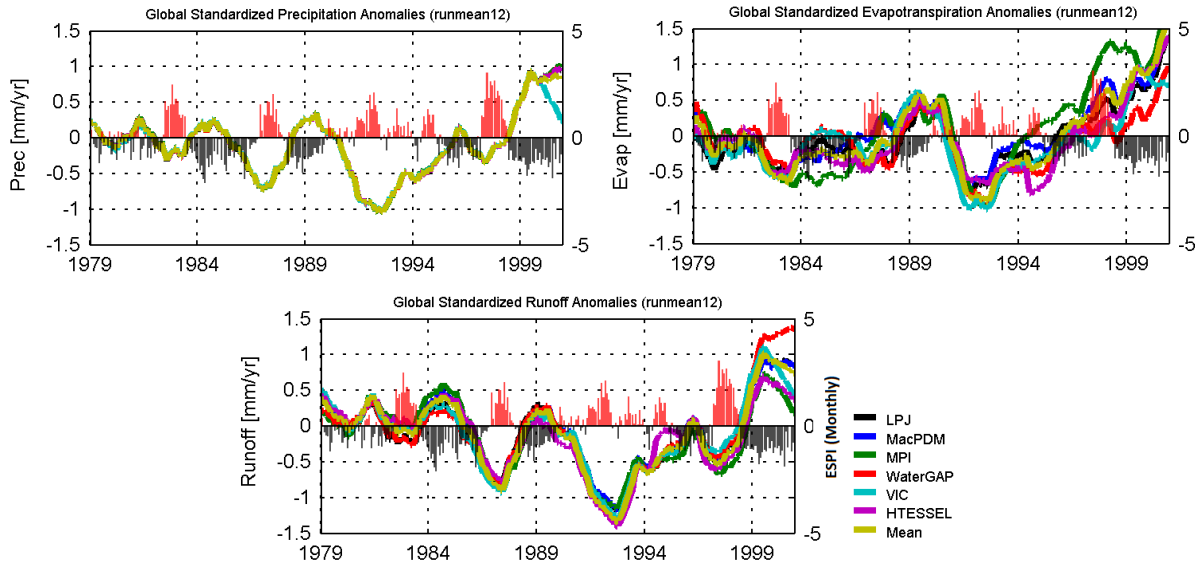

Figure 4.5: Interannual variability of water balance terms anomalies (12-month running average): precipitation, evapotranspiration and runoff. Coloured lines represent each WaterMIP model and ensemble mean. Vertical bars are the monthly time series of ESPI. Red/black bars represent El Niño/La Niña events.

Figure 4.6 relates the global precipitation anomalies with ESPI values, estimated from zonal gradient of precipitation in the equatorial Pacific at monthly scale. There is a relationship between global precipitation anomalies and ESPI indices: negative anomalies correspond to the warm phase (El Niño), while positive anomalies correspond to the cold phase (La Niña). ESPI and precipitation have a coefficient of correlation of -0.56. Negative anomalies of global precipitation correspond to a positive ESPI phase.

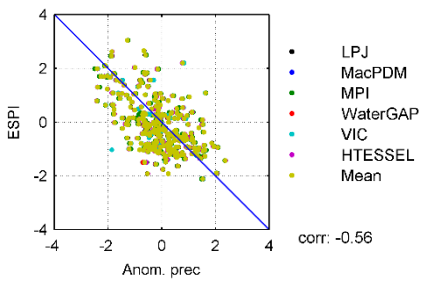

Figure 4.6: Scatter plot between monthly precipitation anomalies and ESPI index. The coefficient of correlation is -0.56.

4.1.2.3 Annual cycle

The annual cycle of precipitation, evapotranspiration and runoff over land is pronounced due to asymmetry of land between the two hemispheres (Trenberth et al., 2007). The seasonality for each component is revealed more clearly with the breakdown in hemispheric contributions: a minimum of precipitation and evapotranspiration during Northern Hemisphere's winter and the opposite at Southern Hemisphere (Figure 4.7). In the Northern Hemisphere, evapotranspiration exceeds total runoff almost all of the time, except from November to January. Interdecadal variability is small and the interannual variability inter-decade is not changed (figures not shown).

Terrestrial water storage includes all water stored on land (Hirschi et al., 2007). Here we investigate the seasonal evolution of ΔTWS (includes all water stored on land) in an ensemble of 30-year-long climate simulations (1971-1999). In order to highlight the different behaviour in main zonal areas, 3 regions are defined: Northern Hemisphere (limited at the South by Tropic of Cancer), Southern Hemisphere (limited at the North by Tropic of Capricorn) and Tropics. The weak seasonal cycle of tropical ΔTWS and precipitation is due to the meandering of the ITCZ.

Northern hemisphere ΔTWS is positive during October to March due to winter precipitation. The surface loses water (negative ΔTWS) during spring and summer due to melt induced runoff in spring and increased evaporation in late spring and summer.

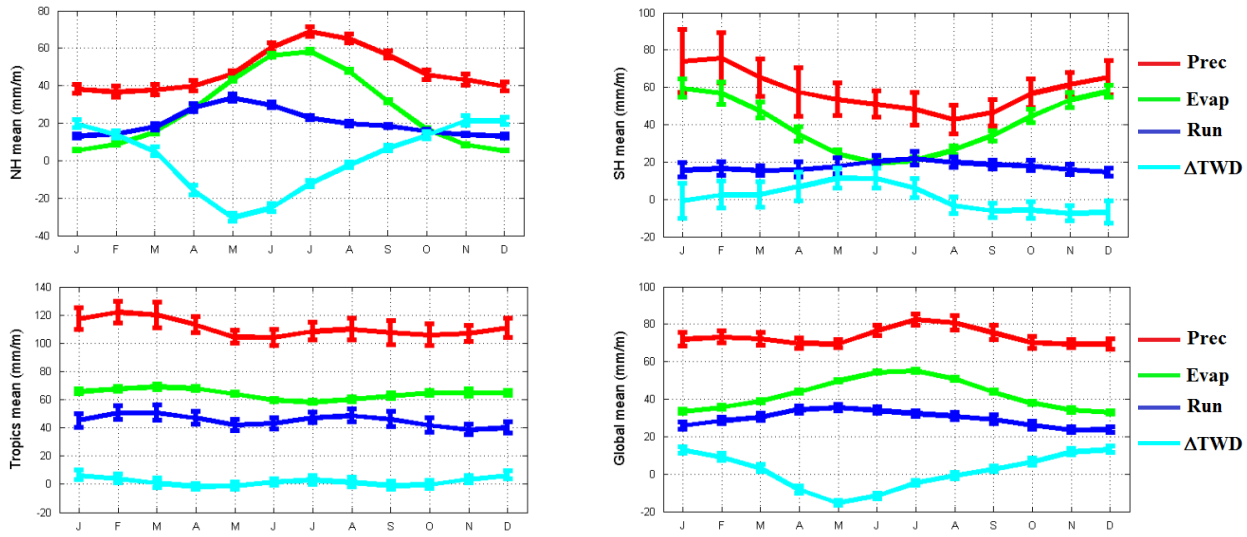

Figure 4.7: Annual cycle of land precipitation (red), land evapotranspiration (green), land runoff (blue) and ΔTWS (cyan) at northern hemisphere, southern hemisphere, tropics and global from 1971-2000 (ensemble of six models models). Vertical bars are standard deviation errors, corresponding to intra-annual variation. Units in mm/month. Different scales.

By construction, differences in precipitation are negligible, while evapotranspiration and runoff, calculated internally by each model, varies. HTESSEL predicted the highest evapotranspiration, except during Summer (JJA), where MPI had the highest values (results not shown). The lowest annual cycle of evapotranspiration was simulated by the LPJ model. These values agree, as expected, with the interannual variability shown previously, in Figure 4.3. Figure 4.8 presents boxplots of global averages of evapotranspiration and runoff for northern and southern hemisphere, tropics and global for each waterMIP model, respectively. Multimodel runoff variability in the NH exceeds the corresponding variability in the tropics and southern hemisphere. MPI and HTESSEL present the highest evapotranspiration range in the NH.

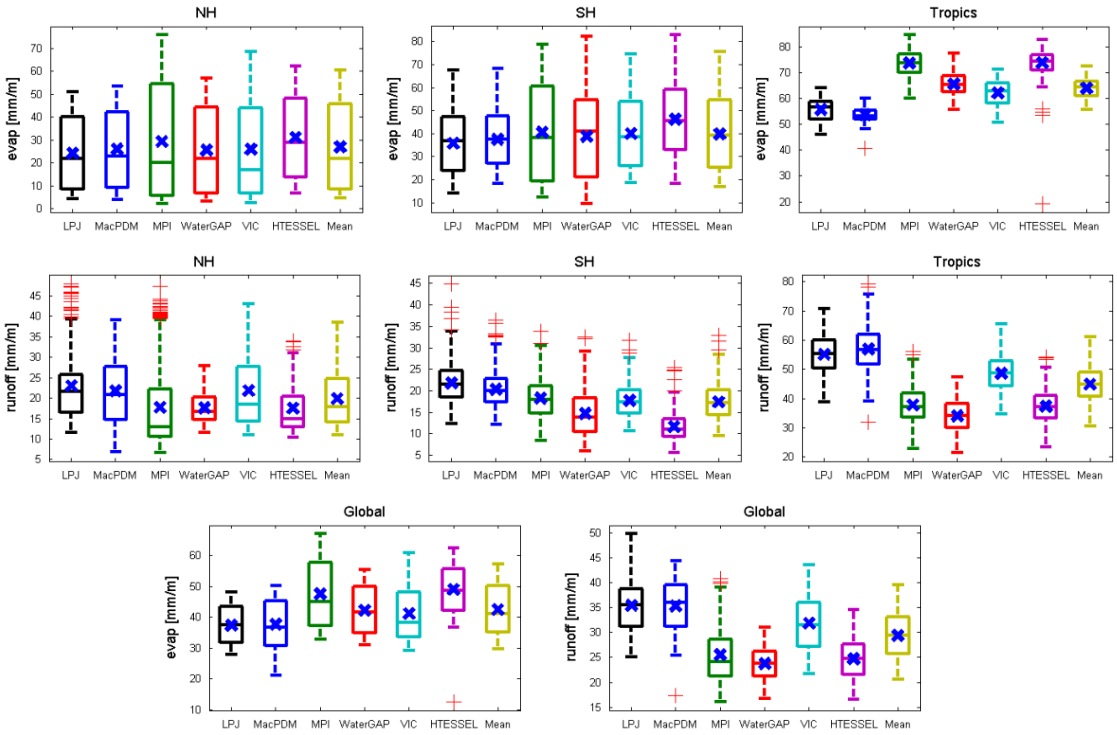

Figure 4.8: Boxplot of global averages of evapotranspiration and runoff for: LPJ, MacPDM, MPI, WaterGAP, VIC, HTESSEL and ensemble of models. Units are in mm per month. The central box represent the central 50 % of data. Its lower and upper boundary lines are at 25 %/75% quantile of the data. The central line and cross indicates the median and mean of data, respectively. Two vertical extending from central box indicating the remaining data outside the central box that are not regarded as outliers. These lines extend maximally to 3/2 time the height of the central box but not past the range of data.

Some differences in simulated runoff and evapotranspiration could be explained by model parameterizations, although the processes included and parameterizations used are not distinct to either land surface models or global hydrological models. Results show that differences between model parameterizations are a major source of uncertainty. Figure 4.9 shows the annual cycle of zonal standard deviation for each component for MPI and HTESSEL, a hydrological and a land surface model.

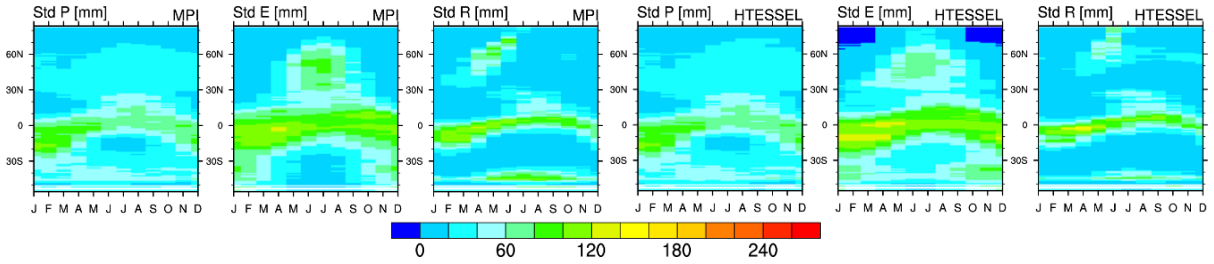

Figure 4.9: Standard deviation of zonal precipitation, evapotranspiration and runoff for MPI and HTESSEL models.

Figure 4.10 illustrates variations in seasonality from Pole to Pole. Evapotranspiration and runoff patterns are intimately linked to precipitation. P, E and R are highest in the tropics; the peak of evaporation occurs during the rainy season. The excess of precipitation leaves the surface as runoff. Runoff is also influenced by the freeze-thaw seasonality in boreal areas, and by the intensity and frequency of precipitation events. Melting of ice and snow occurs during late spring (April to July) of high latitudes (Figure 4.10), where runoff exceeds 100 mm/month in some models. Water stored as ice and snow limits runoff during the winter and increases this flux in the spring due to thaw. Each model partitions precipitation into evaporation and runoff. MACPDM and WATERGAP have the highest and smallest values of runoff, respectively. Evaporation is largest in HTESSEL and smallest in MACPDM.

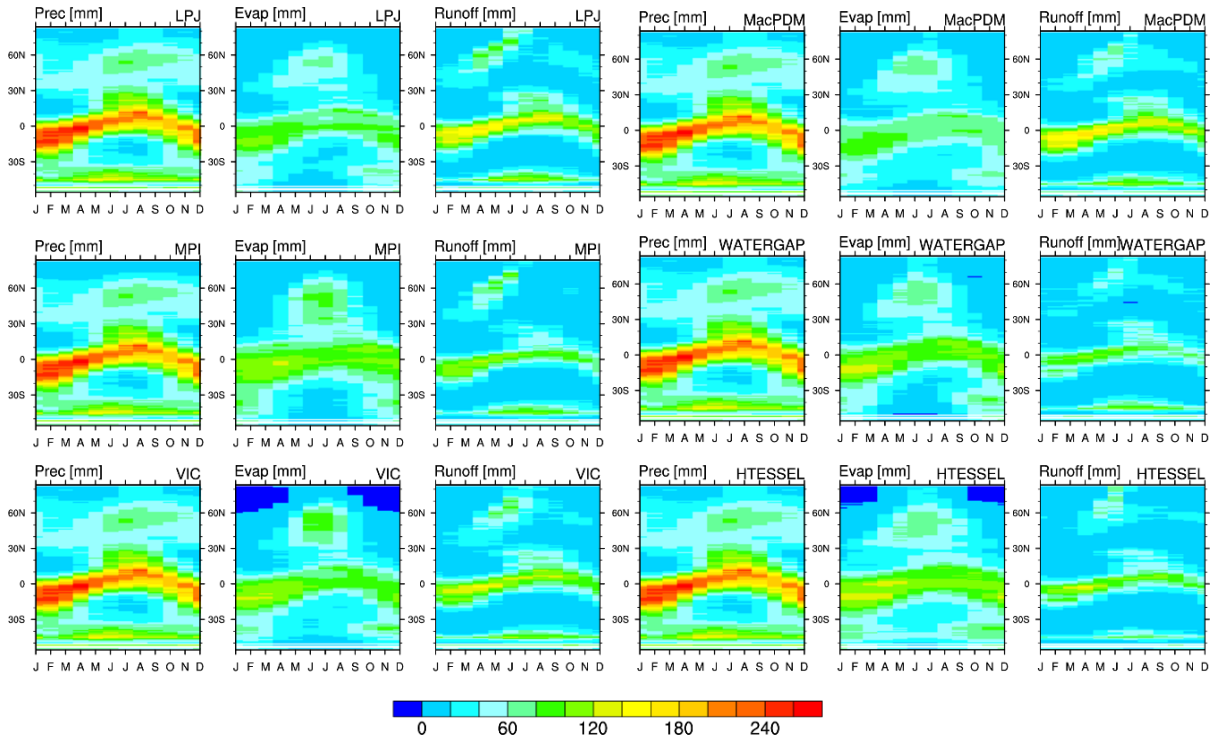

Figure 4.10: Simulated annual cycle over land computed from [1971-2000] of the zonal precipitation (left), evapotranspiration (middle) and runoff (right): LPJmL, MacPDM, MPI-HM, WaterGAP, VIC, and HTESSEL. Units in kg $m^{-2}month^{-1}$.

4.1.2.4 Global E-P over land

In a steady state, precipitation P exceeds evapotranspiration E over land and the residual water runs off, resulting in a continental freshwater discharge into the oceans (Dai and Trenberth, 2002). Climatologically, runoff can be expressed as the difference between evapotranspiration and precipitation, E – P. This difference can be shown by global maps, see Figure 4.11, that shows where water evaporates (red) and precipitates (blue). The low latitude rainfall region known as the Inter-tropical Convergence Zone (ITCZ) and monsoon zone, where P > E, with precipitation exceeding evaporation in the range 25-150 mm/month. Trenberth et al. (2007) estimated about 5 mm/day, about 150 mm/month, (see figure 3 from Trenberth et al 2007) from ERA-40 reanalysis in ITCZ zone.

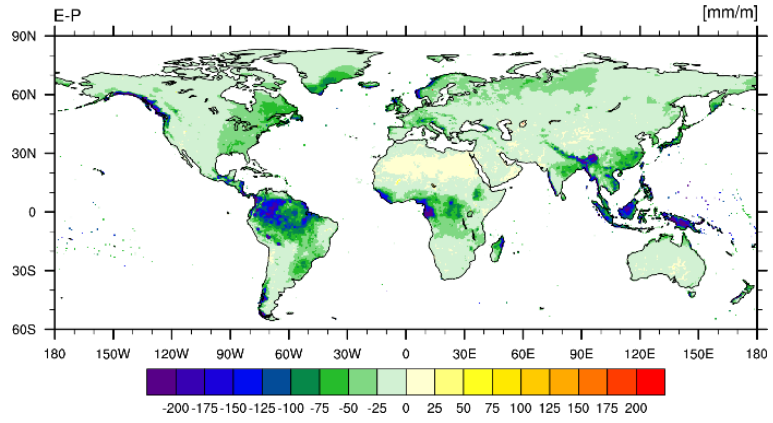

Figure 4.11: The monthly-mean distribution of (E-P) from the ensemble of models from WaterMIP models from [1971-2000]. Units in mm/month. E: monthly mean evapotranspiration; P: monthly mean precipitation.

For any shorter period, surface E – P is balanced by total runoff (surface and subsurface runoff) and by water variation in soil moisture and groundwater. The partitioning of precipitation into evapotranspiration and runoff is highly dependent on the moisture status of the land surface, especially the amount of soil moisture available for evapotranspiration, which in turn depends on properties of the land cover such as the rooting depth of plants. Small values of E – P occur over Eurasia, North America and Australia. The zonal mean of seasonal variation of E – P for each model is expressed by Figure 4.12. Precipitation exceed evapotranspiration (P > E) throughout most of the year, as expected over land. Negative values of E – P located almost everywhere with maximum value in tropical zone, where

precipitation exceeds evapotranspiration, revealing the ITCZ position. The largest negative values of E – P occur in the ITCZ zone during September-November; LPJ and MacPDM models have the most negative E – P. These results agree with Trenberth et al. (2007).

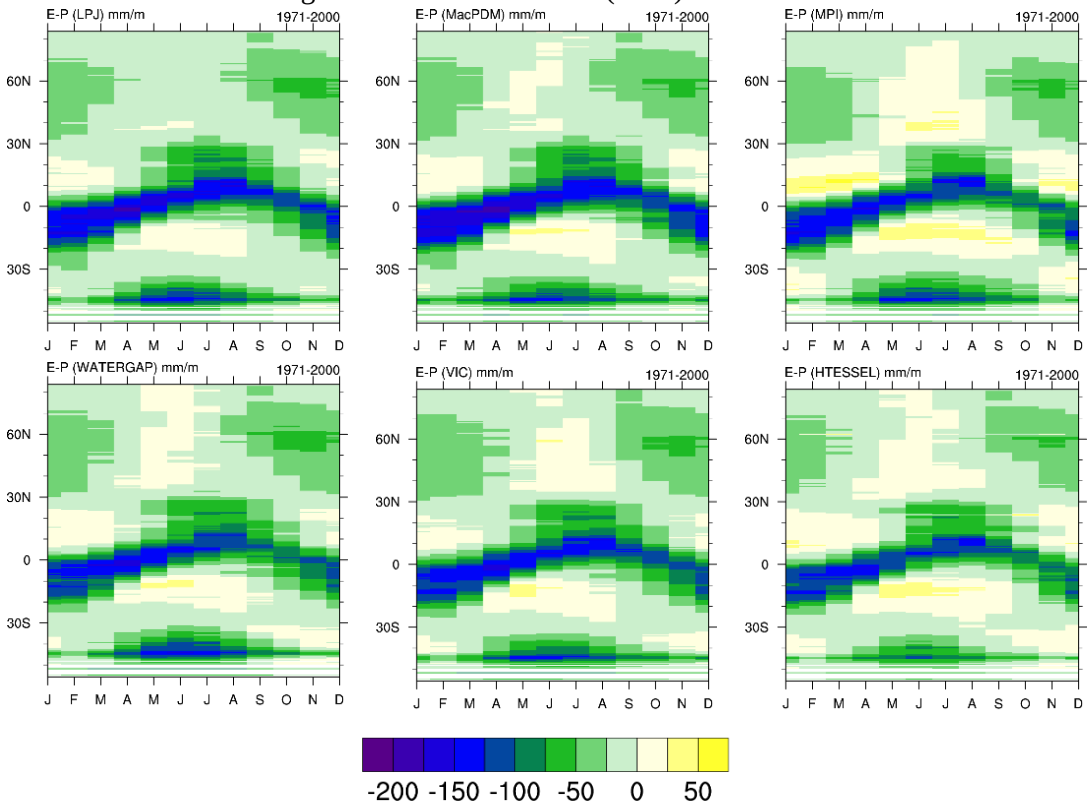

Figure 4.12: Zonal mean over land for the mean annual cycle of E-P from 1971-2000 for the difference between evapotranspiration and precipitation: LPJmL, MacPDM, MPI-HM, WaterGAP, VIC, and HTESSEL.

Runoff fractions are calculated as runoff divided by precipitation. Figure 4.13 show box plots illustrating the simulated runoff fractions for all models, each LSM and GHMs and the ensemble model (Mean) for northern, NH, and southern hemisphere (SH), tropics and global land. The multi-model mean simulated runoff fraction ranges from 0.15 to 0.7, without outliers. The average runoff fractions are lower for MPI and HTESSEL, than for most other models. At the southern hemisphere, the variability is higher for all models, except MPI. There are less outliers in the southern hemisphere.

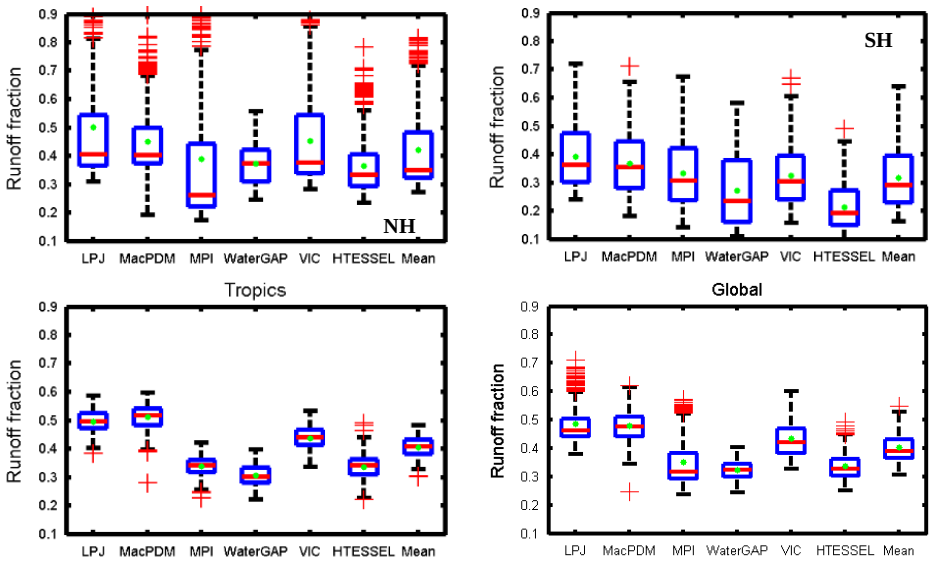

Figure 4.13: Box plots illustrating the smallest simulated runoff fractions, lower quartiles (25th percentiles), medians (red line), upper quartiles (75th percentiles), and the largest simulated runoff fraction for waterMIP models and ensemble (Mean): (top) north and south hemisphere; (bottom) tropics and global land. The whiskers extend to the most extreme data point not considered outliers, and outliers are plotted individually. The central green point is the average.

4.1.2.5 Regional Drought Characterization – Europe

Drought can be defined in several ways. Dai (2011) defined it as a recurring extreme climate event characterized by below-normal water availability over a period of months to years. Precipitation, as well as evapotranspiration, are the primary factor that controls the formation and persistence of drought conditions. The low or non-precipitation is often combined with high evaporation rates. Drought assessment is conventionally based on drought indices for the identification of drought intensity, duration and its areal extent.

There are several drought studies at regional and global scale. Sheffield et al. (2004) analysed the pattern and frequencies of drought over North America. The drought index used provides a physically based and consistent estimate of the drought state, which can be implemented into an operational drought-monitoring tool. Van der Schrier et al. (2006a, 2006b) calculated summer PDSI (Palmer Drought Severity Index) over North America and Europe for 1901–2000 and identified the 1930s and 1950s as the driest periods of the record over North America and the late 1940s to early 1950s over Europe. Recently, Sheffield and Wood (2007) analysed drought occurrence over global areas for 1950-2000 using soil moisture data from a simulation of the terrestrial water cycle using VIC land surface model.

As indicated in previous studies, drought analysis has been performed to identify anomalies determined and characterized by drought indicators, which allow the detection of drought or flood events. These indices were developed to identify and quantify drought's magnitude, duration, intensity and spatial extension, and to improve techniques for drought early warning and management (Vicente-Serrano, 2006). There are several types of indices able to quantify the severity of the drought events, based on precipitation, soil moisture, etc. (examples on table 1, Heim 2002). Based on a large number of drought index parameters, it is possible to define drought in terms of meteorological, hydrological, agricultural, and socio-economic conditions. More recent studies show a relatively large spread on trends in global droughts and or dryness since the middle of the 20th century (Sheffield et al., 2012; Dai, 2013; Donat et al., 2013; van der Schrier et al., 2013; Orlowsky and Seneriratne, 2013).

Soil moisture drought, which uses observed or simulated soil moisture data, can be used to indicate drought situations (Wanders et al., 2010). This indicator focuses on soil moisture anomalies with respect to the season and location. For that analysis, precipitation is not directly taken into account. Soil moisture acts as an integrator of precipitation with different time scales for each point, determined by the forcing and soil physical characteristics (Sheffield and Wood, 2007; and Dutra et al., 2008).

Considering $\theta_{i,j}$ total depth soil moisture, in a specific grid point, for month i and year j, with $i = 1, \dots, 12$ and $j = 1, \dots, N$, NSM (Normalized Soil Moisture) in month i and year j can be defined as:

$$NSM_{i,j} = \frac{\theta_{i,j} - \overline{\theta_i}}{s_i} \qquad \overline{\theta_i} = \frac{1}{N}\sum_{j=1}^{N}\theta_{i,j} \qquad s_i = \sqrt{\frac{1}{N-1}\sum_{j=1}^{N}\left(\theta_{i,j} - \overline{\theta_i}\right)^2} \qquad (4.1)$$

where $\overline{\theta_i}$ and s_i are the mean monthly values and standard deviation, respectively. NSM is a normalized index that uses the standard deviation as a measure of interannual variability (Dutra et al., 2008).

Another index used in drought studies is the Standard Precipitation Index, SPI, which is based only on precipitation; it is the most robust index used to identify drought events. SPI can be computed at a variety of time scales for any location in the world that has a precipitation record, being useful for both short-term agricultural and long-term hydrological applications. SPI is computed by fitting a probability density function to a frequency distribution of precipitation summed over the time scale of interest (McKee et al., 1993). Positive SPI values indicate larger than median precipitation, and negative values indicate smaller than median precipitation. The Standard Precipitation Index is the cumulative precipitation deviation from the climatological average, expressed as a fraction of standard deviation. It can be calculated for any time scale, e.g.: 3-, 6-, 9-, 12- or 24-month. 12-month SPI reflects long-term precipitation patterns. The shorter time scales address meteorological and agricultural drought while the longer ones focus on hydrological drought. The time scale of 24 months is adequate for the investigation of long-term aspect of dryness and wetness. Table 4.6 defines four drought categories for the SPI

indicator. Dutra et al. (2008) compared NSM with SPI from observations, at several time scales, and the Palmer Drought Stress Index (PDSI) for the ERA-40 period over the Iberian Peninsula. The highest correlations were found between SPI-12 and NSM.

Table 4.6: Drought classification by SPI value and corresponding event probabilities.

SPI value	Category	Probability (%)
2.00 or more	Extremely wet	2.3
1.50 to 1.99	Severely wet	4.4
1.00 to 1.49	Moderately wet	9.2
0 to 0.99	Middle wet	34.1
0 to -0.99	Mild drought	34.1
-1.00 to -1.49	Moderate drought	9.2
-1.50 to -1.99	Severe drought	4.4
-2.00 or less	Extreme drought	2.3

Hereafter, a drought assessment will be presented, by calculating two indices, namely, the Standard Precipitation Index and the Normalized Soil Moisture, based on monthly precipitation and soil moisture, respectively. Multi-model soil moisture was simulate by six waterMIP models (see Table 4.2) and used to estimate NSM index. These indices were analysed and compared with SPI index estimated from monthly WFD precipitation data (GPCC version). Model intercomparison will help to reveal strengths and weakness of the individual models. In this study only SPI-12 month was analysed and compared with NSM.

Droughts in Europe are not rare. During the last thirty years the Europe had several drought events, with severe impacts to agriculture and society. Large areas of Europe have been affected by drought during the XX century. Within the WFD period, the most severe European drought in the recent past occurred in 1976 over Northern Europe (Scandinavia to France). In northern Europe 1976 was the year of most spatially extensive drought at annual timescale and 1996 was the equivalent year at 3-month timescale (Sheffield and Wood, 2007).

To investigate the differences between drought indices, comparisons were carried out between SPI and NSM indices. The area selected was 11 ºW to 40 ºE, 34 ºN to 73 ºN. The temporal correlation was estimated for SPI time scales ranging from 3 to 24 months with NSM (figure not shown), and compared for individual months and models (Figure 4.14 and Figure 4.15, respectively). Only the SPI with maximum correlation was retained, the time scale of 12 months, this result agrees with Dutra et al. (2008). The two indices are highly correlated in the southern Europe, however there are no statistically significant during April to July in central Europe (figure not shown). Figure 4.14 shows the correlation between NSM and SPI-12 in January and July.

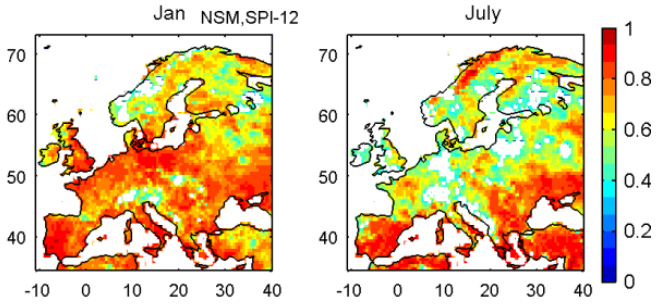

Figure 4.14: Maps of temporal correlation for January and July between NSM (multi-model mean) and SPI-12 over Europe.

The total correlation allows evaluate differences between models, Figure 4.15. VIC model has the highest temporal correlation, in contrast with WaterGAP with the lowest correlation, especially in southern part of Europe. All the correlations shown are significantly different from zero at the 95% confidence level.

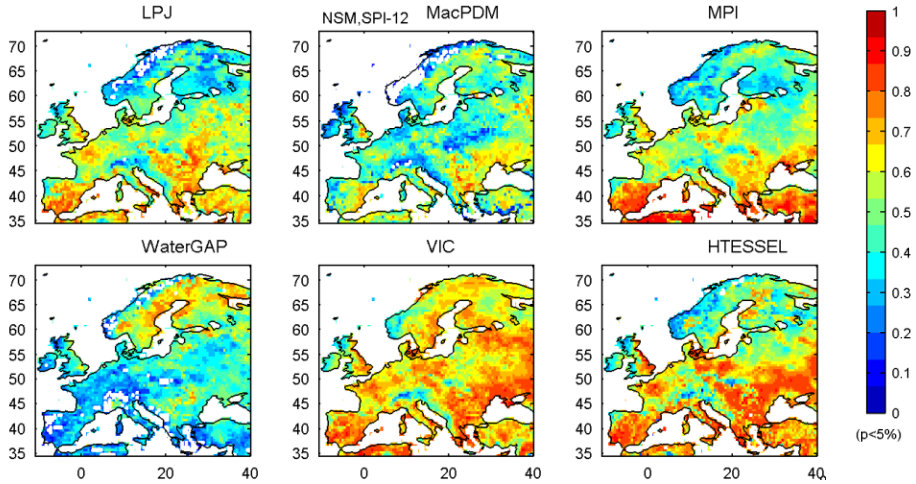

Figure 4.15: Maps of temporal correlation between NSM and SPI-12 over Europe: LPJ, MacPDM, MPI, WaterGAP, VIC and HTESSEL models.

As shown in Figure 4.14, the temporal correlation varies monthly: higher correlations in March and October and lower values in May (Figure 4.16). In Figure 4.16 the annual cycle of spatial correlation between NSM and SPI-12 is quantified, from spatial average of soil moisture and precipitation, respectively. In general, better correlations are achieved in July to May, with correlations reaching 0.5 in most cases. Between April to June there are some notable differences among the models, with the lowest correlation except to HTESSEL and VIC model, which occurs in December. VIC model presents the highest correlation, which varies between 0.7 and 0.2, in contrast with MacPDM model whose correlation ranges from 0.4 to -0.2. Only VIC correlation is statistically significant from January to November.

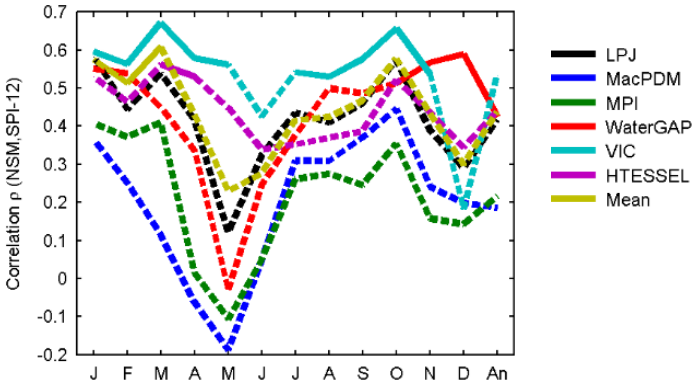

Figure 4.16: Annual correlation between NSM and SPI-12 over Europe. (p-value 5 %)

The temporal evolution patterns of wet and dry events are shown in Figure 4.17 (SPI and multi-model NSM indices) and Figure 4.18 (waterMIP NSM index). Several drought episodes were detected: in the mid-1970s, late 1980s to mid-1990s. 1970s droughts were the most extreme situation over Europe (about 40 % of European area was in drought, see Figure 4.19). 1976's drought was one of most extensive European drought. Short events were found in mid-1980s. The late 1980s and mid-1990s episodes were prolonged in time with few extreme situations detected essentially by NSM indicator.

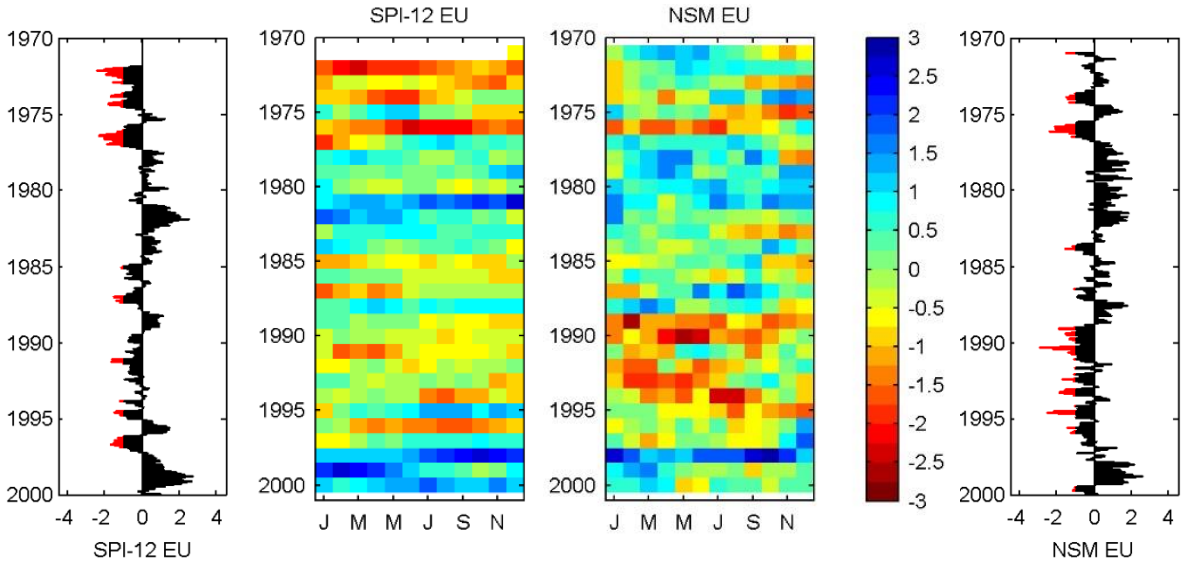

Figure 4.17: Time series of drought indices for Europe from 1971 to 2000: NSM and SPI-12. Normalized soil moisture, estimated from model ensemble soil moisture and standard precipitation index for 12-months time scale. Red zones are dry months (drought events) and blue are wet months (flood events). Enhanced zones indicates values below -1.

The temporal distribution of drought can be characterized by global average drought indicators. Figure 4.17 shows the temporal distribution of monthly NSM and SPI-12 drought indices over Europe from 1971 to 2000. The pattern of events between NSM and SPI-12 indices is similar, except early 1970s and the intensity of drought in early 1990s. Early 1970s is characterized by SPI-12 as a severe drought, while NSM do not consider the land in stress. The opposite situation happens in the beginning of 1990s.

Figure 4.18 shows time series of NSM calculated for each waterMIP model. The indices are in agreement for the 30-year period: dry events in mid-1970 and late 1980s to mid-1990s; and wet events in late 1970s to mid-1980s and late 1990s. MacPDM model presents a spin-up problem, with a very dry period in the beginning of the time-series. The temporal distribution of NSM index varies with the large-scale model analysed. The most intense drought events (red grid boxes) occurs more frequently in the models MacPDM, MPI, WaterGAP, (9 events) while moderate to severe droughts are more commons in HTESSEL model (62 events) (yellow grid boxes), Figure 4.18.

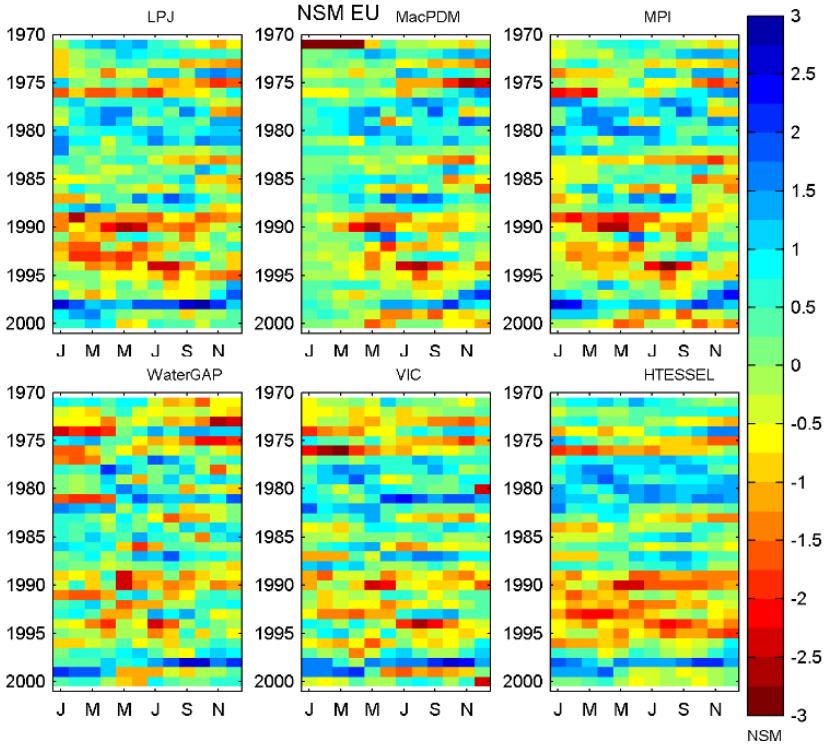

Figure 4.18: NSM and SPI-12 over Europe, estimated from monthly soil moisture and precipitation, respectively.

The identification in terms of spatial coverage for various regions is based on different thresholds of duration and intensity. The percentage of grid points affected by dry events quantifies the extension of land under drought conditions. Figure 4.19 shows the time series of percentage area in the Europe which is experiencing moderate to extreme drought (index lesser than -1). The number of periods of drought can be identified in the peaks in the percentage area undergoing such drought: 1973, 1976, 1984, 1988-92, 1995 and 1999. The most extensive drought occurred in 1976, with more than 15 % of Europe in extreme drought during the summer (6 % for NSM index). In September 1976, the percentage of land under drought conditions detected by NSM is lower than SPI index: 21 % (14 % for NSM index) of land surface was affected by an extreme drought.

The mid-1980s and early 1990s show a dry spell (low index value) spanning a number of years which reflect the long period of drought that occurred in the anomalous circulation pattern that caused rainfall deficits over a large area interspersed with short wet periods.

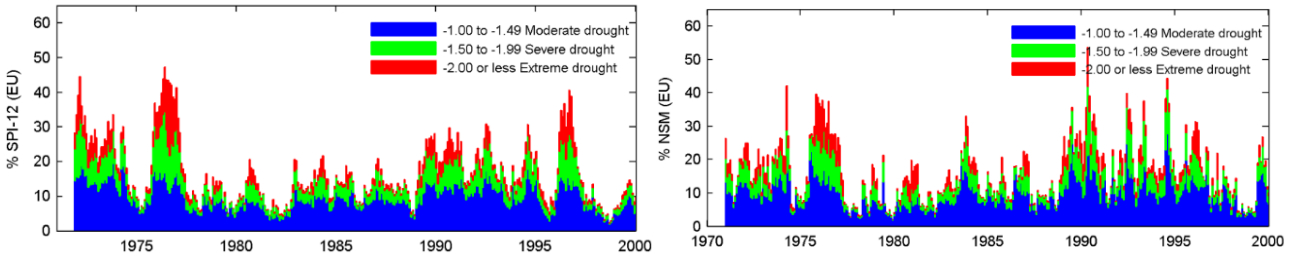

Figure 4.19: Time series of areal extension (%) of moderate drought (blue), severe drought (green) and extreme drought (red) over Europe for [1971-2000]: SPI (left) and multi-model NSM (right).

Figure 4.20 presents the spatial distribution of drought (indices lesser than -1) by decade over European area. The pattern of the drought events is similar, with more events in central Europe (France) and Scandinavia, reaching 6 months per year. The NSM multi-model index, estimated from multi-model soil moisture (average from waterMIP models), have a lower frequency of dry months per year. The number of droughts increases in the south Europe and Mediterranean area.

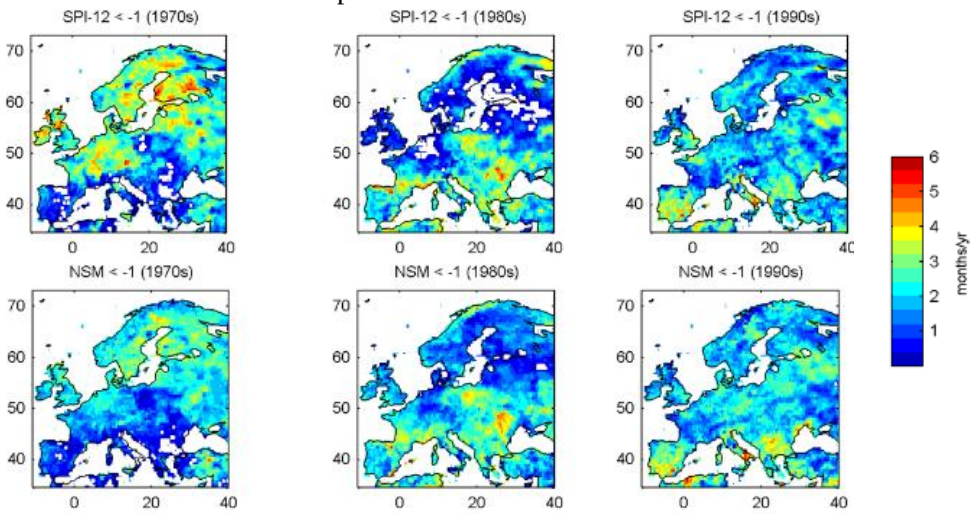

Figure 4.20: Mean of drought events over Europe events (index drought < -1) by decade: SPI-12 (top) and NSM multi-model index (bottom). Units in months in drought per year.

The number of extreme drought events (drought index lesser than -2) is shown by Figure 4.21 for SPI-12 and NSM multi-model indices. The major droughts occurred in northern part of Europe with more than 20 days per year in extreme drought. Iberian Peninsula does not exceed 10 days per year. The number of extreme drought is similar for both indices, but the number of extreme droughts occur with a greater frequency over central and Eastern Europe, and with a lower frequency along much of the north western seaboard, the Mediterranean seaboard, and the Alps.

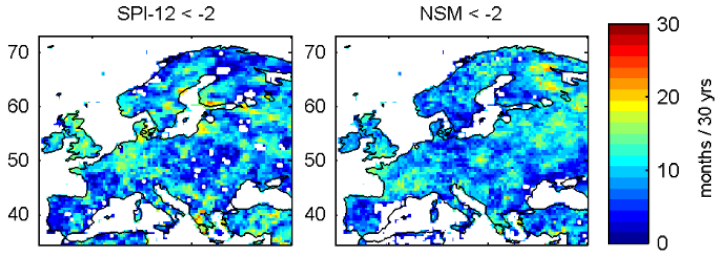

Figure 4.21: Distribution of the number of months in extreme drought over Europe (1971 – 2000). A drought event occurs when the drought indicator (SPI-12 or NSM) is lesser than -2 (extreme drought). NSM is the multi-model index.

The number and spatial distribution of drought events varies with the model. There are differences between six different large-scale models, presented in Figure 4.22. Each panel shows the number of months in extreme drought (NSM < -2) from 1971 to 2000. MacPDM presents the higher number of extreme drought events while LSMs, VIC and HTESSEL, have the least number of extreme droughts. The distribution of extreme droughts events depends on the model. MacPDM, MPI and WaterGAP simulate more extreme dry events (about 6 %) than other models (Figure 4.22). These more extreme droughts are located in central to northern part of Europe.

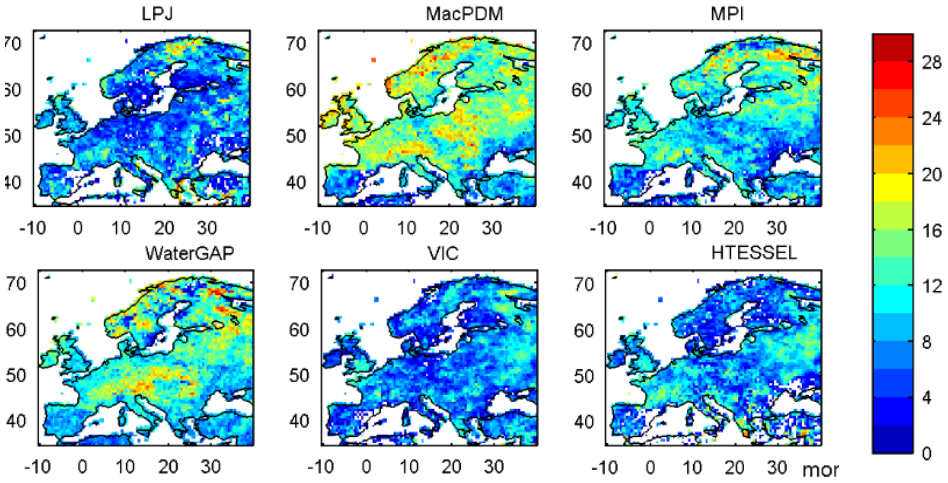

Figure 4.22: Number of months in extreme drought, normalised soil moisture lesser than -2, from 1971 to 2000, estimated by various GHM and LSM. Units in months per 30 years.

SPI-12 gives an estimative of the severity or precipitation deficits for an accumulation period of 12 months, while the analysis of the anomalies of the soil moisture provides clear evidence of the areas suffering due to the precipitation shortage. Lag cross-correlation has been done between SPI-12 and NSM with 1 to 12 month-lag. Cross correlation provides information that assists in determining the time-lag relationship between both indices, determining the best time-lag period of SPI (precipitation) that influences the NSM index. Selected models show strong relationships, except MacPDM and WaterGAP. There is a distinct precession in the level of the correlation (higher correlation coefficients) for different models. Only VIC and HTESSEL show relatively significant correlation until lag-2, mainly in Southern Europe. This signal remains at 12 months behind of time in the Mediterranean area for HTESSEL model. The cross-correlation coefficients are significant at the -8 to 1 lags, mainly in central and south Europe (except WaterGAP model). The lags at which the cross-correlation coefficient values are significant lie anywhere from 6 months, except LPJ, VIC and HTESSEL model.

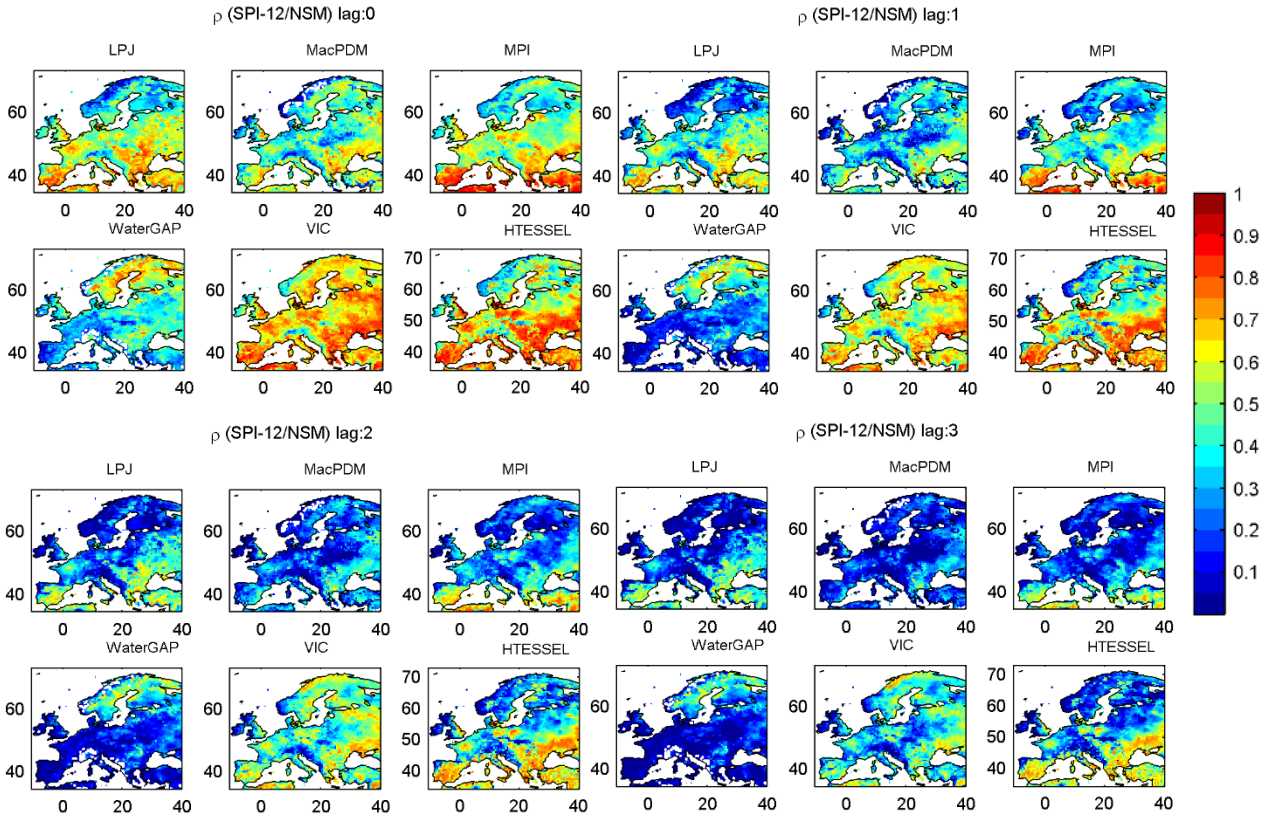

Figure 4.23: Lag cross-correlation between SPI-12 and NSM.

One of the more intense droughts over Europe occurs in 1976 (more than 50 % of European area in Figure 4.19). The extension of the drought event is shown in Figure 4.24 and Figure 4.25. Both indices, NSM and SPI-12, catch the extension of the drought.

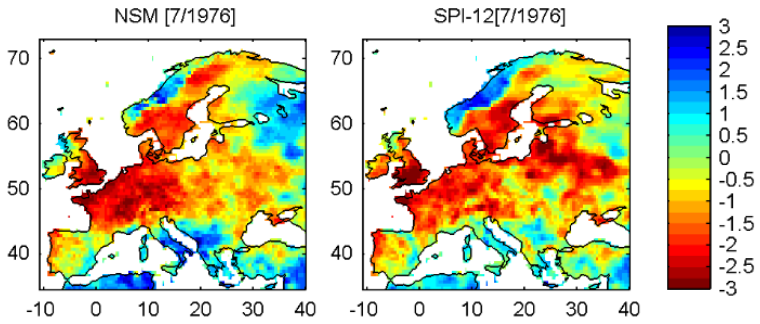

Figure 4.24: Drought indices over Europe in July 1976: NSM multimodel index (left) and SPI index (right).

Although all models are able to identify the 1976's drought, WaterGAP model sensed a drought less severe than expected by precipitation index. NSM estimated by WaterGAP soil moisture is not lesser than -1, against the other models.

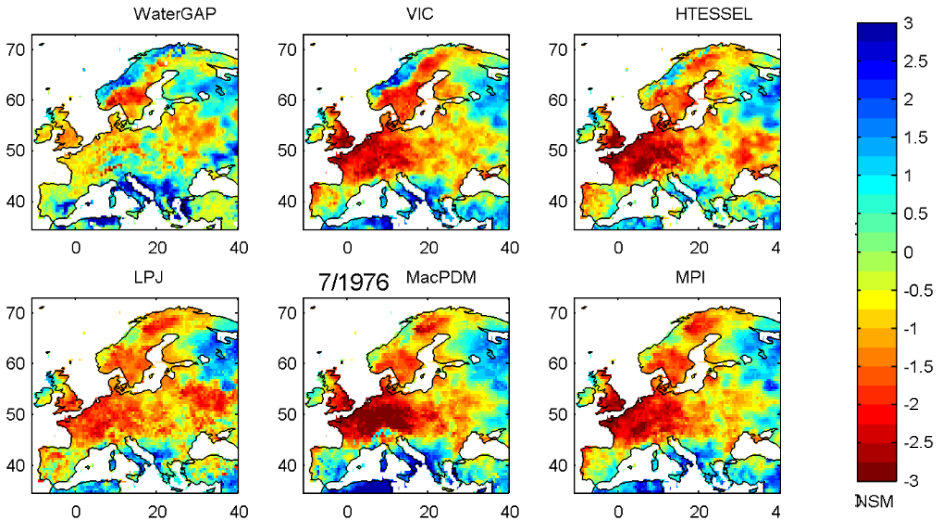

Figure 4.25: Drought extension over Europe in July 1976. NSM varies between -3 (drought event, at red) and 3 (flood events at blue)

4.1.3 Multimodels results

In this section an ensemble of 2 land surface models and 4 hydrological models from WaterMIP intercomparison project were used to calculate the global water cycle over land for a thirty-yr period [1971-2000]. Continental surface hydrological budget was estimated successfully and compared to multimodel ensemble from WaterMIP project. Results are equivalent to Haddeland et al. (2011), where the multimodel global terrestrial water balance was estimated from six land surface models and five global hydrological models from WaterMIP project for a 15-yr period [1985-1999 with a mean forcing of 872 mm/yr of global precipitation; evapotranspiration ranges from 415 to 586 mm/yr; and runoff ranges from 290 to 457 mm/yr. For a 30-yr period [1971-2000], global mean precipitation ranges from 837 to 917 mm/yr. Simulated global terrestrial evapotranspiration, excluding Greenland and Antarctica, ranges from 497 to 523 mm/yr, and simulated runoff ranges from 331 to 395 mm/yr, about 42 % (~ 53 000 km^3/yr) of precipitation runs off from surface. The interannual variation in multimodel mean predicted global runoff is much larger. Over land simulated global evapotranspiration is nearly 73 000 km^3/yr and total runoff about 53 000 km^3/yr. Estimated mean annual precipitation was 880 mm/yr, that ranges from 857 and 903 mm/yr. Interannual variability of evapotranspiration and runoff ranges from 485 to 535 and 350 to 386, respectively.

The relationship between the components of the hydrological cycle and climate indices, related to ENSO, was also investigated. A negative correlation between continental precipitation anomalies (evapotranspiration and total runoff) and ESPI index was found.

Regional hydrological drought was qualitatively examined (characteristics and spatio-temporal evolution) on a European scale. The NSM drought index, based on offline modelled soil moisture of WaterMIP models, was used as a drought index and compared with SPI-12. Both indices displayed some spatial characteristics of droughts over Europe. The essential characteristics of drought (intensity, duration, and spatial coverage) were also correctly detected by multimodel NSM index and confirmed by SPI-12. Extreme drought events, classified by SPI-12 and NSM-multimodel, occur with greater frequency over continental Eastern Europe. Despite being the model that produces less droughts in the early 1990s, WaterGAP results show fewer droughts in the early 1990s. However this is the model that detects more extreme droughts. SPI-12 are correlated with NSM, with the weaker correlation in spring, due to snow melting. MacPDM and MPI have the weaker correlation, except MPI in southern Europe (about 0.8).

Results show little inter-model variability. However, the ensemble gives a satisfactory hydrological characterization of the surface. In the next section the impact of forcing is presented to assess the surface energy balance.

4.2 Sensitivity study

Land surface models, as described in the previous section, simulate the temporal evolution of the water balance, as well as the energy balance near the land surface.

This section evaluates the performance of the land surface model HTESSEL (see section 2.3, Chapter 2). The objective of the analysis is: i) to assess model sensitivity to meteorological forcing and physical processes; and ii) to evaluate the global energy balance over land. To assess the impact of the meteorological forcing data, a set of integrations with perturbed forcing was produced. These integrations allow for focusing on the effect of the forcing and physical processes modifications. Perturbed parameter ensembles are created to assess uncertainty based on HTESSEL model and benefit from the explicit control of parameter perturbations. This allows statistical methods to determine which parameters are the main drivers of uncertainty across the ensemble. Daily and seasonal averages are then compared to a number of FLUXNET sites (see Chapter 2, section 2.4.1), with a focus on energy balance at surface: net radiation, flux of sensible and latent heat.

HTESSEL is here used to study the variability of global energy cycle over land to meteorological forcing and physical processes. A sensitivity analysis was performed in order to quantify the uncertainty in the simulation of the energy cycle. The main objective is to characterize sources of uncertainty, such as: correction of systematic errors in precipitation; aerosols effect on solar radiation; wind speed variation; increase or decrease in air temperature; physical process of model (soil hydrology and carbon), etc. To assess the performance of HTESSEL in simulating energy over land, the disturbed simulations (see Table 4.7) are compared to WFD simulation, the control, as well as data from FLUXNET project. In this study we analyse results from 15-year (1985-1999) offline simulations using the land surface model HTESSEL at a global and compare these results at a local scale. Data is available at a daily resolution.

The range of simulations helps to characterize the uncertainty due to (i) land surface model parametrization and (ii) meteorological forcing changes. Accurate specification of the changes is essential for to understand hydrological and energy cycle modelling. Surface energy fluxes are checked at local scale using daily or monthly measurements.

4.2.1 Methodology and data

Land surface model HTESSEL experiences, forced with disturbed meteorological data, are presented in Table 4.7. The description of the physical model, such as differences in the representation of soil hydrology and the representation of the hydrology, were also analysed using three different versions of the model: HTESSEL, TESSEL and, more recently, CTESSEL. The control experience, referred as WFD, was driven with GPCC precipitation version and SWdown aerosol corrected. The uncertainty was evaluated by inserting small disturbances to atmospheric forcing: precipitation source (GPCC vs. CRU version) were changed; the intensity of the wind was modified, adding and decreasing 10% to wind speed; fix aerosols of solar radiation was removed in accordance with the instructions indicated by Weedon et al. (2010, 2011); air temperature was increased and decreased by 2° C. This modification of the air temperature also affects air humidity and, for this reason, it was important to carry out the transformation of specific humidity.

To simplify the interpretation of the results, simulations were assigned to different process categories, depending on the variable or model: precipitation, solar radiation, air temperature, wind speed and physical process. In order to evaluate the uncertainty associated to the model's hydrology was also tested with the old soil hydrology (TESSEL), and with the new carbon implementation, CTESSEL (see detailed description in Chapter 2, section 2.3). Each simulation used in this analysis is listed in Table 4.7. All simulations were carried out from 1980 to 1999. To minimize the influence of initial conditions, the first 5 years of the simulations were excluded.

Table 4.7: Simulation design of sensitivity tests. WFD simulation forced by WFD 3-hourly data (SWdown corrected and GPCC precipitation version), is the reference simulation in this study.

Source of uncertainty			**Meteorological forcing/ Method**
Rainf & Snowf	Precipitation	WFD[1]	Precipitation bias corrected (GPCC)
		CRU	Precipitation bias corrected (CRU)
SWdown	Shortwave downward radiation	WFD[1]	SWdown corrected with aerosols
		SW	SWdown without aerosols correction
Tair	Air temperature	TM2	More 2 °C air temperature
		TL2	Less 2°C air temperature
Wind	Wind speed	WM10	More 10 % wind speed
		WL10	Less 10 % wind speed
Physical processes	Surface hydrology	TESSEL	Without the new soil hydrology scheme
	Carbon cycle	CTESSEL	(see Chapter 2, section 2.3.4)

[1]WFD is the reference simulation: HTESSEL driven by WFD forcing dataset (GPCC precipitation and SWdown aerosols corrected).

4.2.2 Analysis of the global energy balance

The global energy balance over land can be expressed analysing global maps of solar downward radiation (SWnet), longwave radiation (LWnet), or net radiation (Rn), and sensible and latent heat (H and LE, respectively). Due to the large amount of data in sensitivity analysis (global daily data during 15 years), the global analysis consist in global maps, seasonal cycles and time-series of global means. Finally, the simulated values are compared with existing observations at daily scale.

4.2.2.1 Seasonal cycle of energy variables at the global scale

Incoming shortwave radiation incident at the Earth's surface is the primary energy source for the land surface and drives evapotranspiration and snowmelt. The seasonal cycle of global energy over land, weighted by the cosine of latitude, are presented in Figure 4.26 and Figure 4.27. These graphs represent the global annual variation over land, from poles to equator. SWnet radiation annual cycle does not present significant differences between simulations except the no aerosols corrected, SW test. The differences are more significant between June and September; it ranges about 10 Wm^{-2} from TM2 to TL2 simulations, green and red line, respectively. The annual amplitude of SWnet ranges between 70 and 72 Wm^{-2}. SW test has the highest variation. LWnet annual amplitude do not present an important variation except for temperature tests, with a higher amplitude for TM2 test and a small amplitude for TL2 test, 14 and 11 Wm^{-2}, respectively.

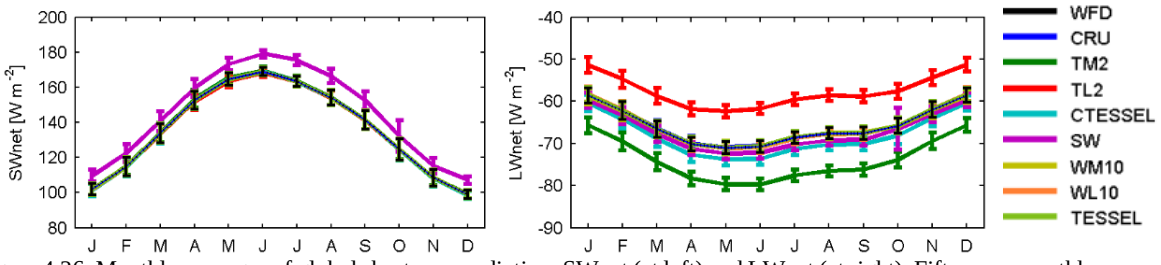

Figure 4.26: Monthly averages of global shortwave radiation: SWnet (at left) and LWnet (at right). Fifty-year monthly averages of energy [1985-1999]. Vertical bars are the stand deviation of daily mean values.

Latent and sensible heat fluxes reflect evapotranspiration and air temperature influence. The air temperature, affected by solar radiation changes and 2 degrees perturbations, explain the differences observed in sensible heat, H, annual cycle (Figure 4.27 pink, red and dark green lines, respectively). Otherwise, Rn annual cycle (Figure 4.27), reflects SWnet and LWnet impacts. Globally, not correcting the aerosols have comparable effects to the 2ºC decrease of air temperature on annual of net radiation. TL2 and SW have a similar impact, except in H, where differences occur in JAS.

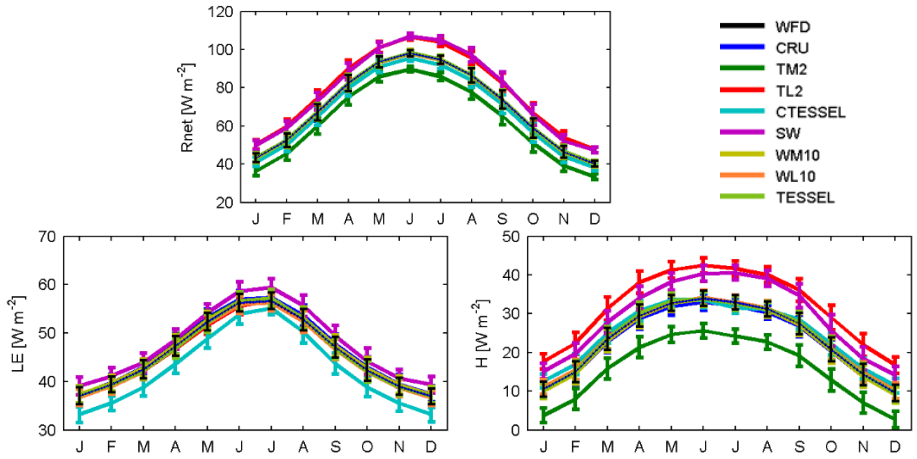

Figure 4.27: Modelled mean monthly averages of global net radiation (top), sensible (left), and latent heat (at right). Fifty-year monthly averages of energy (1985-1999). Vertical bars are the stand deviation of daily mean values.

Surface components of annual means of energy balance components of each sensitivity analysis (Table 4.8) are compared with values presented by Trenberth et al. (2009): ERA-40 (Feb 1985 to Apr 1989) and their best-estimated surface energy balance (Mar 2000 to May 2004). Slight differences exist in the land and ocean masks, and in period of study, so that the global value may consist of slightly different weights for each component. In Table 4.8, values are given to the first decimal place because this is necessary to resolve the NET, even though the values are not accurate to that level.

For the surface LW radiation, one of the principle uncertainties in the surface energy budget, the results are highly dependent on the cloud-base height and radiative proprieties. The LWnet flux for WFD, the reference simulation is 66 Wm^{-2}. LWnet radiation is high for TM2, circa 74 Wm^{-2}, and low for TL2, 58 Wm^{-2}, due to changes of 2 ºC in air temperature, while changes in aerosols (SW) and in carbon parameterization (CTESSEL) increase about 2 Wm^{-2} (67 Wm^{-2}) and 3 (68 Wm^{-2}), respectively. Net solar radiation at the surface, SWnet, is only affected by aerosols, by 9 Wm^{-2}. Latent heat flux is also affected by aerosols and carbon parameterization, ranging from -3 to 2 Wm^{-2} (43 and 48 Wm^{-2}). Sensible heat flux is sensitive to air temperature changes, ranging from 16 to 32 Wm^{-2} when air temperature is smaller or higher than WFD simulation, TM2 and TL2, respectively.

ERA-40 surface balance energy components presented by Trenberth et al. (2009), from Feb 1985 to Apr 1989 (Table 4.8) are reasonably close, except for the latent heat flux. ERA-40 precipitation values are known to be high and there is a global excess of model precipitation over evaporation (Uppala et al., 2005), affecting surface latent heat flux. For a different period, Trenberth et al. (2009) values are quite different. For the net radiation, Rnet, the result was 65.5 Wm^{-2} and WFD was 69.9. Latent heat fluxes result were 38.5 and 45.8 (Trenberth and WFD, respectively). For the sensible heat flux, Trenberth estimated 27.0 and WFD 23.5 Wm^{-2}. Last column on Table 4.8, net downward energy flux, show a slightly warming of the surface, suggesting that, in the ERA-40, the net downward flux into the ground is too large.

Table 4.8: Surface components of the annual mean energy budget for the global land for the period 1985 to 1999. ERA-40 data for Feb 1985 to Apr 1989 and Trenberth et al. (2009) estimates for Mar 2000 to May 2004 are presented in the first and second lines of the table, respectively. (Wm^{-2}) Net Down is the difference between Rnet and sensible and latent heat.

	Rnet	SWnet	LWnet	LE	H	Net Down
ERA-40	69.0	134.3	65.3	40.9	25.8	2.3
Trenberth et al. (2009)	65.5	145.1	79.6	38.5	27.0	0.0
WFD	69.9	135.7	65.8	45.8	23.5	0.6
CRU	69.7	135.4	65.7	46.4	22.8	0.5
TM2	62.1	136.0	73.9	45.8	15.7	0.6
TL2	77.8	135.4	57.6	45.6	31.6	0.6
CTESSEL	67.3	135.5	68.2	42.6	24.4	0.3
SW	77.4	144.5	67.1	47.9	29.0	0.5
WM10	69.9	135.7	65.8	46.1	23.1	0.7
WL10	69.9	135.7	65.8	45.5	23.8	0.6
TESSEL	70.0	135.7	65.7	45.8	23.6	0.6

The annual amplitude of Rnet varies between 56 Wm^{-2} and 60 Wm^{-2}, for TM2 and SW simulation, respectively (Table 4.9). Differences of annual averages of global energy components are small.

Table 4.9: Annual range of monthly averages of global energy components: net radiation (Rnet); solar downward radiation (SWnet); longwave radiation (LWnet); surface latent heat flux (LE); and surface sensible heat flux (H). Units are in Wm^{-2}.

	Rnet (Wm^{-2})	SWnet (Wm^{-2})	LWnet (Wm^{-2})	LE (Wm^{-2})	H (Wm^{-2})
WFD	58	70	13	20	24
CRU	58	70	12	20	24
TM2	56	70	14	20	23
TL2	59	70	11	20	26
CTESSEL	57	71	13	22	22
SW	60	72	13	20	26
WM10	58	70	12	20	25
WL10	57	70	13	20	24
TESSEL	58	70	13	20	25

A key role of land surface models is to simulate a realistic surface energy partition between latent and sensible heat flux. Less LE pumps less water vapour into the atmosphere contributing to decreasing cloudiness and precipitation; decrease in H tends to cool the planetary boundary layer and reduce convection (Pitman, 2003). Figure 4.28 shows the ratio of latent heat and sensible heat to surface net radiation averaged over land. The models differ significantly between October and February, when net radiation declines. During this period the energy partition varies between 10% for TM2 and 40%, TL2, for sensible heat flux energy and about 70% and reaches around 100% in TL2 and TM2, respectively, for latent heat flux. Temperature controls surface portioning through its effect on the slope of the saturation vapour pressure. Changes in wind or precipitation (CRU) have no impact in surface energy partition. Both results reflect the heating of the surface.

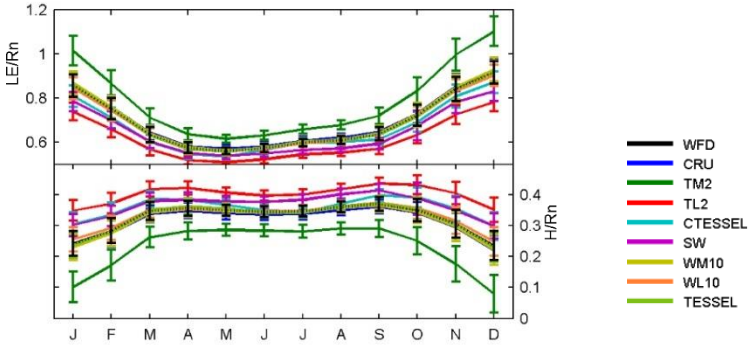

Figure 4.28: Global surface energy partition over land, calculated as the ration between a)surface latent heat flux (LE) and b) sensible heat flux (H) to surface net radiation (Rn=SWnet+LWnet).

4.2.2.2 Interannual variability and impact of forcing uncertainty

To understand the overall impact of the perturbed forcing, errors between each simulation and control experience were estimated for each energy components: mean absolute error (MAE), mean bias error (MBE) and root mean absolute error (RMSE). The estimates allow the comparison between each sensitivity test and control experience (WFD). Mean annual averages of each energy component and the coefficient of variation CV (standard deviation divided by the mean) of control experiment are presented in Figure 4.29 and Figure 4.30. As expected, the highest averages of each component are located in the equatorial zone, decreasing with the pole approach.

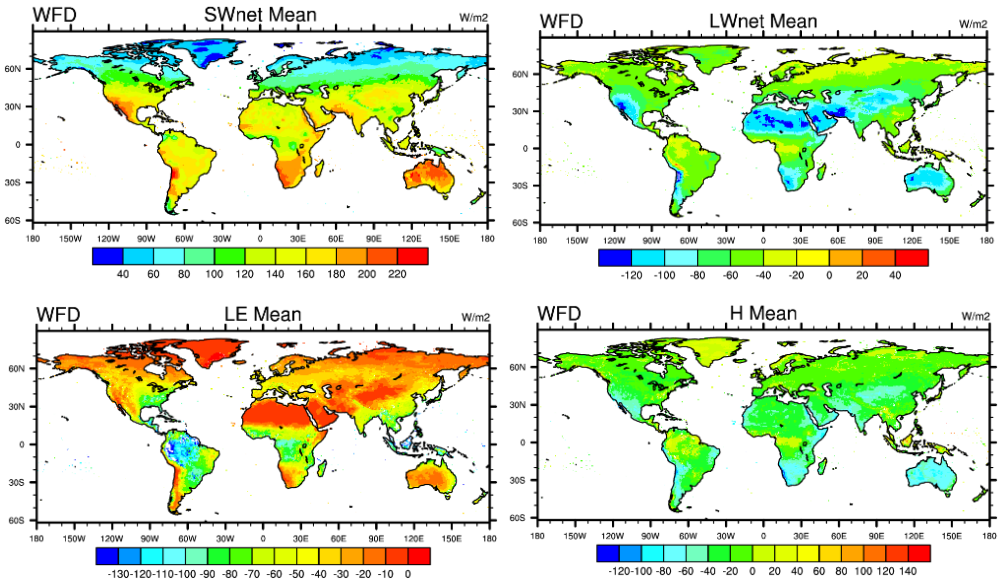

Figure 4.29: Annual average of SWnet, LWnet, LE and H. Positive latent and sensible heat flux correspond to gain of energy by atmosphere. Colorbars are differents.

Coefficient of variation, CV (the ratio of the standard deviation to the mean), quantifies the relative differences between simulations, displayed in Figure 4.30 for WFD. Distributions with CV < 1 are considered low-variance, while those with CV > 1 are considered high-variance. The CV is much higher for SWnet simulated in boreal zones where the spread of simulated SWnet is relatively large. The CV is high for H over Greenland and tropical zone. There are no significant changes between simulations (result not shown).

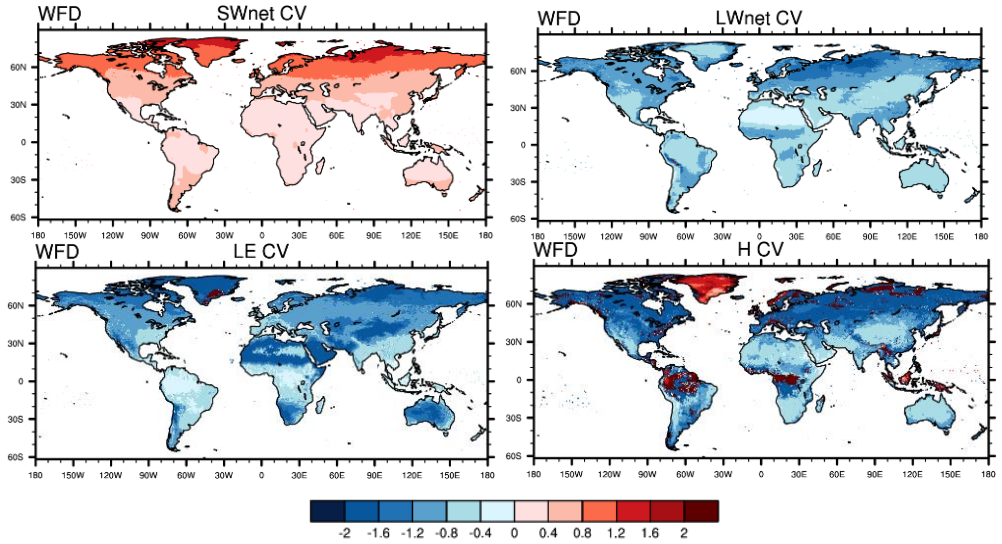

Figure 4.30: Coefficient of variation, CV, of the energy components estimated by HTESSEL forced by WFD dataset.

Figure 4.31 quantify the bias error due to slight changes in meteorological forcing and physics of the model; only CRU, CTESSEL, SW and TM2 are presented. The uncertainty associated with precipitation, CRU, is higher than the associated change in the physical model (TESSEL or CTESSEL). Errors related to the CRU simulation, a different source of precipitation, reach 20 Wm^{-2} for SWnet, over Greenland and Himalayas. Sensible heat flux, H, does not show a significant impact on the bias error (not shown). A warming of 2 ºC at the surface rises SWnet by about 8 $Wm^{-2}$and add 10 Wm^{-2} to the sensible heat flux, H. On the other hand, a decrease of 2 ºC causes a decrease of LWnet, by about 10 Wm^{-2}. In general, TM2 and TL2 have complementary results (result not shown). Perturbations in the forcing involving a decrease of 2 ºC or a decrease in 10 % of the wind speed at the surface appear to have similar order of magnitude effects for surface sensible and heat flux (not shown). Finally, perturbed wind as well as TESSEL simulations do not show any relevant error increment. There are no significant differences in RMSE (figure not shown).

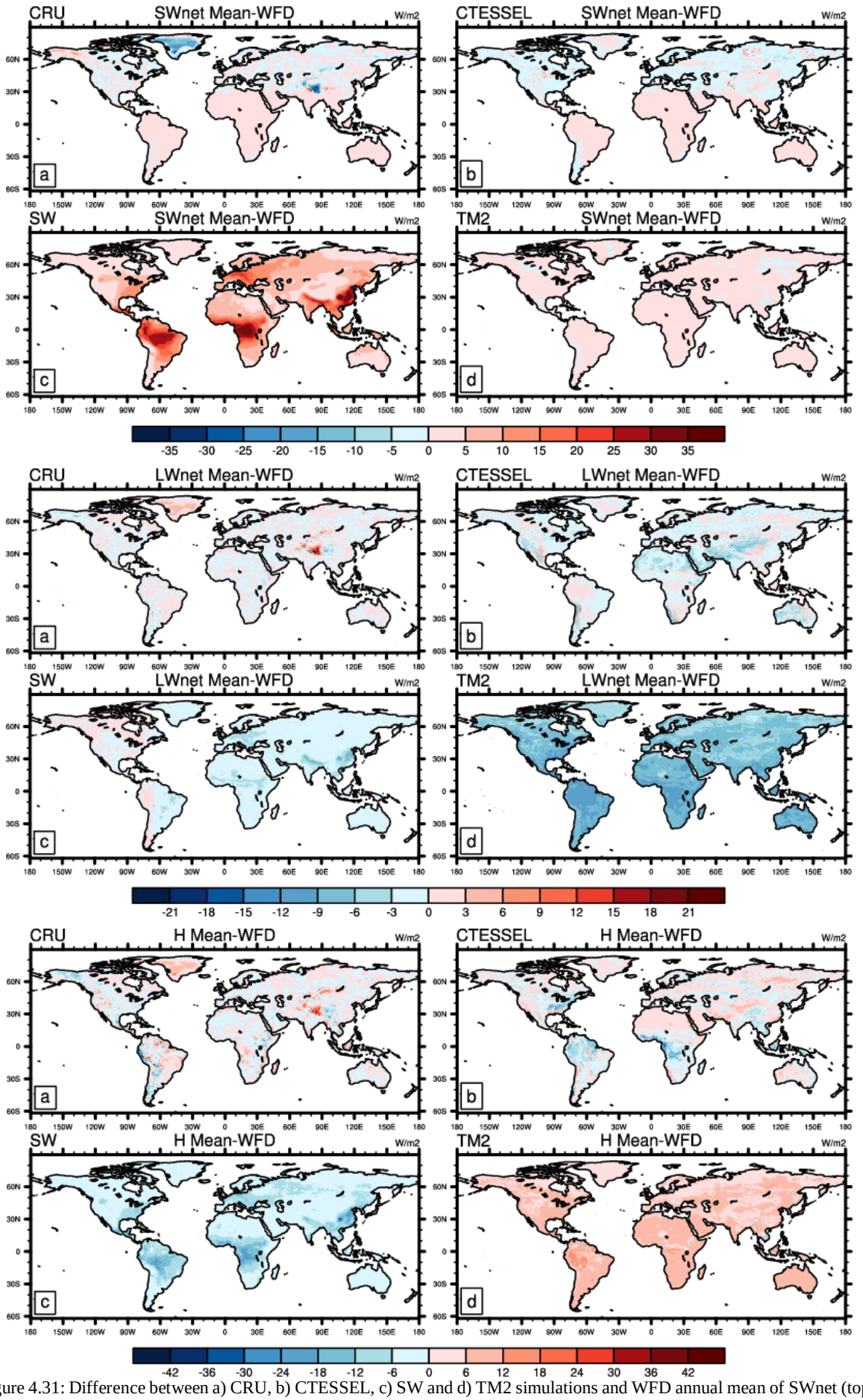

Figure 4.31: Difference between a) CRU, b) CTESSEL, c) SW and d) TM2 simulations and WFD annual mean of SWnet (top), LWnet (middle), and H (bottom). Different scales.

4.2.3 Comparison of observed and simulated data: a site analysis

Data compiled by FLUXNET available from 1994 to 1999 are used to quantify and compare magnitudes in several sites (see detailed description in Table 2.3, Chapter 2). Unfortunately, access to observations is not as easy as it should be, and our ability to make further progress will be hindered. Only overlap periods are shown. Some sites, such as LW, have a low temporal coverage being analysed with special attention. A height correction factor was applied to LWnet to remove systematic errors due to the difference between the altitude of the point in the model and the reference altitude (see section 2.4.1, Table 2.4).

4.2.3.1 Seasonal cycle analysis

To get a single annual cycle, the model output for different years was monthly averaged. These values were computed for selected sites and compared to observed data. Figure 4.32 shows the annual cycle of net radiation, sensible heat and latent heat for 4 FLUXnet sites: continental climate, NB; Mediterranean, SKy; humid temperate, WB; and warm temperate, HE.

Sensible heat and latent heat flux, LE, present a higher variability. In SKy sensible heat, H, is underestimated during autumn and winter. Mediterranean climate has larger productivity and evaporation rates in early spring with a resurgence in early autumn. Net radiation, Rn, annual cycle is well represented by the model, although with quite a large variability at WB and NB sites.

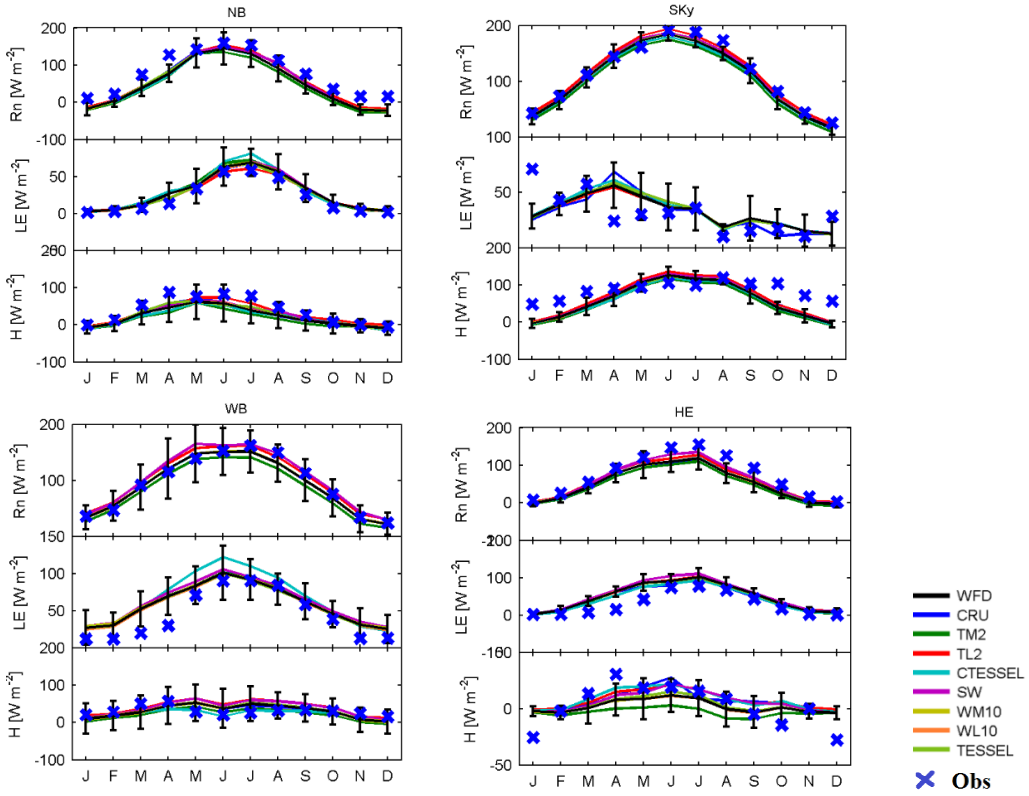

Figure 4.32: Annual cycle of net radiation, Rn, latent heat flux, LE and, sensible heat flux, H in FLUXnet for NB, SKy, WB and HE sites (blue crosses), and perturbed simulations (lines).

Sensitivity of model output to environmental forcing variables can be addressed by residual analysis, assessing potential trends in the residuals by slope and offset of linear regressions between residuals and respective environmental variable. The identity line (y=x line) was drawn as a reference. Another way to display the spreading of errors is to look at scatter plots. Figure 4.33 present the scatter plot for each site of net radiation, sensible heat and latent heat at surface. Simulated net radiation fits reasonably with observations. In general, results are acceptable for WB, but underestimate high values for NB, SKy and HE. NB is located in Canada, while SKy and WB are in USA, eastern and western part, respectively. HE is a French warm temperate. This result is corroborated by the scatter plot of observed versus simulated net radiation over the period of record, as shown in Figure 4.33. The dashed line is the 45º line of perfect agreement. The plot shows agreement over a wide range of Rn, and a tendency toward

under-estimation for the highest latent and sensible heat fluxes and an over-estimation for the smallest values. Latent heat flux, LE, is reasonable for NB, WB and HE, albeit with a tendency for model underestimation. SKy shows poor agreement with observations. Sensible heat flux, H, is reasonable at NB and SKy but shows poor discrimination in HE (only one year available of H) and clearly too much variability in WB.

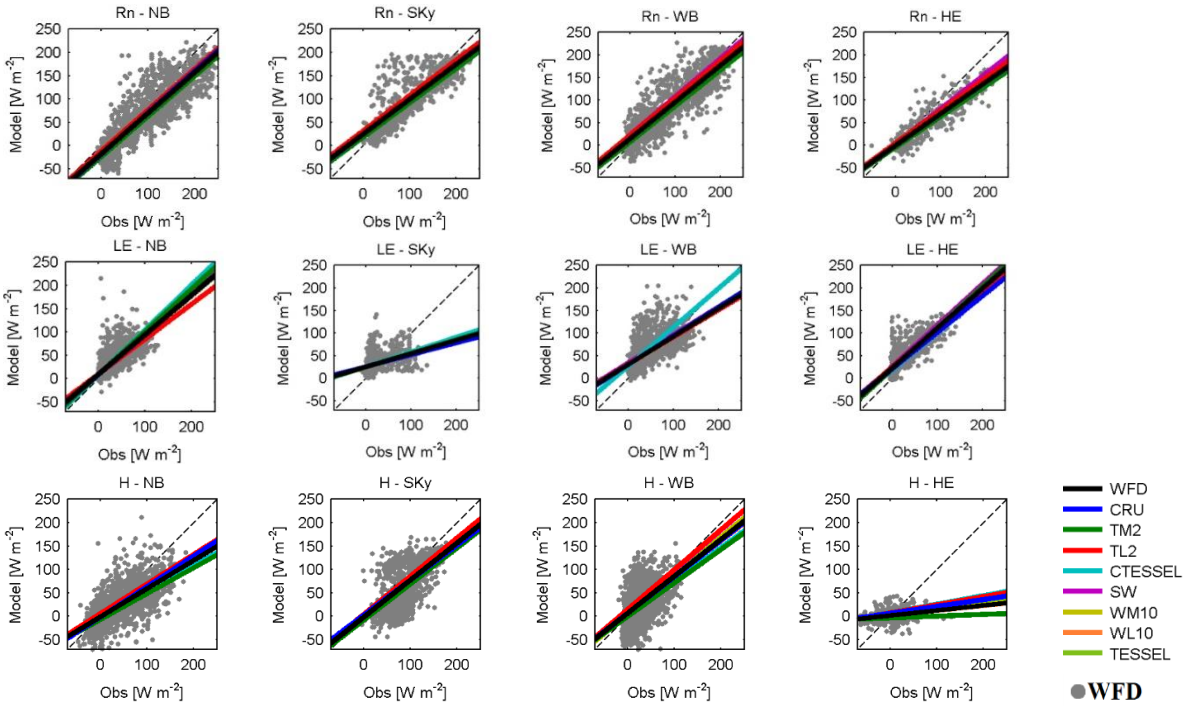

Figure 4.33: Measured values of latent (LE), sensible (H) heat flux and net radiation (Rn) compared to simulated ones. Colours represent the different sensitivity tests. Grey dots are WFD simulation vs. observations. Results from daily values.

Boxplots specify a set of simulations comparing with observation for each site. Net radiation, as shown previously in section 2.4.2, is well represented by the land surface model. On average, the land surface model underestimate the net radiation (HE and NB sites), but discrepancies lay within the range of the expected measurement error, Figure 4.34 and Figure 4.35. In general, modelling averages are slightly smaller than corresponding observations. Highest values were simulated by TL2 and SW, while smaller values were simulated by TM2. These results agree with error measurements show in Figure 4.35. The first simulation, TL2, reduced 2 ºC at surface air temperature while TM2 increase 2 ºC. SW test aerosols correction was removed contributing to a reduction in surface temperature, and consequently an increase in the total radiation at the surface.

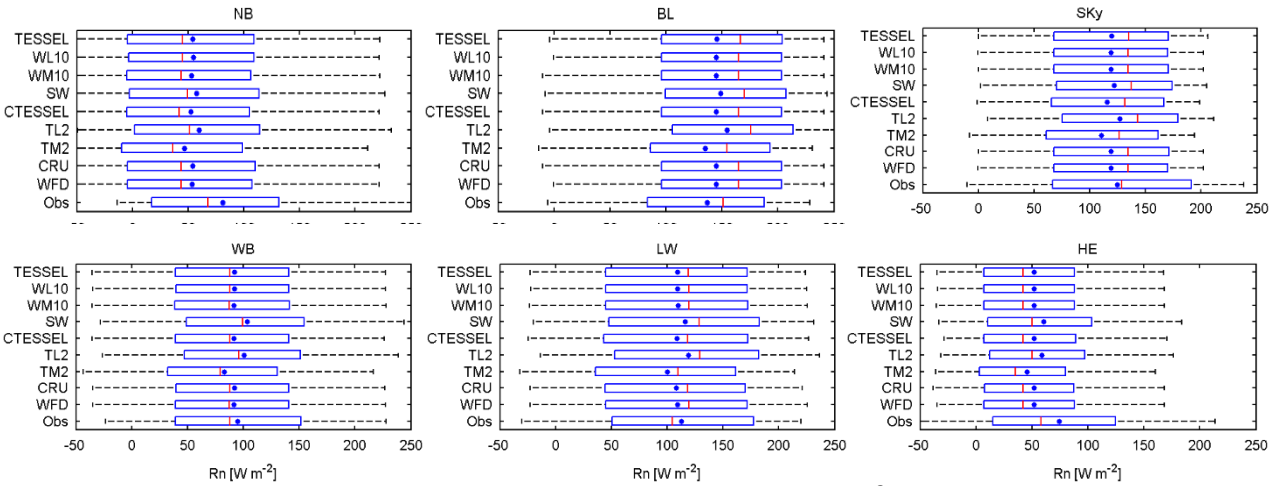

Figure 4.34: Boxplot of net radiation from monthly means for each site. Units are in Wm^{-2}. The central box represent the central 50 % of data. Its lower and upper boundary lines are at 25 %/75% quantile of the data. The central red line and blue point indicates the median and mean of data, respectively. Two vertical extending from central box indicating the remaining data outside the central box that are not regarded as outliers. These lines extend maximally to 3/2 time the height of the central box but not past the range of data. Outliers there are points indicating the remaining data.

4.2.3.2 Error measures

One way to quantify the quality of surface modelling is to use error measures: root mean square error, RMSE; mean bias error, MBE; and mean absolute error, MAE (Figure 4.35). Figure 4.35 summarizes the performance of the individual tests. The highest errors of Rn, RMSE, MBE (negative values) and MAE, were found for TM2 test for all stations, showing the effect of increasing temperature. On the other hand, simulation TL2 present the lowest errors in three sites: NB, SKo and SKy. The latent heat flux does not show a large discrepancy between simulations, except for LW, WB and HE sites. The RMSE varies between 20 and 60 Wm^{-2} for the NB and BL, respectively. BL's bias is higher, about 60 Wm^{-2}, and a correlation lesser than 50 %, see Figure 4.36. Furthermore, errors in the sensible heat flux vary considerably from simulation to simulation. BL site presents the highest errors and is the only site where H is overestimated, about 50 Wm^{-2}. BL data was only measured for three warm seasons, possibly affecting robustness of LE and H results.

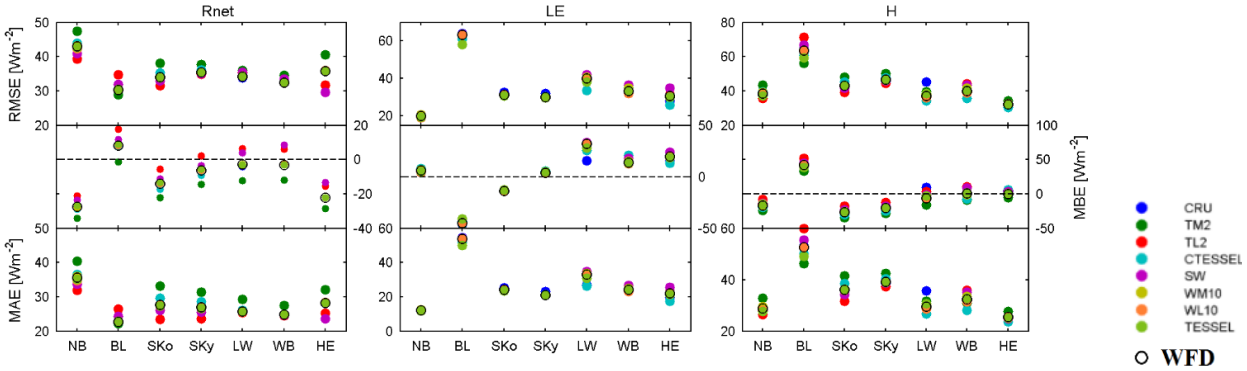

Figure 4.35: Errors of net radiation (Rn), latent heat flux (LE) and sensible heat flux (H) at seven fluxnet sites: a) root mean squared error (RMSE), b) mean bias error (MBE), and c) mean absolute error (MAE). The open circle represents WFD simulation. Units are in Wm^{-2}.

Another way to measure the performance of the model is the coefficient of correlation, ρ. The coefficient of correlation measures the strength and the direction of a linear relationship between observation and simulations. This coefficient measures the linear dependence between two variables, modelled data and observations, in this analysis. It was estimated from daily data for 7 fluxnet sites. The coefficient of correlation (ρ) of three energy components (sensible heat, latent heat and net radiation) are present in Figure 4.36. Rn has the best correlations coefficients, higher than 84 % (96 % from monthly data) for all sites and model simulations. The sensible heat correlation varies considerably in LW, WB and HE sites. In these sites CTESSEL presents the highest correlation. For the latent heat flux, the correlation is lower for BL, SKo, and SKy (about 50%), where there is a considerable difference between the altitude of the stations and forcing.

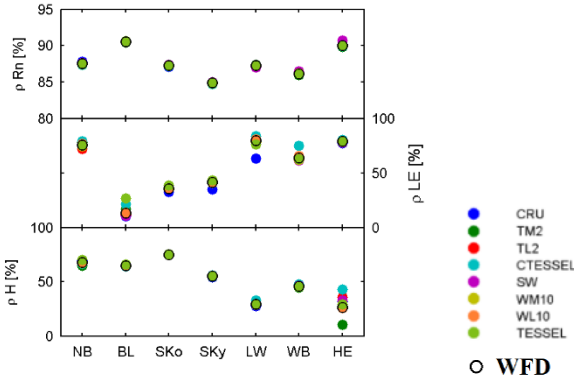

Figure 4.36: Coefficient of correlation (ρ) calculated between sensitivity tests and local observations for sensible heat flux (H), latent heat flux (LE) and net radiation (Rn). The open circle represents WFD simulation.

4.2.4 Concluding remarks – energy cycle

The number of involved parameters in LSM is often large. Sensitivity analysis is a key step to understand the complex relationship between meteorological forcing and energy cycle. In this section, a sensitivity analysis, the ability of HTESSEL respond to slight fluctuations in meteorological forcing and changes in the physical model and its impact on the surface energy cycle were performed. The uncertainty associated to atmospheric forcing and physical processes was assessed in different categories: precipitation, solar radiation, air temperature, wind speed and physical processes.

A 2ºC increase in air temperature had a similar effect to the presence of aerosols in SWnet, while the 2ºC decrease is similar to a decrease of wind speed. Changing the source of precipitation (GPCC or CRU) had lower impact than a specified change in the model's physics (hydrological or carbon version).

Air temperature changes affect mainly LWnet and sensible heat flux, as expected. Changes on Carbon parameterization causes a reduction of sensible heat flux.

ERA-40 surface balance energy components estimated by Trenberth et al. (2009) are reasonably close to WFD results presented here, except for latent heat flux. The latent heat flux discrepancy reflects the global excess of ERA-40 precipitation. Values provided in Trenberth et al. (2009), calculated for a different period, are quite different from WFD: 69.9 (65.5) Wm^{-2} of Rnet; 45.8 (38.5) Wm^{-2} of latent heat flux; and 23.5 (27.0) Wm^{-2} of sensible heat flux, WFD and Trenberth respectively.

Finally a set of FLUXNET sites were selected according to temporal coverage and climate type. Mediterranean sites, as SKy, SKo and BL, are affect by vegetation. Increase in productivity and evaporation rates occurring in late winter/spring and/or autumn are difficult to reproduce by the model, resulting in significant differences between the simulation and the observations of latent heat flux.

Chapter 5 - Global change in future climate

5.1 Global warming and hydrology

The Earth's climate has been changing; global (land and ocean) mean surface temperature has increased, especially since about 1950, by approximately 0.74 [0.56 to 0.92] ºC (1901-2000) (Solomon et al., 2007). The updated linear trend (1880 to 2012) shows a warming of 0.85 [0.65 to 1.06] ºC (Hartmann et al., 2013). Temperature increase is widespread over the globe and more pronounced at higher northern latitudes. Land regions have warmed faster than the oceans. Estimates show that global climate will very likely continue to become warmer in the next 100 years (Solomon et al., 2007).

Surface hydrology is affected by global warming in several ways, including changes in seasonal distribution and amount of precipitation, changes in partition between snow and rain, increased evapotranspiration and a reduction of soil moisture, and accelerated melting of glacier ice (Huntington, 2006). Seasonality of runoff and thaw in mid- and high-latitudes will also change: the winter flow will increase; spring and summer flows will decrease. In semi-arid regions, there are increases in hydrological variability, more frequent and larger floods with higher sediments' deposition and longer droughts. In mountain regions, glaciers will provide extra runoff as the ice disappears. Permafrost loss over extensive continental and mountain areas will cause erosion to the areas affected, aggravated by slow revegetation of terrain following deglaciation in high-mountain areas (Vaughan et al., 2013).

There are several studies about the role of the land surface in future scenarios of global warning (Boé and Terray 2008; Sheffield and Wood, 2008; O'Gorman and Schneider, 2009; Orlowsky and Seneriratne, 2013). Boé and Terray (2008) analysed the uncertainties in summer evapotranspiration changes over Europe, supporting the idea that the changes in evapotranspiration over central Europe are linked to soil moisture and radiative energy at the surface. Sheffield and Wood (2008), analysing potential changes in drought under future global warming, concluded that drought will increase globally over the 21st century. Changes in drought frequency, severity and spatial extent were estimated from soil moisture of multi-models and scenarios. O'Gorman and Schneider (2009) investigated the intensification of precipitation extremes in 21st century simulated with climate models. Impacts of climate change on water availability will depend on the baseline condition of the water supply system and the ability of water resources managers to respond not only to climate change but also to population growth and changes in demands, technology, and economic, social and legislative conditions. Orlowsky and Seneriratne (2013) concluded that GCM uncertainty is the dominant source of uncertainty in future drought projections, larger than uncertainties related to different scenarios. The Intergovernmental Panel on Climate Change Fourth Assessment Report (IPCC AR4) has confirmed that the climate of central and southern Europe may undergo very serious human-induced changes during summer (Christensen et al., 2007), characterized by a large decrease of precipitation and increase of temperature. The magnitude of temperature-driven trends in the future are generally projected to be higher under the Special Report on Emission Scenarios (SRES) mid-high (A2) than under the lower (B1) scenario (Table 5.1). These results determine the potential magnitude of changes that can be expected over the coming century. The SRES scenarios cover a wide range of the main driving forces of future emissions, from demographic to technological and economic developments (Nakicenvoic et al., 2000). These future climates offer various scenarios to describe changes in climate over the next 100 years.

The fifth Assessment Report (AR5), available since 2013, adopted four representative concentration pathways (RPCs). RCP4.5 is closer to SRES B1 and RCP8.5 is somewhat higher than A2 in 2100 and close to the SRES A1F1 scenario (not described in Table 5.1). RCP2.6 is lower than any of the SRES scenarios (Cubasch et al., 2013). In WATCH, previous to 2013, data available to XXI century was based on AR4. Each scenario represents a different mix of change in population, economic output, land use, and energy and technology use, among others, but can be generally characterized by maximum atmospheric CO_2 concentrations. B1 represents relatively slow population growth and an emphasis on environmental protection, with CO_2 concentrations stabilized at 550 ppm by the end of the century. A2 describes a heterogeneous world with continuously increasing global population and regionally

orientated economic development and fragmented technological change; it is generally regarded as a worst-case scenario that sees a four to five-fold increase in CO_2 emissions over 2000–2099 during which CO_2 concentrations increase from about 350 to 850 ppm.

Table 5.1: Main characteristics of IPCC scenarios used in this study (from Morita et al, 2001).

IPCC Scenarios	Main characteristics
B1	*Refers to a convergent world with the same global population that peaks in mid-century and declines thereafter, but with rapid changes in economic structures toward a service and information economy, with reductions in material intensity, and the introduction of clean and resource-efficient technologies. The emphasis is on global solutions to economic, social, and environmental sustainability, including improved equity, but without additional climate initiatives.*
A2	*Describes a very heterogeneous world. The underlying theme is self-reliance and preservation of local identities. Fertility patterns across regions converge very slowly, which results in continuously increasing global population. Economic development is primarily regionally oriented and per capita economic growth and technological changes are more fragmented and slower than in other storylines.*

5.1.1 Climate impacts – Water in the future

Projection of future climate in impact studies is mainly obtained using climate scenarios based on General Circulation Model simulations. Hydrological impacts of climate change are estimated by using the output of general circulation models to define scenarios to force hydrological models. Future projections (temperature and precipitation, mostly) were calculated by global (GCM) or regional (RCM) climate models and then used to simulate future hydrology by hydrological or land surface models. Systematic errors and uncertainties associated to projections and climatic simulations have an important impact in hydrological studies. The magnitude of change differs between climate projections that may have a strong impact in climate. Semi-arid and arid areas (e.g., the Mediterranean Basin, western USA, southern Africa and north-eastern Brazil) are particularly vulnerable to climate change, enduring a reduction of water resources (Meehl et al. 2007; Christensen et al. 2007).

In this chapter the present climate is compared with two future scenarios, to analyse changes of seasonality and trends. In order to predict future climate, hydrological simulations were produced for present climate and two future scenarios using the WFD meteorological forcing generated by ECHAM model.

5.2 Simulated historical and projected climate

The WATCH Driving Data 21st century is similar to the WFD but for the 21st century; it is based on model output rather than interpolated observational data. Two climate scenarios, B1, A2 and a Control were each used to force three global GCMs to produce a total of 9 sets of future driving data at 0.5 degree resolution. The WATCH Forcing Data for future climate was obtained through running three different global climate models (ECHAM5/MPIOM, CNRM-CM3 and LMDZ-4) forced by IPCC SRES B1 (mild changes) and A2 (extreme change) emission scenarios (Chen et al., 2011); the corresponding twentieth century simulations (20C3M) were also performed by the three different climate models. A statistical bias correction methodology for correcting climate output to produce internally consistent fields that have the same statistical distribution of rainfall and temperature as in the observations were applied to the output from twenty-first climate simulations. Precipitation and temperature obtained were bias-corrected in order to address uncertainty related to climate change projections in WATCH. Total precipitation was corrected using transfer functions, and snowfall was corrected accordingly, using the snowfall fraction taken from the GCM. In addition, mean, minimum and maximum daily temperature were also corrected (Piani et al. 2010, Hagemann et al. 2011).

The dataset provides meteorological data daily scale, 0.5x0.5 degree for the period 1960 to 2100 (control and two scenarios), which were further disaggregated to 3-hourly (see description of DDM method on Chapter 3). The output was used directly to force LSM and calculate the corresponding changes in hydrologic and energy fluxes. The land surface model was run over the period [1960-2100] on a global 0.5 degree grid and forced by the driving forcing obtained from three GCMs under present climate and

two scenarios (Chen et al., 2011). Results from the ECHAM climate model were selected to drive HTESSEL in order to estimate future changes in components of the surface hydrological and energy cycle.

The simulation covers all land surface from 1960 to 2100, control, and two scenarios, B1 and A2, with 5 years of spin-up (1960-1965). The hydrological cycle was evaluated and analysed for the terrestrial components of the hydrological cycle focusing on [1971-2000] control period and compared to scenarios simulations in the end of 21st century, [2071-2100]. Global maps are constructed to identify regions where the water cycle and associated water resources are significantly impacted by climate change, and regions vulnerable to these changes in terms of e.g. water availability.

5.3 Temporal fields

Climate change is often measured by changes in primary climate variables such as global surface air temperature and precipitation. Precipitation, air temperature, and evaporative demand are the most relevant climatic drivers for water availability. In addition to temperature, precipitation is an important aspect of climate. Changes in temperature and precipitation will influence hydrologic processes on the land surface, which in turn will cause changes in streamflow but the magnitude and the sign of these changes is uncertain. Inter-annual variability in precipitation is generally much higher than that of temperature. This makes it more difficult to distinguish consistent long-term trends from natural fluctuations.

Global time series of standardized anomalies of global mean air temperature and precipitation from 1965 to 2100 are shown in Figure 5.1. These data were calculated by subtracting the monthly average from each monthly data, then dividing by the standard deviation for each month. Global anomalies are provided with respect to the period [1971-2000], the current climate. In the coming two to three decades projections do not diverge strongly and uncertainty in the sign of change is relatively large over this period. By the middle of the 21st century, annual average air temperature and precipitation are projected to continue to increase. Evolution of global temperature until about 2030 is similar for both scenarios. Beyond the next few decades, temperatures diverge more and more due to the additional emissions of greenhouse gases, until by the end of the 21st century there is a substantial spread in warming between the two scenarios; air temperature anomalies (Figure 5.1 at left) increase rapidly from 2050 to 2100 for the A2 scenario. Warming will continue beyond 2100 under both scenarios, with a steeper increase for the A2 scenario. The global mean temperature change in 2100 is about four standard deviations warmer than climatology for A2, and about two standard deviations for B1. The global temperature anomalies for the 21st century are within the range [+2,+4] °C. Multi-model mean land surface air temperature anomalies in IPCC AR5 are 2.4 ± 0.6 and 4.8 ± 0.9 ºC (2081-2100), for RCP4.5 and RCP8.5, closer to B1 and A2, respectively (table 12.2 in Collins et al., 2013). Precipitation anomalies are less consistent and include both increases and decreases, ranging between –0.02 to +0.1 std (Figure 5.1, right panel). Nevertheless, A2 scenario anomalies are higher than B1 scenario and beyond 2040 the anomalies are positive for both scenarios.

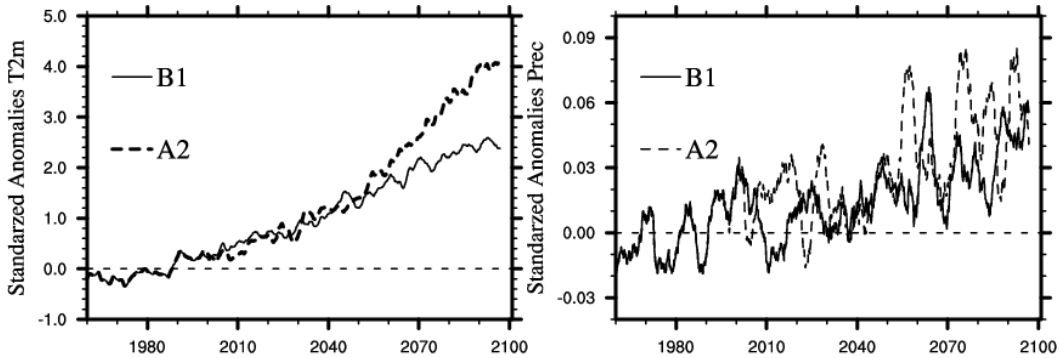

Figure 5.1: Temporal evolution from 1960 to 2100 of 24-monthly running average standardized anomalies of global temperature (left) and precipitation (right) of present and future scenarios (B1 and A2 scenarios, solid and dashed) with respect to [1971-2000] monthly mean average.

Changes in precipitation are much less notable than changes in temperature. Due to the rapid increase in temperature at the end of 21st century, the analysis of the spatial fields will be focused on the period [2071-2100], and compared with the control period, [1971-2000]. Figure 5.2 presents an analysis of land temperature trends between 50 ºN to 50 ºS, in 20° bands. There is evidence that land precipitation will increase in the future. There are different trends in temperature in different parts of the world, with a positive trend in both hemispheres.

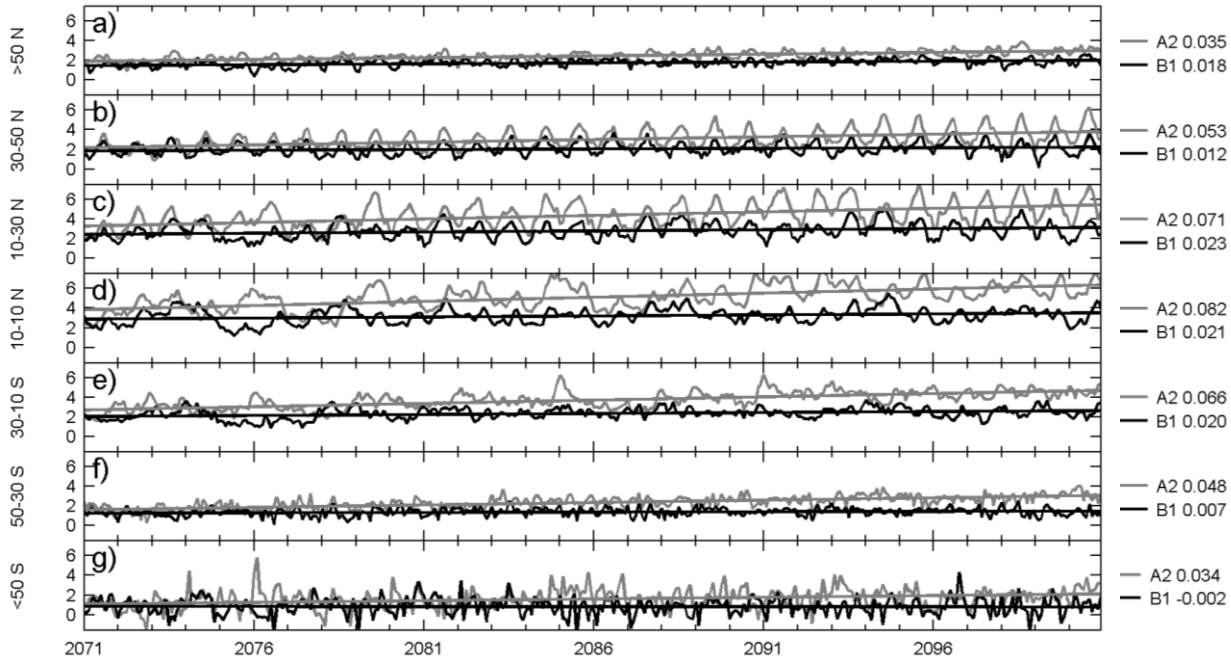

Figure 5.2: 2071-2100 evolution of annual temperature anomalies averaged over land areas for latitudinal bands relative to 1971-2000 climatology (A2 and B1 scenarios, grey and black lines).

5.4 Annual and seasonal regimes

5.4.1 Air temperature and precipitation

Figure 5.3 shows the global average temperature in the current climate (panel c) and the changes at the end of the 21st century [2071-2100] for scenarios B1 and A2 with respect to the period [1971-2000]. The degree of warming depends on the emission scenario, but spatial patterns are quite similar for both scenarios. Land areas warm significantly during the twenty-first century in both simulations, with end-of-century temperature increases from approximately 2 ºC under the lower emissions B1 scenario to 6 ºC in the higher emissions scenario (Figure 5.3, panels a and b). There will be warming in all regions, with the largest values expected in high northern latitudes. Temperature in Siberian region is projected to increase significantly in the future (Christensen et al., 2007; Collins et al., 2013), by a minimum of 6 ºC as compared to the current climate (Figure 5.3c). These differences are higher in A2 scenario, as expected, about 8 to 10 ºC. The patterns of surface air temperature are similar to those in the AR5 for 2081-2100 period (figure 12.11 Collins et al., 2013).

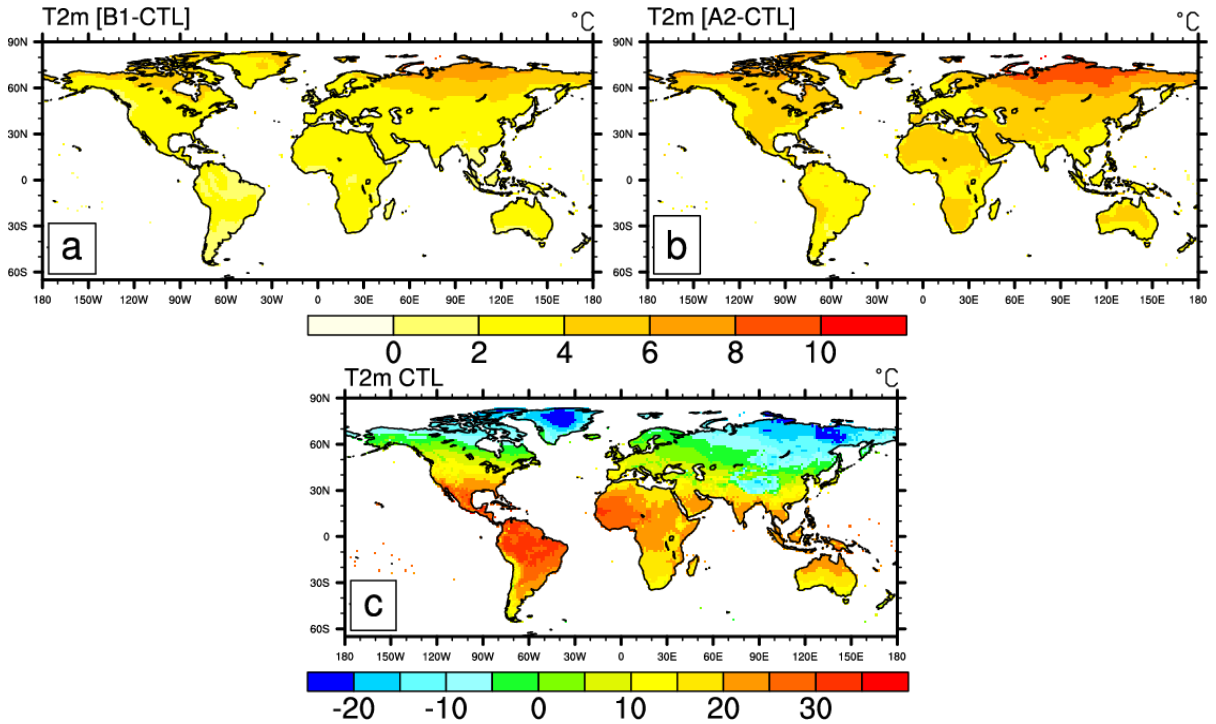

Figure 5.3: Temperature difference between [2071-2100]-[1971-2000] for scenarios B1 and A2, panels a and b, respectively; 30-years average of temperature in current climate, 1971-2000, (c). Units are in degree Celsius.

Standard deviations (STD) of annual average results were computed for temperature (Figure 5.4) and precipitation (not shown). The highest values of STD in the present climate (panel c) are around 2 ºC, located in boreal zones (Figure 5.4c). Largest future changes in interannual variability will take place in the A2 scenario, whose values decrease in boreal eastern Asia and increase slightly in tropical zones, when compared to current climate. In the future, temperature STD will increase 1 ºC on the Iberian Peninsula and Southern Africa and decrease over Alaska, Greenland and part of Eurasia (green to blue in Figure 5.4b). Figure 5.4a does not reveal differences of more than 0.5 ºC (B1 scenario), when compared to current climate.

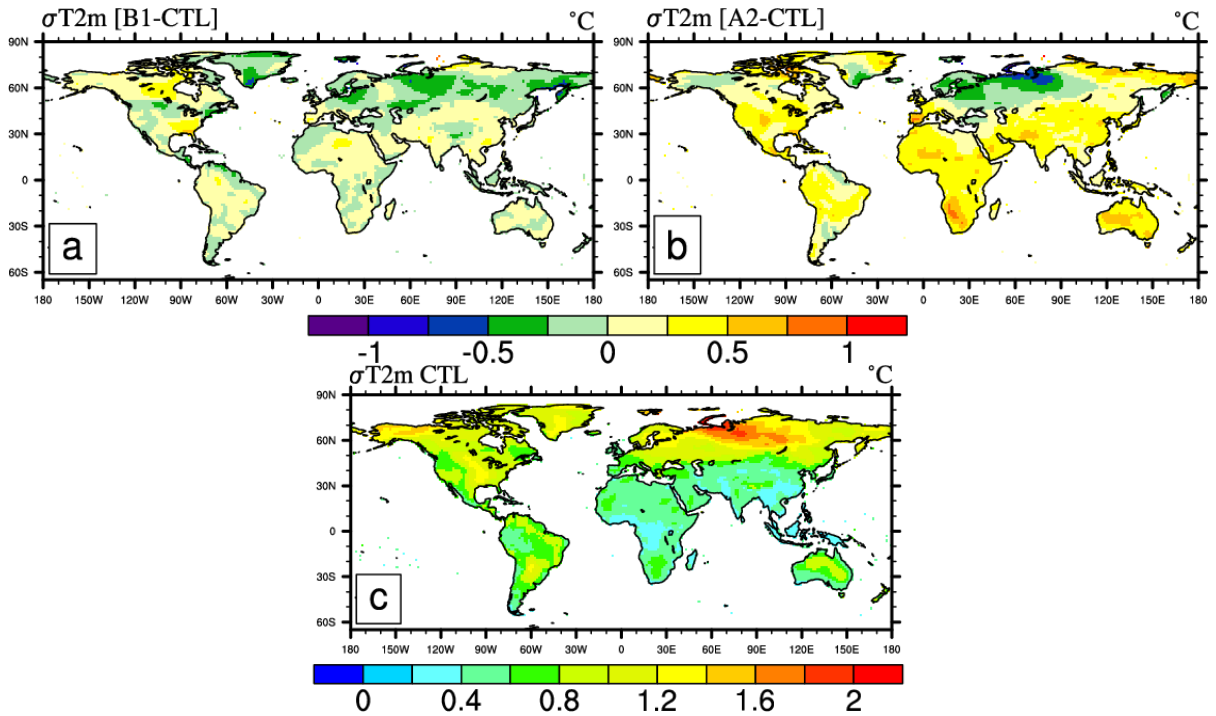

Figure 5.4: Standard deviation of air temperature, σT2m, difference between [2071-1971] for future scenarios B1 and A2, panels a and b, and STD of temperature in current climate [1971-2000], panel c. Units are in ºC.

Another method to analyse the climate change in the future is the temperature trend, which measures the tendency over a period of time. Figure 5.5 show the temperature trend for a 30-year period over present climate and the end of 21st century. Surface temperature in most part of the land has risen (positive trend in Figure 5.5c) during 1971 to 2000. The largest 30-year increase in temperature in the future will occur in the high latitudes land areas of the Northern Hemisphere, 1 to 2.5 ºC per decade in the A2 scenario; it appears that A2 and B1 scenarios will not have reached equilibrium.

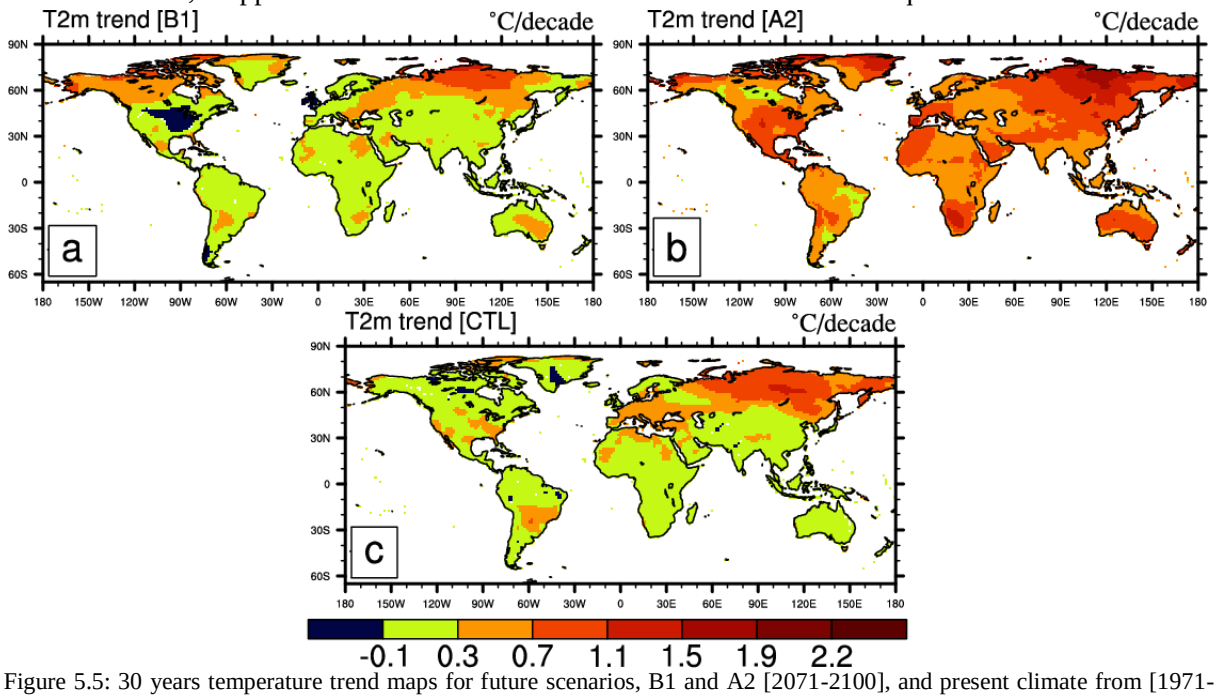

Figure 5.5: 30 years temperature trend maps for future scenarios, B1 and A2 [2071-2100], and present climate from [1971-2000] (c). Units are in ºC per 30 years.

Precipitation, as temperature, will be affected by climate change in the near future. High intensities of precipitation are located in tropical rain belt and mountain zones, reaching 5000 mm per year in some locations (result not shown). By the end of 21st century, land surface simulations indicate precipitation increase in high latitudes and parts of the tropics, and decrease in some sub-tropical and lower mid-latitude regions (e.g. Mediterranean) in both scenarios (Christensen et al., 2013). Projected changes in precipitation and dryness extremes are less clear than those in temperature extremes, despite some robust features, such as increasing dryness over the Mediterranean and increasing heavy precipitation over the Northern high latitudes (Orlowsky and Seneriratne, 2012).

Mediterranean and Amazon basin will experience a decrease (yellow to red values in Figure 5.6) in total average future precipitation (about 300 mm per year). On the other hand, average precipitation in tropical Africa will increase in both scenarios, more than 200 mm/year. As verified for projected temperature, the largest variation in averaged precipitation occurs in the A2 scenario. Precipitation variance will increase in some places, including tropical Africa and America (result not shown).

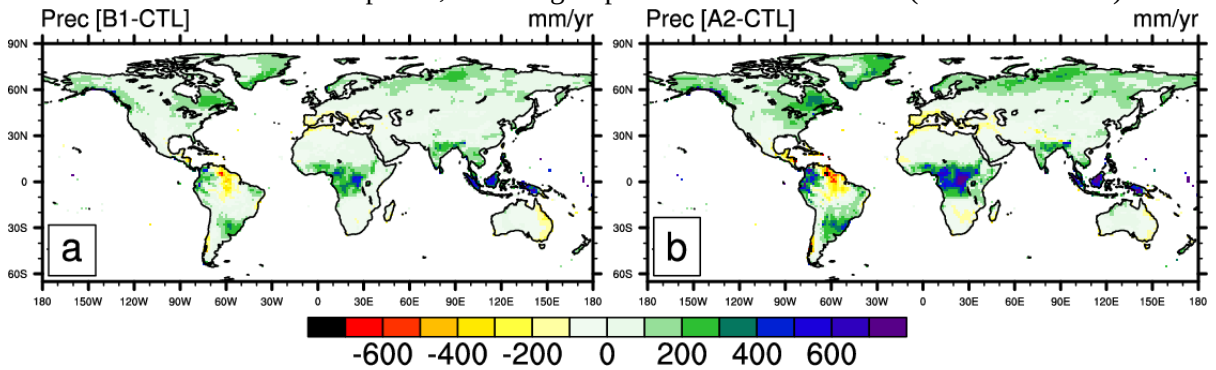

Figure 5.6: Difference between precipitation in future scenarios and [1971-2000] climate, B1 (a) and A2 (b). Positive values (green to blue) represent increase in precipitation and positive values (yellow to red) represent decrease. Units in mm per year.

Trends in precipitation data for global land were also examined (figures not shown). In contrast to air temperature, where a positive trend (increase of air temperature in the future) was detected, precipitation trends vary locally, increasing in some places but reducing in others. Figure 5.7 shows global patterns of projected change in monthly precipitation. Precipitation at the end of the XXI century is expected to increase with respect to current climate, in most land areas. Regions of decrease in precipitation include some dry and semi-arid zones in mid-latitudes, and most subtropical land regions: Mediterranean, Gulf of Mexico, and Australia, yellow areas in figure.

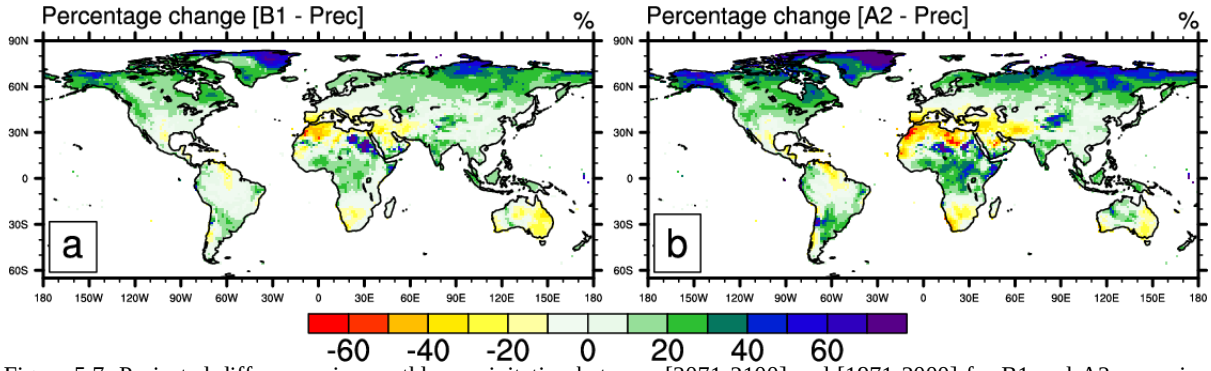

Figure 5.7: Projected differences in monthly precipitation between [2071-2100] and [1971-2000] for B1 and A2 scenarios, respectively. Change in %.

5.4.1.1 Seasonal change of air temperature and precipitation

To show the seasonal behaviour of air temperature and precipitation, each of the variables was averaged over 3-month periods of December-February (DJF) and June-August (JJA), by the end of the 21st century [2071-2100], for both scenarios, B1 and A2 (Figure 5.8 and Figure 5.9, respectively); seasonal temperature changes at the end of the XXI century were obtained subtracting the 1971-2000 corresponding data for each of the scenarios. Temperature changes are positive everywhere, particularly pronounced over the high latitudes during DJF (Northern hemisphere winter), especially in A2 scenario (more than 7 ºC). JJA anomalies do not exceed 5 ºC (3 ºC in the lower emissions B1 scenario). Globally both simulations exhibit more warming in DJF than in JJA.

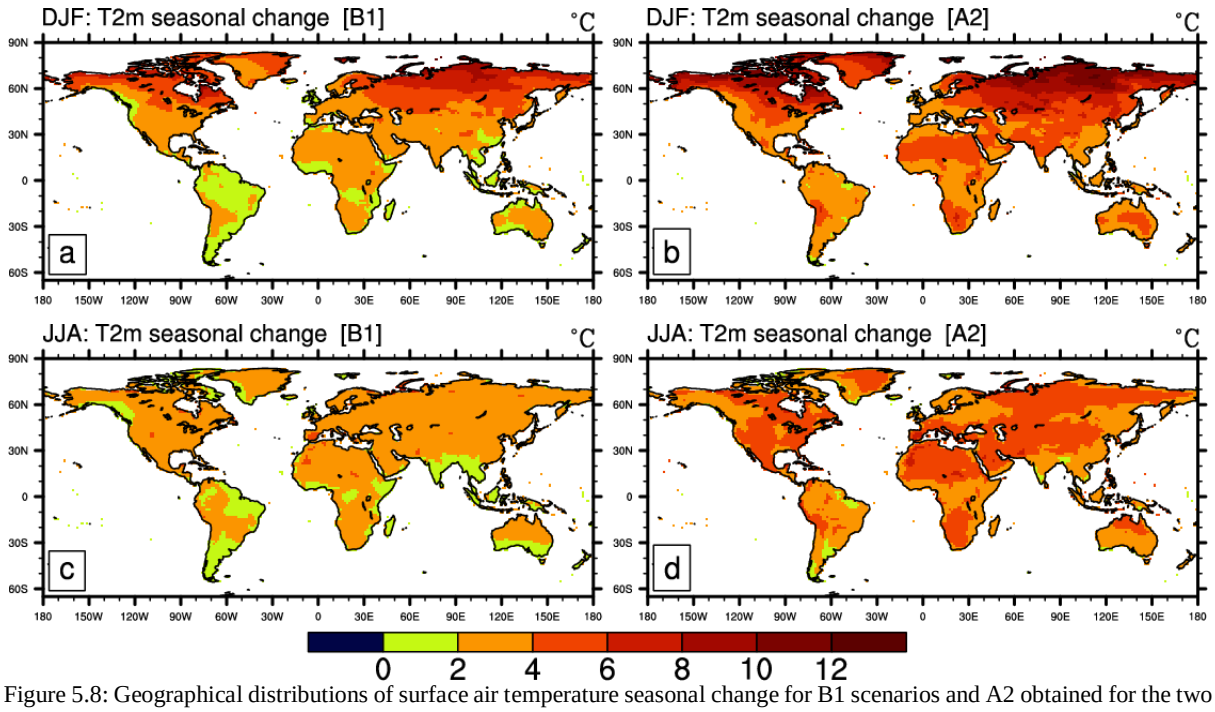

Figure 5.8: Geographical distributions of surface air temperature seasonal change for B1 scenarios and A2 obtained for the two 3-month periods of (a) DJF and (b) JJA averaged over the 30-yr period from 2071 to 2100. Here, the change represents the deviation from the temperature averaged over the 30-yr base period from 1971 to 2000. Units are in ºC.

Large winter temperature variations at high-latitudes (Figure 5.8) may lead to changes in winter snowfall. Precipitation seasonality shows important variations when compared to current climate; this might be particularly relevant for places that rely on seasonal precipitation. In general, seasonal change is positive almost everywhere during DJF, albeit with small light yellow patches indicating decreases of precipitation. In contrast, negative anomalies (yellow to red values) occur at central Europe during summer (JJA) and near Venezuela (Figure 5.9). There is a slight decrease of winter precipitation and increases in summer precipitation are more evident in the A2 scenario (Figure 5.9, panels b and d). In scenario B1, the Indian monsoon precipitation will increase. In contrast, the A2 scenario yields more rainfall, except in the NE of the subcontinent, where there is a decrease of precipitation.

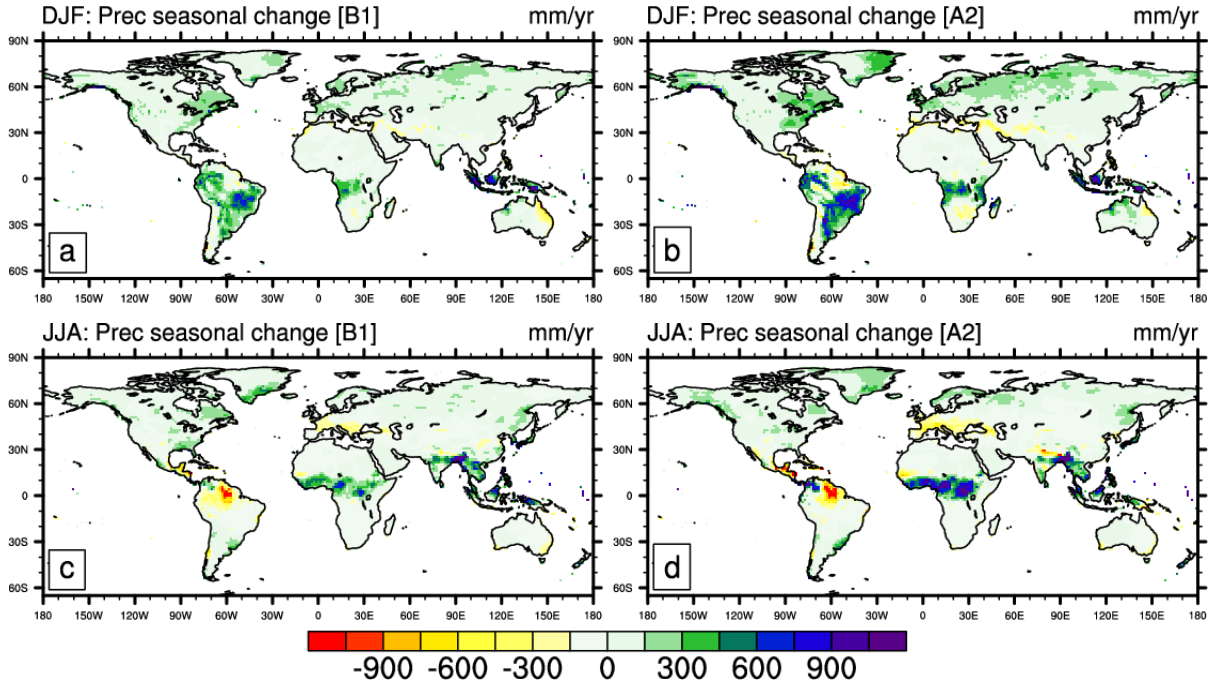

Figure 5.9: As Figure 5.8, but for precipitation. Units are in mm/month.

5.4.2 Total runoff variability

Mean runoff change in the context of climate change has been analysed by several authors. Previous studies show increases of 10 to 40% in the high latitudes of North America and Eurasia and decreases of 10 to 30% in Mediterranean, southern Africa, and western USA/northern Mexico (Milly et al., 2005). 21st century model-projected runoff is expected to decrease in southern Europe, the Middle East, and South western USA and increase in Southern Asia, tropical East Africa and at high northern latitudes. Projected changes in runoff in AR5 show decreases in northern Africa, western Australia, southern Europe and South western USA and increases larger than the internal variability in north western Africa, southern Arabia and south eastern South America associated to the projected changes in precipitation (Kirtman et al., 2013). Distribution of annual runoff is consistent with precipitation, itself related strongly both to topography and closely tied to the Intertropical Convergence Zone and the ascending branch of the Hadley cell. Gudmundsson et al. (2011) analysed projected changes in future runoff variability using a multi-model runoff from A2 emission scenario. Dry regions with little runoff showed the highest variability, whereas in humid areas the runoff variability is lowest. Significant changes in runoff variability were found. A reduction of runoff is expected for northern latitudes and an increase in mid-latitudes (northern and southern hemisphere). Large decreases in runoff in southern Europe and southern Africa are consistent with changes in the Hadley Circulation and related precipitation decrease and warming-induced evapotranspiration increase (Meehl et al., 2007; Collins et al., 2013).

This analysis is based on annual rates of total runoff (i.e. the sum of surface and subsurface runoff). The percent change of annual runoff (Figure 5.10) has a similar pattern to change of annual precipitation shown in Figure 5.7. Areas with highest increase in precipitation correspond to areas with highest

increase of runoff: high latitudes and equatorial regions, wetter conditions for example. Runoff decrease is located in mid-latitudes, southern Europe and subtropical regions, the Gulf of Mexico and Middle America. These regions display a reduction in precipitation and a consequent reduction in total runoff, as shown before (Figure 5.7). In regions where precipitation and runoff are very low (e.g., desert areas) small changes in runoff can lead to large percent changes. The A2 scenario, as expected, is slightly more extreme than B1, especially in the tropics and Mediterranean zone. Percentage changes (PC) patterns confirm previously published results (Milly et al., 2005, Chen et al., 2011 and Gudmundsson et al., 2011). In some areas with projected increases in runoff, different seasonal effects are expected, such as an increased wet season runoff and decreased dry season runoff (Meehl et al., 2007).

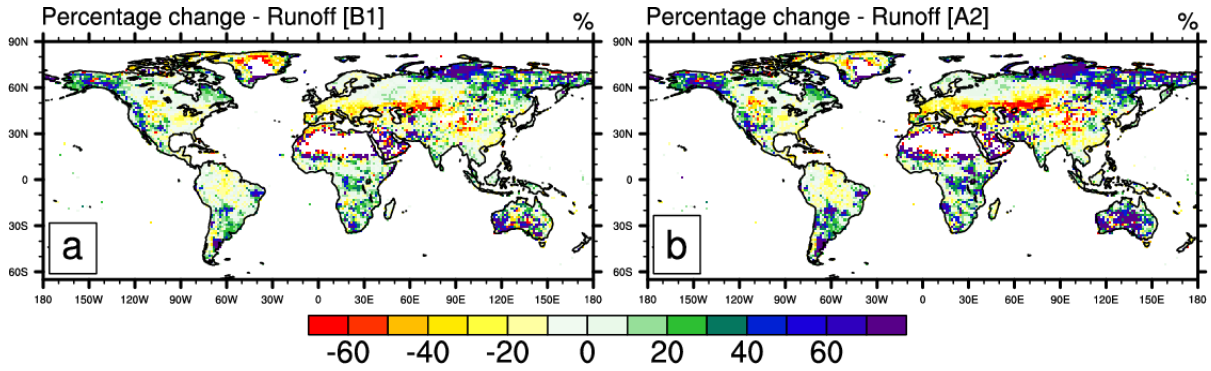

Figure 5.10: Projected changes in mean runoff of monthly runoff in percent from 1971-2000 to 2071-2100, under the B1 and A2 emissions scenarios. Units are in % of change.

5.4.3 Soil moisture

Models simulate the water in the upper few metres of the land surface in varying ways, and evaluation of the soil moisture content is still difficult. Soil moisture climate feedbacks are responsible for a substantial fraction of simulated changes in climate projections (Seneviratne et al., 2006; Boé and Terray, 2008; Diffenbaugh and Ashfaq, 2010; Boberg and Christensen, 2012). It responds to precipitation variability but also affects precipitation though evaporation. Reductions in soil moisture can intensify heat waves (Seneviratne et al., 2006). In high latitude permafrost regions, soil moisture projections are critically important to assessing future climate feedbacks; the current understanding of these processes at scales relevant to climate is poor.

AR4 summarized multi-model projections of 21st century annual mean soil moisture changes as decreasing in the subtropics and Mediterranean region and increasing in east Africa and central Asia (similar to AR5). Figure 5.11 show the spatial distribution of soil moisture percentage change relative to the reference [1971-2000] projected for [2071-2100] under B1 and A2 scenarios, respectively.

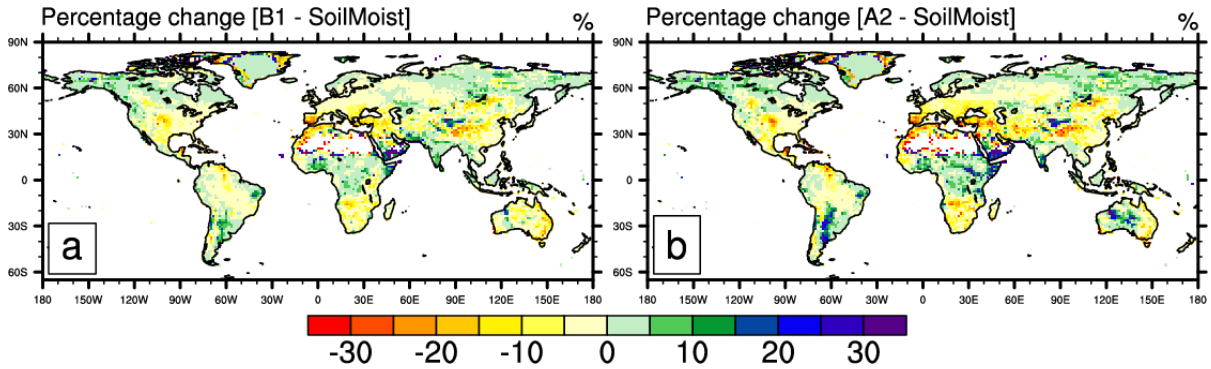

Figure 5.11: Percent change of soil moisture (four layer integrated) percentage change relative to the reference [1971-2000] projected for [2071-2100] from B1 and A2 scenarios, respectively; regions with reference soil moisture smaller than 100 kg/m^2 were masked.

Despite the expected increase in precipitation by the end of the century in both scenarios (Figure 5.6), the average soil moisture decreases in almost all land surface. Percent change of annual mean soil moisture content show decreases in the subtropics and the Mediterranean regions, but there are increases

in East Africa, Central Asia and some regions with increased precipitation. Soil moisture drying in the Mediterranean, Southwest US and southern African regions is consistent with projected changes in Hadley circulation and increased surface temperatures (consistent with RCP8.5 scenario, Collins et al 2013 and Kirtman et al. 2013). These results are most significant under the more pessimistic scenario, A2.

5.4.4 Energy budget

Previous figures show patterns of temperature, precipitation, total runoff change and soil moisture where wet areas become wetter and dry areas dryer. Globally averaged land precipitation is mainly conditioned by shortwave forcing causing the robust pattern of zonal precipitation change. The different properties of vegetation and climate over the surface are reflected in partitioning of net radiation (Rnet) into sensible, latent heat and ground heat (H, LE and G, respectively). The spatial distribution of averaged annual energy budget components (SWnet, LWnet and Rnet) in present climate and both scenarios are shown in Figure 5.12. Increase of surface temperature observed over 21st century causes an increase in moisture content of the atmosphere. If the atmosphere's water vapour increases as temperature rises, so might global cloudiness. Corresponding to this increase, more clouds would affect the net radiation at surface. Low clouds mainly reflect incoming solar radiation back to space, a process that tends to cool the climate, but high clouds mainly also absorb infrared radiation emitted from the Earth, which tends to warm it. Just how the climate will respond to changes in cloudiness will probably depend on the type of clouds that form and their physical properties (Boucher et al., 2013). The Arctic region will warm more rapidly than the global mean (see land mean in Figure 5.3), with associated increase of sown melt and a marked decrease of the surface albedo, and mean warming over land will be larger than over the ocean (Collins et al., 2013; Christensen et al., 2013). Lower surface albedo will lead to warming at the surface and near surface, increase of shallow convection and low clouds. These effects can explain decrease of absorbed future solar radiation over Greenland detected in Figure 5.12 (blue and green areas), conducting to a loss of energy to the atmosphere due to cloud formation at the top of the boundary layer. Changes in humidity are very relevant in the context of glacier variation because of the significant impact humidity has on the partitioning of the available energy into melt and sublimation. The warming leads to an increase of moisture content in the atmosphere, and of clouds, which therefore reduce the quantity of SWnet at surface.

The annual average of net radiation at the surface is expected to increase in tropical America, as a result of decrease of clouds and the reduction of convection in the future. This increase implies an increase in sensible and latent fluxes in the same area (result not shown). The rate at which Rnet is partitioned into energy components is dependent on climatic conditions, species composition, vegetation structure, soil, topography, etc. Although not modelled by the climate models used here, if vegetation type changes, the energy balance of the surface will be greatly changed.

At polar latitudes and in mountainous areas, such observed and predicted changes in climate affect the glacier energy balance through its sensitivity to changes in atmospheric humidity (which governs sublimation), precipitation (whose variability induces a positive feedback on albedo) and cloudiness (which controls the incoming long-wave radiation). In the inner tropics air temperature also significantly influences the energy balance, albeit not through the sensible heat flux, but indirectly through fluctuations in the rain–snow line and hence changes in albedo and net radiation receipts.

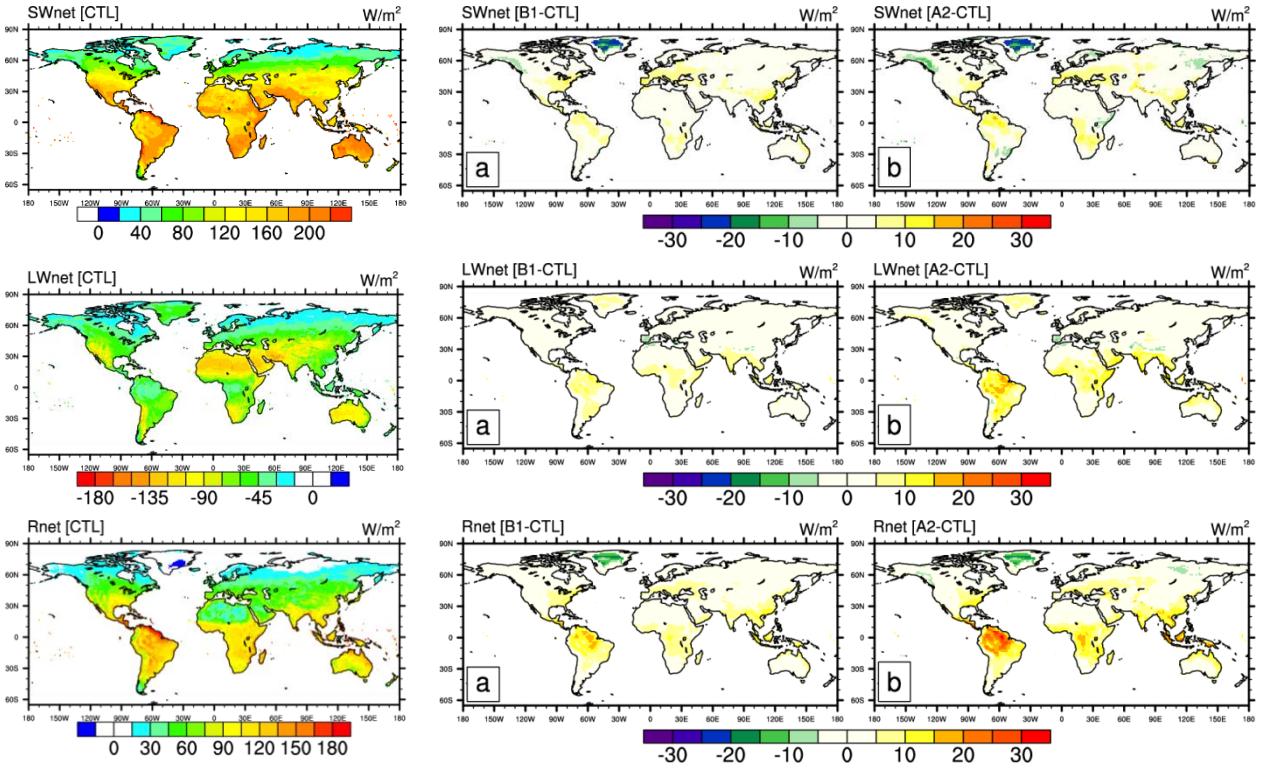

Figure 5.12: Spatial distribution of averaged annual surface short wave net (SWnet), surface long wave net (LWnet) and surface net radiation (Rnet), of current (left-hand side panels) climate; and future, B1 and A2 scenarios difference to current climate, (centre and right-hand side panels).

5.4.5 Climate variables controlling surface hydrology

Figure 5.13 shows mean seasonal variations over latitude of air temperature for current climate and future (B1 and A2) scenarios. Air temperature exhibits seasonality, showing a maximum in summer, and a minimum in winter. Air temperature in the future will increase about 2 ºC with respect to current climate. Most significant differences are located in the equatorial zone and in the southern hemisphere, where there is a slight increase in surface temperature over the entire year.

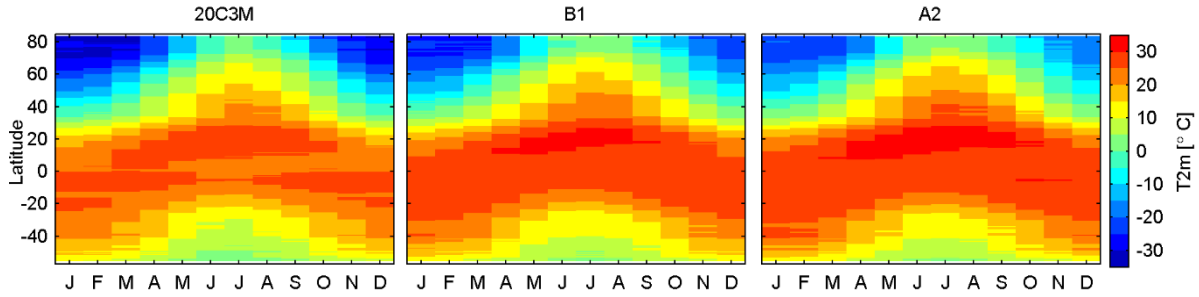

Figure 5.13: Zonally averaged annual cycle of monthly temperature in present [1971-2000] and in future [2071-2100] under B1 and A2 scenarios, respectively.

Precipitation also exhibits a clear seasonality, more pronounced in the tropical zone, with a clear marked rainy season. Interannual variability of precipitation is high (standard deviation about 10 mm). A high standard deviation indicates that the data are spread out over a large range of values. There is a clear increase in precipitation in the future in both scenarios most significant between November and April.

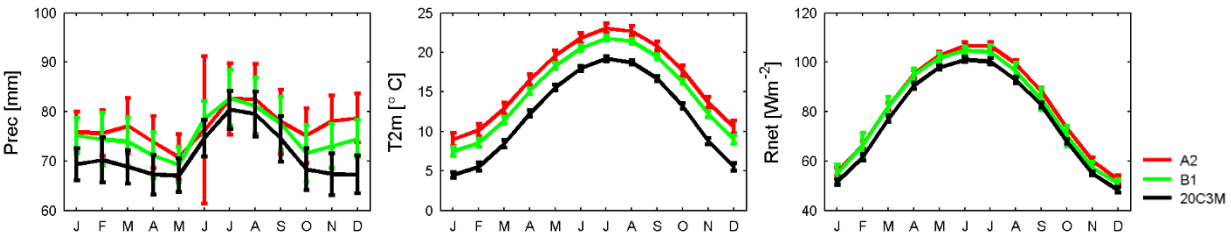

Figure 5.14: Monthly variations of precipitation (a), air temperature (b), and net radiation (c) in Current [1971-2000] (black lines) and Future [2071-2100] (A2: red lines and B1: green lines).

5.5 Changes in spatial distribution in European climate

European climate is changing, with greater warming in winter in the North, and in summer in Southern and Central Europe (Solomon et al., 2007). Annual mean temperature in Europe is likely to increase more than the global mean. Seasonally, the largest warming is likely to be in northern Europe in winter and in the Mediterranean area in summer. Minimum winter temperatures are likely to increase more than the average in northern Europe and similar changes will occur in maximum summer temperatures in southern Europe. Precipitation will increase in Northern Europe and decrease in south, causing more frequent droughts in Southern, Central and Eastern Europe and Mediterranean. There are evidences that temperature will continue to increase throughout the 21st century over all Europe and Mediterranean region (Solomon et al., 2007; Hartmann et al., 2013). Soil moisture has an important control on summer temperature (direct effect on the Bowen ration and low level clouds) and precipitation. Feedbacks between soil moisture, precipitation and temperature are particularly important in transition regions between dry and humid areas.

This section explores changes of water availability that occur by mid-21st century based in B1 and A2 scenarios over Europe (defined by 11.25 ºW – 40.75 ºE longitudes, and 34.25 ºN – 73.75 ºN latitudes); soil moisture will be used as a proxy variable for water availability. Percent change, PC, of precipitation and soil moisture follow a north-south (latitudinal) gradient (Figure 5.15). Positive values, increased in the future, are depicted in blue, while negative values, representing a decrease of water, are depicted in red. In general there is a reduction in the south and an increase in the north, both in precipitation and soil moisture. Changes in seasonality of precipitation are more evident when looking at seasonal variation (Figure 5.16). The general pattern of future change in mean precipitation over Europe includes widespread increases in northern Europe (between +20 to +40 per cent), rather smaller decreases across southern Europe (maximum -60 per cent), and small or ambiguous changes in central Europe.

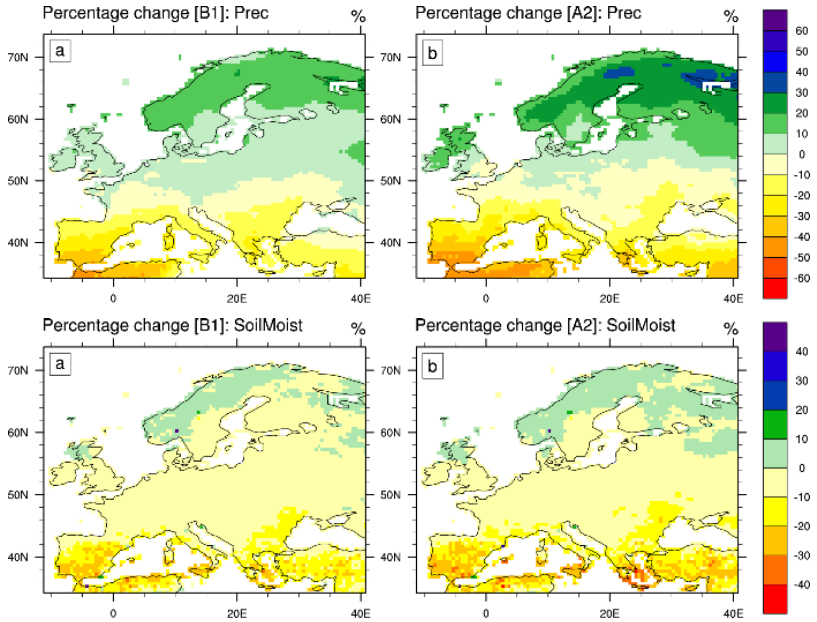

Figure 5.15: Percent change ([2071-2100] – [1971-2000]) in annual precipitation (top) and soil moisture (bottom) for the two IPCC SRES storylines B1 and A2 with climate projected by ECHAM model. Note the different colour scales.

There is a marked contrast between winter and summer patterns of precipitation change. In the winter season most of Europe gets wetter, between +20 and +50 % more water. Mediterranean area is the exception where winters become drier (about –20 %). There is a strong gradient of precipitation change between northern Europe and southern Europe in summer, more precipitation in the north (wetting of up +40 %) in contrast with southern Europe (drying of up to - 60 %). The differences between future climate and the present are more evident in A2 scenario. There is an increase of precipitation in the Northern Europe, and a reduction in the south in all seasons. In Central Europe precipitation increases during winter (DJF) and has a slightly decrease in summer (JJA), as shown on Figure 5.16, panels a and e, and c and g, respectively.

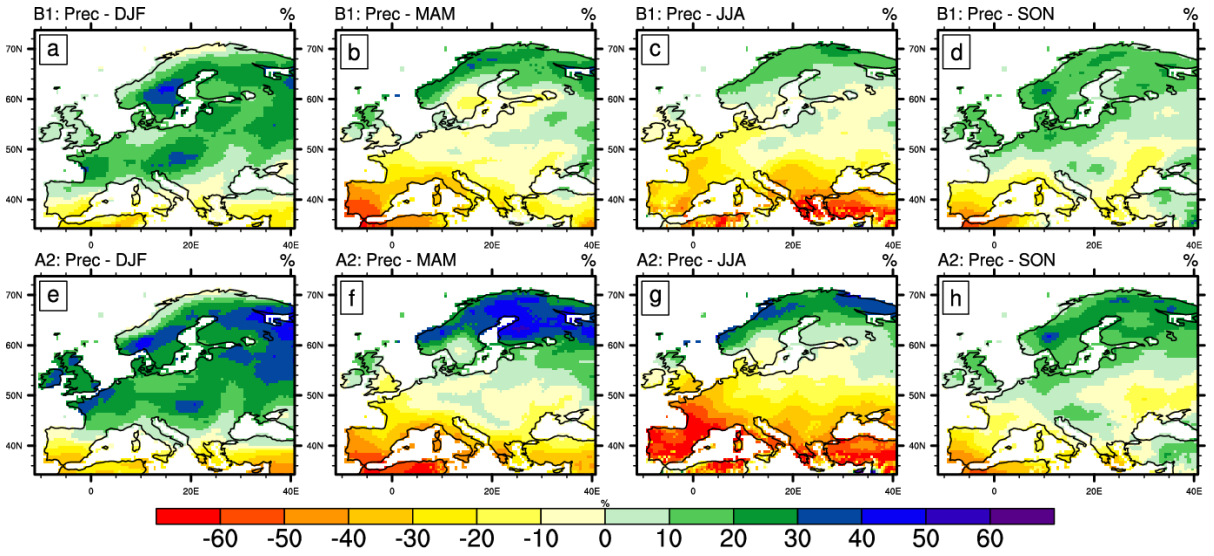

Figure 5.16: Seasonal change in precipitation for December–January–February (DJF), March–April–May (MAM), June–July–August (JJA), September–October–November (SON), for B1 and A2 scenarios, top and bottom, respectively.

The pattern of percent change of total runoff is quite similar to the precipitation pattern (Figure 5.17). Unlike precipitation, total runoff decreases in central Europe and Scandinavia, most evident in summer (about -40 %). There is an increase in winter flows and decrease in summer flows.

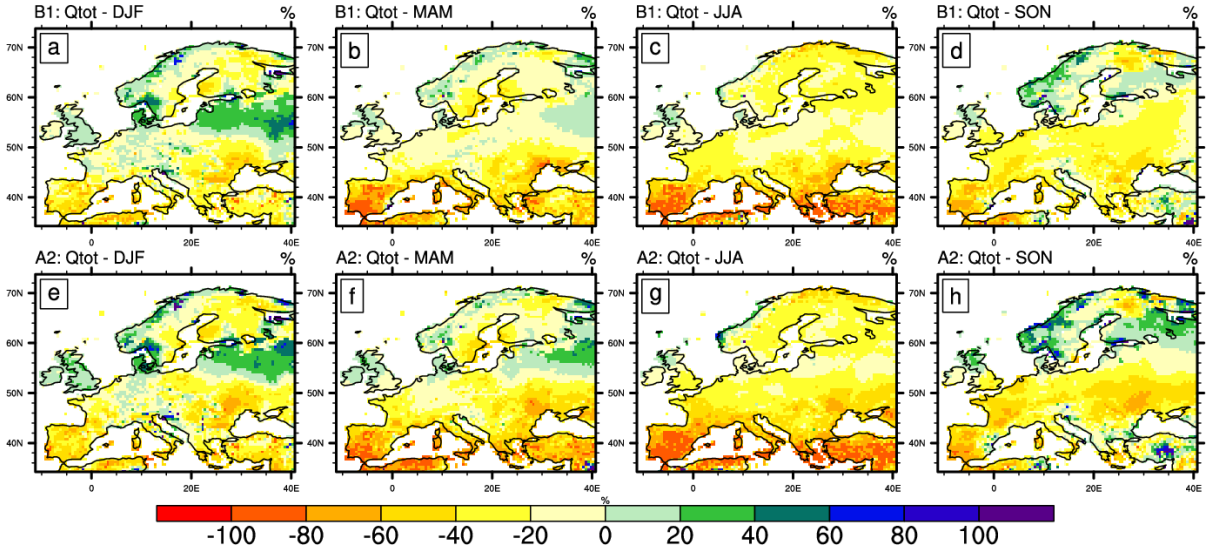

Figure 5.17: As Figure 5.16, but for total runoff, Qtot.

Projections of change in seasonal air temperature and precipitation for 30-years period during late 21st century in north (upper to 47.5 ºN) and south Europe are presented in Figure 5.18 and Figure 5.19. Temperature increase is larger in the cold season, reaching 8 ºC under A2 scenario. Moisture available for precipitation due to temperature increase causes more precipitation in northern Europe during winter. In southern Europe, precipitation, as indicated previously, increases in winter and decreases in summer. Such variations are most evident in Southern Europe (Figure 5.19). This precipitation reduction increases risk of summer drought, mainly in the south. The scatter plots of south Europe reveals an earlier spring (MAM) with less precipitation and warmer temperature.

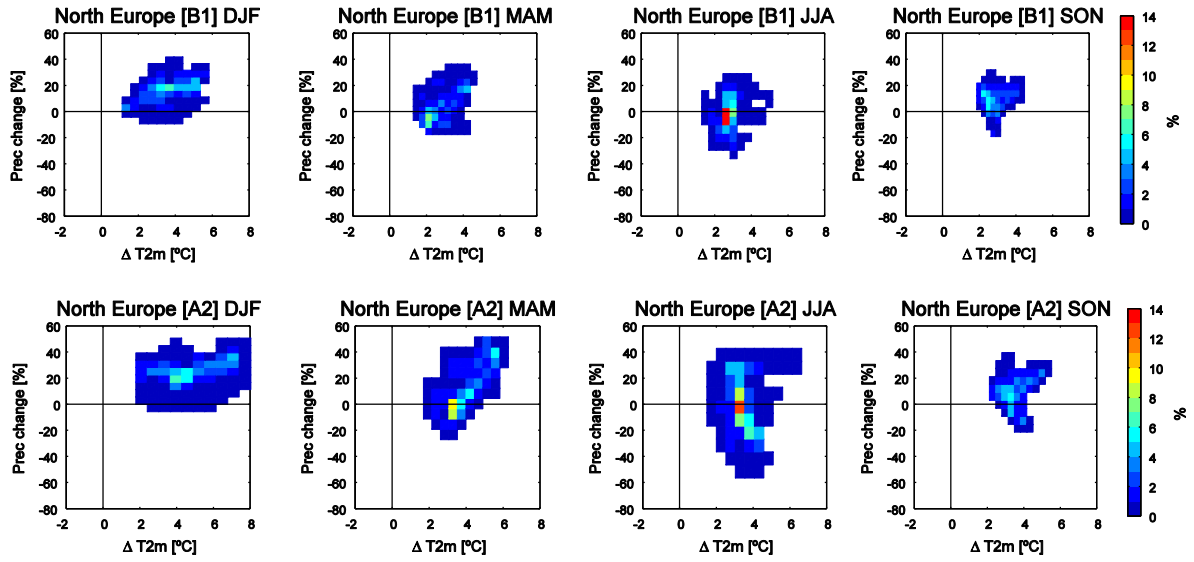

Figure 5.18: Projected climate change by [2071-2100] (relative to the baseline period [1971-2000]) in the Northern Europe during DJF, MAM, JJA and SON under B1 and A2 scenarios, respectively. The x-axis shows temperature changes in ºC, the y-axis precipitation changes in percent. Each point represents percentage of north Europe's land.

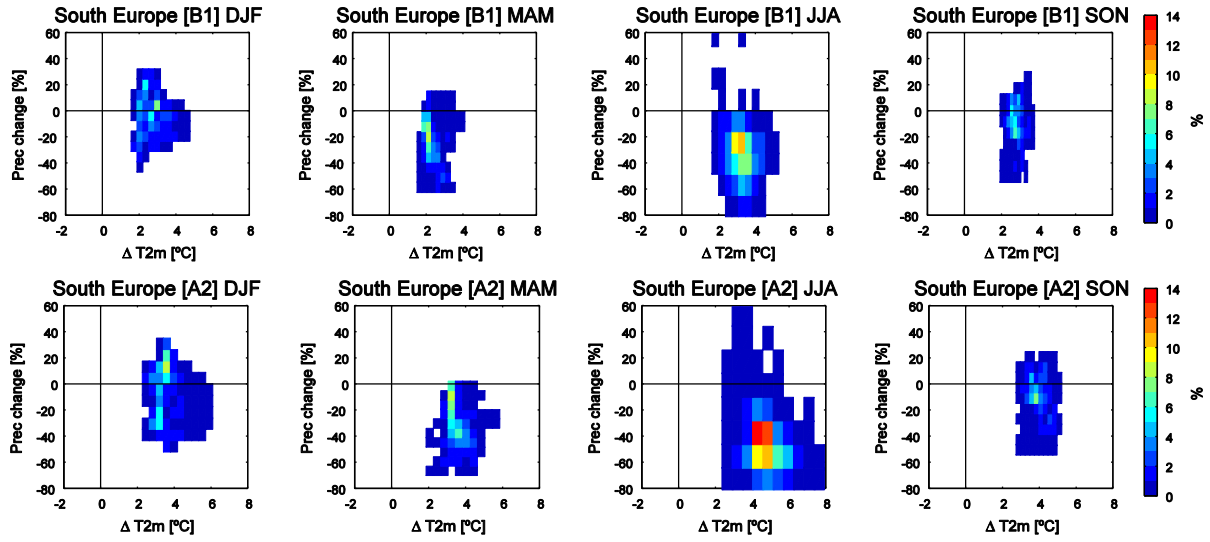

Figure 5.19: As Figure 5.18, but for Southern Europe.

Soil water content change is linked to the precipitation change. Figure 5.20 shows soil moisture seasonal variation in southern Europe against precipitation change by the end of 21st century. Scatter diagrams provide a guidance to assess the likely range of future climate change. These diagrams can be used to define the limits of soil moisture/precipitation change to be employed in climate impact sensitivity studies. Soil moisture variation ranges between -200 kg/m2, and 200 kg/m2, with a strong preference towards drier soils. Decreasing precipitation in Southern Europe is accompanied by increasing temperature (Figure 5.19) resulting in even stronger decreases in soil moisture than would be expected from considering precipitation changes only. There is a decrease of winter and spring soil moisture (Figure 5.20, DJF and MAM panels) and a strong reduction during the warm months (JJA panels), peaking in the autumn (SON panels), due to reduction of precipitation over southern Europe.

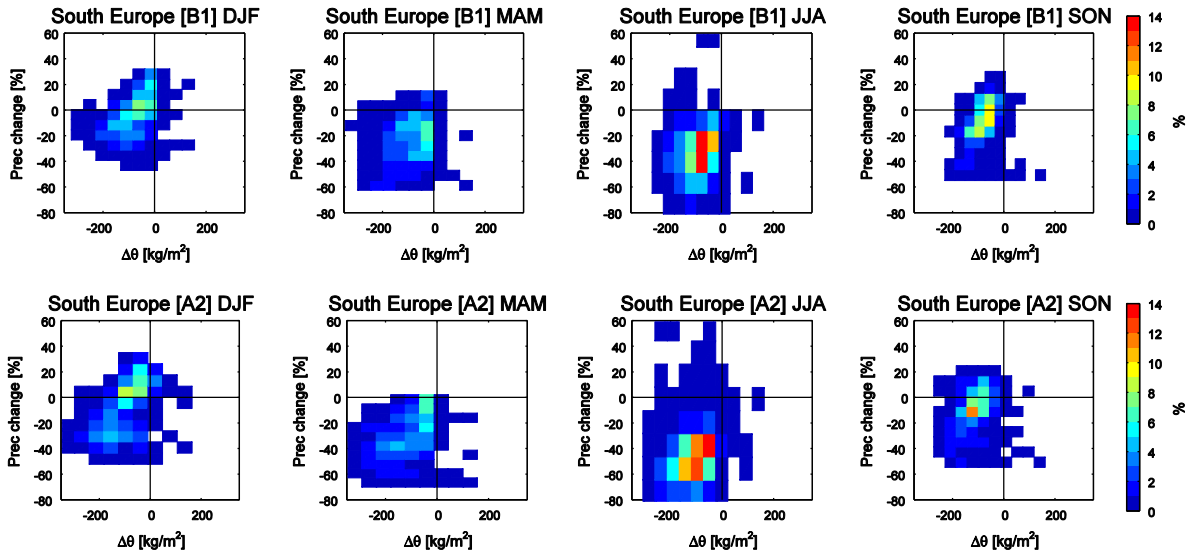

Figure 5.20: As Figure 5.18, but for soil moisture. Only south Europe is presented.

5.5.1 Soil moisture-precipitation feedback

For a given regime of precipitation residence time of soil moisture depends on soil texture class (Balsamo et al., 2009). Four layers in HTESSEL have time scales differents ranging from one day (first layer) to several months (fourth layer). The first layer represents the diurnal cycle, the second layer represents variations between one day and one week, the third layer represents variation between one week and one month, while the fourth layer represents variation with time scales larger than one month (Viterbo and Beljaars, 1995). Time scales of interaction with the layer above and the layer below depend on the soil depth, soil type, hydraulic conductivity and diffusivity, and soil water contents of each layer (Balsamo et al., 2009).

Persistence of soil moisture anomalies can contribute to long-term atmospheric variability over land. The surface climate is closely connected to soil moisture in both prior and lag correlation analyses. It is obvious that there are close correlations among soil moisture, air temperature and precipitation for both preceding and lagged (Orth and Seneviratne, 2014). Dry soil moisture conditions are induced by evapotranspiration deficits (Della-Marta et al., 2007; Vautard et al., 2007), or evapotranspiration excess (Black and Sutton, 2007; Fischer et al., 2007), or a combination of both (Seneviratne et al., 2010) This amplification of soil moisture–temperature feedbacks is suggested to have partly enhanced the duration of extreme summer heat waves in southeastern Europe during the latter part of the 20th century (Hirschi et al., 2011), with evidence emerging of a signature in other moisture-limited regions (Mueller and Seneviratne, 2012). Cross-correlation, that measures the synchronous or lagged relationships, is calculated between soil moisture anomalies in May and precipitation anomalies in Summer (JJA) over Europe, Figure 5.21 cross-correlation analysis shows distinctively positive correlated regions with absolute values in some areas greater than 0.4 during May. Positive correlations suggest that soil moisture anomalies in late spring can affect precipitation anomalies in the subsequent months in the warm season. The cross-correlation between soil moisture anomalies in May and precipitation anomalies during the Summer (JJA) shows two distinct regions in future scenarios: northern Europe and Mediterranean (Figure 5.21). Low correlation in northern Europe reveals that soil moisture does not control subsequent precipitation (wet soil moisture regime or energy limited). Positive correlations in Mediterranean and Eastern Europe suggests that soil moisture anomalies can affect precipitation anomalies in subsequent months, especially for dry soil moisture regimes.

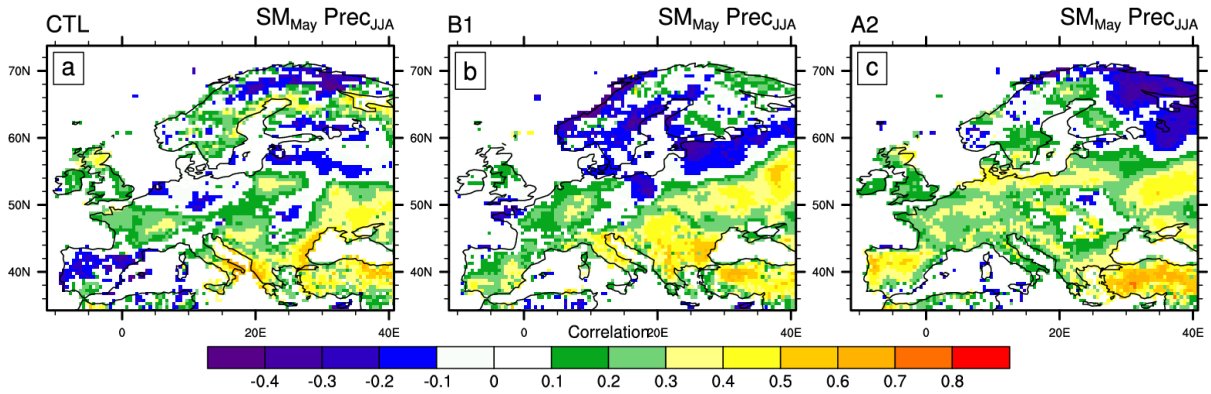

Figure 5.21: Cross-correlation coefficients between May soil moisture anomalies and JJA precipitation anomalies over Europe for present (left column), B1 (middle column) and A2 (right column) scenarios.

Soil moisture anomalies in the future could be reduced significantly for the period 2071 to 2100 compared to the reference period (Figure 5.22). Changes in northern Europe soil moisture are relatively small, but represent a future increase of SM in the future. On the other hand, in central and southern Europe the climate would be drier, causing a significant reduction of soil water content (see soil moisture anomalies in Figure 5.25). This reduction is particularly large during the end of 21st century. There is an increase in the duration of drought periods with greater intensity in southern Europe (see soil moisture anomalies in Figure 5.25), with possible consequences on water resources in summer.

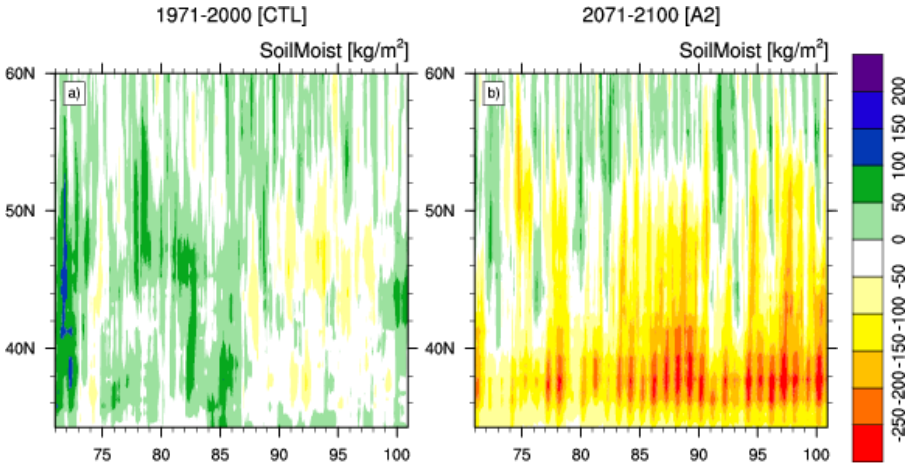

Figure 5.22: Zonal average of soil moisture anomalies over Europe for: a) control, b) A2 scenario. Blue and red values correspond to drought and flood events, respectively. Units are in kg m^{-2}.

5.5.2 Present and future evapotranspiration and total runoff over Europe

In addition to precipitation and soil moisture, it is important to study the future variation of air temperature, evapotranspiration and total runoff over Europe. Runoff production depends on the quantity of precipitation and the antecedent soil moisture. Areas with the highest increase in precipitation will correspond to the areas with the highest increase of runoff. Unrealistic values of super-saturation air surface humidity were filtered out (see section 3.5 in Chapter 3).

Air temperature anomalies over Europe are expected to increase about 2 ºC [5ºC] under B1 [A2] scenarios (Figure 5.23).

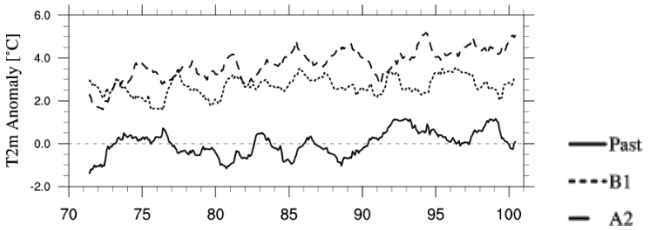

Figure 5.23: 12-month running average of anomalies of air temperature over Europe during [1971-2000], past (solid line) and [2071-2100]: B1 and A2 scenarios (dotted and dashed lines, respectively).

Future projections of precipitation have large interannual variations. These annual fluctuations are accompanied by changes in other components of the hydrological cycle: evapotranspiration, total runoff and soil moisture. The 12-month running average of the main surface water cycle components anomalies (precipitation, evapotranspiration, total runoff and soil moisture) are shown in Figure 5.24.

Soil moisture is removed from soil faster than it can be added by precipitation, soil moisture reaches less 100 kg m^{-2} (negative anomalies), causing a drying of the soil (Figure 5.25, panels a and d) and much larger interannual variation, with possible consequences on availability of fresh water in a future climate.

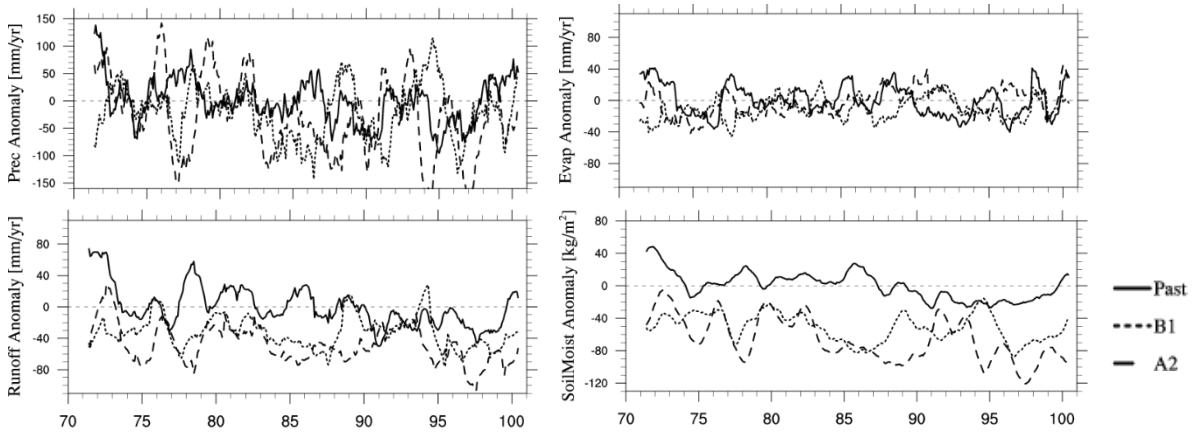

Figure 5.24: Running average of anomalies of precipitation, evapotranspiration, total runoff and soil moisture over Europe, with respect to [1971-2000] average, during [1971-2000] (solid line), [2071-2100] A2 scenarios (dashed line) and [2071-2100] B1 scenarios (dotted line).

Differences between northern and southern Europe are clear: increased precipitation, offset by increased evapotranspiration in northern Europe; and, reduction of rainfall and subsequent reduction of water content in the soil in the south (Figure 5.25 and Figure 5.22).

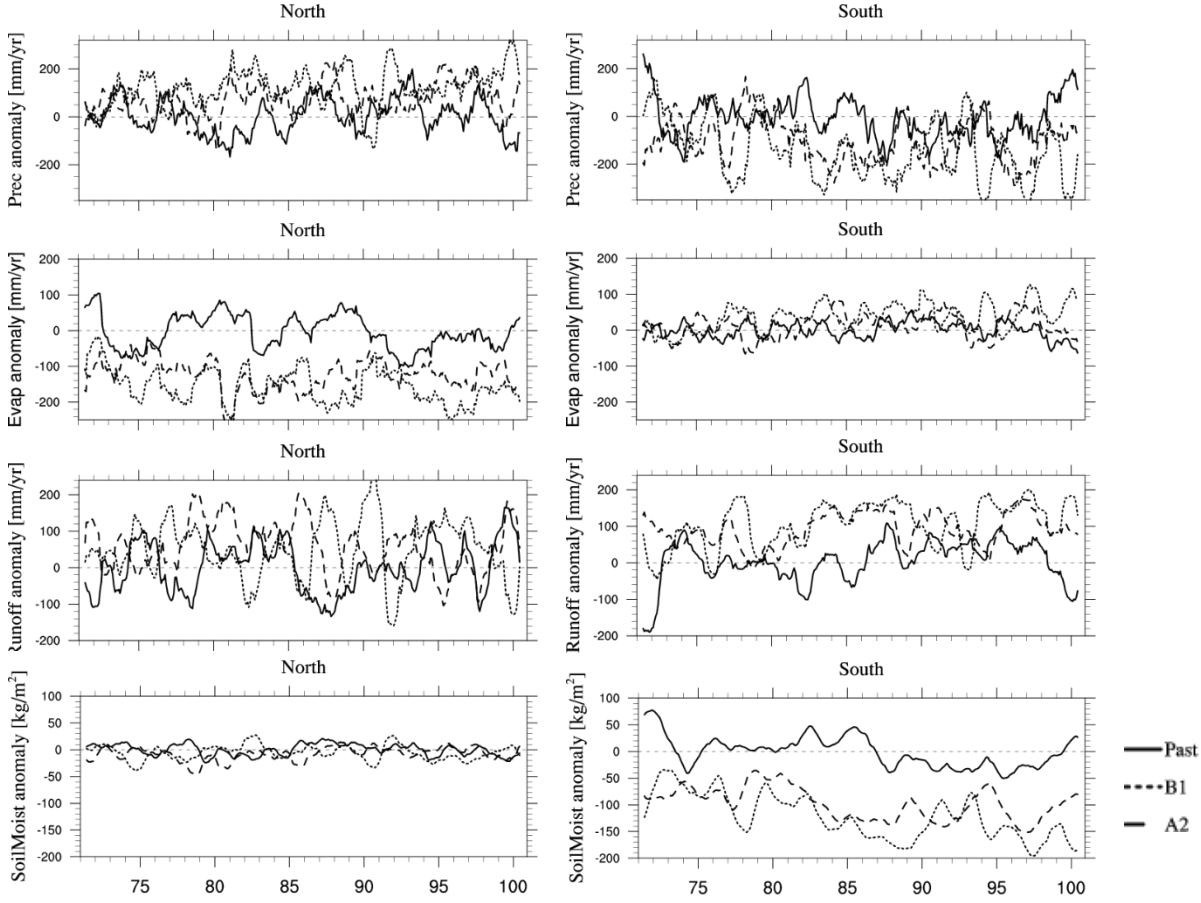

Figure 5.25: As Figure 5.24, but for northern and southern Europe.

5.6 Global patterns of changing extremes

Several examples have been shown in this chapter on future changes in global average temperature and patterns of annual average precipitation. In this section we will explore changes in frequency and intensity of climatic extremes, limiting the analysis to precipitation extremes. The assessment of extremes can be done by examining the amplitude, frequency and persistence of daily maximum and minimum temperature, daily precipitation intensity and frequency, seasonal mean temperature and precipitation, as presented in previous sections. For precipitation, the assessment can be done either in terms of return periods or extremely high rate of precipitation.

Since the mid-20th century the warming has led to changes in temperature extremes; heavy precipitation has probably also increased over this time but vary by region (Hartmann et al., 2013). In future decades, extreme events are very likely to be more frequent and intense (Solomon et al., 2007; Hartmann et al., 2013). The frequency of hydrological extreme events will further increase, together with changes in regional water and heat balances.

To define probabilities of future occurrences of extreme events the frequency analysis is applied. This technique fits a probability distribution to a series of observations. Analysis of extremes is based on the Generalized Extreme Value (GEV) theory. GEV functions were calculated for the baseline period [1971-2000] and for future periods [2001-2100]. Precipitation data used were given by HTESSEL simulation for baseline and future [2071-2100] under two SRES scenarios (B1 and A2) from ECHAM simulation.

5.6.1 Precipitation extremes

Precipitation in the future may decrease in one season and increase in another, while temperature is expected to increase during all seasons (see Figure 5.1). However, extreme precipitation events will become more common, responding to global warming (Trenberth et al. 2003; Allan and Soden, 2008). Extreme precipitation is related to increases in moisture contents; nonlinearity of the Clausious-Clapeyron equation means that the relative increase in precipitation is larger than the relative increase in the temperature; this effect is larger for extreme precipitation (e.g., Allen and Ingram, 2002).

There are several studies using different data sources that reveal uncertainty in precipitation (Sun et al., 2006; Allan and Soden, 2008; Dai, 2006; O'Gorman and Schneider, 2009). Precipitation intensity will increase particularly in tropical and high-latitudes areas, in contrast to mid-continental areas during summer, where drought events will increase. In most tropical and mid- and high-latitudes areas, increase of precipitation extremes is larger than increase on mean precipitation (Bates et al., 2008). There are likely more land regions where the number of heavy precipitation events has increased than where it has decreased. The frequency or intensity of heavy precipitation events has likely increased in North America and Europe. In other continents, confidence in changes in heavy precipitation events is at most medium (Hartmann et al., 2013). Extreme precipitation events over most of the mid-latitude land masses and over wet tropical regions will become more intense and more frequent by the end of this century, as global mean surface temperature increases (Boucher et al., 2013; Collins et al., 2013).

One way to measure the extreme precipitation is the 99.9th percentile of precipitation (O'Gorman and Schneider, 2009). Cumulative probability of precipitation at 99.9th percentile was calculated for [1971-2000] baseline and future scenarios, [2071-2100]. There is a large variation, particularly in the tropics due to the magnitude of precipitation (zonal average in Figure 5.26b). Nevertheless, extreme precipitation is comparable in magnitude in the present and future scenarios. The most significant differences are located in the tropical rain belt (15ºS to 15ºN). The magnitude of precipitation in the control period (20C3M) is similar to the corresponding values computed using monthly observations, except in low latitudes (not shown). Zonal average of annual maximum of precipitation in present climate and future scenarios (Figure 5.26a) is based on daily precipitation data from HTESSEL simulation and observed precipitation, GPCC and CRU monthly data bases. Observed and simulated precipitation time series have similar patterns: higher values at tropical zones and lower precipitation at boreal zones.

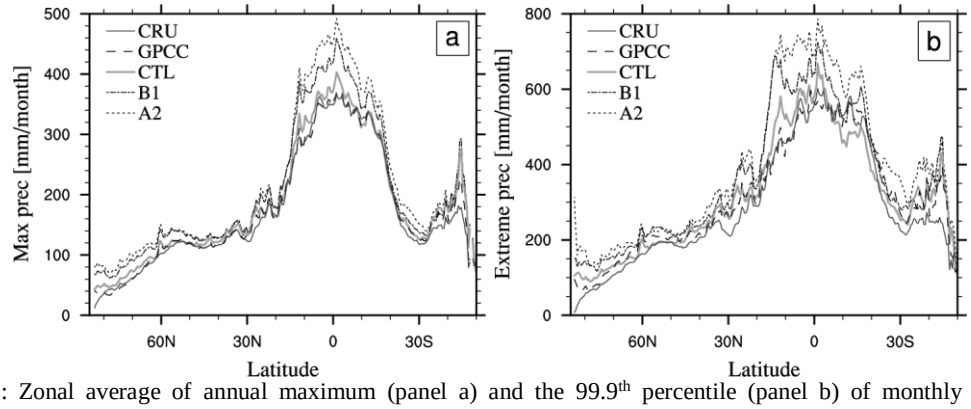

Figure 5.26: Zonal average of annual maximum (panel a) and the 99.9th percentile (panel b) of monthly precipitation (millimetres per month) for the period control [1971-2000] (red), and [2071-2100] for B1 (red) and A2 (blue) scenarios. Only land points.

5.6.2 Precipitation return periods

Average recurrence periods, also known as return periods, are a simple way to assess extreme events in natural phenomena. Return periods are used to estimate both magnitude and frequency of extreme events occurrence. Return levels maps are a common tool used to assess a location's potential for extreme precipitation. The n-return level is the amount exceeded on average once every n years. The n-th year return level is the level which one expects the annual maximum to exceed with probability p = 1/n. For example, a 100-yr return level is expected to be equalled or exceeded every 100 years on average, e.g. a 100 year flood event. This event has a 1% probability of occurring in any given year. The pattern scaling method was applied to the simulation data to obtain the normalized change values for the following extreme precipitation events in terms of their 100-yr return period (Figure 5.27). Extreme events of precipitation will increase. This will be particularly pronounced in tropical and high-latitude region, which are also expected to experience overall increases in precipitation. The late 21st century 100-year return values of maximum precipitation (Figure 5.27a and b) are expected to become more intense.

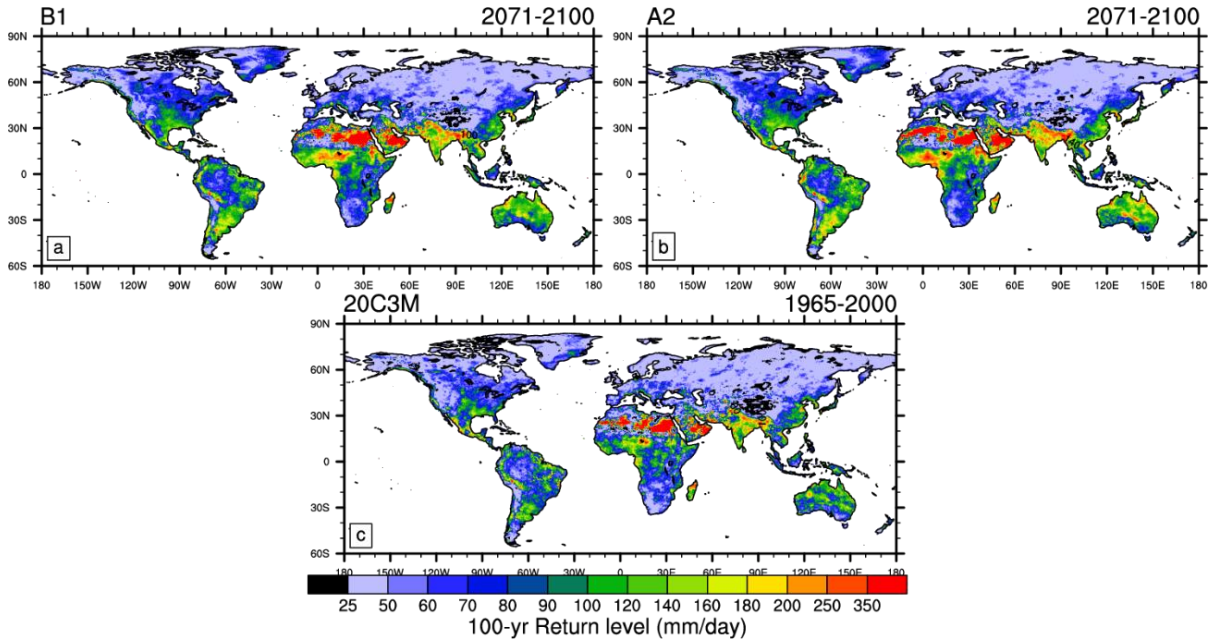

Figure 5.27: 100-yr precipitation return period estimates for B1, A2 scenarios and control period from the fitted GEV distribution. Units are in millimetres per day.

5.7 Conclusions

Global simulations of hydrological cycle were obtained from HTESSEL simulations, forced with ECHAM5/MPIOM global circulation model output. The GCM used to force HTESSEL were run assuming IPCC B1 and A2 emission scenarios. SRES B1 is closer to RCP4.5 in AR5 and RCP8.5 is somewhat higher than A2 in 2100 and close to the SRES A1F1 scenario.

Analysis was based on monthly mean results. For the assessment of changes in global air temperature, precipitation, total runoff and soil moisture, simulations of HTESSEL from the [1971-2000] control period were compared to simulations for the [2071-2100] time interval.

Time series of global temperature and precipitation standardized anomalies were analysed since 1965 to 2100 for B1 and A2 scenarios. The global mean temperature will increase rapidly from 2060 to 2100 reaching about 4 (2) STD warmer than climatology under A2 (B1) scenario. Northern latitudes will warm more (by 6-8 ºC in the SRES A2 scenario) than the southern hemisphere. Both emission paths show the same pattern of warming displayed in the SRES A2 scenario. SRES B1 path, more moderate and optimist, displays only about half of the warming of A2.

Precipitation and total runoff were also compared: increase/decrease in precipitation correspond to increase/decrease in runoff. Mid-latitude regions like southern Europe, and subtropical regions are expected to be drier due to precipitation decrease. The largest percentage changes are at the high latitudes, some dry and semi-arid zones in mid-latitudes, and most subtropical land regions. Mean soil moisture changes decrease in the subtropics and Mediterranean region and increase in east Africa and central Asia.

Future variability of precipitation and soil moisture was evaluated focusing on Europe. Precipitation will increase in the North and reduce in the South at all seasons. In Central Europe precipitation will increase during winter (DJF) and slightly decrease in summer. Changes in precipitation will contribute to a slight increase in soil moisture at north and a significant reduction in central and southern Europe (about 150 mm in southern Europe). Soil moisture-precipitation feedback were investigated over Europe. The influence of soil moisture anomalies on precipitation were assessed. In northern Europe late Spring soil moisture does not control Summer precipitation (energy limited soil moisture regime), while late Spring soil moisture anomalies in Mediterranean and Eastern Europe affect summer precipitation anomalies (water limited soil moisture regime).

Finally, there was a brief assessment of extreme events in the future. The occurrence of more intense precipitation will increase both the moderate scenario (B1) and the more pessimistic (A2). For the current climate, frequency or intensity of heavy precipitation in North America and Europe has been increasing with some seasonal and regional variation.

Chapter 6 - Final Discussion and Conclusions

This thesis was mainly focused on the WATCH EU project, contributing: i) to develop the WATCH Forcing Data; ii) to develop appropriate methodologies to disaggregate daily weather data into subdaily; iii) to produce the necessary data with LSM HTESSEL; and iv) to estimate continental surface water and energy budgets in the XX and XXI centuries, together with error evaluation. The main purpose was to characterize the terrestrial hydrological and surface energy cycles in past and future climates using Land Surface and Global terrestrial Hydrological Models, contributing to a better knowledge of the role of global continental surface.

In Chapter 2 and Chapter 3 development of meteorological and a daily disaggregator method was presented and evaluated. Subsequent chapters (4 and 5) assessed the hydrological and energy cycles on present and future scenarios, respectively. Furthermore, Chapter 4 evaluated results uncertainty due to the choice of type of model (LSM or GHM) and perturbations in meteorological forcing. European drought during second part of XX century was also analysed using a multi-model ensemble. Finally, in Chapter 5, global maps and time series were constructed to identify regions where water and associated water resources are significantly impacted by climate change, and the regions that are vulnerable to these changes. Projections of terrestrial components of hydrological and energy cycle were also evaluated, focusing on the time period of 2071-2100 and compared to 1971-2000 period.

6.1 General Conclusions

Several methodologies to support the creation of the meteorological forcing data and its application in global hydrological models were indicated in this thesis. The analysis was focused on surface water and energy balance, allowing a better knowledge of continental surface as well as limitations of methodologies, available data and/or surface modelling.

The WFD, described in Chapter 2 and Chapter 3, is a meteorological data at subdaily, regularly gridded, half-degree resolution, covering the period 1901-2001, ERA-40 reanalysis based, required to drive hydrological models (land surface and global hydrological models). In In Chapter 2 only precipitation (rainfall and snowfall rate) was described. Other variables (wind speed, air temperature, surface pressure, specific humidity, downward longwave radiation flux and downward shortwave radiation flux) were described by Weedon et al. (2010, 2011).

Bias errors and wet days were corrected to match CRU and GPCC global monthly observations. A method for suppression of wet days was created to correct ERA-40 precipitation overestimation (too many wet days) in the tropics and mid-latitudes; the final results matches the CRU number of wet days in a month. Only smallest daily totals were reset, retaining the spatial continuity and coherence of significant (non-drizzle) frontal precipitation across grid boxes. No wet day was created, avoiding the need to artificially modify downward shortwave, specific humidity, or 2-m temperature. No attempt has been made to modify the other meteorological variables when wet days were removed. Monthly bias correction of precipitation consists on scaling of monthly totals to match GPCC (or CRU) monthly precipitation, minimizing the discrepancies between monthly observations and reanalysis. With small monthly precipitation values in the reanalysis and larger observed values, the necessary bias correction is added every 3 hours to bridge the gap; this procedure can induce spurious drizzle. Fortunately from the point of view of hydrological modelling this low level background precipitation is not significant. Occasionally, adjustment of monthly precipitation totals imply high precipitation rates. To avoid these "outliers" the corresponding 99.999 % lognormal probability precipitation rate replaced the precipitation rates. The adjustment of wind-induced undercatch and wetting losses for global gridded precipitation products were applied using monthly catch ratios. These adjustments accounted for the effects of the effects of wind-induced undercatch of liquid and solid precipitation and wetting losses on monthly means. In general, CRs increase rainfall and snowfall rates, except in Rocky Mountains during cold season. Adam and Lettenmaier (2003) obtained a net increase of 11.7% in global terrestrial mean annual precipitation after catch ratio correction.

WFD on reanalysis period, 1958-2001, (Chapter 2) provided a good representation of the real meteorological events, synoptic activity, and climate trends. The first period, 1901-1957, (Chapter 3) was constructed reordering the ERA-40 and correcting with global monthly observations. This period has similar subdaily to seasonal statistical characteristics but they do not represent particular historical events.

Despite the existence of a more recent reanalysis, ERA-Interim, all the work was based on the ERA-40. Subsequently, a new meteorological forcing was developed, WFDEI. WFDEI meteorological forcing dataset has been generated using the same methodology as the widely used WFD, but making use of the ERA-Interim reanalysis data (Weedon et al. 2014). ERA-I is available on the same spatial resolution but covering 1978-2012. This new database complements WFD, providing a better temporal covering than WFD original. Several bugs were corrected when producing WFDEI, including the artificial drizzle problem described above.

In Chapter 3, a daily disaggregation method (DDM) was developed, tested with WFD data and applied to disaggregate the meteorological forcing data of daily projections from GCM on Chapter 5. This section had the following objectives: (1) to assess and evaluate daily weather data disaggregation methods, and (2) to develop appropriate methodologies to disaggregate daily data into 3-hourly data. Application of disaggregated data to force HTESSEL was useful to assess implications on subsequent hydrological and assess the quality of model results. DDM method plays a key role in the quality of LSM simulations, which need to be forced with subdaily data (3h or 1h, preferably), unlike GHMs. Knowledge of weaknesses of the method is essential for the analysis of the results in Chapter 5.

Results indicated that the model reproduced air temperature data well in most cases, with the notable exception of boreal winter. These results are related to differences in Tair/Qair method during cold season where air temperature does not have a pronounced diurnal cycle. Overall, the main driver of the forcing data used was the precipitation, especially for Mediterranean and Wet Tropical climate. 3h-air temperature, disaggregated by a cosine function, with interpolated linearly pressure and relative humidity were then used to calculate specific humidity. This method maintains consistency between variables and also avoids supersaturation.

The intercomparison experiment performed in Chapter 4 quantified inter-model differences in response to prescribed atmospheric forcing, and demonstrated the impact on continental hydrological cycle. 30-yr simulation results from a multi-model ensemble, 2 land surface and 4 global hydrological models, quantified the global hydrological cycle over land: precipitation, 880±64 mm/yr (127 000 km^3/yr); evapotranspiration, 510±95 mm/yr (73,000 km^3/yr); and total runoff is 368±53 mm/yr (53,000 km^3/yr). This study demonstrated a large range in global water flux and storage terms: global precipitation over land ranges between 837 to 917 mm/yr; evapotranspiration ranges from 497 to 523 mm/yr; and total runoff ranges from 331 to 395 mm/yr. Interannual variability was also assessed. The interannual variation in multimodel mean predicted global runoff is much larger. Values are reasonably close to Trenberth et al. (2007), given the different time periods considered: precipitation as 113,000 km^3/yr, 73,000 km^3/yr of evapotranspiration, and 40,000 km^3/yr of total runoff. No major differences have been found between the models ran at daily or subdaily time steps or between models using different evapotranspiration or runoff schemes.

The terrestrial energy balance over land from 1985 to 1999 was also quantified on Chapter 4. The global net surface radiation is 69.9 Wm^{-2}, from which 23.5 Wm^{-2} is lost to the atmosphere as sensible heat flux and 45.8 Wm^{-2} as latent heat flux. To analyse the sensitivity of LSM to meteorological forcing and physical processes, HTESSEL was driven by a set of perturbed forcing data (temperature, precipitation, wind and radiation) and with different parameterizations (hydrology and carbon). ERA-40 surface balance energy components presented by Trenberth et al. (2009) are reasonable close to WFD, ERA-40 based, except latent heat flux. Independently, Trenberth et al. (2009) values, estimated from Mar 2000 to May 2004, were quite different. For the net radiation, Rnet, the result was 65.5 W, whereas WFD was 69.9 Wm^{-2}. Latent heat flux results were 38.5 and 45.8 (Trenberth and WFD, respectively). For the sensible heat flux, Trenberth estimated 27.0 and WFD is 23.5 Wm^{-2}. Results of sensible heat flux tests

showed that air temperature, aerosols and carbon parameterization are crucial for a good estimation of surface energy budget.

The WATCH Driving Data for the current century, used to drive HTESSEL simulations on Chapter 5, is similar to the WFD but for the 21st century and was constructed from model output instead of interpolated observational data. Two climate scenarios, B1, A2 and a Control were each run through three global GCMs to produce a total of 9 sets of future driving data at 0.5 degree resolution. Due to space and time limitations, the uncertainties due to choice of GCM (ECHAM5/MPIOM, CNRM-CM3 or LMDZ-4) and GHM (WaterMIP models) results were not assessed. To ensure data quality, results were compared with IPCC reports of 2007 and 2013 (AR4 and AR5, respectively). Global land surface temperature show a warming of 2 ºC to 4 ºC at the end of present century, for SRES B1 and A2. Multi-model mean land surface air temperature anomalies are 2.4 ± 0.6 and 4.8± 0.9 ºC (2081-2100), for RCP4.5 and RCP8.5, closer to B1 and A2, respectively (table 12.2 in Collins et al., 2013).Land precipitation will also change. Annual mean precipitation in high latitudes and many mid-latitudes wet regions will increase late in the 21st century, while in many mid-latitudes and subtropical dry regions the mean precipitation will decrease. By the end of this century extreme precipitation events over most the mid-latitudes and over wet tropical regions will become more intense and more frequent, as the mean surface temperature increases. Soil moisture projections in Europe will also dry in the Mediterranean, consistent with projection changes in mean precipitation.

6.2 Recommendations for Future Work

The thesis allowed an assessment of development and application of meteorological data to drive hydrological and land surface models on present and future climate. Nevertheless, there is uncertainty associated with the meteorological forcing and surface modelling. In this thesis several components of the uncertainty were analysed, but there is room for the improvement in the next few years. The following recommendations are suggested for future work to improve the assessment.

Supporting tools for temporal downscale should be improved (e.g. air temperature and moisture in winter polar areas in DDM method). Temporal downscale tools from monthly to daily data (GLM model) and from daily to hourly data (DDM method) can be further improved and tested with several datasets (observations available at monthly or daily scale and/or output of climatic models). The application of DDM and GLM here detailed for disaggregating daily and monthly data may be carried out also with seasonal forecast. Such an application could provide the water and energy balance at the surface at spatial scales and with an unprecedented level of detail.

In WaterMIP ensemble more models should be used to generate an ensemble of models that represent the actual energy and water cycles. Future climate should be also assessed by many other GCM results available in present and future scenarios. There are other model results available in the WATCH project web site that should be used in future work and compared with HTESSEL results. This assessment of the uncertainties due to the choice of GCM and/or GHM could contribute to reduce the uncertainties in hydrological climate projections.

As ERA-I reanalysis continues to be updated in near-real time, WFDEI could be updated in the near future. A system to obtain, as soon as the latest ERA-I month is ready, a planetary hydrological estimate of the energy and water cycles at the surface is computed, will help national hydrological and meteorological services in their monthly assessment of water resources. More thorough comparisons of hydrological and Earth System model output with hydrologically- and phenologically-relevant satellite products would increase confidence on results presented here and encourage further models to use WFDEI dataset.

Finally, further study and comparison with more observed climate data (i.e. more stations and over a longer period) and other data, such as satellite data, are needed to assure a better quantification of energy and hydrological surface.

References

Adam, J. C., and D. P. Lettenmaier, 2003: Adjustment of global gridded precipitation for systematic bias. *Journal of Geophysical Research: Atmospheres*, **108,** 4257, doi:10.1029/2002JD002499.

Adam, J. C., E. A. Clark, D. P. Lettenmaier, and E. F. Wood, 2006: Correction of Global Precipitation Products for Orographic Effects. *Journal of Climate*, **19,** 15-38, doi:10.1175/JCLI3604.1.

Albergel, C., J. C. Calvet, A. L. Gibelin, S. Lafont, J. L. Roujean, C. Berne, O. Traullé, and N. Fritz, 2010: Observed and modelled ecosystem respiration and gross primary production of a grassland in southwestern France. *Biogeosciences*, **7,** 1657-1668, doi:10.5194/bg-7-1657-2010.

Allan, R. P., and B. J. Soden, 2008: Atmospheric Warming and the Amplification of Precipitation Extremes. *Science*, **321,** 1481-1484, doi:10.1126/science.1160787.

Allen, M. R., and W. J. Ingram, 2002: Constraints on future changes in climate and the hydrologic cycle. *Nature*, **419,** 224-232.

Allen, R. G., L. S. Pereira, D. Raes, and M. Smith, 1998: Crop evapotranspiration - Guidelines for computing crop water requirements - FAO Irrigation and drainage paper 56FAO, Rome.

Baldocchi, D., E. Falge, L. Gu, R. Olson, D. Hollinger, S. Running, P. Anthoni, C. Bernhofer, K. Davis, R. Evans, J. Fuentes, A. Goldstein, G. Katul, B. Law, X. Lee, Y. Malhi, T. Meyers, W. Munger, W. Oechel, K. T. Paw, K. Pilegaard, H. P. Schmid, R. Valentini, S. Verma, T. Vesala, K. Wilson, and S. Wofsy, 2001: FLUXNET: A New Tool to Study the Temporal and Spatial Variability of Ecosystem–Scale Carbon Dioxide, Water Vapor, and Energy Flux Densities. *Bulletin of the American Meteorological Society*, **82,** 2415-2434, doi:10.1175/1520-0477(2001)082<2415:FANTTS>2.3.CO;2.

Balsamo, G., F. Pappenberger, E. Dutra, P. Viterbo, and B. van den Hurk, 2011: A revised land hydrology in the ECMWF model: a step towards daily water flux prediction in a fully-closed water cycle. *Hydrological Processes*, **25,** 1046-1054, doi:10.1002/hyp.7808.

Balsamo, G., S. Boussetta, E. Dutra, A. Beljaars, P. Viterbo, and B. Van den Hurk, 2011: Evolution of land surface processes in the IFS, ECMWF Newsletter, 127, 17-22 pp.

Balsamo, G., A. Beljaars, K. Scipal, P. Viterbo, B. van den Hurk, M. Hirschi, and A. K. Betts, 2009: A Revised Hydrology for the ECMWF Model: Verification from Field Site to Terrestrial Water Storage and Impact in the Integrated Forecast System. *Journal of Hydrometeorology*, **10,** 623-643, doi:10.1175/2008JHM1068.1.

Bates, B. C., Z. W. Kundzewicz, S. Wu, and J. P. Palutikof, 2008: Climate change and water., Technical Paper, IV, Intergovernmental Panel on Climate Change, Geneva, 210 pp.

Berg, A. A., J. S. Famiglietti, J. P. Walker, and P. R. Houser, 2003: Impact of bias correction to reanalysis products on simulations of North American soil moisture and hydrological fluxes. *Journal of Geophysical Research: Atmospheres*, **108,** 4490, doi:10.1029/2002JD003334.

Betts, A. K., S.-Y. Hong, and H.-L. Pan, 1996: Comparison of NCEP-NCAR Reanalysis with 1987 FIFE Data. *Monthly Weather Review*, **124,** 1480-1498, doi:10.1175/1520-0493(1996)124<1480:CONNRW>2.0.CO;2.

Betts, A. K., P. Viterbo, and A. C. M. Beljaars, 1998: Comparison of the Land-Surface Interaction in the ECMWF Reanalysis Model with the 1987 FIFE Data. *Monthly Weather Review*, **126,** 186-198, doi:10.1175/1520-0493(1998)126<0186:COTLSI>2.0.CO;2.

Betts, A. K., P. Viterbo, and E. Wood, 1998: Surface Energy and Water Balance for the Arkansas–Red River Basin from the ECMWF Reanalysis. *Journal of Climate*, **11,** 2881-2897, doi:10.1175/1520-0442(1998)011<2881:SEAWBF>2.0.CO;2.

Betts, A. K., J. H. Ball, and P. Viterbo, 2003: Evaluation of the ERA-40 Surface Water Budget and Surface Temperature for the Mackenzie River Basin. *Journal of Hydrometeorology*, **4,** 1194-1211, doi:10.1175/1525-7541(2003)004<1194:EOTESW>2.0.CO;2.

Betts, A. K., J. H. Ball, M. Bosilovich, P. Viterbo, Y. Zhang, and W. B. Rossow, 2003: Intercomparison of water and energy budgets for five Mississippi subbasins between ECMWF reanalysis (ERA-40) and NASA Data Assimilation Office fvGCM for 1990–1999. *Journal of Geophysical Research: Atmospheres*, **108,** 8618, doi:10.1029/2002JD003127.

Betts, A. K., P. Viterbo, A. Beljaars, H.-L. Pan, S.-Y. Hong, M. Goulden, and S. Wofsy, 1998: Evaluation of land-surface interaction in ECMWF and NCEP/NCAR reanalysis models over grassland (FIFE) and boreal forest (BOREAS). *Journal of Geophysical Research: Atmospheres*, **103,** 23079-23085, doi:10.1029/98JD02023.

Black, E., and R. Sutton, 2007: The influence of oceanic conditions on the hot European summer of 2003. *Clim Dyn*, **28,** 53-66, doi:10.1007/s00382-006-0179-8.

Boberg, F., and J. H. Christensen, 2012: Overestimation of Mediterranean summer temperature projections due to model deficiencies. *Nature Clim. Change*, **2,** 433-436, doi:http://www.nature.com/nclimate/journal/v2/n6/abs/nclimate1454.html#supplementary-information.

Boé, J., and L. Terray, 2008: Uncertainties in summer evapotranspiration changes over Europe and implications for regional climate change. *Geophysical Research Letters*, **35,** L05702, doi:10.1029/2007GL032417.

Boone, A., F. Habets, J. Noilhan, D. Clark, P. Dirmeyer, S. Fox, Y. Gusev, I. Haddeland, R. Koster, D. Lohmann, S. Mahanama, K. Mitchell, O. Nasonova, G. Y. Niu, A. Pitman, J. Polcher, A. B. Shmakin, K. Tanaka, B. van den Hurk, S. Vérant, D. Verseghy, P. Viterbo, and Z. L. Yang, 2004: The Rhône-Aggregation Land Surface Scheme Intercomparison Project: An Overview. *Journal of Climate*, **17,** 187-208, doi:10.1175/1520-0442(2004)017<0187:TRLSSI>2.0.CO;2.

Boone, A., B. Decharme, F. Guichard, P. de Rosnay, G. Balsamo, A. Beljaars, F. Chopin, T. Orgeval, J. Polcher, C. Delire, A. Ducharne, S. Gascoin, M. Grippa, L. Jarlan, L. Kergoat, E. Mougin, Y. Gusev, O. Nasonova, P. Harris, C. Taylor, A. Norgaard, I. Sandholt, C. Ottlé, I. Poccard-Leclercq, S. Saux-Picart, and Y. Xue, 2009: The AMMA Land Surface Model Intercomparison Project (ALMIP). *Bulletin of the American Meteorological Society*, **90,** 1865-1880, doi:10.1175/2009BAMS2786.1.

Boucher, O., D. Randall, P. Artaxo, C. Bretherton, G. Feingold, P. Forster, V.-M. Kerminen, Y. Kondo, H. Liao, U. Lohmann, P. Rasch, S. K. Satheesh, S. Sherwood, B. Stevens, and X. Y. Zhang, 2013: Clouds and Aerosols. *Climate Change 2013: The Physical Science Basis. Contribution of Working Group I to the Fifth Assessment Report of the Intergovernmental Panel on Climate Change*, T. F. Stocker, D. Qin, G.-K. Plattner, M. Tignor, S. K. Allen, J. Boschung, A. Nauels, Y. Xia, V. Bex, and P. M. Midgley, Eds., Cambridge University Press.

Boussetta, S., G. Balsamo, A. Beljaars, A.-A. Panareda, J.-C. Calvet, C. Jacobs, B. van den Hurk, P. Viterbo, S. Lafont, E. Dutra, L. Jarlan, M. Balzarolo, D. Papale, and G. van der Werf, 2013: Natural land carbon dioxide exchanges in the ECMWF integrated forecasting system: Implementation and offline validation. *Journal of Geophysical Research: Atmospheres*, **118,** 5923-5946, doi:10.1002/jgrd.50488.

Calvet, J.-C., 2000: Investigating soil and atmospheric plant water stress using physiological and micrometeorological data. *Agricultural and Forest Meteorology*, **103,** 229-247, doi:http://dx.doi.org/10.1016/S0168-1923(00)00130-1.

Calvet, J.-C., and J.-F. Soussana, 2001: Modelling CO_2-enrichment effects using an interactive vegetation SVAT scheme. *Agricultural and Forest Meteorology*, **108,** 129-152, doi:http://dx.doi.org/10.1016/S0168-1923(01)00235-0.

Calvet, J.-C., V. Rivalland, C. Picon-Cochard, and J.-M. Guehl, 2004: Modelling forest transpiration and CO_2 fluxes—response to soil moisture stress. *Agricultural and Forest Meteorology*, **124,** 143-156, doi:http://dx.doi.org/10.1016/j.agrformet.2004.01.007.

Calvet, J.-C., J. Noilhan, J.-L. Roujean, P. Bessemoulin, M. Cabelguenne, A. Olioso, and J.-P. Wigneron, 1998: An interactive vegetation SVAT model tested against data from six contrasting sites. *Agricultural and Forest Meteorology*, **92,** 73-95, doi:http://dx.doi.org/10.1016/S0168-1923(98)00091-4.

Chahine, M. T., 1992: The hydrological cycle and its influence on climate. *Nature*, **359,** 373-380.

Chandler, R. E., 2005: On the use of generalized linear models for interpreting climate variability. *Environmetrics*, **16,** 699-715, doi:10.1002/env.731.

Chandler, R. E., and H. S. Wheater, 2002: Analysis of rainfall variability using generalized linear models: A case study from the west of Ireland. *Water Resources Research*, **38,** 1192, doi:10.1029/2001WR000906.

Chaney, N. W., J. Sheffield, G. Villarini, and E. F. Wood, 2014: Development of a High-Resolution Gridded Daily Meteorological Dataset over Sub-Saharan Africa: Spatial Analysis of Trends in Climate Extremes. *Journal of Climate*, **27,** 5815-5835, doi:10.1175/JCLI-D-13-00423.1.

Chen, C., S. Hagemann, D. Clark, S. Folwell, S. Gosling, I. Haddeland, N. Hanasaki, J. Heinke, F. Ludwig, and F. Voβ 2011: Evaluation of projected hydrological changes in the 21st century obtained from a multi-model ensemble., Technical Report WATCH, 45, 41 pp.

Cho, H.-K., K. P. Bowman, and G. R. North, 2004: A Comparison of Gamma and Lognormal Distributions for Characterizing Satellite Rain Rates from the Tropical Rainfall Measuring Mission. *Journal of Applied Meteorology*, **43,** 1586-1597, doi:10.1175/JAM2165.1.

Christensen, J. H., B. Hewitson, A. Busuioc, A. Chen, X. Gao, I. Held, R. Jones, R. K. Kolli, W.-T. Kwon, R. Laprise, V. Magaña Rueda, L. Mearns, C. G. Menéndez, J. Räisänen, A. Rinke, A. Sarr, and P. Whetton, 2007: Regional climate projections. *Climate Change 2007: The Physical Science Basis, Contribution of Working Group I to the Fourth Assessment Report of the Intergovernmental Panel on Climate Change*, S. S. e. al., Ed., Cambridge University Press, 847–940.

Coe, R., and R. D. Stern, 1982: Fitting Models to Daily Rainfall Data. *Journal of Applied Meteorology*, **21,** 1024-1031, doi:10.1175/1520-0450(1982)021<1024:FMTDRD>2.0.CO;2.

Collins, M., R. Knutti, J. Arblaster, J.-L. Dufresne, T. Fichefet, P. Friedlingstein, X. Gao, W. J. Gutowski, T. Johns, G. Krinner, M. Shongwe, C. Tebaldi, A. J. Weaver, and M. Wehner, 2013: Long-term Climate Change: Projections, Commitments and Irreversibility. *Climate Change 2013: The Physical Science Basis. Contribution of Working Group I to the Fifth Assessment Report of the Intergovernmental Panel on Climate*

Change, T. F. Stocker, D. Qin, G.-K. Plattner, M. Tignor, S. K. Allen, J. Boschung, A. Nauels, Y. Xia, V. Bex, and P. M. Midgley, Eds., Cambridge University Press.

Cowpertwait, P. S. P., and P. E. O'Connell, 1997: A Regionalised Neyman-Scott Model of Rainfall with Convective and Stratiform Cells. *Hydrol. Earth Syst. Sci.*, **1,** 71-80, doi:10.5194/hess-1-71-1997.

Cubasch, U., D. Wuebbles, D. Chen, M. C. Facchini, D. Frame, N. Mahowald, and J.-G. Winther, 2013: Introduction. *Climate Change 2013: The Physical Science Basis. Contribution of Working Group I to the Fifth Assessment Report of the Intergovernmental Panel on Climate Change* T. F. Stocker, D. Qin, G.-K. Plattner, M. Tignor, S. K. Allen, J. Boschung, A. Nauels, Y. Xia, V. Bex, and P. M. Midgley, Eds., Cambridge University Press.

Curtis, S., and R. Adler, 2000: ENSO Indices Based on Patterns of Satellite-Derived Precipitation. *Journal of Climate*, **13,** 2786-2793, doi:10.1175/1520-0442(2000)013<2786:EIBOPO>2.0.CO;2.

Dai, A., 2006: Precipitation Characteristics in Eighteen Coupled Climate Models. *Journal of Climate*, **19,** 4605-4630, doi:10.1175/JCLI3884.1.

——, 2011: Drought under global warming: a review. *Wiley Interdisciplinary Reviews: Climate Change*, **2,** 45-65, doi:10.1002/wcc.81.

——, 2013: Increasing drought under global warming in observations and models. *Nature Clim. Change*, **3,** 52-58, doi:http://www.nature.com/nclimate/journal/v3/n1/abs/nclimate1633.html#supplementary-information.

Dai, A., and K. E. Trenberth, 2002: Estimates of Freshwater Discharge from Continents: Latitudinal and Seasonal Variations. *Journal of Hydrometeorology*, **3,** 660-687, doi:10.1175/1525-7541(2002)003<0660:EOFDFC>2.0.CO;2.

de Lima, M. I. P., and J. Grasman, 1999: Multifractal analysis of 15-min and daily rainfall from a semi-arid region in Portugal. *Journal of Hydrology*, **220,** 1-11, doi:http://dx.doi.org/10.1016/S0022-1694(99)00053-0.

Debele, B., R. Srinivasan, and J. Yves Parlange, 2007: Accuracy evaluation of weather data generation and disaggregation methods at finer timescales. *Advances in Water Resources*, **30,** 1286-1300, doi:http://dx.doi.org/10.1016/j.advwatres.2006.11.009.

Della-Marta, P. M., J. Luterbacher, H. von Weissenfluh, E. Xoplaki, M. Brunet, and H. Wanner, 2007: Summer heat waves over western Europe 1880–2003, their relationship to large-scale forcings and predictability. *Clim Dyn*, **29,** 251-275, doi:10.1007/s00382-007-0233-1.

Diffenbaugh, N. S., and M. Ashfaq, 2010: Intensification of hot extremes in the United States. *Geophysical Research Letters*, **37,** L15701, doi:10.1029/2010GL043888.

Dines, W. H., 1917: The heat balance of the atmosphere. *Quarterly Journal of the Royal Meteorological Society*, **43,** 151-158, doi:10.1002/qj.49704318203.

Dirmeyer, P. A., 2011: A History and Review of the Global Soil Wetness Project (GSWP). *Journal of Hydrometeorology*, **12,** 729-749, doi:10.1175/JHM-D-10-05010.1.

Dirmeyer, P. A., A. J. Dolman, and N. Sato, 1999: The Pilot Phase of the Global Soil Wetness Project. *Bulletin of the American Meteorological Society*, **80,** 851-878, doi:10.1175/1520-0477(1999)080<0851:TPPOTG>2.0.CO;2.

Dirmeyer, P. A., Z. Guo, and X. Gao, 2004: Comparison, Validation, and Transferability of Eight Multiyear Global Soil Wetness Products. *Journal of Hydrometeorology*, **5,** 1011-1033, doi:10.1175/JHM-388.1.

Dirmeyer, P. A., X. Gao, M. Zhao, Z. Guo, T. Oki, and N. Hanasaki, 2006: GSWP-2: Multimodel Analysis and Implications for Our Perception of the Land Surface. *Bulletin of the American Meteorological Society*, **87,** 1381-1397, doi:10.1175/BAMS-87-10-1381.

Donat, M. G., L. V. Alexander, H. Yang, I. Durre, R. Vose, R. J. H. Dunn, K. M. Willett, E. Aguilar, M. Brunet, J. Caesar, B. Hewitson, C. Jack, A. M. G. Klein Tank, A. C. Kruger, J. Marengo, T. C. Peterson, M. Renom, C. Oria Rojas, M. Rusticucci, J. Salinger, A. S. Elrayah, S. S. Sekele, A. K. Srivastava, B. Trewin, C. Villarroel, L. A. Vincent, P. Zhai, X. Zhang, and S. Kitching, 2013: Updated analyses of temperature and precipitation extreme indices since the beginning of the twentieth century: The HadEX2 dataset. *Journal of Geophysical Research: Atmospheres*, **118,** 2098-2118, doi:10.1002/jgrd.50150.

Dutra, E., P. Viterbo, and P. M. A. Miranda, 2008: ERA-40 reanalysis hydrological applications in the characterization of regional drought. *Geophysical Research Letters*, **35,** L19402, doi:10.1029/2008GL035381.

Dutra, E., G. Balsamo, P. Viterbo, P. M. A. Miranda, A. Beljaars, C. Schär, and K. Elder, 2010: An Improved Snow Scheme for the ECMWF Land Surface Model: Description and Offline Validation. *Journal of Hydrometeorology*, **11,** 899-916, doi:10.1175/2010JHM1249.1.

Falge, E., M. Aubinet, P. Bakwin, D. Baldocchi, P. Berbigier, C. Bernhofer, A. Black, R. Ceulemans, K. Davis, A. Dolman, A. Goldstein, M. Goulden, A. Granier, D. Hollinger, P. Jarvis, N. Jensen, K. Pilegaard, G. Katul, P. Kyaw Tha Paw, B. Law, A. Lindroth, D. Loustau, Y. Mahli, R. Monson, P. Moncrieff, E. Moors, W. Munger, T. Meyers, W. Oechel, E. Schulze, H. Thorgeirsson, J. Tenhunen, R. Valentini, S. Verma, T. Vesala,

and S. Wofsy, 2005: FLUXNET Marconi Conference Gap-Filled Flux and Meteorology Data, 1992-2000. Data set. Available on-line [http//www.daac.ornl.gov] from Oak Ridge National Laboratory Distributed Active Archive Center, Oak Ridge, Tennessee, U.S.A. doi:10.3334/ORNLDAAC/811.

Fan, Y., H. M. van den Dool, and W. Wu, 2011: Verification and Intercomparison of Multimodel Simulated Land Surface Hydrological Datasets over the United States. *Journal of Hydrometeorology*, **12,** 531-555, doi:10.1175/2011JHM1317.1.

Fasullo, J. T., 2010: Robust Land–Ocean Contrasts in Energy and Water Cycle Feedbacks. *Journal of Climate*, **23,** 4677-4693, doi:10.1175/2010JCLI3451.1.

Fasullo, J. T., and K. E. Trenberth, 2008a: The Annual Cycle of the Energy Budget. Part I: Global Mean and Land–Ocean Exchanges. *Journal of Climate*, **21,** 2297-2312, doi:10.1175/2007JCLI1935.1.

——, 2008b: The Annual Cycle of the Energy Budget. Part II: Meridional Structures and Poleward Transports. *Journal of Climate*, **21,** 2313-2325, doi:10.1175/2007JCLI1936.1.

Fealy, R., and J. Sweeney, 2007: Statistical downscaling of precipitation for a selection of sites in Ireland employing a generalised linear modelling approach. *International Journal of Climatology*, **27,** 2083-2094, doi:10.1002/joc.1506.

Fischer, E. M., S. I. Seneviratne, P. L. Vidale, D. Lüthi, and C. Schär, 2007: Soil Moisture–Atmosphere Interactions during the 2003 European Summer Heat Wave. *Journal of Climate*, **20,** 5081-5099, doi:10.1175/JCLI4288.1.

Foufoula-Georgiou, E., and D. P. Lettenmaier, 1986: Continuous-Time Versus Discrete-Time Point Process Models for Rainfall Occurrence Series. Water Resources Research, 22, 531-542, doi:10.1029/WR022i004p00531.

Fuchs, T., 2008: GPCC Annual report for year 2008. Development of the GPCC data base and analysis products (available from reports and publications section of the GPCC

homepage - gpcc.dwd.de).

Furrer, E. M., and R. W. Katz, 2007: Generalized linear modeling approach to stochastic weather generators. *Climate Research*, **34,** 129-144, doi:10.3354/cr034129.

——, 2008: Improving the simulation of extreme precipitation events by stochastic weather generators. *Water Resources Research*, **44,** W12439, doi:10.1029/2008WR007316.

Gao, H., Q. Tang, C. R. Ferguson, E. F. Wood, and D. P. Lettenmaier, 2010: Estimating the water budget of major US river basins via remote sensing. *International Journal of Remote Sensing*, **31,** 3955-3978, doi:10.1080/01431161.2010.483488.

Gaume, E., N. Mouhous, and H. Andrieu, 2007: Rainfall stochastic disaggregation models: Calibration and validation of a multiplicative cascade model. *Advances in Water Resources*, **30,** 1301-1319, doi:http://dx.doi.org/10.1016/j.advwatres.2006.11.007.

Gerten, D., S. Schaphoff, U. Haberlandt, W. Lucht, and S. Sitch, 2004: Terrestrial vegetation and water balance—hydrological evaluation of a dynamic global vegetation model. *Journal of Hydrology*, **286,** 249-270, doi:http://dx.doi.org/10.1016/j.jhydrol.2003.09.029.

Gibelin, A.-L., J.-C. Calvet, J.-L. Roujean, L. Jarlan, and S. O. Los, 2006: Ability of the land surface model ISBA-A-gs to simulate leaf area index at the global scale: Comparison with satellites products. *Journal of Geophysical Research: Atmospheres*, **111,** D18102, doi:10.1029/2005JD006691.

Gudmundsson, L., L. M. Tallaksen, and K. Stahl, 2011: Projected changes in future runoff variability - a multi model analysis using the A2 emission scenario., WATCH Technical Report, 49, 11 pp.

Gupta, V. K., and E. Waymire, 1991: On Lognormality and Scaling in Spatial Rainfall Averages? Non-Linear Variability in Geophysics, D. Schertzer, and S. Lovejoy, Eds., Springer Netherlands, 175-183.

Güntner, A., 2008: Improvement of Global Hydrological Models Using GRACE Data. Surv Geophys, 29, 375-397, doi:10.1007/s10712-008-9038-y.

Güntner, A., J. Olsson, A. Calver, and B. Gannon, 2001: Cascade-based disaggregation of continuous rainfall time series: the influence of climate. Hydrol. *Earth Syst. Sci.*, **5,** 145-164, doi:10.5194/hess-5-145-2001.

Güntner, A., J. Stuck, S. Werth, P. Döll, K. Verzano, and B. Merz, 2007: A global analysis of temporal and spatial variations in continental water storage. *Water Resources Research*, **43,** W05416, doi:10.1029/2006WR005247.

Haddeland, I., D. B. Clark, W. Franssen, F. Ludwig, F. Voß, N. W. Arnell, N. Bertrand, M. Best, S. Folwell, D. Gerten, S. Gomes, S. N. Gosling, S. Hagemann, N. Hanasaki, R. Harding, J. Heinke, P. Kabat, S. Koirala, T. Oki, J. Polcher, T. Stacke, P. Viterbo, G. P. Weedon, and P. Yeh, 2011: Multimodel Estimate of the Global Terrestrial Water Balance: Setup and First Results. *Journal of Hydrometeorology*, **12,** 869-884, doi:10.1175/2011JHM1324.1.

Hagemann, S., K. Arpe, and L. Bengtsson, 2005: Validation of the hydrological cycle of ERA-40., ERA-40 Project Report Series, 24, ECMWF.

Hagemann, S., C. Chen, J. O. Haerter, J. Heinke, D. Gerten, and C. Piani, 2011: Impact of a Statistical Bias Correction on the Projected Hydrological Changes Obtained from Three GCMs and Two Hydrology Models. *Journal of Hydrometeorology*, **12,** 556-578, doi:10.1175/2011JHM1336.1.

Harding, R., M. Best, E. Blyth, S. Hagemann, P. Kabat, L. M. Tallaksen, T. Warnaars, D. Wiberg, G. P. Weedon, H. v. Lanen, F. Ludwig, and I. Haddeland, 2011: WATCH: Current Knowledge of the Terrestrial Global Water Cycle. *Journal of Hydrometeorology*, **12,** 1149-1156, doi:10.1175/JHM-D-11-024.1.

Hartmann, D. L., A. M. G. Klein Tank, M. Rusticucci, L. V. Alexander, S. Brönnimann, Y. Charabi, F. J. Dentener, E. J. Dlugokencky, D. R. Easterling, A. Kaplan, B. J. Soden, P. W. Thorne, M. Wild, and P. M. Zhai, 2013: Observations: Atmosphere and Surface. *Climate Change 2013: The Physical Science Basis. Contribution of Working Group I to the Fifth Assessment Report of the Intergovernmental Panel on Climate Change*, T. F. Stocker, D. Qin, G.-K. Plattner, M. Tignor, S. K. Allen, J. Boschung, A. Nauels, Y. Xia, V. Bex, and P. M. Midgley, Eds., Cambridge University Press.

Heim, R. R., 2002: A Review of Twentieth-Century Drought Indices Used in the United States. *Bulletin of the American Meteorological Society*, **83,** 1149-1165, doi:10.1175/1520-0477(2002)083<1149:AROTDI>2.3.CO;2.

Henderson-Sellers, A., A. J. Pitman, P. K. Love, P. Irannejad, and T. H. Chen, 1995: The Project for Intercomparison of Land Surface Parameterization Schemes (PILPS): Phases 2 and 3. *Bulletin of the American Meteorological Society*, **76,** 489-503, doi:10.1175/1520-0477(1995)076<0489:TPFIOL>2.0.CO;2.

Hessami, M., P. Gachon, T. B. M. J. Ouarda, and A. St-Hilaire, 2008: Automated regression-based statistical downscaling tool. *Environmental Modelling & Software*, **23,** 813-834, doi:http://dx.doi.org/10.1016/j.envsoft.2007.10.004.

Hirabayashi, Y., S. Kanae, I. Struthers, and T. Oki, 2005: A 100-year (1901–2000) global retrospective estimation of the terrestrial water cycle. *Journal of Geophysical Research: Atmospheres*, **110,** D19101, doi:10.1029/2004JD005492.

Hirschi, M., S. I. Seneviratne, S. Hagemann, and C. Schär, 2007: Analysis of seasonal terrestrial water storage variations in regional climate simulations over Europe. *Journal of Geophysical Research: Atmospheres*, **112,** D22109, doi:10.1029/2006JD008338.

Hirschi, M., S. I. Seneviratne, V. Alexandrov, F. Boberg, C. Boroneant, O. B. Christensen, H. Formayer, B. Orlowsky, and P. Stepanek, 2011: Observational evidence for soil-moisture impact on hot extremes in southeastern Europe. *Nature Geosci*, **4,** 17-21, doi:http://www.nature.com/ngeo/journal/v4/n1/abs/ngeo1032.html#supplementary-information.

Huntington, T. G., 2006: Evidence for intensification of the global water cycle: Review and synthesis. *Journal of Hydrology*, **319,** 83-95, doi:http://dx.doi.org/10.1016/j.jhydrol.2005.07.003.

Kalnay, E., M. Kanamitsu, R. Kistler, W. Collins, D. Deaven, L. Gandin, M. Iredell, S. Saha, G. White, J. Woollen, Y. Zhu, A. Leetmaa, R. Reynolds, M. Chelliah, W. Ebisuzaki, W. Higgins, J. Janowiak, K. C. Mo, C. Ropelewski, J. Wang, R. Jenne, and D. Joseph, 1996: The NCEP/NCAR 40-Year Reanalysis Project. *Bulletin of the American Meteorological Society*, **77,** 437-471, doi:10.1175/1520-0477(1996)077<0437:TNYRP>2.0.CO;2.

Kanamitsu, M., C.-H. Lu, J. Schemm, and W. Ebisuzaki, 2003: The Predictability of Soil Moisture and Near-Surface Temperature in Hindcasts of the NCEP Seasonal Forecast Model. *Journal of Climate*, **16,** 510-521, doi:10.1175/1520-0442(2003)016<0510:TPOSMA>2.0.CO;2.

Katz, R. W., and M. B. Parlange, 1995: Generalizations of Chain-Dependent Processes: Application to Hourly Precipitation. *Water Resources Research*, **31,** 1331-1341, doi:10.1029/94WR03152.

Kiehl, J. T., and K. E. Trenberth, 1997: Earth's Annual Global Mean Energy Budget. *Bulletin of the American Meteorological Society*, **78,** 197-208, doi:10.1175/1520-0477(1997)078<0197:EAGMEB>2.0.CO;2.

Kinter, J. L., and J. Shukla, 1990: The Global Hydrologic and Energy Cycles: Suggestions for Studies in the Pre-Global Energy and Water Cycle Experiment (GEWEX) Period. *Bulletin of the American Meteorological Society*, **71,** 181-189, doi:10.1175/1520-0477(1990)071<0181:TGHAEC>2.0.CO;2.

Kirtman, B., S. B. Power, J. A. Adedoyin, G. J. Boer, R. Bojariu, I. Camilloni, F. J. Doblas-Reyes, A. M. Fiore, M. Kimoto, G. A. Meehl, M. Prather, A. Sarr, C. Schar, R. Sutton, G. J. van Oldenborgh, G. Vecchi, and H. J. Wang, 2013: Near-term Climate Change: Projections and Predictability. *Climate Change 2013: The Physical Science Basis. Contribution of Working Group I to the Fifth Assessment Report of the Intergovernmental Panel on Climate Change*, T. F. Stocker, D. Qin, G.-K. Plattner, M. Tignor, S. K. Allen, J. Boschung, A. Nauels, Y. Xia, V. Bex, and P. M. Midgley, Eds., Cambridge University Press.

Kottek, M., J. Grieser, C. Beck, B. Rudolf, and F. Rubel, 2006: World Map of the Köppen-Geiger climate classification updated. *Meteorologische Zeitschrift*, **15,** 259-263, doi:10.1127/0941-2948/2006/0130.

Lenters, J. D., M. T. Coe, and J. A. Foley, 2000: Surface water balance of the continental United States, 1963–1995: Regional evaluation of a terrestrial biosphere model and the NCEP/NCAR reanalysis. *Journal of Geophysical Research: Atmospheres*, **105,** 22393-22425, doi:10.1029/2000JD900277.

Li, H., J. Sheffield, and E. F. Wood, 2010: Bias correction of monthly precipitation and temperature fields from Intergovernmental Panel on Climate Change AR4 models using equidistant quantile matching. *Journal of Geophysical Research: Atmospheres*, **115,** D10101, doi:10.1029/2009JD012882.

Maurer, E. P., G. M. O'Donnell, D. P. Lettenmaier, and J. O. Roads, 2001: Evaluation of the land surface water budget in NCEP/NCAR and NCEP/DOE reanalyses using an off-line hydrologic model. *Journal of Geophysical Research: Atmospheres*, **106,** 17841-17862, doi:10.1029/2000JD900828.

McKee, T. B., N. J. Doesken, and J. Kleist, 1993: The relationship of drought frequency and duration of time scales. *Eighth Conference on Applied Climatology*, A. M. Society, Ed., 179-186.

Meehl, G. A., T. F. Stocker, W. D. Collins, P. Friedlingstein, A. T. Gaye, J. M. Gregory, A. Kitoh, R. Knutti, J. M. Murphy, A. Noda, S. C. B. Raper, I. G. Watterson, A. J. Weaver, and Z.-C. Zhao, 2007: Global Climate Projections. *Climate Change 2007: The Physical Science Basis. Contribution of Working Group I to the Fourth Assessment Report of the Intergovernmental Panel on Climate Change*, S. Solomon, D. Qin, M. Manning, Z. Chen, M. Marquis, K. B. Averyt, M. Tignor, and H. L. Miller, Eds., Cambridge University Press.

Meneghini, R., and J. A. Jones, 1993: An Approach to Estimate the Areal Rain-Rate Distribution from Spaceborne Radar by the Use of Multiple Thresholds. *Journal of Applied Meteorology*, **32,** 386-398, doi:10.1175/1520-0450(1993)032<0386:AATETA>2.0.CO;2.

Milly, P. C. D., K. A. Dunne, and A. V. Vecchia, 2005: Global pattern of trends in streamflow and water availability in a changing climate. *Nature*, **438,** 347-350.

Mitchell, T. D., and P. D. Jones, 2005: An improved method of constructing a database of monthly climate observations and associated high-resolution grids. *International Journal of Climatology*, **25,** 693-712, doi:10.1002/joc.1181.

Molnar, P., and P. Burlando, 2005: Preservation of rainfall properties in stochastic disaggregation by a simple random cascade model. *Atmospheric Research*, **77,** 137-151, doi:http://dx.doi.org/10.1016/j.atmosres.2004.10.024.

Morita, T., J. R. Robinson, J. Alcamo, N. Nakicenovic, and K. Riahi, 2001: Greenhouse gas emission mitigation scenarios and implications. *Climate Change 2001: Mitigation, Contribution of Working Group III to the Third Assessment Report of the Intergovernmental Panel Climate Change*, B. Metz, O. Davidson, R. Swart, and J. Pan, Eds., Cambridge University Press.

Mueller, B., and S. I. Seneviratne, 2012: Hot days induced by precipitation deficits at the global scale. *Proceedings of the National Academy of Sciences*, **109,** 12398-12403, doi:10.1073/pnas.1204330109.

Nakicenovic, N., J. Alcamo, G. Davis, B. de Vries, J. Fenhann, S. Gaffin, K. Gregory, A. Grübler, T. Y. Jung, T. Kram, E. L. La Rovere, L. Michaelis, S. Mori, T. Morita, W. Pepper, H. Pitcher, L. Price, K. Riahi, A. Roehrl, H.-H. Rogner, A. Sankovski, M. Schlesinger, P. Shukla, S. Smith, R. Swart, S. van Rooijen, N. Victor, and Z. Dadi, 2000: Special Report on Emissions Scenarios. *A Special Report of Working Group III of the Intergovernmental Panel on Climate Change*, Cambridge University Press, 599.

New, M., M. Hulme, and P. Jones, 1999: Representing Twentieth-Century Space–Time Climate Variability. Part I: Development of a 1961–90 Mean Monthly Terrestrial Climatology. *Journal of Climate*, **12,** 829-856, doi:10.1175/1520-0442(1999)012<0829:RTCSTC>2.0.CO;2.

——, 2000: Representing Twentieth-Century Space–Time Climate Variability. Part II: Development of 1901–96 Monthly Grids of Terrestrial Surface Climate. *Journal of Climate*, **13,** 2217-2238, doi:10.1175/1520-0442(2000)013<2217:RTCSTC>2.0.CO;2.

Ngo-Duc, T., J. Polcher, and K. Laval, 2005a: A 53-year forcing data set for land surface models. *Journal of Geophysical Research: Atmospheres*, **110,** D06116, doi:10.1029/2004JD005434.

Ngo-Duc, T., K. Laval, J. Polcher, A. Lombard, and A. Cazenave, 2005b: Effects of land water storage on global mean sea level over the past half century. *Geophysical Research Letters*, **32,** L09704, doi:10.1029/2005GL022719.

Nijssen, B., R. Schnur, and D. P. Lettenmaier, 2001: Global Retrospective Estimation of Soil Moisture Using the Variable Infiltration Capacity Land Surface Model, 1980–93. *Journal of Climate*, **14,** 1790-1808, doi:10.1175/1520-0442(2001)014<1790:GREOSM>2.0.CO;2.

O'Gorman, P. A., and T. Schneider, 2009: Scaling of Precipitation Extremes over a Wide Range of Climates Simulated with an Idealized GCM. *Journal of Climate*, **22,** 5676-5685, doi:10.1175/2009JCLI2701.1.

Oki, T., 1999: The global water cycle. Global Energy and Water Cycles. K. A. B. a. R. J. Gurney, Ed., Cambridge University Press, 10-29.

Oki, T., and S. Kanae, 2006: Global Hydrological Cycles and World Water Resources. *Science*, **313,** 1068-1072, doi:10.1126/science.1128845.

Olsson, J., 1995: Limits and characteristics of the multifractal behaviour of a high-resolution rainfall time series. *Nonlin. Processes Geophys.*, **2,** 23-29, doi:10.5194/npg-2-23-1995.

Orlowsky, B., and S. Seneviratne, 2012: Global changes in extreme events: regional and seasonal dimension. *Climatic Change*, **110,** 669-696, doi:10.1007/s10584-011-0122-9.

Orlowsky, B., and S. I. Seneviratne, 2013: Elusive drought: uncertainty in observed trends and short- and long-term CMIP5 projections. *Hydrol. Earth Syst. Sci.*, **17,** 1765-1781, doi:10.5194/hess-17-1765-2013.

Orth, R., and S. Seneviratne, 2014: Using soil moisture forecasts for sub-seasonal summer temperature predictions in Europe. *Clim Dyn***,** 1-16, doi:10.1007/s00382-014-2112-x.

Parlange, M. B., and R. W. Katz, 2000: An Extended Version of the Richardson Model for Simulating Daily Weather Variables. *Journal of Applied Meteorology*, **39,** 610-622, doi:10.1175/1520-0450-39.5.610.

Peixoto, J. P., and A. H. Oort, 1992: *Physics of Climate.* American Institute of Physics, 520 pp.

Piani, C., G. P. Weedon, M. Best, S. M. Gomes, P. Viterbo, S. Hagemann, and J. O. Haerter, 2010: Statistical bias correction of global simulated daily precipitation and temperature for the application of hydrological models. *Journal of Hydrology*, **395,** 199-215, doi:http://dx.doi.org/10.1016/j.jhydrol.2010.10.024.

Pitman, A. J., 2003: The evolution of, and revolution in, land surface schemes designed for climate models. *International Journal of Climatology*, **23,** 479-510, doi:10.1002/joc.893.

Roads, J., and A. Betts, 2000: NCEP–NCAR and ECMWF Reanalysis Surface Water and Energy Budgets for the Mississippi River Basin. *Journal of Hydrometeorology*, **1,** 88-94, doi:10.1175/1525-7541(2000)001<0088:NNAERS>2.0.CO;2.

Rubel, F., and M. Kottek, 2010: Observed and projected climate shifts 1901-2100 depicted by world maps of the Köppen-Geiger climate classification. *Meteorologische Zeitschrift*, **19,** 135-141, doi:10.1127/0941-2948/2010/0430.

Rudolf, B., and U. Schneider, 2005: Calculation of gridded precipitation data for the global land-surface using in-situ gauge observations. *Proc. Second Workshop of the International Precipitation Working Group*, 231–247.

Running, S. W., R. R. Nemani, and H. R. D., 1987: Extrapolation of synoptic meteorological data in mountainous terrain and its use for simulating forest evapotranspiration and photosynthesis. *Canadian Journal of Forest Research*, **17,** 472-483.

Safeeq, M., and A. Fares, 2011: Accuracy evaluation of ClimGen weather generator and daily to hourly disaggregation methods in tropical conditions. *Theor. Appl. Climatol.*, **106,** 321-341, doi:10.1007/s00704-011-0438-4.

Sahoo, A. K., M. Pan, T. J. Troy, R. K. Vinukollu, J. Sheffield, and E. F. Wood, 2011: Reconciling the global terrestrial water budget using satellite remote sensing. *Remote Sensing of Environment*, **115,** 1850-1865, doi:http://dx.doi.org/10.1016/j.rse.2011.03.009.

Schneider, U., T. Fuchs, A. Meyer-Christoffer, and B. Rudolf, 2008: Global precipitation analysis products of the GPCC (available from reports and publications section of the

GPCC homepage - gpcc.dwd.de). .

Seneviratne, S. I., P. Viterbo, D. Lüthi, and C. Schär, 2004: Inferring Changes in Terrestrial Water Storage Using ERA-40 Reanalysis Data: The Mississippi River Basin. *Journal of Climate*, **17,** 2039-2057, doi:10.1175/1520-0442(2004)017<2039:ICITWS>2.0.CO;2.

Seneviratne, S. I., D. Luthi, M. Litschi, and C. Schar, 2006: Land-atmosphere coupling and climate change in Europe. *Nature*, **443,** 205-209, doi:http://www.nature.com/nature/journal/v443/n7108/suppinfo/nature05095_S1.html.

Seneviratne, S. I., T. Corti, E. L. Davin, M. Hirschi, E. B. Jaeger, I. Lehner, B. Orlowsky, and A. J. Teuling, 2010: Investigating soil moisture–climate interactions in a changing climate: A review. *Earth-Science Reviews*, **99,** 125-161, doi:http://dx.doi.org/10.1016/j.earscirev.2010.02.004.

Sheffield, J., and E. F. Wood, 2007: Characteristics of global and regional drought, 1950–2000: Analysis of soil moisture data from off-line simulation of the terrestrial hydrologic cycle. *Journal of Geophysical Research: Atmospheres*, **112,** D17115, doi:10.1029/2006JD008288.

——, 2008: Projected changes in drought occurrence under future global warming from multi-model, multi-scenario, IPCC AR4 simulations. *Clim Dyn*, **31,** 79-105, doi:10.1007/s00382-007-0340-z.

Sheffield, J., G. Goteti, and E. F. Wood, 2006: Development of a 50-Year High-Resolution Global Dataset of Meteorological Forcings for Land Surface Modeling. *Journal of Climate*, **19,** 3088-3111, doi:10.1175/JCLI3790.1.

Sheffield, J., E. F. Wood, and F. Munoz-Arriola, 2010: Long-Term Regional Estimates of Evapotranspiration for Mexico Based on Downscaled ISCCP Data. *Journal of Hydrometeorology*, **11,** 253-275, doi:10.1175/2009JHM1176.1.

Sheffield, J., E. F. Wood, and M. L. Roderick, 2012: Little change in global drought over the past 60 years. *Nature*, **491,** 435-438, doi:http://www.nature.com/nature/journal/v491/n7424/abs/nature11575.html#supplementary-information.

Sheffield, J., A. D. Ziegler, E. F. Wood, and Y. Chen, 2004: Correction of the High-Latitude Rain Day Anomaly in the NCEP–NCAR Reanalysis for Land Surface Hydrological Modeling. *Journal of Climate*, **17,** 3814-3828, doi:10.1175/1520-0442(2004)017<3814:COTHRD>2.0.CO;2.

Smith, J. A., and A. F. Karr, 1985: Statistical Inference for Point Process Models of Rainfall. Water Resources Research, 21, 73-79, doi:10.1029/WR021i001p00073.

Solomon, S., D. Qin, M. Manning, R. B. Alley, T. Berntsen, N. L. Bindoff, Z. Chen, A. Chidthaisong, J. M. Gregory, G. C. Hegerl, M. Heimann, B. Hewitson, B. J. Hoskins, F. Joos, J. Jouzel, V. Kattsov, U. Lohmann, T. Matsuno, M. Molina, N. Nicholls, J. Overpeck, G. Raga, V. Ramaswamy, J. Ren, M. Rusticucci, R. Somerville, T. F. Stocker, P. Whetton, R. A. Wood, and D. Wratt, 2007: Technical Summary. *Climate Change 2007: The Physical Science Basis. Contribution of Working Group I to the Fourth Assessment Report of the Intergovernmental Panel on Climate Change*, S. Solomon, D. Qin, M. Manning, Z. Chen, M. Marquis, K. B. Averyt, M. Tignor, and H. L. Miller, Eds., Cambridge University Press.

Stern, R. D., and R. Coe, 1984: A model fitting analysis of rainfall data (with discussion). *Journal of the Royal Statistical Society.*, **A147,** 1-34.

Sun, Y., S. Solomon, A. Dai, and R. W. Portmann, 2006: How Often Does It Rain? *Journal of Climate*, **19,** 916-934, doi:10.1175/JCLI3672.1.

Thornton, P. E., and S. W. Running, 1999: An improved algorithm for estimating incident daily solar radiation from measurements of temperature, humidity, and precipitation. *Agricultural and Forest Meteorology*, **93,** 211-228, doi:http://dx.doi.org/10.1016/S0168-1923(98)00126-9.

Thornton, P. E., S. W. Running, and M. A. White, 1997: Generating surfaces of daily meteorological variables over large regions of complex terrain. *Journal of Hydrology*, **190,** 214-251.

Trenberth, K. E., and J. T. Fasullo, 2008: An Observational Estimate of Inferred Ocean Energy Divergence. *Journal of Physical Oceanography*, **38,** 984-999, doi:10.1175/2007JPO3833.1.

Trenberth, K. E., and G. R. Asrar, 2014: Challenges and Opportunities in Water Cycle Research: WCRP Contributions. *The Earth's Hydrological Cycle*, L. Bengtsson, R. M. Bonnet, M. Calisto, G. Destouni, R. Gurney, J. Johannessen, Y. Kerr, W. A. Lahoz, and M. Rast, Eds., Springer Netherlands, 515-532.

Trenberth, K. E., J. T. Fasullo, and J. Kiehl, 2009: Earth's Global Energy Budget. *Bulletin of the American Meteorological Society*, **90,** 311-323, doi:10.1175/2008BAMS2634.1.

Trenberth, K. E., J. T. Fasullo, and J. Mackaro, 2011: Atmospheric Moisture Transports from Ocean to Land and Global Energy Flows in Reanalyses. *Journal of Climate*, **24,** 4907-4924, doi:10.1175/2011JCLI4171.1.

Trenberth, K. E., A. Dai, R. M. Rasmussen, and D. B. Parsons, 2003: The Changing Character of Precipitation. *Bulletin of the American Meteorological Society*, **84,** 1205-1217, doi:10.1175/BAMS-84-9-1205.

Trenberth, K. E., L. Smith, T. Qian, A. Dai, and J. Fasullo, 2007: Estimates of the Global Water Budget and Its Annual Cycle Using Observational and Model Data. *Journal of Hydrometeorology*, **8,** 758-769, doi:10.1175/JHM600.1.

Troccoli, A., and P. Kallberg, 2004: Precipitation correction in the ERA-40 reanalysis,, ERA-40 Project Report Series, 13.

Troch, P., M. Durcik, S. Seneviratne, M. Hirschi, A. Teuling, R. Hurkmans, and S. Hasan, 2007: New data sets to estimate terrestrial water storage change. *Eos, Transactions American Geophysical Union*, **88,** 469-470, doi:10.1029/2007EO450001.

Twine, T. E., W. P. Kustas, J. M. Norman, D. R. Cook, P. R. Houser, T. P. Meyers, J. H. Prueger, P. J. Starks, and M. L. Wesely, 2000: Correcting eddy-covariance flux underestimates over a grassland. *Agricultural and Forest Meteorology*, **103,** 279-300, doi:http://dx.doi.org/10.1016/S0168-1923(00)00123-4.

Uppala, S. M., P. W. KÅllberg, A. J. Simmons, U. Andrae, V. D. C. Bechtold, M. Fiorino, J. K. Gibson, J. Haseler, A. Hernandez, G. A. Kelly, X. Li, K. Onogi, S. Saarinen, N. Sokka, R. P. Allan, E. Andersson, K. Arpe, M. A. Balmaseda, A. C. M. Beljaars, L. V. D. Berg, J. Bidlot, N. Bormann, S. Caires, F. Chevallier, A. Dethof, M. Dragosavac, M. Fisher, M. Fuentes, S. Hagemann, E. Hólm, B. J. Hoskins, L. Isaksen, P. A. E. M. Janssen, R. Jenne, A. P. McNally, J. F. Mahfouf, J. J. Morcrette, N. A. Rayner, R. W. Saunders, P. Simon, A. Sterl, K. E. Trenberth, A. Untch, D. Vasiljevic, P. Viterbo, and J. Woollen, 2005: The ERA-40 re-analysis. *Quarterly Journal of the Royal Meteorological Society*, **131,** 2961-3012, doi:10.1256/qj.04.176.

van den Hurk, B., P. Viterbo, A. C. M. Beljaars, and A. K. Betts, 2000: Offline validation of the ERA-40 surface scheme, ECMWF Technical Memorandum, 295, 43 pp.

van der Schrier, G., K. R. Briffa, P. D. Jones, and T. J. Osborn, 2006a: Summer Moisture Variability across Europe. *Journal of Climate*, **19,** 2818-2834, doi:10.1175/JCLI3734.1.

van der Schrier, G., K. R. Briffa, T. J. Osborn, and E. R. Cook, 2006b: Summer moisture availability across North America. *Journal of Geophysical Research: Atmospheres*, **111,** D11102, doi:10.1029/2005JD006745.

van der Schrier, G., J. Barichivich, K. R. Briffa, and P. D. Jones, 2013: A scPDSI-based global data set of dry and wet spells for 1901–2009. *Journal of Geophysical Research: Atmospheres*, **118,** 4025-4048, doi:10.1002/jgrd.50355.

van Genuchten, M. T., 1980: A Closed-form Equation for Predicting the Hydraulic Conductivity of Unsaturated Soils1. *Soil Sci. Soc. Am. J.*, **44,** 892-898, doi:10.2136/sssaj1980.03615995004400050002x.

Vaughan, D. G., J. C. Comiso, I. Allison, J. Carrasco, G. Kaser, R. Kwok, P. Mote, T. Murray, F. Paul, J. Ren, E. Rignot, O. Solomina, K. Steffen , and T. Zhang, 2013: Observations: Cryosphere. *Climate Change 2013: The Physical Science Basis. Contribution of Working Group I to the Fifth Assessment Report of the Intergovernmental Panel on Climate Change*, T. F. Stocker, D. Qin, G.-K. Plattner, M. Tignor, S. K. Allen, J. Boschung, A. Nauels, Y. Xia, V. Bex, and P. M. Midgley, Eds., Cambridge University Press.

Vautard, R., P. Yiou, F. D'Andrea, N. de Noblet, N. Viovy, C. Cassou, J. Polcher, P. Ciais, M. Kageyama, and Y. Fan, 2007: Summertime European heat and drought waves induced by wintertime Mediterranean rainfall deficit. *Geophysical Research Letters*, **34,** L07711, doi:10.1029/2006GL028001.

Vicente-Serrano, S., 2006: Differences in Spatial Patterns of Drought on Different Time Scales: An Analysis of the Iberian Peninsula. *Water Resour Manage*, **20,** 37-60, doi:10.1007/s11269-006-2974-8.

Vinukollu, R. K., R. Meynadier, J. Sheffield, and E. F. Wood, 2011: Multi-model, multi-sensor estimates of global evapotranspiration: climatology, uncertainties and trends. *Hydrological Processes*, **25,** 3993-4010, doi:10.1002/hyp.8393.

Viterbo, P., and A. C. M. Beljaars, 1995: An Improved Land Surface Parameterization Scheme in the ECMWF Model and Its Validation. *Journal of Climate*, **8,** 2716-2748, doi:10.1175/1520-0442(1995)008<2716:AILSPS>2.0.CO;2.

Viterbo, P., A. Beljaars, J.-F. Mahfouf, and J. Teixeira, 1999: The representation of soil moisture freezing and its impact on the stable boundary layer. *Quarterly Journal of the Royal Meteorological Society*, **125,** 2401-2426, doi:10.1002/qj.49712555904.

Waichler, S. R., and M. S. Wigmosta, 2003: Development of Hourly Meteorological Values From Daily Data and Significance to Hydrological Modeling at H. J. Andrews Experimental Forest. *Journal of Hydrometeorology*, **4,** 251-263, doi:10.1175/1525-7541(2003)4<251:DOHMVF>2.0.CO;2.

Wallis, T. W. R., and J. F. Griffiths, 1995: An assessment of the weather generator (WXGEN) used in the erosion/productivity impact calculator (EPIC). *Agricultural and Forest Meteorology*, **73,** 115-133, doi:http://dx.doi.org/10.1016/0168-1923(94)02172-G.

Wanders, N., H. A. J. van Lanen, and A. F. van Loon, 2010: Indicators for drought characterization on a global scale., WATCH Technical Report, 24, 93 pp.

Wang, Y., Z. Yan, and R. E. Chandler, 2010: An analysis of mid-summer rainfall occurrence in eastern China and its relationship with large-scale warming using generalized linear models. *International Journal of Climatology*, **30,** 1826-1834, doi:10.1002/joc.2018.

Weedon, G. P., G. Balsamo, N. Bellouin, S. Gomes, M. J. Best, and P. Viterbo, 2014: The WFDEI meteorological forcing data set: WATCH Forcing Data methodology applied to ERA-Interim reanalysis data. *Water Resources Research***,** n/a-n/a, doi:10.1002/2014WR015638.

Weedon, G. P., S. Gomes, P. Viterbo, H. Österle, J. C. Adam, N. Bellouin, O. Boucher, and M. Best, 2010: The WATCH forcing data 1958-2001: A meteorological forcing dataset for land surface and hydrological models., Technical Report WATCH, 22, 41 pp.

Weedon, G. P., S. Gomes, P. Viterbo, W. J. Shuttleworth, E. Blyth, H. Österle, J. C. Adam, N. Bellouin, O. Boucher, and M. Best, 2011: Creation of the WATCH Forcing Data and Its Use to Assess Global and Regional Reference Crop Evaporation over Land during the Twentieth Century. *Journal of Hydrometeorology*, **12,** 823-848, doi:10.1175/2011JHM1369.1.

Widén-Nilsson, E., S. Halldin, and C.-y. Xu, 2007: Global water-balance modelling with WASMOD-M: Parameter estimation and regionalisation. *Journal of Hydrology*, **340,** 105-118, doi:http://dx.doi.org/10.1016/j.jhydrol.2007.04.002.

Wilby, R. L., L. E. Hay, and G. H. Leavesley, 1999: A comparison of downscaled and raw GCM output: implications for climate change scenarios in the San Juan River basin, Colorado. *Journal of Hydrology*, **225,** 67-91, doi:http://dx.doi.org/10.1016/S0022-1694(99)00136-5.

Wild, M., A. Ohmura, H. Gilgen, and E. Roeckner, 1995: Validation of General Circulation Model Radiative Fluxes Using Surface Observations. *Journal of Climate*, **8,** 1309-1324, doi:10.1175/1520-0442(1995)008<1309:VOGCMR>2.0.CO;2.

Wild, M., D. Folini, C. Schär, N. Loeb, E. Dutton, and G. König-Langlo, 2013: The global energy balance from a surface perspective. *Clim Dyn*, **40,** 3107-3134, doi:10.1007/s00382-012-1569-8.

Wilks, D. S., 1995: *Statistical Methods in the Atmospheric Sciences.* Academic Press, 467 pp.

——, 1999: Interannual variability and extreme-value characteristics of several stochastic daily precipitation models. *Agricultural and Forest Meteorology*, **93,** 153-169, doi:http://dx.doi.org/10.1016/S0168-1923(98)00125-7.

Wilks, D. S., and R. L. Wilby, 1999: The weather generation game: a review of stochastic weather models. *Progress in Physical Geography*, **23,** 329-357, doi:10.1177/030913339902300302.

Willett, K. M., N. P. Gillett, P. D. Jones, and P. W. Thorne, 2007: Attribution of observed surface humidity changes to human influence. *Nature*, **449,** 710-712, doi:http://www.nature.com/nature/journal/v449/n7163/suppinfo/nature06207_S1.html.

Wood, E. F., D. P. Lettenmaier, X. Liang, D. Lohmann, A. Boone, S. Chang, F. Chen, Y. Dai, R. E. Dickinson, Q. Duan, M. Ek, Y. M. Gusev, F. Habets, P. Irannejad, R. Koster, K. E. Mitchel, O. N. Nasonova, J. Noilhan, J. Schaake, A. Schlosser, Y. Shao, A. B. Shmakin, D. Verseghy, K. Warrach, P. Wetzel, Y. Xue, Z.-L. Yang, and Q.-c. Zeng, 1998: The Project for Intercomparison of Land-surface Parameterization Schemes (PILPS) Phase 2(c) Red–Arkansas River basin experiment:: 1. Experiment description and summary intercomparisons. *Global and Planetary Change*, **19,** 115-135, doi:http://dx.doi.org/10.1016/S0921-8181(98)00044-7.

Yan, Z., S. Bate, R. E. Chandler, V. Isham, and H. Wheater, 2002: An Analysis of Daily Maximum Wind Speed in Northwestern Europe Using Generalized Linear Models. *Journal of Climate*, **15,** 2073-2088, doi:10.1175/1520-0442(2002)015<2073:AAODMW>2.0.CO;2.

Yan, Z., S. Bate, R. E. Chandler, V. Isham, and H. Wheater, 2006: Changes in extreme wind speeds in NW Europe simulated by generalized linear models. *Theor. Appl. Climatol.*, **83,** 121-137, doi:10.1007/s00704-005-0156-x.

Yeh, P. J. F., and J. S. Famiglietti, 2008: Regional terrestrial water storage change and evapotranspiration from terrestrial and atmospheric water balance computations. *Journal of Geophysical Research: Atmospheres*, **113,** D09108, doi:10.1029/2007JD009045.

Yeh, P. J. F., M. Irizarry, and E. A. B. Eltahir, 1998: Hydroclimatology of Illinois: A comparison of monthly evaporation estimates based on atmospheric water balance and soil water balance. *Journal of Geophysical Research: Atmospheres*, **103**.

Appendix I - Statistical indicators of accuracy

Three usual statistical indicators of accuracy are the mean bias error (MBE), the mean absolute error (MAE) and the root mean square error (RMSE). Mean bias error provides information about the average difference in the mean over the entire dataset when compared against another reference series of values. Mean absolute error measures the average of magnitude of the errors. Root mean square error also measures the average of magnitude of the error, but uses the quadratic weighting, with results in large errors carrying more weight. Together, MBE, MAE, and RMSE can be used to assess the accuracy of a dataset compared to reference.

Systematic errors can be quantified by analysing the statistical bias, which can be measured using the following equation for mean bias error:

$$\mathrm{MBE} = \left[n^{-1} \sum_{i=1}^{n} e_i \right] = \overline{P} - \overline{O} \tag{I.1}$$

where, $\overline{O}$, and e_i are the model predicted and observed means, respectively. MAE, defined as the arithmetic mean of the absolute difference between the members of each pair, is zero when the forecast are perfect (P = O) and increases when the discrepancies between predictions and observations increases. This quantity is interpreted as the magnitude of the errors of forecasts.

$$\mathrm{MAE} = \left[n^{-1} \sum_{i=1}^{n} |e_i| \right] \tag{I.2}$$

Another common measure of the quality of forecasts is the MSE, the mean of the squared differences between pairs (P, O). This measurement is similar to the above, but in this case, uses the square of the differences instead of absolute value. MSE is more sensitive to large errors than the MAE, therefore higher values correspond to large discrepancies in the data. The squared root of the MSE, RMSE, with the same physical dimensions of the variable, indicates the typical magnitude of the prediction errors.

$$\mathrm{RMSE} = \left[n^{-1} \sum_{i=1}^{n} |e_i|^2 \right]^{1/2} \tag{I.3}$$

MBE can convey useful information, but should be interpreted cautiously since it is inconsistently related to typical error magnitude, other than being an underestimate ($\mathrm{MBE} \leq \mathrm{MAE} \leq \mathrm{RMSE}$).

Another indicator is the standard deviation (STD). STD is a measure of data spread given in the same units as the actual values. The STD is a good unbiased estimate for the normal distribution but can become a highly unreliable estimate if skewness exists in the data.

The forecast's quality can also be evaluated by analysing the ratio of Nash-Sutcliffe efficiency (NS), calculated from the simulation reference or observations and each of the simulations.

$$\mathrm{NS} = 1 - \frac{\sum (x - y)^2}{\sum (y - \overline{y})^2} \tag{I.4}$$

where xi and yi are simulated and measured observations, respectively; n is the number of paired observations and $\overline{y}$ is the mean of measured observations. The range of efficiency NS, proposed by Nash and Sutcliffe (1970), lies between 1.0 (perfect) fit and -∞. An efficiency lower than zero indicates that the mean value of the observed time series would have a better predictor than the model or, in other words, when the residual variance (described by the numerator in the expression above), is larger than the data variance (described by the denominator).

Appendix II - GLM Stochastic Weather Generator

II.1 Weather Generators

The lack of global meteorological observations to force model simulations is one of the problems in hydrological modelling. Whenever possible, observations should drive land surface and hydrological models. Unfortunately in most cases, when observations are present, only temperature and precipitation are measured routinely. In Chapter 2 a new forcing data, re-analysis based, for hydrological studies, was presented (Weedon et al., 2010, 2011). Such data were treated in a different way for the ERA-40 period (Chapter 2) and prior to the ERA-40 period (Chapter 3). Prior to 1958, the lack of reanalysis leads to the use of empirical correction methods that maintain the monthly properties of observed data.

In recent years numerous large-scale atmospheric forcing data sets have been developed without reanalysis products (Nijssen et al., 2001; Hirabayashi et al., 2005). Nijssen et al. (2001) produced a 14-yr global atmospheric data based on daily observations. Hirabayashi et al. (2005) created a 100-yr daily atmospheric forcing from monthly precipitation and temperature, applying statistical parameters derived from daily or 3-hourly observations.

Methods presented in Chapter 2 and Chapter 3 belong to a family of statistical methods, known as weather generators (WG). Weather generators are often used to provide input for hydrological modelling, producing a realistic daily variability. WG are applied point by point and, therefore, are not necessarily connected to large scale predictors. Nevertheless, WG reflect large-scale temporal variability.

There is a large number of weather generators proposed that differ in their assumption as well as their theoretical and technical complexity (Wilks and Wilby, 1999). The most popular approaches assume that the variable of interest can be described by a linear model including a first order autoregressive component, a Markov process (Wilby et al., 1999; Wilks and Wilby, 1999, Hessami et al., 2008; Furrer and Katz, 2007). Modern statistical tools, including ridge regression (Hessami et al., 2008) and generalised linear models (Furrer and Katz, 2007; Fealy and Sweeney, 2007), have extended weather generators. Weather Generators are popular statistical models of observed sequences of weather data at a certain site (Wilks and Wilby, 1999). Most of them focus on the daily time scale, but sub-daily models are also available (Katz and Parlange, 1995). Stochastic WG generally have a similar structure, with precipitation considered to be the primary variable and the others as secondary. The development of such models involves two steps: (1) modelling daily precipitation and (2) the remaining variables conditional on precipitation occurrence. Weather generators usually produce series at a daily time resolution of precipitation but also other variables dependent on precipitation such as maximum and minimum temperature, solar radiation, relative humidity and/or wind speed (Wallis and Griffiths, 1995; Parlange and Katz, 2000). Depending on whether the day is wet or dry, other meteorological variables are determined by regression relationships with precipitation and values of the variables on the previous day. The regression relationships maintain both the cross- and auto-correlations between and within each variable. The statistical properties of the simulated daily weather sequences are controlled by the parameters of the weather generator at a particular location. There are dependence between temperature and precipitation. The adequacy of the stochastic models varies with the climate characteristics of the locations. For example, Wilks (1999) found the first-order Markov model to be adequate for the central and eastern USA, but spell length models performed better in the western USA. Markov models estimate precipitation considering the probability of rainfall on a given day, conditional on whether it rained on previous days; while spell-length models take in account precipitation happening in spells of dry or wet days, with the length of a spell having a particular probability. An alternative approach would include stochastic mechanisms of storm arrivals able to produce the clustering found in observed sequences (e.g., Smith and Karr, 1985; Foufoula-Georgiou and Lettenmeier, 1986; Gupta and Waymire, 1991; Cowpertwait and O'Connell, 1997). Generalized Linear Models (GLM) are linear regression statistical

tools for temporal downscaling of meteorological variables; GLM are statistically more consistent than the semi-empirical models presented in Chapter 2 and Chapter 3.
Papers in the applied literature (Yan et al., 2002; Chandler and Wheater, 2002; Chandler, 2005; Furrer and Katz, 2007) have suggested some new solutions, within the framework of generalized linear models. GLMs can simplify the effort involved in the stochastic modelling of daily weather variables.
Generalized Linear Models are an extension of linear regression models (Coe and Stern, 1982; Stern and Coe, 1984; Chandler and Wheater, 2002). Its application is one of the possible solutions for creating time series of meteorological data that could be used to create an alternative meteorological forcing. The basic principle behind the generalized linear model is that the systematic component of the linear model can be transformed to create an analytical framework that closely resembles the standard linear model but accommodates a wide variety of nonnormal and noninterval measured outcome variables. An error component is distributed independently with mean zero and constant variance. A "link function" is employed to GLM to define the relationship between the systematic component of data and the outcome variable in such a way that asymptotic normality and constancy of variance are no longer required. In many situations, regression-like methods provide an appealing alternative; however, their potential has not been fully explored. This is largely because of perceived difficulties in representing the complex structure of climatological datasets in a regression model.
Furrer and Katz (2007) proposed a technique to fit stochastic weather generators to daily data, that can incorporate annual cycles or long-term trends, as well as, to condition the model on indices of large scales atmospheric or oceanic circulation such as the El Niño Southern Oscillation phenomenon, ENSO. In this appendix the methodology indicated by Furrer and Katz (2007) was generalized to the entire globe to create global synthetic data of precipitation and air temperature. The precipitation occurrence and intensity components of this GLM stochastic weather generator are essentially the same as those in Stern and Coe (1984), who used GLM to model daily precipitation amount as a chain dependent process with annual cycles in the parameters. The GLM model based on regression between daily temperature and precipitation is parameterised locally using current climate data, and then applied for an alternative present or future climate. This series of precipitation and temperature can be used to test the sensitivity of HTESSEL model to perturbed forcing. The main purpose of this study was to evaluate the implementation of a generalized linear model for the daily temperature and precipitation in all land points. Lastly, the weather generator time series were used to assess the new temperature and precipitation using the HTESSEL land surface model.

II.1.1 Application to daily weather

Stochastic models, such as GLMs, are widely used for precipitation and temperature modelling. GLMs offer a flexible and rigorous formal framework within which to distinguish between possible climate change scenarios and are able to deal with high levels of variability, such as those typically associated with daily precipitation sequences. This type of models can be a powerful tool for interpreting historical precipitation records (Chandler and Wheater, 2002). In addition to precipitation, stochastic GLM approach has been adapted to any meteorological variable, including temperature and wind speed (Yan et al., 2002; Yan et al., 2006).
Stochastic weather generators have a relatively simple structure, making feasible modelling multiple variables, incorporating annual cycles, and introducing other covariates, such as climate indices (e.g. the ENSO phenomenon, Furrer and Katz, 2007). Rainfall time series have been successfully fitted by generalized linear models (Coe and Stern, 1982; Stern and Coe, 1984). Yan et al. (2002, 2006) assessed GLM models to the daily maximum wind speed simulation in the north-western part of Europe and part of North Atlantic. Posteriorly, Furrer and Katz (2007) adjusted a regression model to the maximum and minimum temperature as well as rainfall on tropical site. They showed that the GLM approach could be applied to parametric weather generators, modelling more than one daily weather variable at a given site simultaneously. Furthermore, the occurrence in mid-summer rainfall in eastern China was modelled by Wang et al. (2010) using binomial generalized linear models based on observations. These models

included an intraseasonal variation, previous day's rainfall to represent the Markov chain structure of daily rainfall occurrence, and the south-north thermal gradient in eastern China, expressed by a zonal mean temperature difference in the region, to represent a large-scale climate background. For the interpretation of climate variability, this is probably more than adequate; however, if fitted models are subsequently to be used for risk assessment purposes, then the systematic tail structure may require further investigation. Posteriorly, high precipitation amounts were investigated by Furrer and Katz (2008). They focus on the parametric type of stochastic weather generator, introduced by Furrer and Katz (2007), in attempting to improve the simulation of high precipitation amounts. They relied on the statistical theory of extreme values to guide their choice of improvements on precipitation modelling. The main difficulties in GLM models are caused by the spatial nature of climate data. Chandler (2005) analysed spatial and temporal dependencies in climatological datasets. However, the relationships between variables tend to be similar at neighbouring stations in multisite modelling.

Precipitation Occurrence

The conditional probability of precipitation on day t (p_t) is the probability of a day is wet, $p_t = \Pr\{J_t = 1\}$. This occurrence depends on the previous day J_{t-1}, modelled as a first-order Markov chain. A binomial GLM with logistic link function, $g(x) = \ln\frac{x}{1-x}$, to link covariates is the ideal model to occurrence data, i.e. a 0 or 1 variable (Chandler and Wheater, 2002). The primary covariate is the precipitation occurrence on the previous day, J_{t-1}. Further covariates, such as a seasonal cycle or a climatic index can be introduced sequentially, decided by the BIC (Bayesian Information Criterion) criterion, or sequentially removed until finding the lesser AIC (Akaike Information Criterion).

Interaction terms between covariates and the occurrence of precipitation on the previous day allow different effects of covariates depending on the values of J_{t-1}, if this day was rainy or not. Interactions of a seasonal cycle with J_{t-1}, for example, allow for $p_{01}(t)$ and $p_{11}(t)$ to have different seasonal cycles. More precisely p_t is linked to J_{t-1} and the vector of covariates $\mathbf{Z_t}$. Specifying the predictands as the log-odds transformation of the precipitation probability ensures that the predicted values are correctly bounded so that negative probabilities are not possible:

$$\ln\frac{p_t}{1-p_t} = \mu + \alpha J_{t-1} + \mathbf{Z_t'\beta} + J_{t-1}\mathbf{Z_t'\gamma} \qquad \text{(II.1)}$$

$J_{t-1} = i, i = 0, 1$ is a binary variable representing the presence or absence of precipitation on the previous day, $\boldsymbol{\beta}$ and $\boldsymbol{\gamma}$ are the daily regression predictors, and the symbol $(')$ denotes transpose. Rearranging equation (II.1), we retrieve the transition probabilities of Markov chain:

$$p_{i,1}(t) = \frac{\exp(\mu + \alpha i + \mathbf{Z_t'\beta} + i\mathbf{Z_t'\gamma})}{1 + \exp(\mu + \alpha i + \mathbf{Z_t'\beta} + i\mathbf{Z_t'\gamma})} \quad i = 0,1 \qquad \text{(II.2)}$$

Besides a mean signal and the occurrence of rain on the precious day, a seasonal cycle was introduced using $C_t = \cos(2\pi \times t/365)$ and $S_t = \sin(2\pi \times t/365)$. Climatic indices can also be introduced, as well as interaction terms between the seasonal cycle and the previous day's occurrence, i.e. $J_{t-1}C_t$ and $J_{t-1}S_t$, to the binomial GLM for precipitation occurrence. Following (II.1), that summarizes the covariates of precipitation occurrence modelling, equation (II.2) for precipitation occurrence can be rewritten as:

$$\ln\frac{p_t}{1-p_t} = \mu + \alpha J_{t-1} + \beta_1 C_t + \beta_2 S_t + \beta_3 E_t + \gamma_1 J_{t-1}C_t + \gamma_2 J_{t-1}S_t + \beta_4 J_{t-1}E_t \qquad \text{(II.3)}$$

β_1 and β_2 determine the phase and amplitude of the sine wave for the annual cycle in these conditional probabilities, γ_1 and γ_2 allow the annual cycle to be separate for the two conditional probabilities.

II.1.1.1 Precipitation Intensity

If a day is wet, a rainy day ($J_t = 1$), the amount of precipitation on such day has to be determined. Precipitation intensity, I_t, on wet days is frequently modelled using a gamma GLM with a logarithmic link function, or a similar probability distribution function. Its conditional distribution has a constant shape parameter, independent of the vector of covariates $\mathbf{Z_t}$ and the mean (Furrer and Katz, 2007). I_t is gamma distributed with conditional mean μ_t on day t:

$$\ln \mu_t = \mu + \mathbf{Z_t'\beta} \tag{II.4}$$

where t is such that $J_t = 1$ and μ and vector $\boldsymbol{\beta}$ contain parameters. The logarithm of the mean precipitation amount in equation (II.4) ensures that negative mean precipitation amounts are not possible. The intensity on a given day, by assumption, does not depend on the intensity or occurrence the day before (no autoregressive type term). The seasonal cycle and the climate index are considered as covariate in the gamma GLM. The covariates of precipitation intensity model, represented by equation (II.4), are:

$$\ln \mu_t = \mu + \beta_1 \cos\frac{2\pi t}{T} + \beta_2 \sin\frac{2\pi t}{T} + \beta_3 Z_t \tag{II.5}$$

Here the coefficients β_1 and β_2 determine the phase and amplitude of the sine wave for the annual cycle in the mean intensity.

II.1.1.2 Maximum and minimum temperature

Minimum, X, and maximum,Y, temperature are modelled using separate first order autoregressive AR(1) processes with covariates, which are coupled through the introduction of lagged values of the respective other temperature variable as a covariate. At time t, the temperature depends only on their value at time $t-1$ and that, given some appropriate covariates such as a seasonal cycle, they are normally distributed.

$$X_t = \mu_{X,0} + \mu_{X,1}J_t + \phi_X X_{t-1} + \psi_X Y_{t-1} + \mathbf{Z_t'\beta_X} + \varepsilon_{X,t} \tag{II.6}$$

$$Y_t = \mu_{Y,0} + \mu_{Y,1}J_t + \phi_Y Y_{t-1} + \psi_Y X_t + \mathbf{Z_t'\beta_Y} + \varepsilon_{Y,t} \tag{II.7}$$

where $\varepsilon_{X,t}$ and $\varepsilon_{Y,t}$ are the error terms, uncorrelated (i.e. no cross correlation), zero-mean normal with constant conditional variances σ_{X^2} and σ_{Y^2} (i.e. independent of t). Additional covariates, such as a seasonal cycle or a climate index, are given by the vector $\mathbf{Z_t}$. $\mu_{X,1}$ and $\mu_{Y,1}$allow for the mean Tmin and Tmax, respectively, to be dependent on whether or not precipitation occurs. ϕ_X and ϕ_Y allow dependence on the same temperature on the previous day (first-order autocorrelation); ψ_X and ψ_Y allow dependence between Tmin and Tmax. They correspond to the lag 1 cross correlation for Tmin and the lag 0 cross correlation for Tmax conditionally on all the other variables in the models. Tmin, observed in the early morning hour of each day t, is modelled before Tmax (usually in the early afternoon). This mean that the Tmin of day t is closer, in temporal distance, to the Tmax of day $t-1$ than the Tmax of day t is to the Tmin of day $t-1$. This approach does not guarantee that Tmax is higher than Tmin. A seasonal cycle given by C_t and S_t and a climate index E_t, were associated to the equations (II.6) and (II.7). Therefore the temperature variables are modelled by:

$$X_t = \mu_{X,0} + \mu_{X,1}J_t + \phi_X X_{t-1} + \psi_X Y_{t-1} + \beta_{X,1}C_t + \beta_{X,2}S_t + \beta_{X,3}E_t + \varepsilon_{X,t} \tag{II.8}$$

$$Y_t = \mu_{Y,0} + \mu_{Y,1}J_t + \phi_Y Y_{t-1} + \psi_Y X_t + \beta_{Y,1}C_t + \beta_{Y,2}S_t + \beta_{Y,3}E_t + \varepsilon_{Y,t} \tag{II.9}$$

The normally distributed errors $\varepsilon_{X,t}$ and $\varepsilon_{Y,t}$ are uncorrelated. The models of maximum and minimum temperatures, modelled separately, are applied using lm function instead of glm function previously used. The best model is selected automatically according to the AIC criterion.

II.1.2 Summary description

The covariates and its description of each GLM model (precipitation occurrence, precipitation intensity, maximum and minimum of temperature) are summarized in Table II.1. Precipitation occurrence, p_t, depends on the previous day modelled by a first-order Markov chain; β_1 and β_2 terms introduce a seasonal cycle, while $\boldsymbol{\gamma}$ correspond to interaction terms between seasonal cycle and the previous day's occurrence; β_3 and β_4 introduze a climate effect. If it is a rainy day, the precipitation intensity is estimated by a gamma GLM or similar probability distribution function. An annual cycle is imposed (β_1 and β_2 terms) in the form of a sine wave and the climate index effect. Air temperature, maximum and minimum, are determinate after precipitation occurrence using separate first order autoregressive processes AR(1). Both temperatures are coupled with the introduction of lagged values of the respective other temperature variable. As in general, the minimum of temperature occurs in the early morning hours of the day, Tmin is estimated before Tmax. In addition to the referred terms, is still introduced a seasonal cycle as well as climate index. The stochastic behaviour of both temperatures is introduced by normally distributed errors, $\varepsilon_{X,t}$ and $\varepsilon_{Y,t}$.

Table II.1: List of covariates and their description of GLM model: logistic GLM for precipitation occurrence, $p_t = P_r\{J_t = 1\}$; Gamma GLM for mean precipitation intensity, μ_t; and coupled univariate models for minimum (X_t) and maximum (Y_t) daily temperature, essentially equivalent to bivariate AR(1). $C_t = \cos(2\pi \times t/365)$ and $S_t = \sin(2\pi \times t/365)$.

Model	Covariates	Covariate category
Precipitation occurrence $\ln \frac{p_t}{1-p_t}$	μ	Mean
	αJ_{t-1}	Autocorrelation
	$\beta_1 C_t + \beta_2 S_t$	Seasonality (Single annual cycle)
	$\beta_3 E_t$	Single climate index effect
	$\gamma_1 J_{t-1} C_t + \gamma_2 J_{t-1} S_t$	Interaction (Two annual cycles)
	$\beta_4 J_{t-1} E_t$	Different climate index effect
Precipitation intensity $\ln \mu_t$	μ	Mean (Single gamma distribution)
	$\beta_1 C_t + \beta_2 S_t$	Seasonality (Annual cycle)
	$\beta_3 Z_t$	Climate index effect
Minimum temperature X_t	$\mu_{X,0} + \mu_{X,1} J_t$	Mean (Dependence on precipitation)
	$\phi_X X_{t-1}$	Autoregressive term
	$\psi_X Y_{t-1}$	Dependence: cross-correlation term
	$\beta_{X,1} C_t + \beta_{X,2} S_t$	Seasonality: Seasonal cycle
	$\beta_{X,3} E_t + \varepsilon_{X,t}$	Climate index and error
Maximum temperature Y_t	$\mu_{Y,0} + \mu_{Y,1} J_t$	Mean (Dependence on precipitation)
	$\phi_Y Y_{t-1} + \psi_Y X_t$	Autoregressive/dependence: cross-correlation term
	$\beta_{Y,1} C_t + \beta_{Y,2} S_t$	Seasonality (Seasonal cycle)
	$\beta_{Y,3} E_t + \varepsilon_{Y,t}$	Climate index and error

II.2 Model Fitting

The following section assesses the ability of the GLM to capture important aspects of WFD precipitation and temperature. The fitted model was used to simulate daily rainfall and temperature sequences for 44 years using data from daily WFD, since 1958 to 2001. For simplicity, the processes (occurrence, intensity, maximum and minimum temperatures) are treated separately in the model identification exercise. For a detailed study some sites with different climate characteristics were selected. The method of selection ensures that the estimates of regression parameters associated with each explanatory variable are statistically significant. All the concepts are easy to implement using readily available software; moreover, they are relatively cheap computationally and are therefore suitable for use with large datasets. All models are fitted with R1 (R Core Team, 2012), using the functions glm or lm. They require only an additional parameter to specify the variance and link functions. The main objective is to consider the effects of different covariates in the models for precipitation and temperature. Covariates were sequentially removed until finding the lesser AIC.

[1]R is a freely available (at no cost) software environment for statistical computing and graphics (http://www.r-project.org/).

Two sources of precipitation and air temperature were used: daily mean and maximum and minimum of temperature from WFD and monthly data from CRU and GPCC. The daily data span four decades, the period 1958-2001, but only 1980-2001 were analysed. The bias error present in GLM output was removed and applied a similar methodology as presented in Chapter 2 and Chapter 3. Eventually global time series of daily temperature and precipitation are disaggregated from daily to 3-hourly data and used to conduct HTESSEL model from 1980 to 2001 (see Chapter 3, section 3.3).

II.2.1 Global modelling calibration

GLM model calibration was completed for global scale using 44 years (1958 to 2001) from WFD daily precipitation and temperature (maximum and minimum). The covariates of each model (occurrence, intensity and both temperatures), were estimated locally. The estimated coefficients for all components of the GLM weather generator fitted to land are represented in Figure II.1, Figure II.3, Figure II.5 and Figure II.6. White spaces on maps indicate that the specified covariate was not selected for the model.

II.2.1.1 Precipitation

The pattern of occurrence coefficients (Figure II.1), reflects the global variability of logarithm of precipitation's occurrence. Lower values of precipitation occurrence are located in North Africa, while higher values are in tropical zone, as expected. The most influent covariate is the occurrence of rain on the previous day (p_{11}), Figure II.1b, indicating that a rainy day is, in most cases, followed by a rainy day. Furthermore the seasonality of p_t, represented by sine and cosine covariates, varies locally. The highest probabilities correspond to South America, South of Africa, and Northern part of Australia (orange at panels c and d of Figure II.1). The seasonality, imposed by β terms, reflects the difference between the different precipitation regimes while interaction terms between seasonality and the previous day's occurrence, γ_1 and γ_2, allow different cyclic behaviour of the model. In regions as Eurasia, northern Africa (desert), Canada and southern part of South America these terms were not selected.

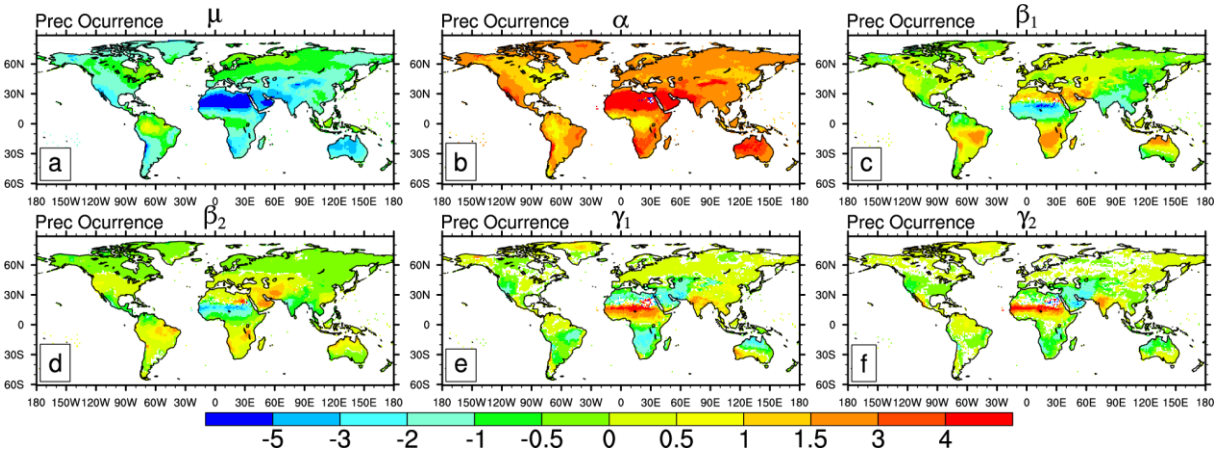

Figure II.1: Estimated coefficients of the precipitation occurrence model, pt (see Table II.1): μ intensity; α previous day's occurrence; $\beta_1$and β_2 annual cycle; γ_1 and γ_2 interaction terms, between the seasonal and the previous day's occurrence. Precipitation occurrence coefficients are adimensional.

To estimate the amount of daily precipitation the shape of gamma distribution and its relative standard error were calculated (Figure II.2). As the shape factor increases, the mean increases and the skewness decreases, to the point where probability density function is almost symmetrical. Higher values of the shape parameter provides a more intense precipitation (for example, in tropical areas). Observed pattern agrees with precipitation, as expected.

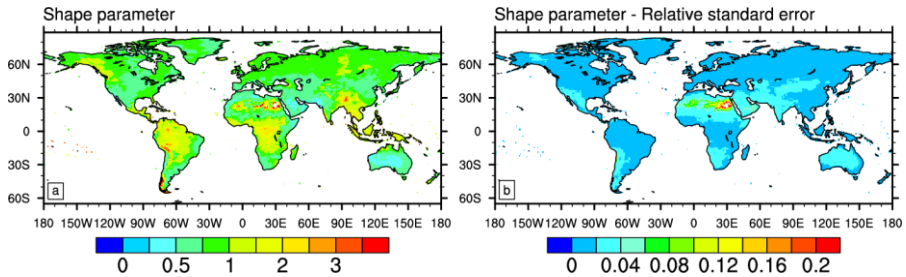

Figure II.2: Shape parameter of the gamma distribution after fitting a Gamma generalized linear model. At the left side, a, is the maximum likelihood estimate and at right, b, is the approximate standard error, the squared-root of the reciprocal of the observed observation, divided by the estimate value, the relative standard error.

Precipitation intensity covariates are presented in Figure II.3. μ_t is the mean intensity of precipitation and β terms reflect the seasonality of precipitation intensity.

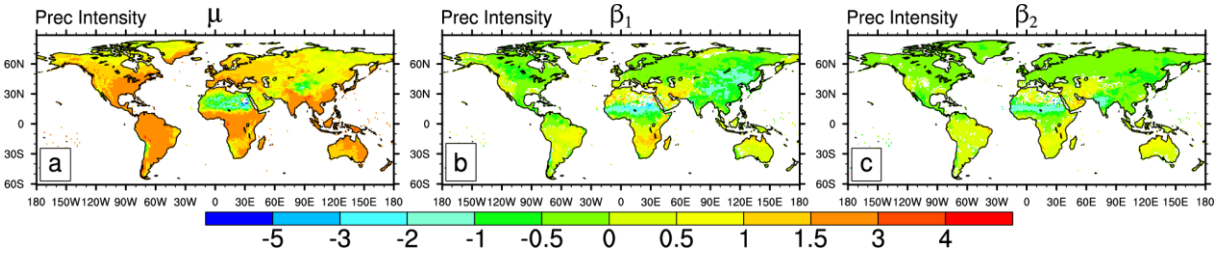

Figure II.3: Estimated coefficients of the precipitation intensity model, μ_t (see Table II.1): μ is the mean intensity; β_1 and β_2 the annual cycle. Units are in mm.

II.2.1.2 Air temperature

Daily temperature variability is imposed by a random error described, $\varepsilon_{X,t}$ e $\varepsilon_{Y,t}$ for minimum and maximum temperature, respectively, by a normal distribution with expected value zero and standard deviation (a constant variance of σ_{X^2} and σ_{Y^2}). The standard deviation for Tmin and Tmax models are presented by Figure II.4, which varies between 0 and 5 ºC.

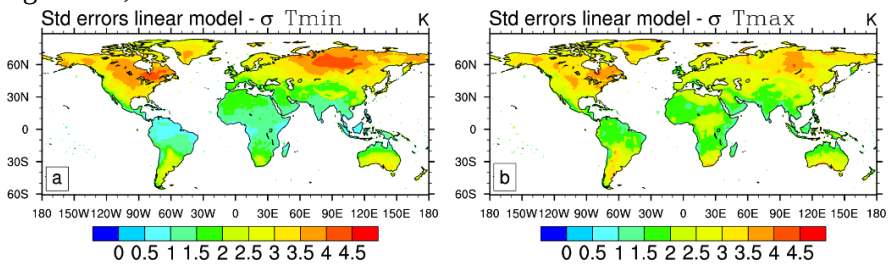

Figure II.4: The square root of estimated variance (σ, standard deviation) of the random error: a) σ_{Tmin}, minimum temperature; b) σ_{Tmax}, maximum temperature.

Figure II.5 and Figure II.6 list the parameters estimate of GLM weather generator for minimum (Tmin) and maximum temperature (Tmax), respectively.

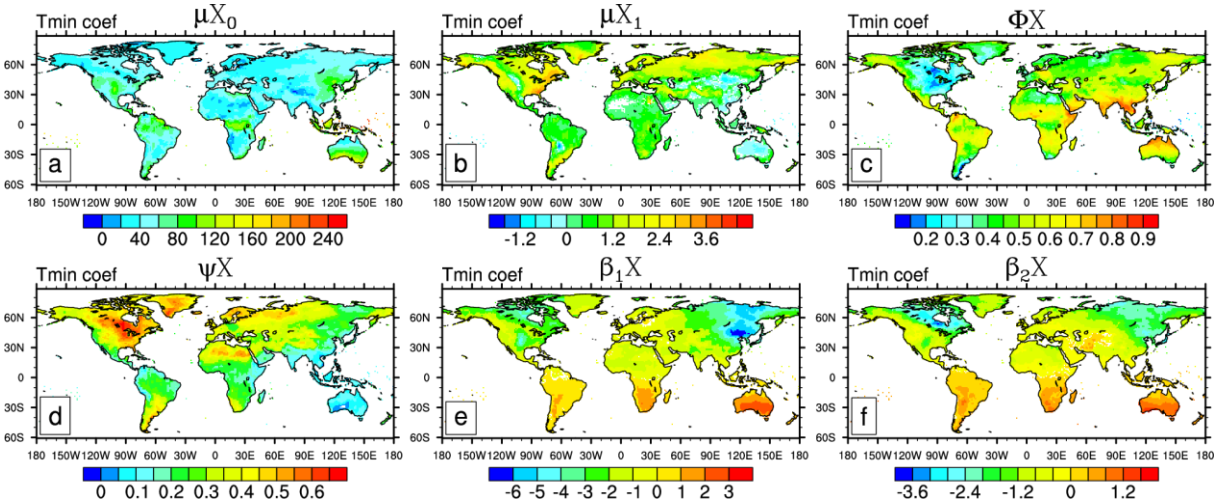

Figure II.5: Global map of estimated coefficients of minimum temperature, X (see Table II.1): $\mu_{X,0} + \mu_{X,1}$, dependence on precipitation; ϕ_X, autoregressive term; ψ_X, crosscorrelation term; $\boldsymbol{\beta}$ seasonal cycle.

μ_{X_0} and μ_{X_1} coefficients are the annual mean of maximum temperature in dry and wet days. Φ_Y and ψ_Y coefficient reflects the autoregressive and crosscorrelation terms. $\beta_{1,2}$ are the seasonal terms.

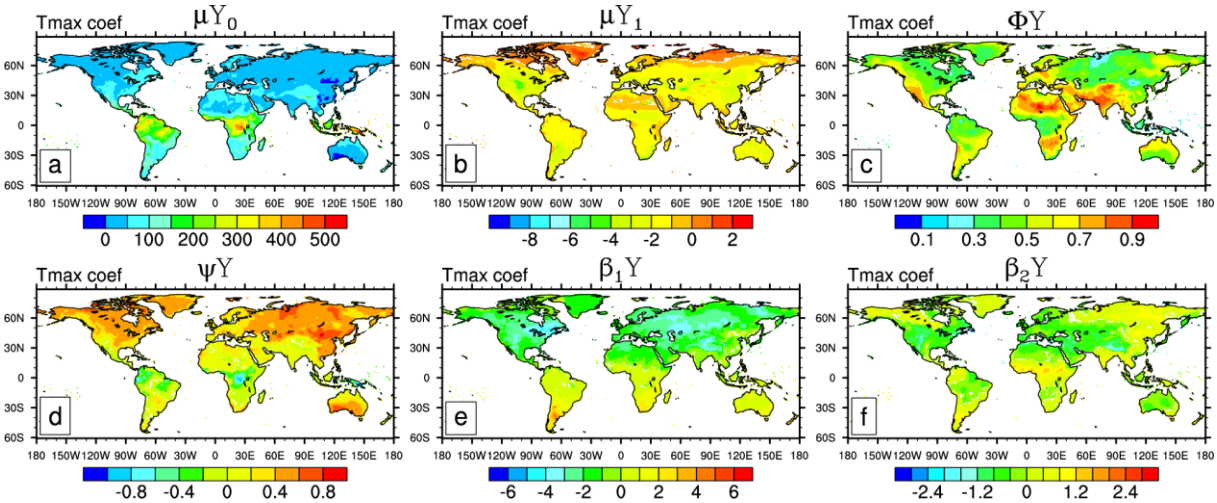

Figure II.6: As Figure II.5, but for maximum temperature, Y, (see Table II.1): dependence on precipitation ($\mu_{Y,0} + \mu_{Y,1}$); ϕY_{t-1}, autoregressive term; $\psi_Y X_t$, crosscorrelation term; $\boldsymbol{\beta}$, seasonal cycle.

II.2.2 Performance of GLM modelling

In this section, the GLM described above was applied to reproduce WFD data which was analysed on two spatial scales: global average and a few selected grid points. The following section summarises the results of the stepwise regression, used for model identification for land points considered.

The aim of this work was to test the applicability of a GLM to simulate precipitation and temperature as well as to assess its performance over land. GLM model, calibrated by daily precipitation and maximum and minimum temperatures from WFD dataset (coefficients of calibration were discussed on previous figures: Figure II.1, Figure II.3, Figure II.5 and Figure II.6) is ready to reproduce original data (daily data from WFD dataset). To analyse the performance of GLM model a set of data were created and compared with calibration data before any correction (se next section, Table II.3). The data produced, although not representing any given year, were compared with WFD data at daily scale. After model adjustment resulting data are able to generate daily series of precipitation and air temperature statistically consistent and comparable calibration data (daily average of WFD).

One way to show the distribution of data is a boxplot analysis. Boxplots of precipitation (wet days) and temperature (maximum and minimum) in wet and dry days are presented in Figure II.7 and Figure II.8, respectively for each land points selected. Precipitation seems well represented, although presenting a slight difference in tropical wet climate where variability of GLM precipitation is lower than WFD precipitation. In general, fitted data (GLM) presents lower precipitation values (except into Mediterranean climate), indicating that extreme values could not be well represented by GLM product. Remember that this analysis was carried out before the application of corrections (wet or/and bias correction). The most notable difference was found for temperature in dry days in continental subarctic climate. In both cases, calibrate or modelled data, temperature (maximum and minimum) is slightly skewed to higher temperature.

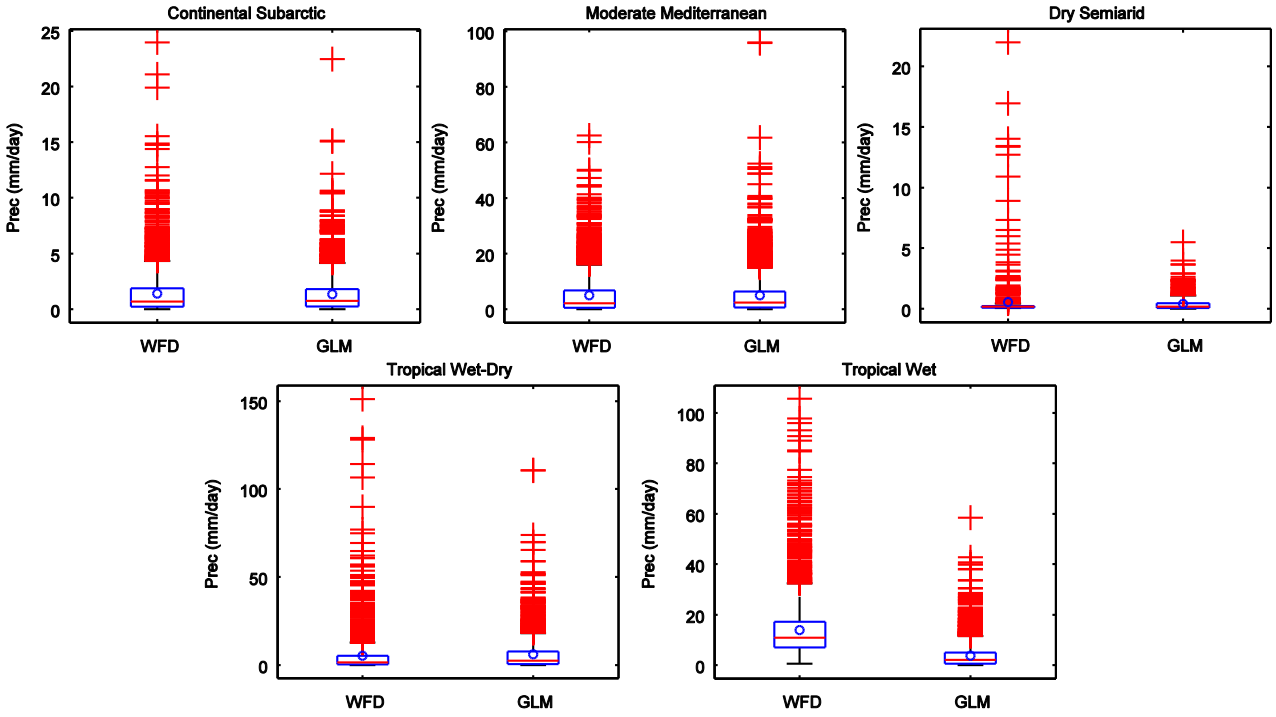

Figure II.7: Boxplot of daily precipitation for WFD and GLM data (daily values) for 20 years, from 1980 to 2001. On each box, the central mark is the median, the edges of the box are the 25th and 75th percentiles (q1 and q3 quantiles), the whiskers extend to the most extreme data points not considered outliers, and outliers are plotted individually. Outliers are plotted if they are larger than $q_3 + 1.5(q_3 - q_1)$ or smaller than $q_1 - 1.5(q_3 - q_1)$.

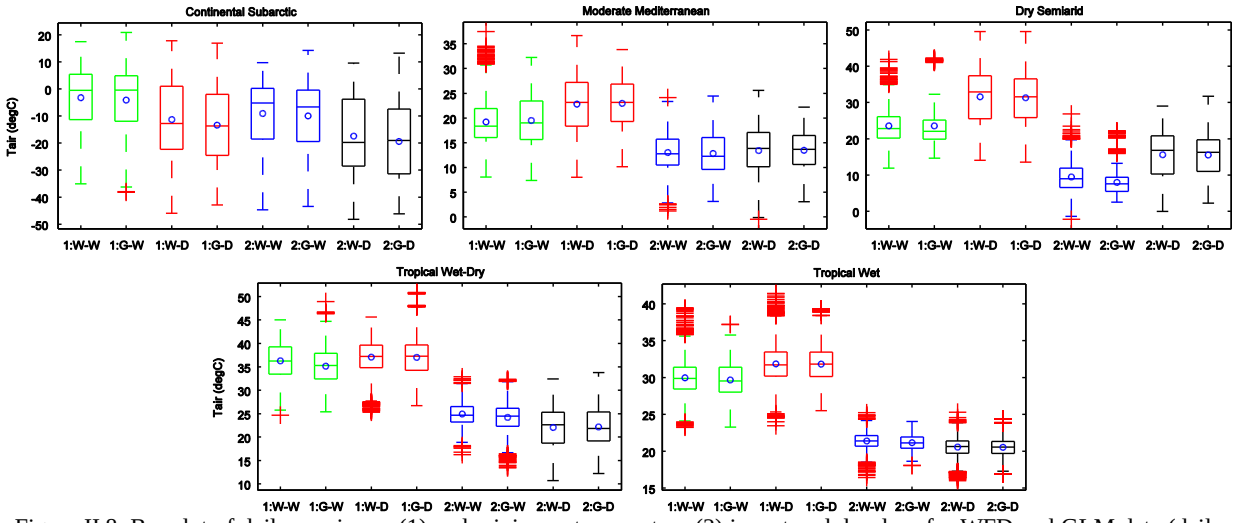

Figure II.8: Boxplot of daily maximum (1) and minimum temperature (2) in wet and dry days for WFD and GLM data (daily values) from 1980 to 2001. On each box, the central mark is the median, the edges of the box are the 25th and 75th percentiles (q1 and q3 quantiles), the whiskers extend to the most extreme data points not considered outliers, and outliers are plotted individually. Outliers are plotted if they are larger than $q_3 + 1.5(q_3 - q_1)$ or smaller than $q_1 - 1.5(q_3 - q_1)$.

Figure II.9 display quantile-quantile plots of daily precipitation and air temperature (maximum/minimum) at dry and wet days from GLM model against calibration data, WFD daily data. Air temperature series, Tmax and Tmin, seem to have the same type of distribution (the qq-plot is a straight line), showing a slight bias in the highest temperature (Figure II.9, bottom line). However, for precipitation series, this only happens in Mediterranean and tropical wet climates at lighter intensities. In dry semiarid and tropical wet-dry, precipitation is underestimated. In the first case the model does not produce enough precipitation. These results revel a dependency on type of precipitation: fairly realistic (unbiased) at low intensities, but underestimated for moderate and high intensities in most places.

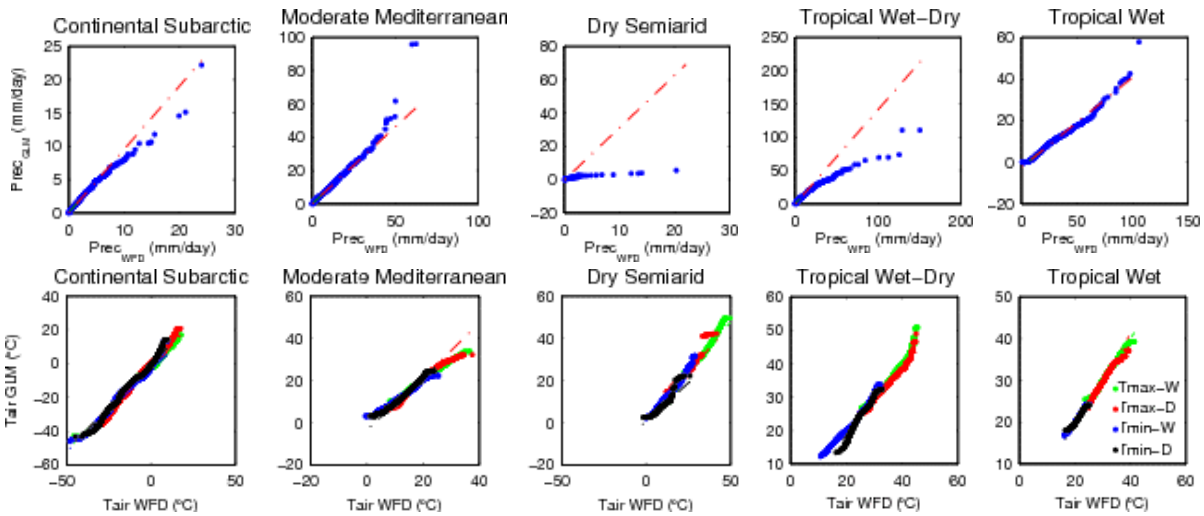

Figure II.9: Quantile-quantile plot of daily precipitation (top line) and maximum and minimum of temperature from GLM model against WFD data. Green and blue dots at bottom line are maximum and minimum temperature at wet day, while red and black dots are in dry days.

II.2.2.1 Seasonal cycle

Seasonal behaviour of global annual cycle of precipitation (first column) and temperature (maximum and minimum) estimated by GLM model (without bias correction) and WFD data is represented in Figure II.10. Boxplots represent the variability of GLM daily data while green crosses and red dots represent the monthly mean from WFD and GLM daily data, respectively. Continental subartic climate air temperatures are overestimated from January to March, revealing limitations of air temperature. Air temperature (maximum and minimum) in tropical wet-dry climate show a few limitations in dry season.

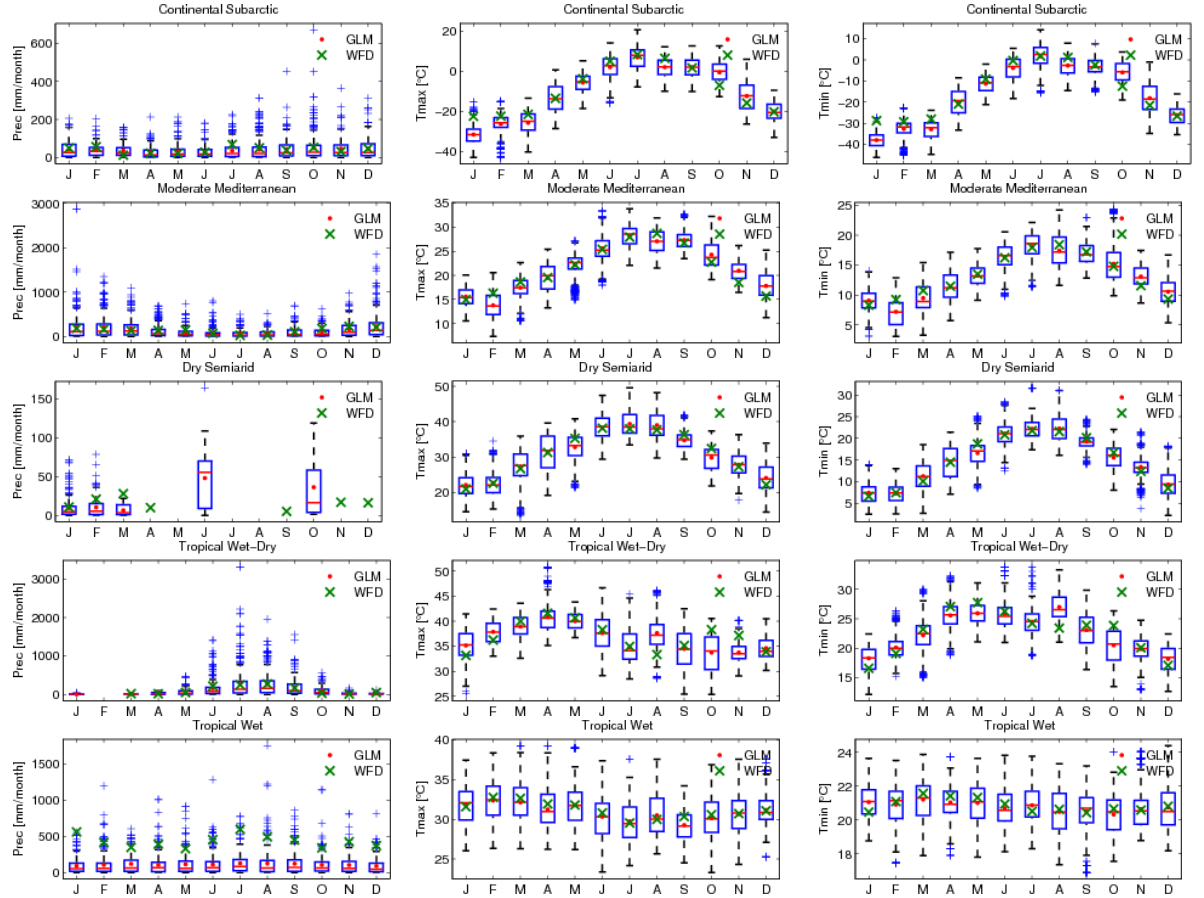

Figure II.10: Boxplot of global precipitation and temperature (maximum and minimum) per month (daily data). Green crosses correspond to daily mean of WFD maximum temperature (1980 to 2001) and red dots to daily mean from GLM model. Different scales. Units are in Celsius degrees and millimetres per month, respectively.

The seasonal behaviour of WD (wet days) is quite similar to WFD's wet days, indicating that GLM model is able to reproduce a similar number of WD (not shown). All sites follow the precipitation seasonal cycle; however, in March, June and July, the number of WD is overestimated in Moderate Mediterranean climate. The largest differences occur during the summer in the subarctic and Mediterranean climate, with overestimation of wet days. In dry semiarid, during November to January, the number of fitted wet days is lesser than observed wet days. The difference is higher than 10 days in November and December. Due to its nature, precipitation is the variable with the largest differences between original and simulated data, blue and pink bars, respectively. In dry semiarid climate the precipitation doesn't excess 8 mm per month. Precipitation was underestimated from October to January. There are no significant differences in temperature, except in October for tropical wet-dry climate.

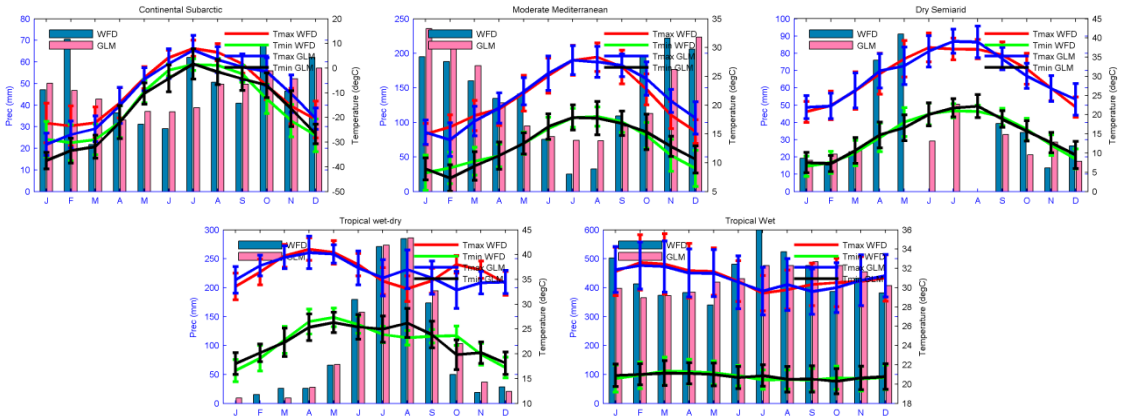

Figure II.11: Average monthly number of WD per month: WFD at blue and GLM at pink. Annual cycle for precipitation and maximum and minimum temperature.

II.2.3 HTESSEL modelling

In order to produce plausible time series of precipitation and air temperature, the fitted model was employed, followed by daily disaggregation to 3-hourly data (see Chapter 3, section 3.3) and, finally the wet-days and bias correction indicated by Weedon et al. (2011). Eventually, the HTESSEL model was forced by WFD off-line atmospheric forcing variables at a 3-hourly time interval replacing the temperature and precipitation by the new data (see Table II.3).

To assess the performance of HTESSEL when forced by GLM model data, 10 time series of precipitation and temperature (maximum and minimum) were created for a selection of 5 sites. These time series aimed to show the variability intrinsic to the GLM (the random factor); these differences were not relevant and will not be presented. Apart from other variables (see Chapter 4), land surface models, such as HTESSEL, need, consistent time series of precipitation (rainfall and snowfall, separately) and air temperature, to simulate the hydrology at the surface.

First, GLM precipitation and temperature were produced; then the wet days correction was applied to precipitation, removing the excess of wet days compared to CRU wet days; finally, biases were removed to recreate time series of precipitation, GPCC and CRU version, and temperature from 1980 to 2001 (see methodology in Table II.2). The split between rain and snow was made considering as snowfall all precipitation occurring in subfreezing temperatures. Bias correction was also applied to air temperature data with the corresponding adjustment in specific humidity.

Table II.2: Methods applied in rainfall, snowfall and air temperature.

Method		**Rainfall**	**Snowfall**	**Tair**
Disaggregation	Daily	GLM: Precipitation		GLM: Tmax; Tmin
	3 hourly	Cascade model/ Uniform model		Sinusoidal model
Correction	Wet days	CRU TS 2.1	CRU TS 2.1	-
	Bias	CRU TS 2.1 / GPCCv4	CRU TS 2.1 / GPCCv4	CRU TS 2.1

We investigate the use of the statistical general linear model to describe data from a suite of HTESSEL integrations, so that each of the integrations is a combination between WFD, the calibration data and GLM data (description in Table II.3).

Table II.3: Description of HTESSEL integrations. The forcing data consists of a mixture between WFD and data generated by the GLM (precipitation or air temperature). Both variables were bias corrected by GPCC and CRU monthly observations. Specific humidity were also corrected to avoid supersaturation.

Simulation	**Forcing data**	
	WFD	**GLM**
WFD (GPCC)	Prec GPCC (unbiased)	-
WFD (CRU)	Prec CRU (unbiased)	-
GLM (TQ)	Others	Tair and Qair
GLM (Prec-G)	Others	Prec GPCC (unbiased)
GLM (Prec-C)	Others	Prec CRU (unbiased)
GLM (TQP-G)	Others	Prec GPCC (unbiased), Tair and Qair
GLM (TQP-C)	Others	Prec CRU (unbiased), Tair and Qair

Continental water balance and soil moisture were analysed and compared with WFD simulations (CRU and GPCC version) at a global scale from 1980 to 2001. Energy balance at the surface is not affected at monthly, daily or hourly scale (result not shown).

II.2.3.1 Global water balance

The annual cycle of the global mean water cycle over land is presented in Figure II.12. Most differences lie between simulations with WFD precipitation (both WFD and GLM (TQ) simulations on Table II.3) and GLM precipitation, therefore, more precipitation (also evapotranspiration) occurs with WFD precipitation. The total runoff does not appear to have a significant seasonal variation.

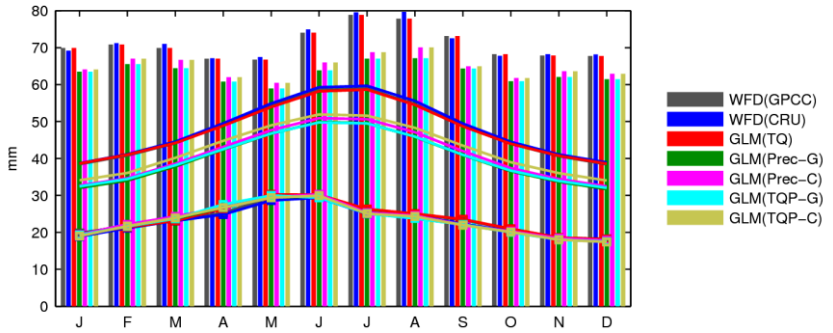

Figure II.12: Annual cycle of global land water balance components for 1980-2000: precipitation (bars), evapotranspiration (undotted lines) and total runoff (squares). Each simulation are represented by one colour. Units are in millimetres per month.

In the following section we present a comprehensive analysis to identify the most vulnerable regions to soil moisture content. The marked difference between GLM and WFD precipitation has a significant impact on the overall evapotranspiration (Figure II.12) affecting also the content of SM.

II.2.3.2 Soil water

The retention of moisture, or water, in the soil and the attendant runoff from naturally occurring rainfall or snow melt depends of quantity of available water at surface. Soil moisture from HTESSEL integrations (Table II.3) was assessed, to evaluate model's accuracy time series of the four layer's integrated soil moisture content is shown in the Figure II.13 for five selected points.

Most obvious differences are located in the continental subarctic and semi-arid climate, reflecting the differences in precipitation forcing. Differences in the WFD precipitation forcing (Prec-C – Prec-G) are larger than corresponding differences in GLM forcing. There is a clear impact on soil water, especially during the initial period (1985-1990) of the Continental subarctic. In boreal regions, the scatter in soil water reflects the partition of precipitation into rain and snow and, to a lesser extent, rainfall at negative temperatures and air temperature.

While HTESSEL integration show good skills in capturing soil surface variability for moderate Mediterranean and tropical wet-dry climate, they tend to overestimate SM for moderate Mediterranean and underestimate for wet-dry climate, due to underestimation of precipitation.

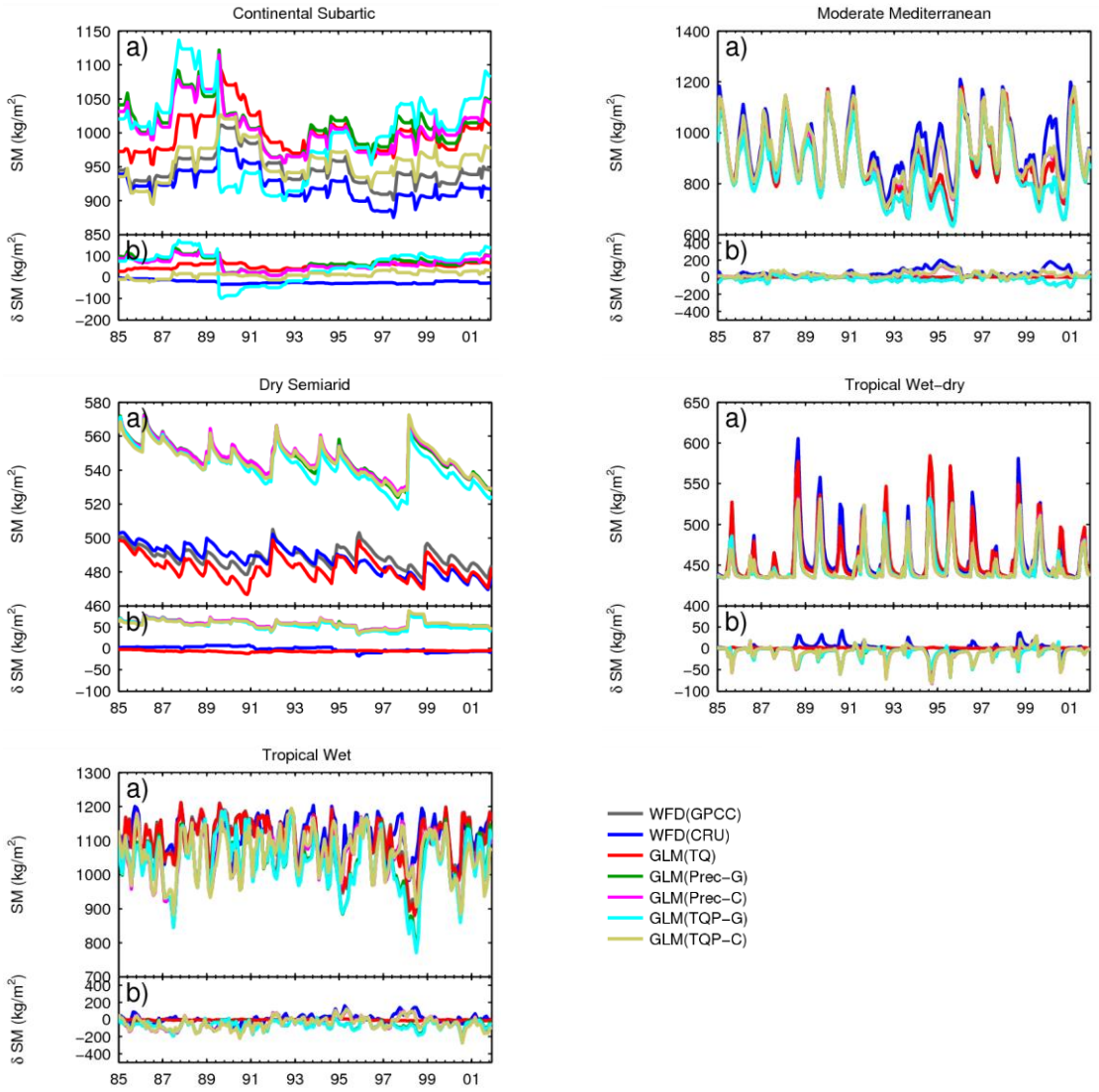

Figure II.13: Time series of monthly (a) soil moisture (four layer integrated) and (b) the difference between each simulation and WFD(GPCC) simulation from 1985 to 2001 of: WFD (GPCC), WFD (CRU), GLM (Prec-G), GLM (Prec-C), GLM (TQ), GLM (TQP-C), and GLM (TQP-G) (see Table II.3). Units are um kg m-2.

The major discrepancies are associated with precipitation input, in contrast with GLM air temperature (Figure II.14, panel b). Figure II.15 and Figure II.16 coefficient of correlation, ρ, and Nash–Sutcliffe model efficiency coefficient, NS), respectively, show the performance of GLM model to simulate monthly soil moisture content at global scale for 1985 to 2001. Pattern of correlation and efficiency of SM reveals GLM precipitation (Figure II.15 and Figure II.16, panel c and d) affect areas generally throughout mountainous, ice-covered and arid regions (e.g. Himalayas, Andes and Rocky Mountains, Greenland, Australian and Sahara desert). However, with GLM air temperature, simulated SM do not change much, even though Greenland and high latitudes of Eurasia have lower correlation and coefficient of efficiency (Figure II.15 and Figure II.16, panel b).

According to simulation results of soil moisture, GLM (TQ) has a good accuracy (NS near 1) except at high latitudes. In the remaining simulations the greatest differences are found in the deserts (Sahara and inner Australia) as well as in the Himalayas Mountains and Greenland (ice-covered regions).

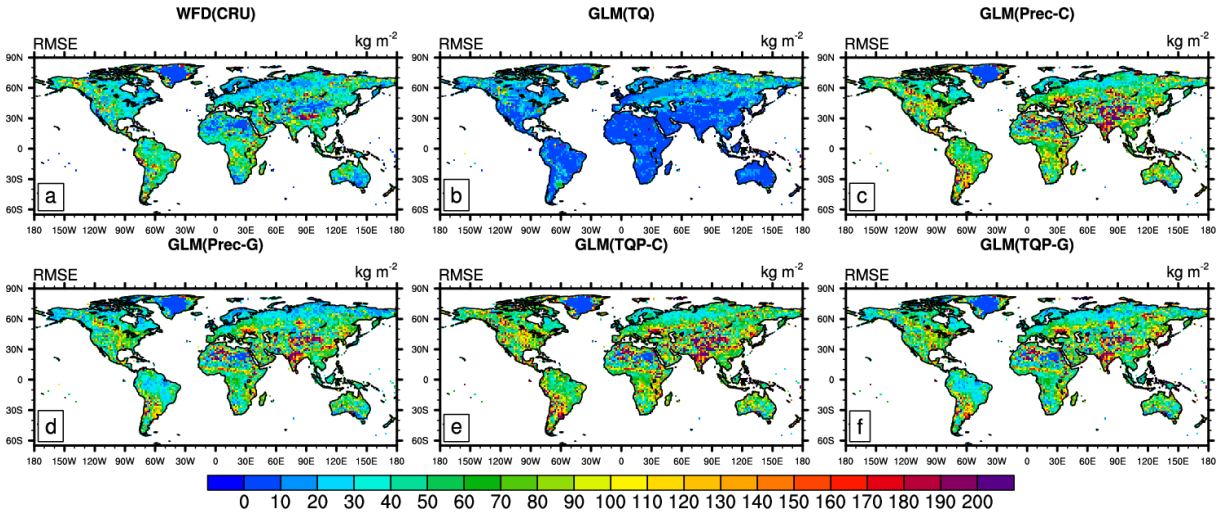

Figure II.14: Root mean square error of monthly soil moisture from 1985 to 2001 between WFD (GPCC) and: WFD (CRU), GLM (Prec-C), GLM (Prec-G), GLM (TQ), GLM (TQP-G), and GLM (TQP-C).

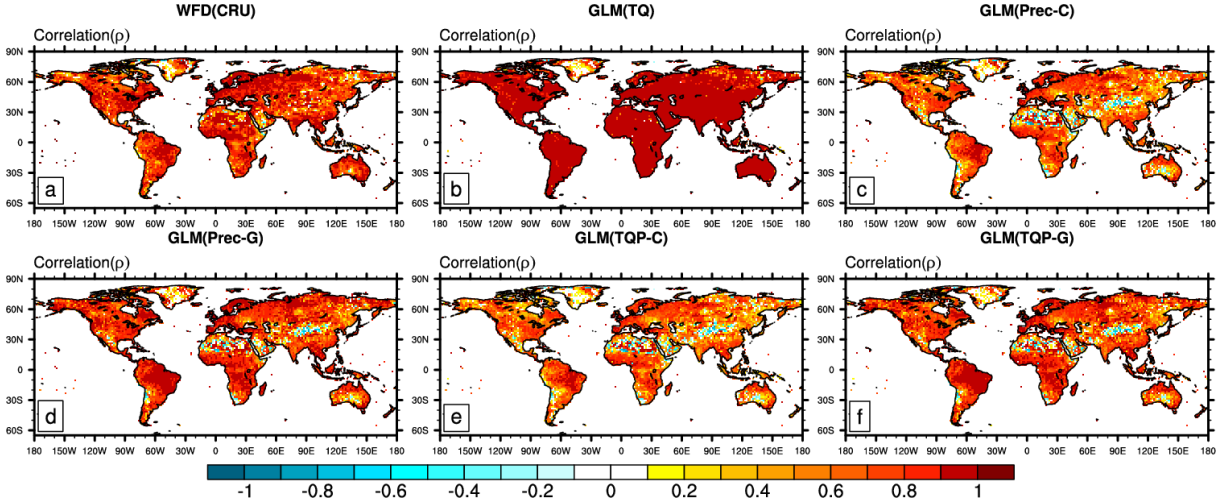

Figure II.15: Coefficient of correlation of monthly soil moisture from 1985 to 2001 between WFD (GPCC) and: WFD (CRU), GLM (Prec-C), GLM (Prec-G), GLM (TQ), GLM (TQP-G), and GLM (TQP-C).

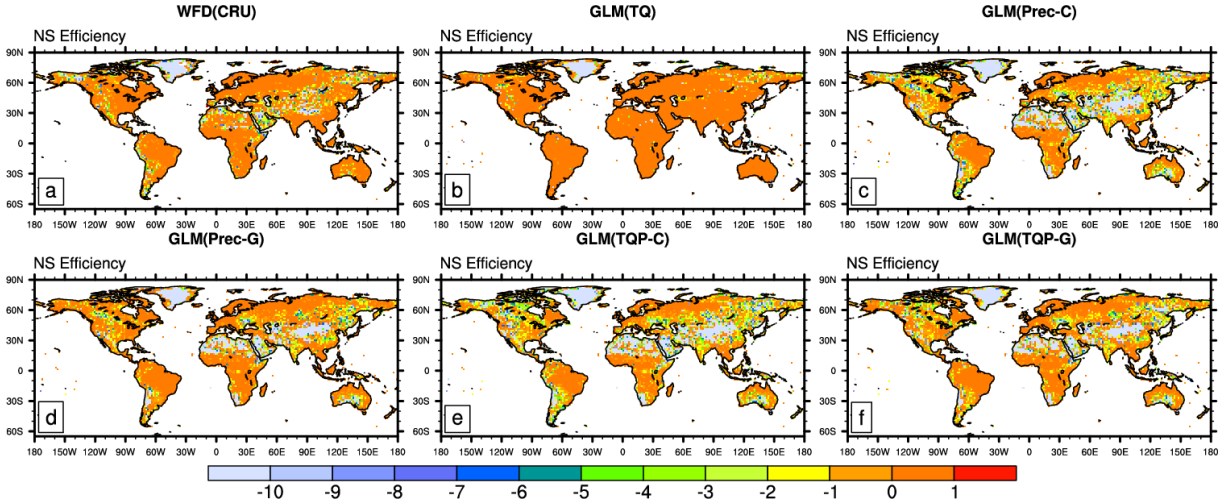

Figure II.16: Nash–Sutcliffe model efficiency coefficient of soil moisture between WFD(GPCC) and: a) WFD(CRU); b) GLM(TQ); GLM(Prec-C); c) GLM(Prec-G); d) GLM (TQ); e) GLM (TQP-C), and f) GLM (TQP-G).

II.3 General discussion and conclusions

The primary objective of this appendix was the assessment the GLM model to reproduce temporal and spatial patterns of air temperature and precipitation from WFD daily data. The secondary goal was to evaluate the effect of them in land surface scheme HTESSEL driven by a mix of WFD and GLM data (air temperature and precipitation). Lastly the statistical spatial structure of large-scale modelled soil moisture from HTESSEL integrations forced by GLM precipitation and air temperature was analysed and compared with soil moisture from reference integration, WFD-GPCC.

Results indicate a tendency for the GLM precipitation input estimates different soil moisture in equatorial zone, Eurasia and eastern North America, and in high latitudes when only GLM temperature is changed. The GLM based weather generator for precipitation and temperature proved to be powerful tools, that successful captured the main aspects of precipitation and temperature variability. Most relevant are the ability to capture mean annual cycles as well as monthly variability.

The large majority of published work with GLM is done at point or small region scale. The quick exploratory test of the application of GLM to a global scale revealed an adequate performance for most locations. Notable exceptions occur at semi-arid areas and polar regions, with a performance clearly below the quality of those done with the WATCH Forcing dataset. May be the use of more covariates, or a regional application of covariate could improve the results.

Appendix III - GEV Distribution

One way to assess the frequency of extreme events is the use of the distribution function of extreme values. The cumulative distribution function of the GEV (Generalized extreme value) distribution can be given by:

$$F(x) = \exp\left\{-\left(1 + k\frac{x-\xi}{\alpha}\right)^{-1/k}\right\} \qquad 1 + k\frac{x-\xi}{\alpha} > 0 \qquad \text{(III.1)}$$

where μ, μ and k are the location, scale and shape parameters, respectively. A particular case of eq. (III.1) for $k \to 0$ is the Gumbel distribution:

$$F(x) = \exp\left\{-\exp\left(1 + k\frac{x-\xi}{\alpha}\right)\right\} \qquad -\infty < x < \infty \qquad \text{(III.2)}$$

The cases with $k > 0$ and $k < 0$ are known as the Frechet, and the negative Weibull distribution, respectively. The parameters of the GEV distribution are ξ (location parameter), α (scale parameter) and k (shape parameter). The Gumbel (GEV type I) is obtained when k=0. For k>0, the distribution has a finite upper bound at $\xi + \alpha/k$ and corresponds to the GEV type III distribution for maxima that are bounded from above.

The GEV theory allows the analysis of extreme precipitation. The parameter k is usually greater than zero for precipitation data, although sometimes the Gumbel distribution is adequate. The parameters of the generalized extreme value distribution (GEV distribution) are calculated by the method of maximum likelihood. The analysis was applied to annual maximum of daily precipitation for each grid point from HTESSEL simulation (ECHAM simulation).

The shape, scale and location parameter of GEV and their parameter standard errors were calculated by gevfit and gevlike MatLAB functions, respectively, from maximum of daily precipitation.

Extreme value distributions are used to model the occurrence of extremes (i.e. extreme deviations from the median of a probability distribution). The parameters for GEV distribution are taken from a model fitted to annual maximum daily mean precipitation from 1965-2000 and 2071-2100.

Scale parameter governs the tail behaviour of the distribution. The shape parameter, k, presents a slight variation, ranging from 1 in the deserts, and -0.4 in some areas of the surface. Positive values of shape parameters (k>0) correspond to Frechet distribution, although in some places the Gumbel distribution was a good option. The parameter standard errors vary between 0.06 and 0.76 in desert of Sarah. They are slightly higher during the control period.

The generalized extreme-value distribution (GEV) incorporated Gumbel's type I (k=0), Frechet's type II (k<0), and the Weibull or type III (k>0) distribution. The GEV distribution has cumulative distribution function:

$$F(x) = \begin{cases} \exp\left\{-\left[1 - k\frac{x-\xi}{\alpha}\right]^{1/k}\right\} & k \neq 0 \\ \exp\left\{-\exp\left[-\frac{x-\xi}{\alpha}\right]\right\} & k = 0 \end{cases} \qquad \text{(III.3)}$$

where $\xi + \alpha/k \leq x < \infty$ for $k < 0$, $-\infty \leq x < +\infty$ for $k = 0$, and $-\infty < x \leq \xi + \alpha/k$ for $k > 0$. Here ξ, α and k are the location, scale, and shape parameters, respectively. Quantiles of the GEV distribution are given in terms of the parameters and the cumulative p by:

$$x_p = \begin{cases} \xi + \frac{\alpha}{k}\left[1 - \left(-\ln(p)\right)^k\right] & k \neq 0 \\ \xi - \alpha\ln\left(-\ln(p)\right) & k = 0 \end{cases} \qquad \text{(III.4)}$$

III.1 L Moments

The L moment estimators for the GEV distribution are:

$$\hat{\xi} = \hat{\lambda}_1 - \hat{\alpha}/\hat{k}\{1 - \Gamma(1+\hat{k})\}$$
$$\hat{\alpha} = \frac{\hat{\lambda}_2 \hat{k}}{(1-2^{-\hat{k}})\Gamma(1+\hat{k})} \qquad \text{(III.5)}$$
$$\hat{k} = 7.8590\, c + 2.9554\, c^2 \qquad c = 2/(3+\hat{\tau}_3) - \log(2)/\log(3)$$

Here the final $\hat{k}$ function is a very good approximation for $\hat{k}$ in the range $(-0.5, 0.5)$.The L moment estimators $\hat{\lambda}_1, \hat{\lambda}_2, \hat{\lambda}_3$ and $\hat{\tau}_3 = \hat{\lambda}_3/\hat{\lambda}_2$ (L skewness) were obtained by using an unbiased estimator of the first three PWMs (probability-weighted moment) defined as:

$$\beta_r = \xi + \frac{\alpha}{k}\left[1 - (r+1)^{-k}\Gamma(1+k)\right]/(r+1) \qquad \text{(III.6)}$$

The unbias estimator of β_r is:

$$b_r = \sum_{i=1}^{n}\left[\frac{(i-1)(i-2)(i-3)\ldots(i-r)}{n(n-1)(n-2)\ldots(n-r)}x_{(i)}\right] \qquad r = 0,1,2,\ldots, \qquad \text{(III.7)}$$

where $x_{(i)}$ are the ordered observations from a sample of size $n\{x_{(1)} \le x_{(2)} \le \cdots \le x_{(n)}\}$ and where $\lambda_1 = \beta_0$, $\lambda_2 = 2\beta_1 - \beta_0$ and $\lambda_3 = 6\beta_2 - 6\beta_1 + \beta_0$.

The moment estimators of the parameters of the GEV distribution are given by:

$$\hat{\xi} = \hat{\mu} - \frac{\hat{\alpha}}{\hat{\kappa}}\{1 - \Gamma(1+\hat{k})\}$$
$$\hat{\alpha} = \frac{\hat{\sigma}|\hat{\kappa}|}{\left\{\Gamma(1+2\hat{k}) - \left[\Gamma(1+\hat{k})\right]^2\right\}^{1/2}} \qquad \text{(III.8)}$$
$$\hat{\gamma} = \text{sign}\,(\hat{\kappa}) \cdot \frac{-\Gamma(1+3\hat{k}) + 3\Gamma(1+\hat{k})\Gamma(1+2\hat{k}) - 2\left[\Gamma(1+\hat{k})\right]^3}{\left\{\Gamma(1+2\hat{k}) - \left[\Gamma(1+\hat{k})\right]^2\right\}^{3/2}}$$

where sign $(\hat{\kappa})$ is plus or minus 1 depending on the sign of $\hat{\kappa}$, $\Gamma()$ is the gamma function, and $\hat{\mu}$, $\hat{\alpha}$, and $\hat{\gamma}$ are the sample mean, standard deviation, and skewness, respectively. There is no explicit solution of the skewness equation for k, which requires an iterative solution. For $\hat{k} > -1/3$ the first three moments of the GEV distribution are finite; the r-th moment exists if only $\hat{k} > -1/r$.

III.2 Maximum Likelihood Estimators

If the set $\{x_i\}$ are independent and identically distributed from a GEV distribution, then the log-likehood function for a sample of n observations $\{x_1, x_2, \ldots, x_n\}$ is:

$$\ln[L(\theta|x)] = -n\ln(\alpha) + \sum_{i=1}^{n}\left[\left(\frac{1}{k} - 1\right)\ln(y_i) - (y_i)^{1/k}\right] \qquad \text{(III.9)}$$

where $\theta = (\xi, \alpha, k)$ and $y_i = [1 - (k/\alpha)(x - \xi)]$. The MLE of ξ, α, and k can be identified by solving the following sustem of equations, which correspond to setting to zero the first derivates of $\ln[L(\theta|x)]$ with respect to each parameter. Thus:

$$\frac{1}{\alpha}\sum_{i=1}^{S}\left[\frac{1-k-(y_i)^{1/k}}{y_i}\right] = 0$$
$$-\frac{S}{\alpha} + \frac{1}{\alpha}\sum_{i=1}^{S}\left[\frac{1-k-(y_i)^{1/k}}{y_i}\left(\frac{x_i-\xi}{\alpha}\right)\right] = 0 \qquad \text{(III.10)}$$
$$-\frac{1}{k^2}\sum_{i=1}^{S}\left\{\ln(y_i)\left[1-k-(y_i)^{1/k}\right] + \frac{1-k-(y_i)^{1/k}}{y_i}k\left(\frac{x_i-\xi}{\alpha}\right)\right\} = 0$$

The Newton-Raphson method was used to solve the likelihood equations above following Hosking [1985] and MacLeod [1989].

III.3 Modelling Data with the Generalized Extreme Value Distribution in MatLAB

The function gevfit returns both maximum likelihood parameter estimates, and (by default) 95% confidence intervals. As an alternative to confidence intervals, we can also compute an approximation to the asymptotic covariance matrix of the parameter estimates and, from that, extract the parameter standard errors, using the function gevlike. To visually assess how good the fit is, we looked at plots of the fitted probability density function (PDF) and cumulative distribution function (CDF).

While the parameter estimates may be important by themselves, a quantile of the fitted GEV model is often the quantity of interest in analysing block maxima data. For example, the return level Rm is defined as the block maximum value expected to be exceeded only once in m blocks. That is just the $(1-1/m)^{th}$ quantile. We can plug the maximum likelihood parameter estimates into the inverse CDF to estimate Rm for m=10, by the function gevinv.